IntechOpen

High Energy and Short Pulse Lasers

Edited by Richard Viskup

HIGH ENERGY AND SHORT PULSE LASERS

Edited by **Richard Viskup**

High Energy and Short Pulse Lasers
http://dx.doi.org/10.5772/61628
Edited by Richard Viskup

Contributors

Akira Endo, Rachit Sharma, Chayan Mitra, Masaki Nakano, Qiang Hao, Tingting Liu, Heping Zeng, Hanieh Fattahi, Valery Losev, Leonid Dmitrievich Mikheev, Mitra Radmanesh, Amirkianoosh Kiani, Mendykhan Khasenov, Tobias Mey, Yuzhai Pan, Abubaker Hassan Hamad, K. Zhukovsky, Juhee Yang, Byunghak Lee, Bosu Jeong, Sergey Chizhov, Elena Sall, Vladimir Yashin, Uk Kang, Guang-Hoon Kim, Lucia Marin-Biolan, Jongmin Lee, Yiqing Huang, Meng Lin, Liang Hu, Fabio Frassetto, Paolo Miotti, Luca Poletto

Notice

First published in Croatia, 2016 by INTECH d.o.o.
eBook (PDF) Published by IN TECH d.o.o.
Place and year of publication of eBook (PDF): Rijeka, 2019.
IntechOpen is the global imprint of IN TECH d.o.o.
Printed in Croatia

Legal deposit, Croatia: National and University Library in Zagreb

Additional hard and PDF copies can be obtained from orders@intechopen.com

High Energy and Short Pulse Lasers
Edited by Richard Viskup
p. cm.
Print ISBN 978-953-51-2606-5
Online ISBN 978-953-51-2607-2
eBook (PDF) ISBN 978-953-51-5078-7

Contents

Preface

The development and the application of the lasers have changed over the last almost 60 years, since the first idea of optical maser explored by Gordon Gould in 1956, and have dramatically moved forward all research.

While owning the first lasers was the sole privilege of highly advanced countries in the world up to the current time, this trend is shifting, and other universities around the globe are extending the capabilities of their departments and divisions dealing with optics, photonics, and lasers and its applications. Initially, the first lasers possessed very low gain in laser emission, low power in continuous wave (cw) or very long laser pulses. During the last half century, we have seen how these trends exponentially graduated, followed by rapid increase in laser power, starting from few milliwatts (1963), watts (1965), kilowatts (the late 1960s), megawatt (1970), gigawatt (pulsed lasers with peak power) (1975), terawatt (the 1980s), and petawatt (first peak power laser) (1996). Exawatt (EW) peak power laser is currently under development within the European project called Extreme Light Infrastructure (ELI) that should be soon ready to deliver extremely high peak EW power laser pulse.

The time duration of laser pulses also evolved from nanosecond (ns) and picosecond (ps) laser pulses in 1970 up to first femtosecond (fs) pulse from dye laser (1980) and later from solid-state laser, Ti/sapphire; the femtosecond pulses were obtained in the 1990s. The first attosecond pulses were reported in 2001 pioneered from high-harmonic generation (HHG) process.

At present we can speak about two main streams in high-power laser technology. In the first stream, we can include large-scale laser laboratories whose main task is to possess extra-high-peak power and/or ultra-short pulse lasers for study of terawatt (TW), petawatt (PW), and future exawatt (EW) laser interactions, acceleration of particles, or hot dense thermal plasma for the laser fusion.

Into the second stream, we can include the small-scale laboratories that are using for its research commercial sources of laser radiation—ns, ps, or fs laser beam.

The main task of this book is to expand the knowledge of the readers in both of these separate streams, which are often perceived as diametrically different and distinct. Why both streams? The answer is relatively easy; this is due to their common essence—the photons and light coherency.

This book is divided into six main sections dealing with short and ultrashort laser pulses, laser-produced soft X-ray sources, large-scale high-power laser systems, free-electron lasers, fiber-based sources of short optical pulse, and applications of short pulse lasers. In each chapter readers can find fascinating topics related to the high energy and/or short pulse la-

ser technique. Naturally it is not possible to include all topics into this book, and neither was it meant like that. This book should serve as an engaging motivation for the readers to search for more scientific publications about this fascinating laser era.

It will be exciting to observe what the further development of lasers and its applications will offer within the next 60 years and how it will influence our everyday life. As the consequence of the progressive development of these technologies, it initially enabled a day-to-day usage of the LED diodes for lighting of our homes or LED displays, up to the applications in nanotechnology for production of electronic chips, in measurement diagnostics, in medicine, in biomedical technology, in mechatronics, in engineering, in automotive and aviation industry, as well as for the security and in defense technology.

In conclusion, I would like to thank all of the authors for conscientious preparation and formulation of individual book chapters that should serve the broad spectrum of readers of different expertise, layman, undergraduate and postgraduate students, scientists, and engineers, who may in this book find easily explained fundamentals as well as advanced principles of particular subjects related to high energy and short pulse laser phenomenon. Each chapter has well-compiled references of particular subject, from reviews to more advance literature, for eager readers who may find more details or further relevant work into each subtopic.

Finally, I would like to wish all the readers a pleasant experience during the reading of this exciting research and gaining new knowledge, which hopefully will be used for further explorations of this topic, with new ideas, research, and applications for our upcoming generation, in peace.

RnDr. Dr. Eng. Richard Viskup, MSc., MPhil., PhD
Johannes Kepler University Linz,
Austria

Section 1

Short and Ultrashort Laser Pulses

Chapter 1

Generation of High-Intensity Laser Pulses and their Applications

Tae Moon Jeong and Jongmin Lee

Additional information is available at the end of the chapter

http://dx.doi.org/10.5772/64526

Abstract

The progress in the laser technology makes it possible to produce a laser pulse having a peak power of over PW. Focusing such high-power laser pulses enables ones to have unprecedentedly strong laser intensity. The laser intensity over 10^{19} W/cm^2, which is called the relativistic laser intensity, can accelerate electrons almost to the speed of light. The acceleration of charged particles using such a high-power laser pulse has been successfully demonstrated in many experiments. According to the recent calculation using the vector diffraction theory, it is possible, by employing a tight focusing geometry, to produce a femtosecond (fs) laser focal spot to have an intensity of over 10^{24} W/cm^2 in the focal plane. Over this laser intensity, protons can be directly accelerated almost to the speed of light. Such ultrashort and ultrastrong laser intensities will bring ones many opportunities to experimentally study ultrafast physical phenomena we have never met before. This chapter describes how to generate a high-power laser pulse. And, then the focusing characteristics of a femtosecond high-power laser pulse are discussed in the scalar and the vector diffraction limits. Finally, the applications of ultrashort high-power laser are briefly introduced.

Keywords: ultrashort laser pulse, high-intensity laser pulse, chirped pulse amplification, charged particle acceleration, tight focusing

1. Generation of ultrashort laser pulses

Femtosecond (fs) high-power laser pulses having a peak power of PW or higher are being produced for the study of laser-matter interactions in the relativistic intensity regime. An ultrashort laser pulse is generated in a mode-locked laser oscillator in the front and its energy is amplified in the following amplifiers. The mode locking is a technique to produce laser

pulses having a pulse duration in the ultrashort time scale such as picosecond (ps) or fs [1, 2]. In the technique, a gain or a loss of an oscillator is modulated in an active or a passive manner. Saturable absorber is a typical optical element modulating a loss in an oscillator. Nonlinear effect dependent on the laser intensity is used to realize a saturable absorption instantaneously responding to the intensity. Under the saturable absorption, a laser pulse experiences a lower loss at a higher intensity. As a result, a higher intensity part of a laser pulse grows much stronger and the temporal duration becomes shorter during the saturable absorption process.

As the pulse duration of a laser pulse decreases, the spectrum of the pulse becomes broader and the pulse encounters the dispersion effect in the medium. The dispersion effect frequently tends to broaden the pulse duration. Without any dispersion control device, the resultant pulse duration is determined by the balance between the pulse shortening due to the saturation absorption and the pulse broadening due to the dispersion. With a proper dispersion control device, the dispersion in a laser pulse is compensated and the pulse duration is mostly determined by the spectral bandwidth of the laser pulse. The minimum pulse duration obtainable with a spectral bandwidth is known as the transform-limited pulse duration. Up to date, sub-10 fs laser pulses from an oscillator are generated by compensating for the dispersion effect with prism pairs [3]. In this section, the basic principle of the mode-locking technique is explained for generating an ultrashort laser pulse and the formation of an ultrashort laser pulse is described.

1.1. Short pulse generation by locking phase of longitudinal mode

When a laser oscillator is formed with an optical length of L, the wavelength of standing waves inside the oscillator is determined by $2L/m$ (m is a positive integer), and alternatively, the frequency by $\nu_m = m \times c/2L$ (or $\omega_m = m \times \pi c/L$). The oscillating frequency in the oscillator is limited by a gain spectrum and it is called the longitudinal mode of the oscillator. A laser pulse can be decomposed into the summation of each electric field having different modes, and the resultant electric field of the pulse can be written as a superposition of oscillating modes:

$$E(z,t) = \sum_m E_m \exp\left\{ i\omega_m \left(t - \frac{z}{c} \right) \right\}. \tag{1}$$

In a free running laser, the phase relation among oscillating modes is random and this is the origin of a short-timescale random intensity fluctuation. The phase relation between modes can be constant (i.e., $\nu_m - \nu_{m-1}$ = constant) under a specific condition. The situation of having the constant phase relation between modes is mentioned as "mode-locked." In this case, the intensity of the resultant electric field is given by

$$I(z,t) = |E(z,t)|^2 = |E_0(z,t)|^2 \frac{\sin^2\{m\omega_m(t - z/c)/2\}}{\sin^2\{\omega_m(t - z/c)/2\}}. \tag{2}$$

As can be seen in Eq. (2), a strong intensity peak can grow in the resonator when oscillating electric fields are added under the mode-locking condition. This is the basic principle for generating a mode-locked laser pulse (see **Figure 1**). As expected in Eq. (2), the pulse duration of a mode-locked laser pulse is determined by the number of oscillating modes. For example, a Ti:sapphire laser that typically produces 10-fs laser pulses contains several hundred-thousand modes in the spectral bandwidth. Up to date, a number of mode-locking techniques have been introduced to generate ps and fs laser pulses, but the underlying physics is basically the same and the question is how to realize locking longitudinal modes.

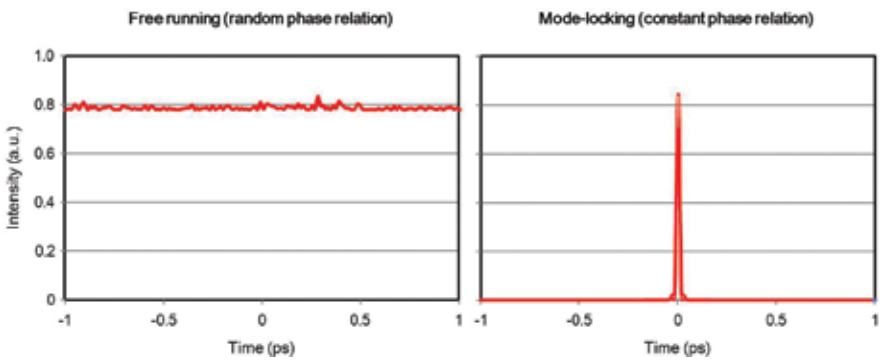

Figure 1. Power at free running and mode-locked operations. When the phase relation is random among longitudinal modes, the intensity has fluctuation because of the beating among modes (left). On the other hand, a single high peak laser pulse is formed under the constant phase relation between modes (right).

1.2. How to lock phases of longitudinal modes

In the early history of mode-locking technique, an active loss element operating at an rf-frequency was installed in an oscillator. The element periodically inducing intensity loss initiates an intensity modulation at a repetition rate corresponding to the round-trip time. A periodic loss at a round-trip time forces to form a laser pulse inside the oscillator. This is known as the active mode-locking technique. Another technique is to introduce a passive-type intensity modulation to the oscillator. Thus, in the passive mode-locking technique, an optical element that has an intensity-dependent loss is installed in the oscillator. The intensity peak in the temporal domain has higher transmittance and energy gain, but a lower intensity part has lower transmittance and energy gain. The lower intensity part is relatively suppressed by the intensity-dependent loss when an intensity fluctuation circulates in the oscillator. As the intensity peak grows, the number of oscillating modes becomes larger and larger in the spectral domain, and the phase relation between modes is automatically locked to form a laser pulse.

1.2.1. Saturable absorption

Some materials have a property that the absorption of light decreases as increasing the light intensity. This kind of material is known as the saturable absorber. In the saturable absorber, the light propagating in the medium transfers its energy to electrons in the ground level and

excites them to higher energy levels. The light intensity decreases as the light propagates in the medium. The light absorption becomes very weak when the number of electrons in the ground level becomes sufficiently low, and the rest of light energy almost transmits the medium. At a time later, the excited electrons spontaneously decay into the ground level and the number of ground electrons is recovered to be ready to absorb energy from light. This phenomenon is known as the saturable absorption. The saturable absorber can be divided into slow and fast saturable absorbers, depending on the recovery time τ_r. In the slow saturable absorber, the recovery time is slower than the pulse duration τ_p and it is assumed to be shorter than the round-trip time under the mode-locking condition. Most saturable absorbers used as the form of solid state and semiconductor have the slow recovery property. In a slow saturable absorber, the intensity-dependent loss is described as follows:

$$\frac{dL}{dt} = -\frac{L - L_0}{\tau_r} - \frac{I}{F_{sat}} L . \tag{3}$$

Here, L_0 is the unsaturated loss and F_{sat} is the saturation fluence. Since $\tau_r \gg \tau_p$, the second term on the right-hand side of Eq. (3), is dominant and the loss exponentially decreases with respect to the pulse fluence $\int_{-\infty}^{t} I(t)dt$. For the slow absorber, two mode-locking regimes are possible depending on the soliton effect. Without the soliton effect, a slow saturable absorber absorbs the leading part of a pulse while the trailing part is less absorbed. The pulse formation is mostly determined by balancing between the net gain and losses. As a result, a pulse profile becomes shortened, and the pulse duration obtainable in this case is estimated by [4]

$$\tau_p = \frac{1.07}{\Delta \nu_g} \sqrt{\frac{g}{\Delta R}} . \tag{4}$$

Here, $\Delta \nu_g$ is the FWHM gain bandwidth, assuming a Gaussian-shaped gain spectrum, and ΔR is the modulation depth. As will be discussed later, the laser pulse can be broadened by the dispersion. Under a proper condition, the shortening and broadening processes can be balanced. Thus, for a slow saturable absorber with the soliton effect, a short laser pulse is generated by the self-phase modulation (SPM) in combination with an appropriate amount of negative dispersion. In this case, the pulse duration can be estimated by [4]

$$\tau_p \approx 1.76 \times \frac{2|D|}{\gamma_{SPM} E_p} . \tag{5}$$

Here, D is the group delay dispersion (GDD) per cavity round trip, γ_{SPM} is the SPM coefficient (in rad/W) per round trip, and E_p is the pulse energy. **Figure 2(a)** and **(b)** shows the pulse formation with the slow saturable absorber. The laser pulse is formed when the loss decreases below the gain. The gain can be either unsaturated or saturated during the saturation absorption process. Under the unsaturated gain, the laser pulse gains energy quickly in the beginning

of the saturation absorption process. When the gain is saturated during the saturable absorption, the decrease in the gain is slightly delayed and thus the net gain exists for the pulse formation.

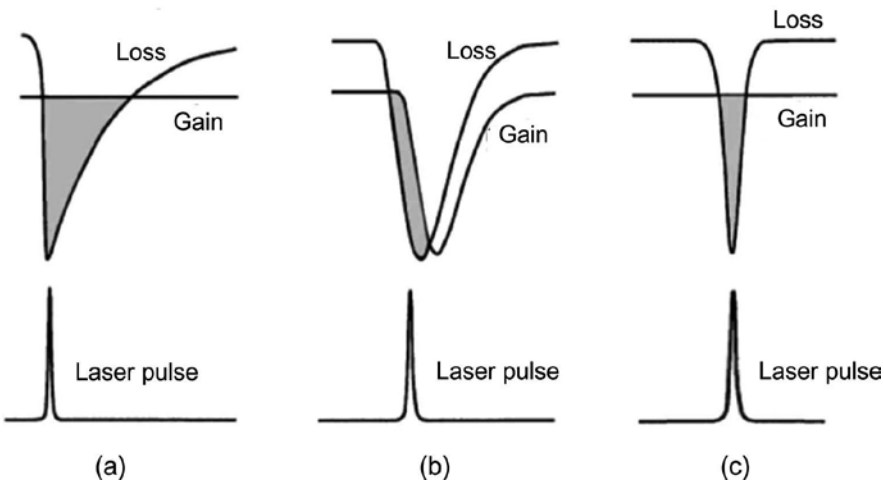

Figure 2. Laser pulse formation with saturable absorbers. The gain is not saturated in (a), but the gain is saturated in (b) during the saturation absorption process. (c) The absorption is quickly recovered in the fast saturable absorber. The laser pulse is formed when the loss decreases below the gain.

The absorption by the material is assumed to be instantaneously recovered in the fast saturable absorber (see **Figure 2(c)**). Thus, a higher intensity in the pulse center experiences a higher transmittance and a lower intensity in the side is suppressed by the saturable absorption. When a fast saturable absorber is installed in an oscillator, the intensity of a transmitted laser pulse increases in a gain medium at a growing rate of

$$\frac{dI}{dz} = \frac{g_0 I}{1 + I/I_{sat}}. \tag{6}$$

Here, I_{sat} is the saturation intensity and g_0 is the unsaturated small signal gain. Thus, the pulse profile is controlled by the intensity, and a higher gain at a higher intensity leads to the pulse shortening. The pulse duration is given by [5]

$$\tau_p \cong \frac{0.79}{\Delta\nu}\left(\frac{g}{L}\right)^{1/2}\left(\frac{I_{sat}}{I}\right)^{1/2}, \tag{7}$$

with the assumption of a hyperbolic secant pulse profile. Here, $\Delta\nu$ is the gain bandwidth, g is the gain defined by $g_0/(1 + I/I_{sat})$, and L is the saturated loss. In reality, the fast saturable absorbing material operating in the femtosecond regime does not exist. Instead, there are materials having a strong nonlinear effect. These materials can possess the property of ultrafast

loss modulation that is induced by the nonlinear effect. The ultrashort pulse formation by these materials can be considered as the mode locking by the fast saturable absorber. In this section, self-phase modulation as a nonlinear effect which induces ultrafast change in reflection or transmission is discussed.

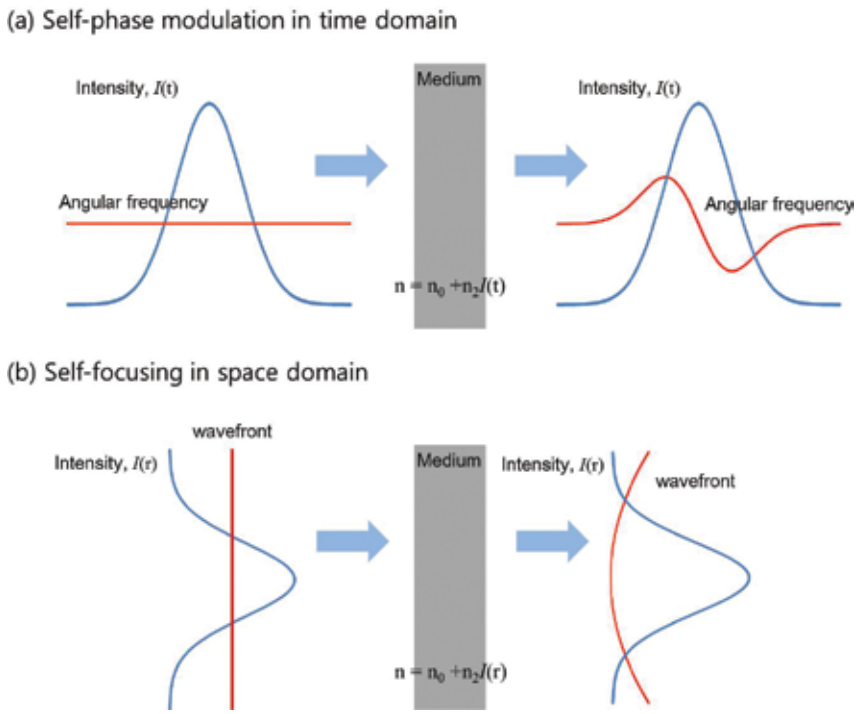

Figure 3. (a) Self-phase modulation in time induces the time-dependent phase variation. The lower angular frequency in the rising part and the higher angular frequency in the falling part are induced. (b) Self-phase modulation in space makes the wavefront quadratically curved.

When a light pulse passes through a medium, it experiences an intensity-dependent change in refractive index. This phenomenon is known as the Kerr effect. The Kerr effect can induce an instantaneous loss modulation and make a medium to act as a fast saturable absorber (see **Figure 3**). In order to derive how the Kerr effect is related with the instantaneous loss modulation, let us consider the refractive index depending on the laser intensity which is given by

$$n = n_0 + n_2 I. \tag{8}$$

Here, n_0 is the normal refractive index and n_2 is the nonlinear refractive index related with the Kerr effect. After a nonlinear medium, the phase of the laser pulse is modified by

$$\phi = nkd = n_0 kd + n_2 Ikd. \tag{9}$$

http://dx.doi.org/10.5772/64526

With a Gaussian pulse profile, $I = I_0 \exp\left(-2t^2/\tau_p^2\right)$, in time, the second term on the right-hand side in Eq. (8) induces time-dependent phase variation, and the angular frequency is calculated as

$$\omega = -\frac{d\phi}{dt} = -\frac{d}{dt}\left(nkd\right) = -n_2 kd\frac{dI}{dt} = \frac{4n_2 kdI_0 t}{\tau_p^2}\exp\left(-2t^2/\tau_p^2\right). \tag{10}$$

Thus, after a nonlinear medium, a laser pulse has lower frequency components in the rising edge and higher frequency components in the falling edge. When a Gaussian pulse having these induced frequency components is coherently added to the original one, the constructive interference occurs at the pulse center, but the destructive interference occurs at the edge. The constructive and destructive interferences induce an instantaneous reflectance change in time. This leads to the pulse shortening effect in time. Nonlinear coupled-cavity mode-locking technique introduced as the additive-pulse mode locking (APM) uses the instantaneous reflectance change induced by the self-phase modulation [6].

A similar phenomenon happens in the spatial domain as well. With a Gaussian beam profile, $I = I_0 \exp\left(-2r^2/w_0^2\right)$, in space, the phase at a radial position, r, is given by

$$\phi(r) = n_2 kdI(r) = n_2 kdI_0 \exp\left(-2r^2/w_0^2\right) \approx n_2 kdI_0\left(1-\frac{2r^2}{w_0^2}\right). \tag{11}$$

with an approximation of $\exp\left(-2r^2/w_0^2\right) \approx \left(1-2r^2/w_0^2\right)$. The phase variation induced by the nonlinear effect makes the wavefront quadratically curved in the radial direction. This means that, after the nonlinear medium with a positive nonlinear refractive index, the phase at a higher intensity becomes retarded to the phase at a lower intensity. The focal length induced by the quadratic curvature is calculated as

$$f_{nl} = -\frac{dr}{d\phi} = \frac{w_0^2}{4n_2 dI_0}. \tag{12}$$

This phenomenon is known as the self-focusing. Kerr-lens mode-locking (KLM) technique employs the self-focusing to induce an instantaneous intensity-dependent transmittance [7]. In the KLM technique, a higher intensity part can be separated by the self-focusing in combination with an aperture. A higher intensity part in time and space domain has a higher transmittance because of the self-focusing. As a result, a higher intensity grows as a laser pulse circulates in a oscillator. The KLM technique forms an ultrashort pulse using this pulse shortening process. In the technique, a gain medium in the resonator also acts as a nonlinear medium that induces the self-focusing.

1.3. Dispersion

When a laser pulse propagates in a material with a length of d, the phase is given by the refractive index, $n(\omega)$, of the medium as follows:

$$\phi(\omega) = n(\omega) \cdot k \cdot d = \frac{n(\omega) \cdot \omega \cdot d}{c}. \tag{13}$$

The refractive index of a medium is a function of the angular frequency and can be expressed as the Sellmeier's formula of wavelength as follows:

$$n^2(\lambda) = 1 + \frac{B_1\lambda^2}{\lambda^2 - C_1} + \frac{B_2\lambda^2}{\lambda^2 - C_2} + \frac{B_3\lambda^2}{\lambda^2 - C_3}. \tag{14}$$

with the help of definition, $\lambda = 2\pi c/\omega$. Here, B_1, B_2, B_3, C_1, C_2, and C_3 are known as Sellmeier's coefficients for material. Because of the refractive index of material depending on the wavelength, the phase of an ultrashort laser pulse after material experiences a distortion known as the dispersion. The dispersion is responsible for the broadening of a pulse duration and the distortion of the pulse profile in time. In order to see the effect of dispersion, let us express the spectral phase depending on the angular frequency as the Taylor expansion,

$$\phi(\omega) = \sum_{m=0}^{\infty} (\omega - \omega_0)^m \left.\frac{\partial^m \phi(\omega)}{\partial \omega^m}\right|_{\omega=\omega 0} = \frac{d}{c}\sum_{m=0}^{\infty} (\omega - \omega_0)^m \left.\frac{\partial^m \{\omega \cdot n(\omega)\}}{\partial \omega^m}\right|_{\omega=\omega 0}. \tag{15}$$

Now, we define derivatives as

$$\left.\frac{\partial^n \phi(\omega)}{\partial \omega^n}\right|_{\omega=\omega 0} = \left.\frac{\partial^n \{\omega \cdot n(\omega)\}}{\partial \omega^n}\right|_{\omega=\omega 0} = D_n(\omega = \omega_0). \tag{16}$$

Because the material has a refractive index depending on the frequency, Eqs. (15) and (16) show interesting properties when a laser pulse with a broad spectrum propagates in the material. The first term, $D_0 = d \cdot \omega \cdot n/c$, in the phase relation represents a phase propagation in the material. The second term defined by $D_1(\omega = \omega_0) = \partial\phi(\omega)/\partial\omega|_{\omega=\omega 0}$ is known as the group delay (GD) that can be interpreted as d/v_g. Here, v_g is the group velocity and represents the pulse propagation in the material. The third term defined by $D_2(\omega = \omega_0) = \partial^2\phi(\omega)/\partial\omega^2|_{\omega=\omega 0}$ is known as the group delay dispersion (GDD) that is responsible for the temporal broadening of a pulse. The temporal broadening by the group delay dispersion is sometimes known as the chirping which originally means the frequency change in time.

Two kinds of temporal broadenings are possible depending on the sign of D_2. When the sign of D_2 is positive, a long (red-like) wavelength component travels faster than a blue-like one in the pulse. On the other hand, a short (blue-like) wavelength component travels faster than a red-like one with a negative sign of D_2. A pulse is said to be positively chirped when a red-like

http://dx.doi.org/10.5772/64526

wavelength component travels faster, or to be negatively chirped when a blue-like wavelength component travels faster (see **Figures 4** and **5**).

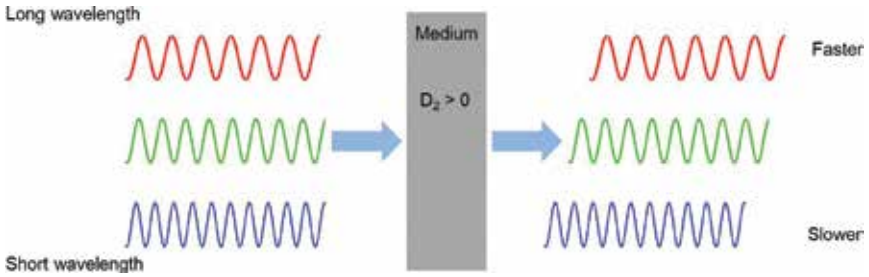

Figure 4. Refractive index depending on the wavelength induces the group delay dispersion (GDD). In the positive GDD, the long-wavelength electromagnetic field travels faster than the short-wavelength electromagnetic field in the medium.

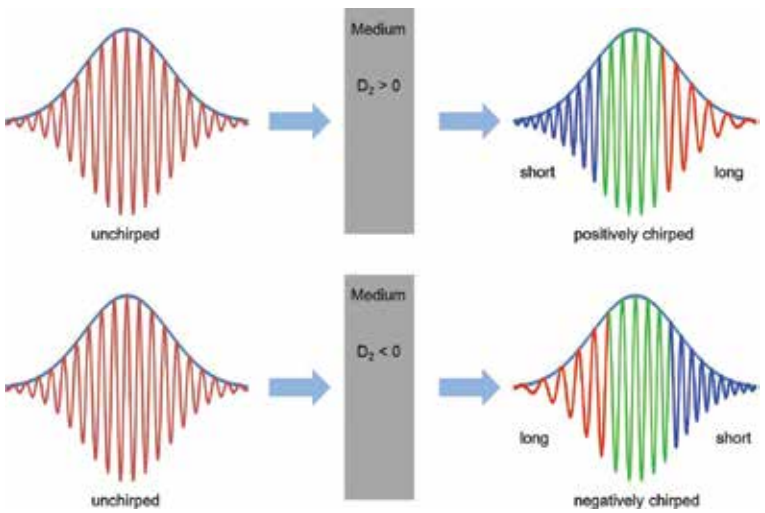

Figure 5. Frequency chirping in the laser pulse. In the upper drawing, a short laser pulse experiences the positive chirping, thus the long-wavelength (red) component arrives faster than the short-wavelength (blue) component in the laser pulse. In the lower drawing, a short laser pulse experiences the negative chirping, thus the short-wavelength (blue) component arrives faster than the long-wavelength (red) component. The pulse duration is broadened by the positive or negative chirping.

Higher-order derivatives in the Taylor expansion affect the pulse profile in time as higher-order dispersions. Even-order dispersions are responsible for the symmetric distortion of a laser pulse in time and odd-order dispersions are responsible for the antisymmetric distortion in the laser pulse. The dispersion control and compensation are key techniques to have a transform-limited laser pulse with a given spectrum. Third-order dispersion (TOD) and fourth-order dispersion (FOD) should be considered to be compensated for the generation of transform-limited pulse.

2. Amplification of ultrashort laser pulses

The energy of a mode-locked laser pulse with a pulse duration of 1 ps or below typically ranges from 10^{-12} to 10^{-10} J. The ultrashort laser pulse cannot be directly amplified in amplifiers because of damage issues in optical elements due to the nonlinear effect and the low-energy extraction efficiency. These hurdles were detoured by employing the chirped-pulse amplification (CPA) technique devised by Strickland and Mourou [8]. The key idea of the CPA technique is to temporarily stretch a laser pulse before amplification, to amplify the energy of the stretched pulse, and finally, after energy amplification, to compress the pulse duration to the original level. The CPA technique was well demonstrated in many systems around the world [9], and now it is used for producing the relativistic laser intensity (>10^{18} W/cm^2).

The control of pulse duration is usually performed by an optical setup which uses the GDD induced by the grating. The stretched pulse duration ranges from few hundreds of ps to nanosecond (ns). The stretched pulse is amplified in a series of amplifier chain including regenerative and/or multipass amplifiers. The output energy can be estimated from the Frantz-Nodvik equation. In this section, the basic principles for controlling the pulse duration and for amplifying the energy are explained.

2.1. Stretching of an ultrashort laser pulse before amplification

The control of pulse duration using the dispersion was first proposed by Treacy [10]. In the proposal, two gratings with a normal separation distance of b are placed in the parallel geometry to induce a negative GDD. The total amount of GDD can be controlled by the separation distance. According to the Treacy's proposal, when a laser pulse passes through an optical setup shown in **Figure 6**, the group delay dispersion (GDD) experienced by a laser pulse is given by

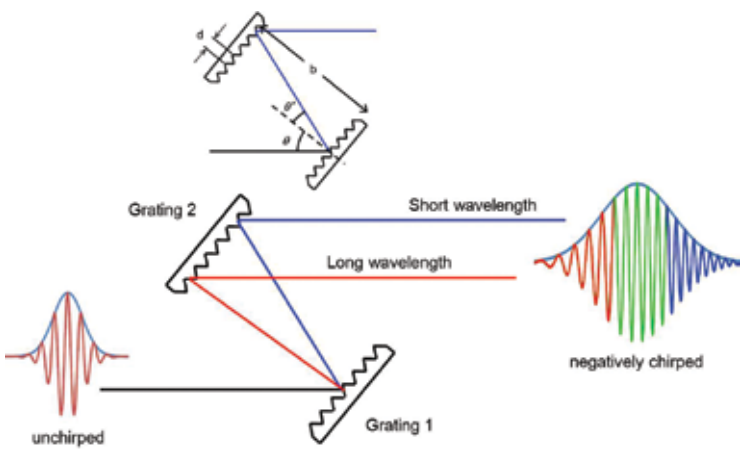

Figure 6. Parallel grating pulse stretching scheme. The parallel grating pulse stretcher introduces a negative GDD to the laser pulse.

http://dx.doi.org/10.5772/64526

$$\left.\frac{d^2\phi}{d\omega^2}\right|_{\omega 0} = -\frac{\lambda_0}{2\pi c^2}\left(\frac{\lambda_0}{d}\right)^2 \frac{b}{\cos^3\theta'(\lambda_0)}. \tag{17}$$

Here, d is the groove spacing of grating and θ' is the diffraction angle. The first-order diffraction is only considered in this case. The diffraction angle is calculated by the grating equation as follows:

$$d\left(\sin\theta' - \sin\theta\right) = \lambda. \tag{18}$$

As shown in Eq. (17), the parallel grating geometry always introduces the negative GDD, and thus the blue-like wavelength component travels faster than the red-like one. The positive GDD can be either introduced by installing a telescope in the parallel grating geometry, which was proposed by Martinez [11]. A telescope is an optical device that induces an angular dispersion. The GDD induced by an angular dispersion is given by

$$\left.\frac{d^2\phi}{d\omega^2}\right|_{\omega 0} \approx -\frac{L_p \cdot \omega_0}{c}\left(\left.\frac{d\alpha}{d\omega}\right|_{\omega 0}\right)^2 \tag{19}$$

with an approximation of $\cos\alpha \gg \sin\alpha$. In the equation, α is the deviation angle at the reference wavelength and L_p is the propagation distance after the surface of an angularly dispersive element. When a laser pulse propagates an optical setup shown in **Figure 7**, the angular dispersion is magnified by a factor of M, which is the magnification of a telescope. Then, the GDD induced by the angular dispersion after the propagation of z' is

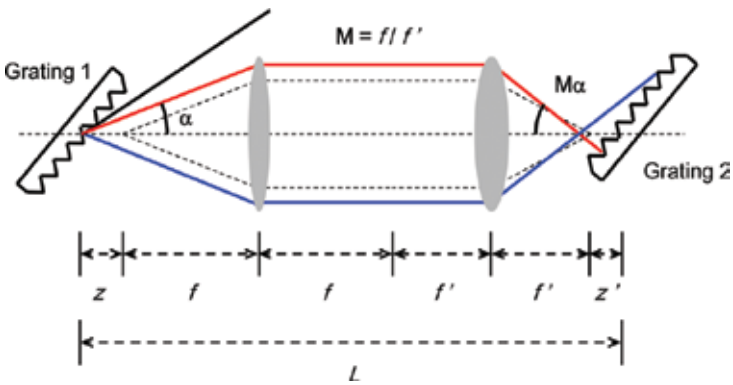

Figure 7. GDD control by the grating pair with a telescope inside. The grating pair with the telescope can induce the positive and negative GDD depending on the total length between gratings. The negative GDD is obtained by $L/2 < (f + f')$. The positive GDD is obtained by $L/2 < (f + f')$.

$$\left.\frac{d^2\phi}{d\omega^2}\right|_{\omega 0} = -\frac{\omega_0}{c}\left(\left.\frac{d\alpha}{d\omega}\right|_{\omega 0}\right)^2 z' M^2. \tag{20}$$

As shown in **Figure 7**, the propagation distance z' is given by $L - 2(f + f')$ and the magnification by f/f'. The positive GDD can be obtained when $L - 2(f + f') < 0$ or $L/2 < (f + f')$. This condition can be met by moving a second grating before the focal point F'. In general, the first lens can be placed at a position of $z + f$. Then, an additional GDD, $\frac{d^2\phi}{d\omega^2}\Big|_{\omega 0} = -\frac{\omega_0}{c}\left(\frac{d\theta'}{d\omega}\Big|_{\omega 0}\right)^2 z$, by an angular dispersion after the propagation of z should be added to Eq. (20) to obtain

$$\left.\frac{d^2\phi}{d\omega^2}\right|_{\omega 0} = -\frac{\omega_0}{c}\left(\left.\frac{d\theta'}{d\omega}\right|_{\omega 0}\right)^2 \left(z'M^2 + z\right). \tag{21}$$

In many cases, a reflecting mirror can be put after the first lens to reduce the cost and space. The positive GDD induced by two grating geometry having a telescope can be compensated for with the parallel grating pair. This is important because the pulse duration stretched by the positive or negative GDD can be recompressed by the negative or positive GDD. This is the principle for stretching and compressing an utrashort laser pulse in the CPA technique. In a common CPA technique, a pulse stretcher introduces a positive GDD to the laser pulse and a pulse compressor introduces a negative GDD. The reason for this is that the material dispersion used in amplifier systems also produces a positive GDD. If a laser pulse has negative GDD by a stretcher, the pulse duration of a pulse is shortened as the pulse propagates in a medium having a positive GDD. This might induce damage on optical elements that the pulse propagates. The other combination that uses a pulse stretcher introducing negative GDD and a pulse compressor introducing positive GDD is also possible. This combination is known as the down-chirped pulse amplification (DCPA) technique and also demonstrated with a grating stretcher and bulk material compressor. Although the DCPA technique works for the energy amplification of an ultrashort laser pulse, the pulse duration of the pulse is somewhat broadened because higher-order dispersions, such as TOD and FOD, induced by media in the laser system remain uncompensated. As mentioned earlier, third-order dispersion (TOD), and fourth-order dispersion (FOD) should be corrected or optimized to obtain a nearly transform-limited pulse duration through the pulse compressor.

The misalignment in the parallelism of a grating induces an additional angular dispersion in the spatial domain. This is known as the spatial chirping. The spatial chirping can easily be examined by monitoring the intensity distribution of a focal spot. If there is the spatial chirping in the laser beam profile, a focal spot is elongated along the chirping direction. Sometimes, the elongation by the spatial chirping is confused with astigmatism in the beam. However, the spatial chirping can be discriminated by the through-the-focus image because the elongation by the spatial chirping is not rotated by 90 degrees while the elongation by astigmatism can be rotated.

2.2. Rate equation

When a laser pulse passes through an amplification medium, the pulse obtains energy gain from the medium. The energy gain comes from a stored energy in the medium which is provided by an external power source. Absorption by the transition between electronic energy

http://dx.doi.org/10.5772/64526

levels is used to store an external energy. Electrons at a lower energy level are excited to a higher energy level through the pumping process. When an electromagnetic wave (photon) with a specific wavelength defined by the atomic energy transition is radiated to an excited atom, the atom emits the same electromagnetic wave (photon) as the incoming one. This means that an incoming electromagnetic wave is amplified in intensity. This dynamics can be described by the rate equation. In order to describe the situation mathematically, let us consider a four-energy-level system shown in **Figure 8**.

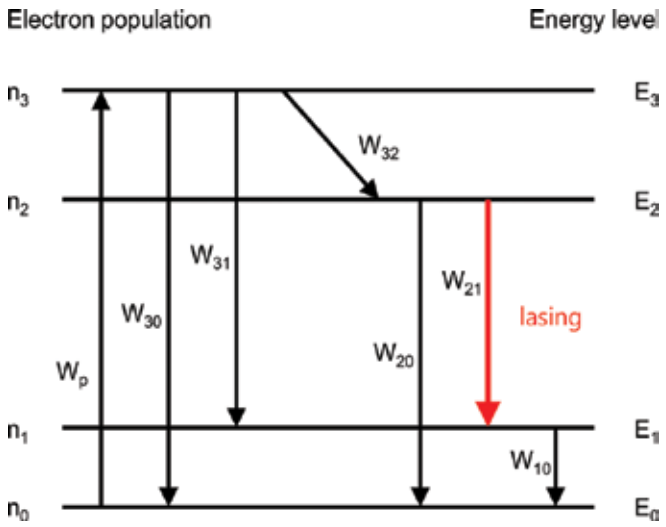

Figure 8. Diagram for energy levels, level transition rate, and the number of electrons at the energy level. In the four-level system, the storage of external energy is accomplished by the absorption due to the electronic transition from level 0 to level 3, and the lasing or energy gain is obtained by the electronic transition from level 2 to level 1.

In a four-level system shown in **Figure 8**, electrons at the lowest energy level 0 are excited to level 3 by the pumping process. The changing rate for the excited electron population increases by the electron population at level 0 and the pumping rate W_p. In a short time, electrons at level 3 lose their energy and decay into level 2 with a transition probability W_{32}. Electrons at level 3 also decay into level 1 and 0 with probabilities W_{31} and W_{30}. The changing rate for electron population at level 2 increases with the number of electrons at level 3 and the transition probability W_{32}, and it decreases with the number of electrons at level 2 and transition probabilities W_{21} and W_{20} to level 1 and level 0, respectively. The main lasing action or energy gain happens with the transition from level 2 to level 1. Under this circumstance, the rate equations for electrons at each level can be expressed as

$$\frac{dn_3}{dt} = W_p n_0 - W_{32} n_3 - W_{31} n_3 - W_{30} n_3 , \tag{22-1}$$

$$\frac{dn_2}{dt} = W_{32} n_3 - W_{21} n_2 - W_{20} n_2 , \tag{22-2}$$

$$\frac{dn_1}{dt} = W_{31}n_3 + W_{21}n_2 - W_{10}n_1 , \tag{22-3}$$

$$\frac{dn_0}{dt} = -W_p n_0 + W_{30}n_3 + W_{20}n_2 + W_{10}n_1 . \tag{22-4}$$

Although rate equations for level 1 and level 0 are not explained here, those can be easily derived from **Figure 8**. In the four-level system, it is assumed that electron populations at levels 1 and 3 are very small because of the rapid transition to other levels, i.e., n_2, $n_0 \gg n_3$, n_1. The total number, n, of electrons is determined by the sum of electron numbers at levels 0 and 2, i.e., $n = n_2 + n_0$. In the steady-state condition, the change of electron populations at levels 3 and 2 are very small as well; so, we assume $\frac{dn_3}{dt} = \frac{dn_2}{dt} \approx 0$. From Eqs. (22-1) and (22-2), we obtain

$$\frac{n_2}{n_0} = \frac{W_p}{(W_{21} + W_{20})} \frac{W_{32}}{(W_{32} + W_{31} + W_{30})} . \tag{23}$$

At level 2, the approximation of $W_{21} \gg W_{20}$ is valid because the lasing action or gain is dominant. And, electron transition from level 3 to level 2 is most dominant to the other transition and thus $W_{32} \gg W_{31}$, W_{30}. Under these conditions, Eq. (23) reduces to

$$\frac{n_2}{n_0} = \frac{W_p}{W_{21}} \tag{24}$$

According to Eq. (24), a laser pulse can have energy gain when $n_2 > n_0$. The population inversion happens when the difference, $\Delta n = n_2 - n_0$, in electron numbers at levels 2 and 0 is positive. Under the heavily pumping condition, most electrons exist in level 2, and the number of electrons (n_2) at level 2 approximately equals n_0. The population inversion is given by

$$\Delta n = n_2 \left(1 - \frac{W_{21}}{W_p}\right) \approx \frac{n}{1 + W_{21}/W_p} . \tag{25}$$

By using the relation of $W_{21}/W_p = I(z)/I_{sat}$, Eq. (25) becomes $\Delta n \approx n/(1 + I/I_{sat})$. When a low-intensity laser pulse propagates in the gain medium, the intensity growing rate is linear with the product of propagation distance and population inversion as shown below:

$$\frac{dI(z)}{dz} = I(z)\sigma_{21}\Delta n . \tag{26}$$

Here, σ_{21} is the emission cross section. By inserting the relation of $\Delta n \approx n/(1 + I/I_{sat})$ into Eq. (26), the growing rate for the intensity becomes

$$\frac{dI(z)}{dz} = I(z)\frac{\sigma_{21}n}{1+I(z)/I_{sat}} \text{ or } \frac{dI(z)}{dz} = g(z)I(z). \tag{27}$$

In Eq. (27), the gain $g(z)$ is defined by $g_0/(1 + I(z)/I_{sat})$ and g_0 is defined by $\sigma_{21}n$. When the intensity of a laser pulse is small enough, the intensity exponentially grows with $I_0 \exp(\int g(z)dz)$. The gain, $\exp(\int g(z)dz)$, at a small input intensity is known as the small signal gain. As the intensity becomes stronger, the growing rate for the intensity starts to be lowered and the intensity linearly grows with gL in the saturation regime, where L is the medium length.

2.3. Energy amplification

The small signal gain describes how much intensity or energy can be achieved with a given small input intensity. The small intensity means an intensity level that does not affect the population inversion. In this subsection, we will describe the energy amplification in an amplifier system. A single-pass energy gain can be measured by putting a detector before and after the amplification medium during the energy measurement experiment. The small signal and single-pass gain, G_0, at the first pass is given by $\exp(\int g(z)dz)$ or simply by

$$G_0 = \exp(g_0 L). \tag{28}$$

Here, g_0 is the measured gain coefficient and L is the medium length. Using the Frantz-Nodvik equation [12], the output energy of a laser pulse at the ith round trip in the amplifier can be expressed by

$$F_i = F_{sat} \ln\left[1 + G_i\left\{\exp\left(\frac{F_{i-1}}{F_{sat}}\right) - 1\right\}\right]. \tag{29}$$

Here, F means the fluence of a laser pulse defined by $\int_{-\infty}^{\infty} I(z, t)dt$ and the subscripts (i and $i - 1$) mean the ith and ($i - 1$)th round trips. F_{sat} is the saturation fluence. In a multipass amplifier system, an amplified laser pulse is reinjected into the amplifier medium. Thus, the gain decreases as the input intensity increases. The reduced gain at the ith round trip can be calculated from the gain and the fluence at the ($i - 1$)th round trip as follows:

$$G_i = \left\{1 - \left(1 - \frac{1}{G_{i-1}}\right)\exp\left(-\frac{F_{i-1}}{F_{sat}}\right)\right\}^{-1}. \tag{30}$$

Figure 9 shows the amplified output energy as a function of the round trip in a multipass amplifier. In the calculation, the Ti:sapphire crystal is assumed as an amplifier medium. The saturation fluence of the Ti:sapphire crystal is 1.2 J/cm^2 and the small signal gain of 3.5 is assumed. The energy exponentially increases in the first few round trips, but the energy

linearly increases as the energy becomes comparable to the saturation energy of the amplifier medium. Finally, the output energy is saturated at a certain energy level which is close to the saturation fluence.

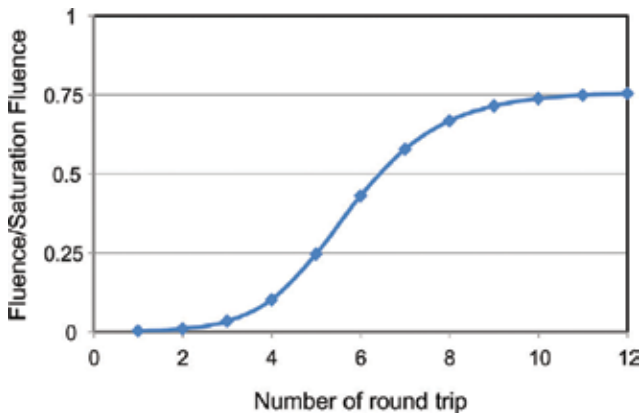

Figure 9. Fluence of the laser pulse with respect to the number of round trip. The input fluence was 1 mJ and the small signal gain was assumed to be 3.5.

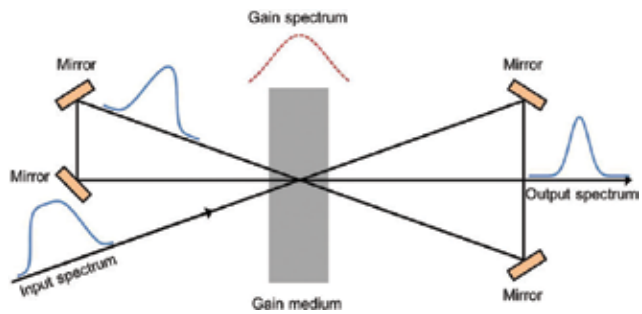

Figure 10. Diagram explaining the gain narrowing effect. The origin of the gain narrowing effect is an un-equal gain at a different wavelengths. The wavelength component at a higher gain grows faster than that at a lower gain. The gain narrowing effect broadens the pulse duration of the compressed pulse.

A series of amplifier system including a regenerative amplifier and multiple-stage amplifiers are used for energy amplification. The final output energy ranges from a couple of J to ~100 J, depending on the peak power level. The pulse energy should be amplified by a factor of ~10^{12} while keeping the pulse characteristics the same. This is not easy because of the gain narrowing effect induced by the different gains at different wavelengths. The gain narrowing phenomenon happens because a wavelength component located at a higher gain becomes stronger than a wavelength component at a lower gain as shown in **Figure 10**. The gain narrowing broadens the pulse duration of a compressed pulse. Several techniques, such as input intensity modulation, wavelength mismatch between the input and gain spectrum, gain saturation, and so on, have been developed to minimize the gain narrowing effect.

The amplified spontaneous emission (ASE) occurred in a large size gain crystal reduces an overall gain and deteriorates the spatial profile of a laser pulse as shown in **Figure 11**. A spontaneous emission traveling in the transverse direction of the gain medium has energy gain before the laser pulse arrives. When the gain and the size of gain medium are small, the ASE is negligible during the amplification process. However, as the size of gain medium is large enough with a considerable gain, the ASE becomes significant. In order to reduce the ASE, the gain medium is enclosed by the light-absorption cooling liquid having a refractive index similar to the gain medium. With the cooling liquid, the spontaneous emission transmits the boundary between the gain medium and cooling liquid, and scattered in the mount. Thus, the ASE reflected from the boundary can be suppressed. Sometimes, the spontaneous emission has enough energy gain even in a single transverse pass. In this case, a delayed pumping scheme can be useful to reduce the ASE.

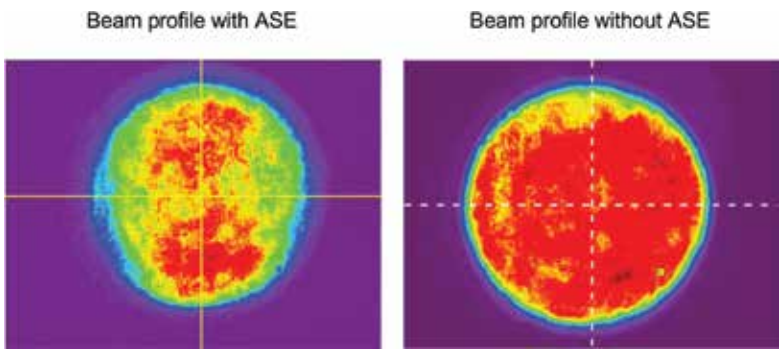

Figure 11. Laser beam profile with and without the amplified spontaneous emission (ASE). The ASE reduces energy gain and deteriorates beam profile.

Since the demonstration of laser in 1960, the laser technology has continuously advanced to build petawatt (PW) laser systems. In 1999, the first CPA PW laser has been demonstrated using a Ti:sapphire/Nd:glass hybrid system [13]. Almost a decade later, 30 fs 1 PW laser operating at 0.1 Hz repetition rate was developed [14] and more recently an amplifier for 5 PW laser system has been successfully demonstrated [15]. Now, fs and 10 PW laser systems are under construction through the European Extreme Light Infrastructure (ELI) program.

3. Focusing ultrashort laser pulses

An amplified and compressed laser pulse is focused on solid or gas target for laser-matter interaction studies. Concave mirrors are generally used and the intensity reaches at a relativistic level, $>10^{18}$ W/cm^2. The size of a focal spot is proportional to the focal length of a mirror and a shorter focal length is preferable to reach a higher intensity. Thus, one particular research interest is to tightly focus a laser pulse to reach an unprecedented intensity level. The paraxial approximation, which is commonly used in calculating focal spots under high *f*-number

conditions, becomes invalid under tight focusing (low *f*-number) conditions. Intensities of a focal spot that have other polarization components different from an incident polarization are assumed to be negligible in the paraxial approximation. However, under tight focusing conditions, intensities at different polarizations increase and modify the overall intensity distribution of a focused laser pulse.

The intensity distributions of all polarization components of a focal spot formed under a tight focusing condition can be calculated by vector diffraction integrals developed by Stratton and Chu [16]. Recently, the intensity distributions of a focused fs high-power laser pulse under a tight focusing condition were intensively examined [17]. In this section, the intensity distributions of a tightly focused laser spot are described. The accurate assessment of the peak power and information on the intensity distribution are beneficial in simulating and predicting the motion of charged particles under a super-strong laser pulse that is provided by a tight focusing scheme.

3.1. Modeling of focusing scheme with low *f*-number parabolic mirror

The parabolic mirror is used as a focusing mirror because of its quadratic surface profile. A linearly polarized (x-polarized) laser pulse having an electric field distribution, $E_{\mathrm{inc}}(\theta_S, \phi_S)$, is incident on a parabolic mirror along the negative *z*-direction (**Figure 12**). By using Sttraton and Chu's vector diffraction integrals, the electric fields at all polarization components can be expressed as follows:

$$E_x(x_P, y_P, z_P) \sim \int_{\theta m}^{\pi}\int_0^{2\pi} d\theta_S d\phi_S E_{inc}(\theta_S, \phi_S) \exp\{-ik\varphi(x_P, y_P, z_P, \theta_S, \phi_S)\} \frac{2f\sin\theta_S}{(1-\cos\theta_S)} \times\left\{1-\frac{\sin\theta_S\cos\phi_S}{1-\cos\theta_S}\left(1-\frac{1-\cos\theta_S}{i2kf}\right)\frac{2f\sin\theta_S\cos\phi_S - x_P(1-\cos\theta_S)}{2f}\right\}, \tag{31-1}$$

$$E_y(x_P, y_P, z_P) \sim \int_{\theta m}^{\pi}\int_0^{2\pi} d\theta_S d\phi_S E_{inc}(\theta_S, \phi_S) \exp\{-i\varphi(x_P, y_P, z_P, \theta_S, \phi_S)\} \frac{2f\sin\theta_S}{(1-\cos\theta_S)^2} \times\left\{\sin\theta_S\cos\phi_S\left(1-\frac{1-\cos\theta_S}{i2kf}\right)\frac{2f\sin\theta_S\sin\phi_S - y_P(1-\cos\theta_S)}{2f}\right\}, \tag{31-2}$$

$$E_z(x_P, y_P, z_P) \sim \int_{\theta m}^{\pi}\int_0^{2\pi} d\theta_S d\phi_S E_{inc}(\theta_S, \phi_S) \exp\{-i\varphi(x_P, y_P, z_P, \theta_S, \phi_S)\} \frac{2f\sin\theta_S}{(1-\cos\theta_S)^2} \times\sin\theta_S\cos\phi_S\left\{1-\left(1-\frac{1-\cos\theta_S}{i2kf}\right)\frac{2f\cos\theta_S - z_P(1-\cos\theta_S)}{2f}\right\}, \tag{31-3}$$

and

$$\varphi(x_P, y_P, z_P, \theta_S, \phi_S) = k(z_P\cos\theta_S + x_P\sin\theta_S\cos\phi_S + y_P\sin\theta_S\sin\phi_S). \tag{31-4}$$

Here, f is the focal length of a mirror. x_P, y_P, and z_P represent positions at vicinities of the focal point. θ_S is the polar angle measured from the positive z-axis and ϕ_S is the rotational angle measured from the positive x-axis. The minimum angle, $\theta_{\min}$, determines the f-number of the mirror. The distance between the source (s) and observation (p) points is expressed as $2f/(1 - \cos\theta_S)$ for the intensity of a laser spot and as $2f/(1 - \cos\theta_S) - \rho_P\{\cos\theta_S \cos\theta_P + \sin\theta_S \sin\theta_P \cos(\phi_S - \phi_P)\}$ for the phase of the spot.

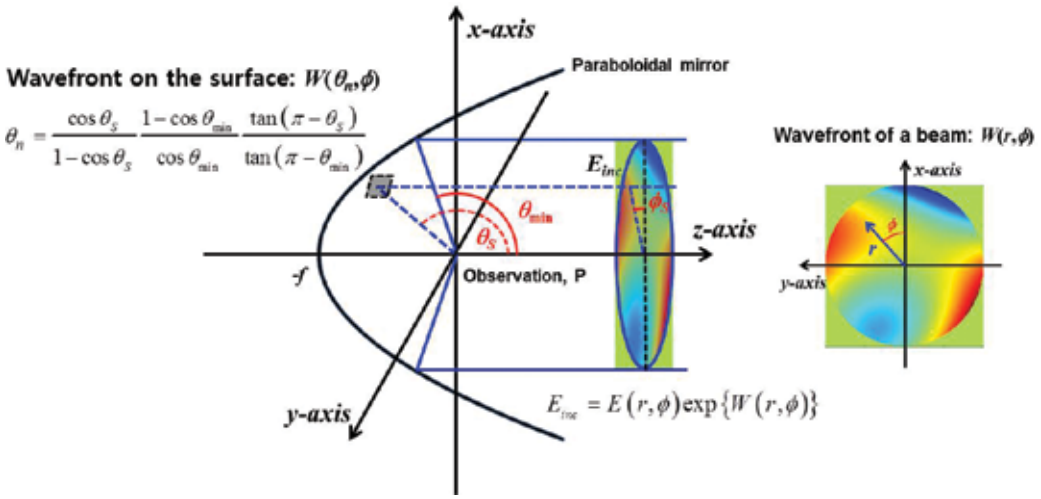

Figure 12. On-axis focusing scheme for an aberrated laser beam with a low f-number parabolic mirror.

The wavefront aberration of a laser pulse is one of the factors that determines the intensity distribution of a focal spot. The wavefront aberration is the phase delay function across the laser beam and included in the incident electromagnetic field of a laser pulse as follows:

$$E_{inc}(\theta_S,\phi_S) = E_0(\theta_S,\phi_S)\exp\{ikW_{inc}(\theta_n,\phi_S)\}. \tag{32}$$

Here, θ_n can be interpreted as a normalized radius defined by $(\pi - \theta_S)/(\pi - \theta_{\min})$. The wavefront aberration is expressed by the Zernike polynomials as $W_{inc}(\theta, \phi) = \sum_{u,v} c_u^v Z_u^v(\theta_n, \phi_S)$. In this case, c_u^v means the Zernike coefficient, and $Z_u^v(\theta_n, \phi_S)$ is the Zernike polynomial for the uth radial and the vth azimuthal orders, respectively. The entire phase function on the mirror surface is modified as $k(z_P \cos\theta_S + x_P \sin\theta_S \cos\phi_S + y_P \sin\theta_S \sin\phi_S) + kW_{inc}(\theta_n, \phi_S)$. For a high f-number case, θ_S and θ_n are almost the same, and the wavefront, $W_S(\theta_n, \phi_S)$, on the mirror surface is almost equivalent to $W_{\text{inc}}(\theta_S, \phi_S)$. However, as the f-number of a parabolic mirror decreases, the wavefront on the mirror surface becomes different from the wavefront of an incident wave. In this case, the normalized radius, θ_n, on the mirror surface is modified and given by

$$\theta_n = \frac{\cos\theta_S}{1-\cos\theta_S}\frac{1-\cos\theta_{\min}}{\cos\theta_{\min}}\frac{\tan(\pi-\theta_S)}{\tan(\pi-\theta_{\min})}. \tag{33}$$

The change in wavefront aberration due to the polarization rotation after reflection from a mirror surface should be considered for the effect of polarization. Thus, after reflection from a parabolic mirror, the normal vector to the wavefront surface is expressed by $2\hat{n}(\vec{S}\cdot\hat{n})-\vec{S}$ as shown below:

$$2\hat{n}(\vec{S}\cdot\hat{n})-\vec{S} = (\hat{x}\sin\theta_S\cos\phi_S + \hat{y}\sin\theta_S\sin\phi_S - \hat{z}\cos\theta_S)W_S(\theta_n,\phi_S) \tag{34}$$

Expressions for normal vectors on a parabolic mirror surface which are given by

$$n_x = \frac{\sin\theta_S\cos\phi_S}{\left[2(1-\cos\theta_S)\right]^{1/2}},\ n_z = \left(\frac{1-\cos\theta_S}{2}\right)^{1/2},\ \text{and}\ n_y = \frac{\sin\theta_S\sin\phi_S}{\left[2(1-\cos\theta_S)\right]^{1/2}} \tag{35}$$

are used in the calculation of Eq. (34). Finally, the wavefront component that propagates to the ρ-direction contributes to the formation of an intensity distribution near the focal plane and is given by

$$\left[2\hat{n}(\vec{S}\cdot\hat{n})-\vec{S}\right]\cdot\vec{k}_\rho = \frac{2\pi}{\lambda}W_S(\theta_n,\phi_S)\left\{\sin^2\theta_S\cos 2\phi_S + \cos^2\theta_S\right\} \tag{36}$$

with $\hat{\rho} = \hat{x}\sin\theta_S\cos\phi_S - \hat{y}\sin\theta_S\sin\phi_S - \hat{z}\cos\theta_S$. But, as expected in Eq. (36), the contribution by the $\{\cdot\}$ term is not significant when $\sin^2\theta_S\cos 2\phi_S \ll \cos^2\theta_S$.

3.2. Coherent superposition of monochromatic fields for femtosecond focal spot

A femtosecond laser pulse typically has a broad spectrum of several tens of nm, thus the effect of broad spectrum of a femtosecond laser pulse on the focal spot should be considered in order to accurately describe the focal spot of a femtosecond laser pulse. The spatial and temporal profiles of a femtosecond focal spot can be calculated by the superposition of monochromatic electric fields near the focal point. The resultant electric fields for a femtosecond focal spot are expressed with spectral amplitude and phase as below (see **Figure 13**):

$$\begin{aligned} E_{x,y,z}(x_P,y_P,z_P) = {} & R_{\lambda 1}\exp(i\alpha_{\lambda 1})E_{x,y,z}(\lambda_1 : x_P,y_P,z_P) + R_{\lambda 2}\exp(i\alpha_{\lambda 2})E_{x,y,z}(\lambda_2 : x_P,y_P,z_P) + \\ & \cdots + R_{\lambda n}\exp(i\alpha_{\lambda n})E_{x,y,z}(\lambda_n : x_P,y_P,z_P) \end{aligned}. \tag{37}$$

Here, R_λ defined by $\sqrt{I_\lambda / I_{\lambda,\max}}$ and α_λ are the relative amplitude and the spectral phase at a given wavelength, respectively. The subscripts (x, y, z) represent the polarization directions and $E_{x,y,z}(\lambda_n : x_P, y_P, z_P)$ induces the monochromatic electric field. Contrary to the monochromatic case, a different field oscillation period at a different wavelength induces a phase mismatch

among waves at different wavelengths and reduces the intensity quickly as the observation position moves away from the origin of the focal plane. The intensity distribution along the propagation direction can be interpreted as the temporal profile of a femtosecond focal spot. Thus, the resultant electric fields, $E_{x,y,z}(x_P, y_P, z_P)$, provide the spatial and temporal (spatiotemporal) intensity distributions of a laser focal spot. The resultant electric fields are numerically calculated. In the calculation, the spectrum is sliced into n components. The monochromatic electric field distributions at all polarization components are obtained from Eqs. (31-1)–(31-4). The relative amplitude ratio and the spectral phase are obtained by the measurement of a laser pulse. After calculating the resultant electric fields, the final intensity distributions at all polarization components become

$$I_{x,y,z}(x_P, y_P, z_P) \propto \left|E_{x,y,z}(x_P, y_P, z_P)\right|^2. \tag{38}$$

This approach provides information on intensity distribution at all polarization components both in temporal and spatial domains and it is also valid under high f-number focusing conditions as well. The sum of all polarization components given by $I_x(x, y, z) + I_y(x, y, z) + I_z(x, y, z)$ is the intensity distribution measured by an image-sensing device.

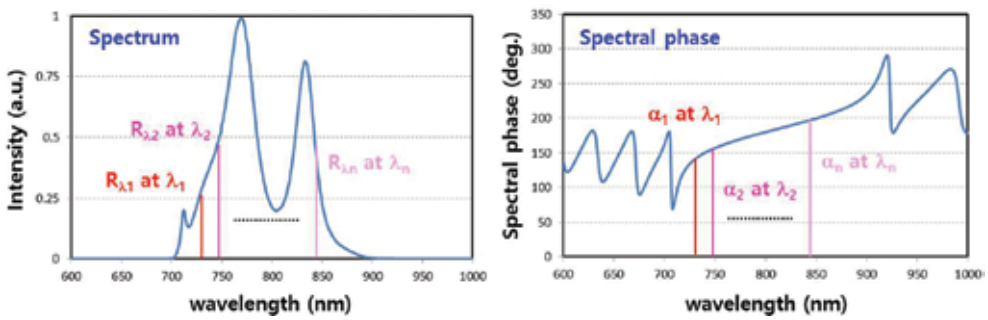

Figure 13. Spectrum and spectral phase for calculating the femtosecond focal spot.

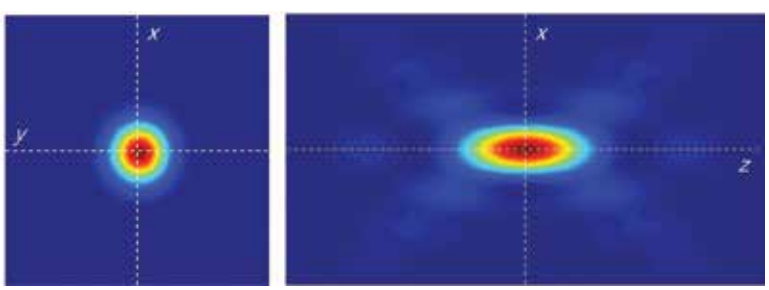

Figure 14. Three-dimensional intensity distribution of the continuous wave and spatially uniform laser beam under loose focusing condition. The x-polarized beam is assumed and the laser beam propagates along the −z direction. Under the far-field approximation, the x-polarization component is only considered to calculate the intensity distribution.

3.3. Intensity distribution in the focal plane and its vicinity

Under the loose focusing condition ($f/\# >> 1$), the intensity distribution having the same polarization as an incoming laser pulse is only considered, and other polarization components ($I_y(x, y, z)$ and $I_z(x, y, z)$) are ignored. In this case, the far-field approximation is applied and the Fourier transform of an incoming electric field, which is derived from the scalar diffraction integral, is widely used to obtain the intensity distribution of a focal spot. **Figure 14** shows the typical intensity distributions in the x-y plane and the x-z plane.

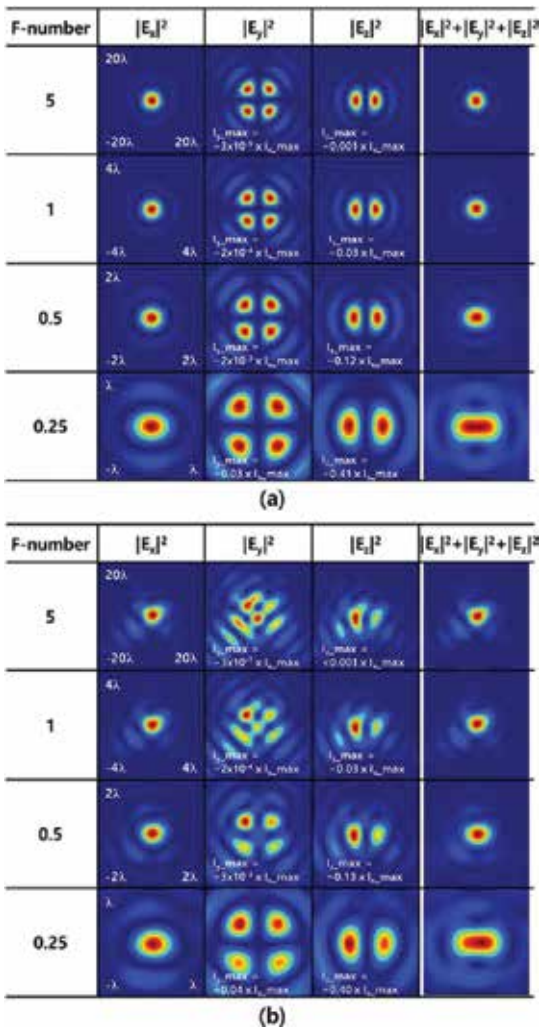

Figure 15. The change in intensity distributions as the f-number decreases. The intensity distributions for a continuous wave and uniform laser beam are calculated in the focal plane. (a) The ideal uniform laser beam profile without wavefront aberration is assumed as an input. (b) The uniform beam profile with wavefront aberration is assumed as an input.

http://dx.doi.org/10.5772/64526

Intensities having other polarizations different from an incoming laser pulse increase under the tight focusing condition. Typical aspects under tight focusing conditions are the increase in the intensity of a longitudinal polarization component and the elongation of a focal spot along the polarization direction. **Figure 15(a)** shows the change in the intensity distribution when the *f*-number of a parabolic mirror decreases from 5 to 0.25. The peak intensity of a longitudinal component, I_z, increases up to 41% of that of I_x under *f*/0.25 condition. But, compared to the x-polarization component, the peak intensity of the y-polarized component, I_y, is still negligible. Because of the increase of intensity in the longitudinal component and the deformation of x-polarized intensity, the resultant intensity is elongated in the polarization direction as shown in **Figure 15(a)**.

Figure 15(b) shows the change of a focal spot for an aberrated laser pulse as the *f*-number decreases. A small amount of wavefront aberration (c_2^{-2} = 0.07 μm, c_3^{-3} = 0.05 μm, c_3^{-1} = 0.04 μm, and c_3^{1} = 0.02 μm) was introduced to the laser pulse to investigate the effect of wavefront aberration on the focal spot. The figure shows how the focal spot of an aberrated laser pulse is influenced by the focusing condition. Under a high *f*-number condition (*f*/5), the focal spot of an aberrated laser pulse is determined by the spatial characteristics of the laser pulse, such as wavefront aberration and spatial profile. The shape of the focal spot was almost same as that obtained with the Fourier transform method because the focusing condition and the amount of wavefront aberration did not violate the far-field and thin-lens approximations. Instead, under lower *f*-number conditions, focal spots are also influenced by the vectorial properties, resulting in the elongation along the polarization direction. With a given amount of wavefront aberration, the peak intensity of a longitudinal component, I_z, increases up to 40% of that of I_x under *f*/0.25 condition. Further calculation with a higher amount of wavefront aberration (c_2^{2} = c_2^{-2} = c_3^{-1} = 0.15 μm) shows that intensity distribution under *f*/0.5 focusing condition was still different from the intensity distribution obtained with the Fourier transform method.

Figure 16 shows spatiotemporal intensity distributions of femtosecond focal spots for an aberrated laser pulse under two different focusing conditions (*f*/3 and *f*/0.5). The Zernike coefficient that are used again include c_2^{-2} = 0.07 μm, c_3^{-3} = 0.05 μm, c_3^{-1} = 0.04 μm, and c_3^{1} = 0.02 μm. In the figure, the intensity distributions in the *x*-*y* plane provide information on spatial profiles of a femtosecond focal spot, and the intensity distributions in the *x*-*z* plane provide information on temporal profiles. By assuming a 12 fs, 10 PW, uniformly circular, and aberrated laser pulse as an input, peak intensities for x-polarized component increases up to ~8.8×10^{22} W/cm^2 for *f*/3 and ~ 2.5×10^{24} W/cm^2 for *f*/0.5, respectively. Under same conditions, peak intensities for longitudinal component rapidly increase to ~3.1×10^{20} W/cm^2 and ~2.4×10^{23} W/cm^2. These intensities along the *z*-direction should be taken into account to better describe the motion of charged particles under an extremely strong EM field that is formed by tightly focusing a femtosecond high-power laser pulse.

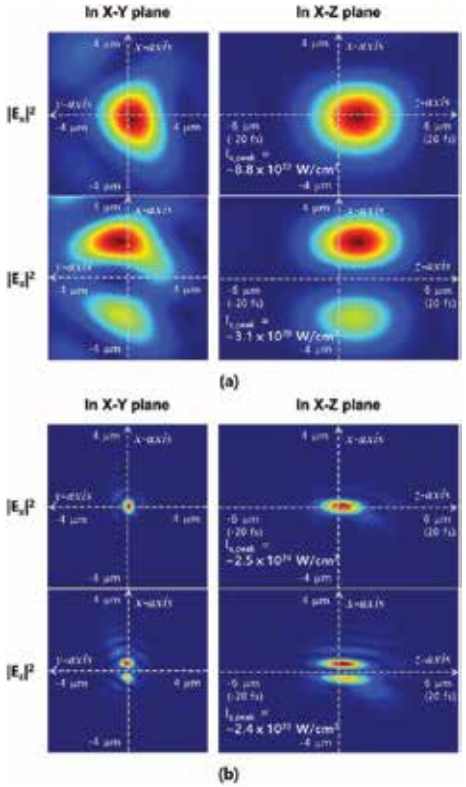

Figure 16. The spatiotemporal intensity distributions of a focal spot with (a) an *f*/3 parabolic mirror and (b) an *f*/0.5 parabolic mirror. The peak intensities of I_x reach ~8.8 × 10^{22} W/cm^2 and ~2.5 × 10^{24} W/cm^2 for *f*/3 and *f*/0.5 focusing conditions, respectively. The transverse intensity distribution is expressed in the *x*-*y* plane and the longitudinal intensity distribution is expressed in the *x*-*z* plane.

4. Interaction of an intense laser pulse with plasma

Under a strong electromagnetic field, the motion of an electron is governed by the Lorentz force as follows:

$$\frac{d\left(\gamma m_0 \vec{v}\right)}{dt} = -e\vec{E} - e\left(\frac{\vec{v}}{c} \times \vec{B}\right). \tag{39}$$

Here, m_0 is the electron rest mass, c is the speed of light, and γ is the Lorentz factor. When the electromagnetic field is not strong enough, the $\frac{\vec{v}}{c} \times \vec{B}$ term on the right-hand side is much less than the first term on the right-hand side and negligible. In this case, the Lorentz force is reduced to $d(m\vec{v})/dt = -e\vec{E}$. By assuming the sine wave for the electric field and replacing the time derivative by $-i\omega$, then the speed of an electron is

http://dx.doi.org/10.5772/64526

$$v = \frac{e}{m\omega} E(t). \tag{40}$$

The maximum speed of an electron is given by $v_{max} = eE_0/m\omega$. By comparing the maximum speed of an electron and the speed of light, we define $\beta = v/c$. In the nonrelativisitic approach, we can consider $\beta = 1$ as a reference. Then, the intensity required for an electron to have the speed of light c is given by

$$I = \frac{\varepsilon_0 c}{2}\left(\frac{2\pi mc^2}{\lambda e}\right)^2. \tag{41}$$

The intensity for the speed of light is ~ 2.14 × 10^{18} W/cm^2 for the 0.8 μm wavelength. In the nonrelativistic approach, the intensity of 10^{18} W/cm^2 is roughly estimated for electrons to have a quiver motion in which the speed is close to the speed of light. The intensity of 10^{18} W/cm^2 is known as the relativistic intensity for the electromagnetic field.

As shown in the previous section, the relativistic intensity is easily obtained by focusing a femtosecond high-power laser pulse. The femtosecond focal spot has a finite extent in the temporal and spatial domains. Let us expand the electric field of a high-power laser pulse in the Taylor series at a position of x_0, then we obtain

$$E_x(r) \simeq E_x(r)\big|_{r=x0}\cos(kz-\omega t) + x\left.\frac{\partial E_x(r)}{\partial x}\right|_{r=x0}\cos(kz-\omega t) + \cdots \tag{42}$$

By inserting the first term on the right-hand side in Eq. (42) into the first term in Eq. (39) and solving the equation, the velocity and the position of electron are given by

$$v_x = -\frac{eE_x(r)\big|_{r=x0}}{m\omega}\sin(kz-\omega t) \text{ and } x = -\frac{eE_x(r)\big|_{r=x0}}{m\omega^2}\cos(kz-\omega t). \tag{43}$$

In order to see the effect of the intensity (or field) gradient of a focused intensity, let us put the expression of x in Eq. (43) into Eq. (42) and consider the Lorentz force again. Then, we obtain

$$m\frac{d}{dt}v_x = -\frac{e^2}{2m\omega^2}\left.\frac{\partial E_x^2(r)}{\partial x}\right|_{r=x0}\cos^2(kz-\omega t). \tag{44}$$

By taking the cycle average of the force, Eq. (44) becomes

$$m\frac{d}{dt}v_x = -\frac{e^2}{4m\omega^2}\left.\frac{\partial E_x^2(r)}{\partial x}\right|_{r=x0}. \tag{45}$$

Eq. (45) means that an electron can be pushed by the intensity or the field gradient. The force due to the intensity gradient is known as the ponderomotive force.

When a high-power laser pulse is focused in a gas target, the target immediately turns into the plasma medium. Electrons in the plasma medium feel the ponderomotive force by the laser pulse in temporal and spatial domains, and those are pushed by a focused laser field and separated from the background ions. The separation of electrons from background ions induces a strong electric field by the space charge effect. The periodic motion of oscillation for electrons occurs around heavy ions as the laser pulse propagates. The resultant pattern of alternating positive and negative charges is known as the plasma wave or laser wake. The laser wake field supports a very strong longitudinal electric field of 1 GeV/cm. Some of returning electrons can be captured into the laser wake and accelerated by the laser wake field up to GeV level. This is a short description of the laser wake field acceleration [18] (**Figure 17(a)**). Recent experiments using the laser wake field acceleration showed the quasimonoenergetic multi-GeV electron beams by focusing petawatt laser pulses [19–21]. The acceleration of electrons to 10 GeV or even 100 GeV level is now being pursued for the development of a compact electron accelerator.

Protons are also accelerated by a high-power laser pulse. In this case, a high-power laser pulse is focused onto a solid target. When a high-power laser pulse is focused on a thin metal target, the target immediately turns into plasma, and electrons in the plasma are accelerated toward the laser beam propagation direction by the ponderomotive force. Then there exists an electric field between accelerated electrons and background ions. The electric field can be used to accelerate protons existing in the metal as impurities [22, 23] (**Figure 17(b)**). At a lower laser intensity, the energy distribution for electrons is broad and the resultant proton energy distribution is also broad. As the laser intensity increases, proton energy distribution can be reduced by a narrow electron energy distribution by the radiation pressure. This is an indirect proton acceleration using electron acceleration. Protons can be directly accelerated to the light speed by an electromagnetic field as shown in Eq. (45). However, because of the proton mass, reaching to the speed of light by directly accelerating proton with an electromagnetic field requires a higher laser intensity up to ~10^{24} W/cm^2, which is sometimes called the ultrarelativistic laser intensity. One of the ways for efficiently reaching at the ultrarelativistic laser intensity is to employ a tight focusing scheme. Based on the recent progress in the high-power laser, the demonstration of ultrarelativistic laser intensity will be possible soon.

Energetic charged particles driven by high-power laser pulses are directly used for medical applications including radiation therapy and imaging. For example, energetic proton beams having an energy range of 100–200 MeV can be used for the radiation tumor therapy [24]. When proton beams is irradiated to tumors in human body, protons dramatically lose their energy and produce x-rays in the tumor. The produced x-ray destroys DNA chains in a tumor cell and eventually kills the tumor cell. Electron beams with an energy range of 6–20 MeV can also be used for treating cancers locating at skin and lip, chest-wall and neck, respiratory and digestive-track lesions, or lymph nodes [25]. Research on stable and reliable production of energetic particles is of great interest for developing a compact particle accelerator for medical applications.

http://dx.doi.org/10.5772/64526

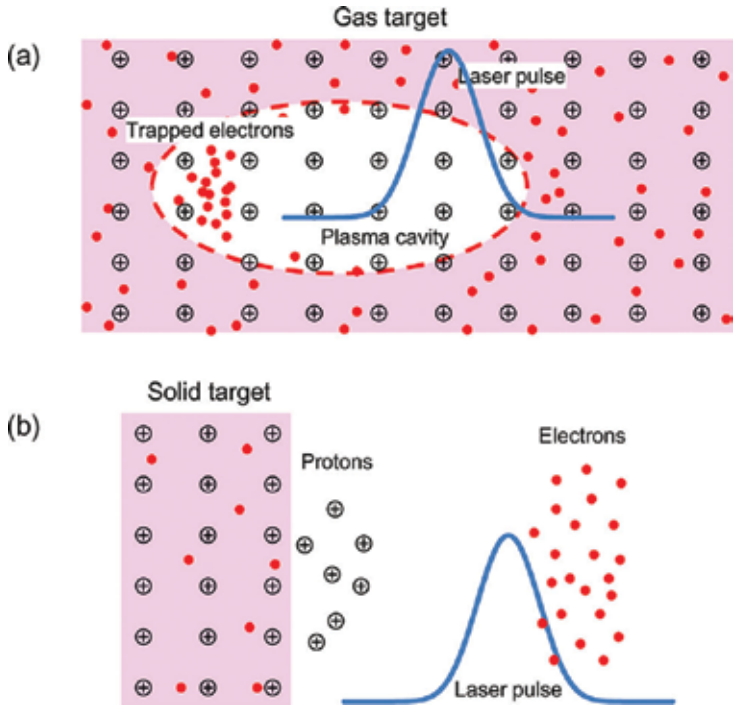

Figure 17. (a) Electron acceleration though the laser wake field. The laser pulse is focused onto the gas target. The electrons are captured in the plasma cavity and accelerated by the cavity. (b). Proton acceleration. The accelerated electrons by the laser pulse pull proton on the metal surface.

High-brightness and high-energy photons (x-ray and γ-ray) can be produced through the laser-plasma accelerator as well. By comparing to the large-scale facilities, such as synchrotron and XFEL, the laser-plasma accelerator produces high-energy photon providing an attosecond temporal resolution and subatomic spatial resolution in a small size and reasonable cost. High-energy photon can be used for research pertaining to ultrafast electron dynamics in atoms, molecules, plasmas, and solids. In the laser-plasma accelerator, many processes producing energetic photon sources, such as high harmonic generation [26], undulator radiation [27], betatron radiation [28], and Compton scattering [29], were proposed and some of them have been experimentally demonstrated. So far, basic applications for high-intensity laser pulses were described. Other interesting research topics related to fundamental physical processes are well described elsewhere [30].

5. Conclusion

The high-power laser facility is being developed for performing research on the laser-matter interaction in the relativistic and ultrarelativistic intensity regimes. The high-power laser pulse immediately ionizes solid and gas targets and makes the target medium plasma. The intensity

can make use of the laser pulse as a small-scale and versatile particle accelerator. This is a primary purpose for developing high-intensity laser facilities. The interaction between an intense laser pulse and energetic charged particles produces high-energy photon as well. Many interesting schemes, such as undulator radiation, betatron radiation, and inverse Compton scattering, have been studied for producing high-energy photons. The high-energy photons can be used in many disciplines including industrial application, medical imaging, nuclear engineering, national security, and so on. As the intensity obtainable with the high-power laser pulse increases over 10^{24} W/cm^2, some of the fundamental physical processes can be investigated by light pulses with an ultrashort time scale. Since the invention of laser, the application field of laser has been dramatically expanded as the laser intensity increases. Now, the acceleration of charged particle by intense coherent light field became possible in the relativistic laser intensity regime, and new era for studying the laser-plasma interaction in the ultrarelativistic laser intensity regime will be open soon.

Author details

Tae Moon Jeong and Jongmin Lee*

*Address all correspondence to: leejm@gist.ac.kr

Handong Global University, Pohang, Republic of Korea

References

[1] L. E. Hargrove, R. L. Fork, and M. A. Pollack. Locking of He-Ne laser modes induced by synchronous intracavity modulation. Appl. Phys. Lett. 1964;5(1):4–5.

[2] C. V. Shank and E. P. Ippen. Subpicosecond kilowatt pulses from a mode-locked cw dye laser. Appl. Phys. Lett. 1974;24(8):373–375.

[3] U. Morgner, F. X. Kartner, S. H. Cho, Y. Chen, H. A. Haus, J. G. Fujimoto, E. P. Ippen, V. Scheuer, G. Angelow, and T. Tschudi. Sub-two-cycle pulses from a Kerr-lens mode-locked Ti:sapphire laser. Opt. Lett. 1999;24:411–413.

[4] R. Paschotta and U. Keller. Passive mode locking with slow saturable absorbers. Appl. Phys. B. 2001;73:653–662. DOI: 10.1007/s003400100726

[5] O. Svelto. Principles of Lasers. 4th ed. New York: Springer; 1998. 343 pp.

[6] H. A. Haus, J. G. Fujimoto, and E. P. Ippen. Structures for additive pulse mode locking. J. Opt. Soc. Am. B. 1991;8(10):2068–2076. DOI: 10.1364/JOSAB.8.002068

[7] D. E. Spence, D. E. Kean, and W. Sibbet. 60-fsec pulse generation from a self-mode-locked Ti:sapphire laser. Opt. Lett. 1991;16:42–44.

[8] D. Strickland and G. Mourou. Compression of amplified chirped optical pulses. Opt. Commun. 1985;6:219–221.

[9] T. M. Jeong and J. Lee. Femtosecond petawatt laser. Ann. Phys. (Berlin). 2014;526(3–4): 157–172. DOI: 10.1002/andp.201300192

[10] E. Treacy. Optical pulse compression with diffraction gratings. IEEE J. Quantum Electron. 1969;5(9):454–458. DOI: 10.1109/JQE.1969.1076303

[11] O. Martinez. 3000 times grating compressor with positive group velocity dispersion: application to fiber compensation in 1.3–1.6 μm region. IEEE J. Quantum Electron. 1987;23(1):59–64. DOI: 10.1109/JQE.1987.1073201

[12] L. M. Frantz and J. S. Nodvik. Theory of pulse propagation in a laser amplifier. J. Appl. Phys. 1963;34(8):2346–2349.

[13] M. D. Perry, D. Pennington, B. C. Stuart, G. Tietboh, J. A. Britten, C. Brown, S. Herman, B. Golick, M. Kartz, J. Miller, H. T. Powell, M. Vergino, and V. Yanovsky. Petawatt laser pulses. Opt. Lett. 1999; 24(3):160–162.

[14] J. H. Sung, S. K. Lee, T. J. Yu, T. M. Jeong, and J. Lee. 0.1 Hz 1.0 PW Ti:sapphire laser. Opt. Lett. 2010;35(18):3021–3023.

[15] Y. Chu, Z. Gan, X. Liang, L. Yu, X. Lu, C. Wang, X. Wang, L. Xu, H. Lu, D. Yin, Y. Leng, R. Li, and Z. Xu. High-energy large-aperture Ti:sapphire amplifier for 5 PW laser pulses. Opt. Lett. 2010;40(21):5011–5014.

[16] J. Stratton and L. Chu. Diffraction theory of electromagnetic waves. Phys. Rev. 1939;56(1):99–107.

[17] T. M. Jeong, S. Weber, B. Le Garrec, D. Margarone, T. Mocek, and G. Korn. Spatio-temporal modification of femtosecond focal spot under tight focusing condition. Opt. Express. 2015;23(9):11641–11656 . DOI: 10.1364/OE.23.011641

[18] T. Tajima and J. M. Dawson. Laser electron accelerator. Phys. Rev. Lett. 1979;43(4):267–270.

[19] N. M. Hafz, T. M. Jeong, I. W. Choi, S. K. Lee, K. H., Pae, V. V. Kulagin, J. H. Sung, T. J. Yu, K.-H. Hong, T. Hosokai, J. R. Cary, D.-K. Ko, and J. Lee. Stable generation of GeV-class electron beams from self-guided laser–plasma channels. Nat. Photon. 2008;2:571–577.

[20] H. T. Kim, K. H. Pae, H. J. Cha, I. J. Kim, T. J. Yu, J. H. Sung, S. K. Lee, T. M. Jeong, and J. Lee. Enhancement of electron energy to the multi-GeV regime by a dual-stage laser-Wakefield accelerator pumped by petawatt laser pulses. Phys. Rev. Lett. 2013;111(16): 165002.

[21] W. P. Leemans, A. J. Gonsalves, H.-S. Mao, K. Nakamura, C. Benedetti, C. B. Schroeder, C. Tóth, J. Daniels, D. E. Mittelberger, S. S. Bulanov, J.-L. Vay, C. G. R. Geddes, and E.

Esarey. Multi-GeV Electron beams from capillary-discharge-guided subpetawatt laser pulses in the self-trapping regime. Phys. Rev. Lett. 2014;113(24):245002.

[22] S. P. Hatchett, C. G. Brown, T. E. Cowan, E. A. Henry, J. S. Johnson, M. H. Key, J. A. Koch, A. B. Langdon, B. F. Lasinski, R. W. Lee, A. J. Mackinnon, D. M. Pennington, M. D. Perry, T. W. Phillips, M. Roth, T. C. Sangster, M. S. Singh, R. A. Snavely, M. A. Stoyer, S. C. Wilks, and K. Yasuike. Electron, photon, and ions beams from the relativistic interaction of Petawatt laser pulses with solid targets. Phys. Plasma. 2000;7(5):2076–2082.

[23] A. Macchi, F. Cattani, T. V. Liseykina, and F. Cornolti. Laser acceleration of ion bunches at the front surface of overdense plasmas. Phys. Rev. Lett. 2005;94:165003.

[24] S. V. Bulanov and V. S. Khoroshkov. Feasibility of using laser ion accelerators in proton therapy. Plasma Phys. Rep. 2002;28:453–456.

[25] K. R. Hogstrom and P. R. Almond. Review of electron beam therapy physics. Phys. Med. Biol. 2006;51:R455–R489. DOI: 10.1088/0031-9155/51/13/R25

[26] I. J. Kim, K. H. Pae, C. M. Kim, H. T. Kim, H. Yun, S. J. Yun, J. H. Sung, S. K. Lee, J. W. Yoon, T. J. Yu, T. M. Jeong, C. H. Nam, and J. Lee. Relativistic frequency upshift to the extreme ultraviolet regime using self-induced oscillatory flying mirrors. Nat. Commun. 2012;3:1231. DOI: 10.1038/ncomms2245

[27] M. Fuchs, R. Weingartner, A. Popp, Z. Major, S. Becker, J. Osterhoff, I. Cortrie, B. Zeitler, R. Hörlein, G. D. Tsakiris, U. Schramm, T. P. Rowlands-Rees, S. M. Hooker, D. Habs, F. Krausz, S. Karsch, and F. Grüner. Laser-driven soft-X-ray undulator source. Nat. Phys. 2009;5:826–829. DOI: 10.1038/NPHYS1404

[28] A. Rousse, K. Ta Phuoc, R. Shah, A. Pukhov, E. Lefebvre, V. Malka, S. Kiselev, F. Burgy, J.-P. Rousseau, D. Umstadter, and D. Hulin. Production of a keV X-ray beam from synchrotron radiation in relativistic laser-plasma interaction. Phys. Rev. Lett. 2004;93:135005.

[29] N. D. Powers, I. Ghebregziabher, G. Golovin, C. Liu, S. Chen, S. Banerjee, J. Zhang, and D. P. Umstadter. Quasi-monoenergetic and tunable X-rays from a laser-driven Compton light source. Nat. Photon. 2014;8:28–31. DOI: 10.1038/NPHOTON.2013.314

[30] G. Mourou, T. Tajima, and S. Bulanov. Optics in the relativistic regime. Rev. Mod. Phys. 2006;78:309–371.

Chapter 2

High-Power Diode-Pumped Short Pulse Lasers Based on Yb:KGW Crystals for Industrial Applications

Guang-Hoon Kim, Juhee Yang, Byunghak Lee,
Bosu Jeong, Sergey Chizhov, Elena Sall,
Vladimir Yashin and Uk Kang

Additional information is available at the end of the chapter

http://dx.doi.org/10.5772/64571

Abstract

A diode-pumped, ultrafast Yb:KYW laser system utilizing chirped-pulse amplification (CPA) in a dual-slab regenerative amplifier (RA) with spectral shaping of seeding pulse from a master oscillator (MO) has been developed. A train of compressed pulses with pulse length of 181 fs, repetition rate up to 500 kHz, and average power exceeding 15 W after compression and pulse picker was achieved.

Keywords: lasers, diode-pumped, laser amplifiers, solid-state lasers, ytterbium lasers, ultrafast lasers, mode-locked lasers, ultrafast lasers

1. Introduction

Energetic (dozens of μJ) optical pulses with femtosecond (fs) pulse lengths and hence ultrahigh focused intensities in the range of 10^{12}–10^{16} Wcm^{-2} are capable of ablating a wide range of materials including metals, semiconductors, ceramics, polymers, biological tissue, and dielectrics [1–3]. Femtosecond laser ablation has been demonstrated to be a powerful tool for various technologies [2]. Due to rapid energy delivery, the laser-plasma interaction is avoided and heat-affected zones in the irradiated targets are strongly localized with minimal residual damage. This allows generation of well-defined microstructures with high quality and reproducibility [1–3].

Femtosecond laser sources based on Yb-doped laser materials became promising tool for various technological and industrial applications including femtosecond lasers. Among Yb-media ytterbium tungstates (Yb:KYW/Yb:KGW), crystals Yb:$KY(WO_4)_2$ (Yb:KYW) or Yb:$KGd(WO_4)_2$ (Yb:KGW) exhibits an attractive set of parameters that makes it as one of the best choices for high-power fs lasers operating around 1 μm [4]. Bandwidth of Yb:KGW/Yb:KYW is sufficient for amplification of sub-200 fs pulses, but typical pulse length on the output of Yb:KYW amplifier system is limited on the level 300–400 fs [5, 6] primarily due to gain narrowing [7, 8]. A promising method to reduce the effect of gain narrowing and to increase the effective gain bandwidth is to combine laser media with separated gain maxima and to overlap broadband gain. Using Yb:KYW crystals with different orientation of crystallographic axes, e.g. N_g- and N_p-cut orientation, this approach has been realized in [9]. Another way for increasing gain bandwidth is using special spectral filters introducing controlled losses at maximum gain spectrum [7].

In this review chapter we present combination of those approaches to a double-slab regenerative amplifier (RA). Each slab is pumped separately, which enables additional possibility to control gain. Furthermore as a seed source, we used high-power master oscillator (MO) based on N_p-cut Yb:KYW crystal with output pulse length ~100 fs and central wavelength agreed well with spectral gain profile of regenerative amplifier. A highly efficient stretcher and compressor based on single transmitted diffraction grating are used for stretching and recompressing initial pulses after master oscillator.

2. Design of high-average power Yb:KGW laser system

The laser was realized as a chirped-pulse amplification (CPA) system [10]. The system shown in **Figure 1** consists of a femtosecond master oscillator (MO) based on Yb:KGW crystal, a

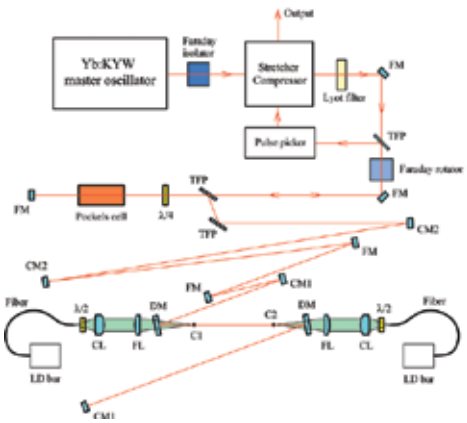

Figure 1. Schematic layout of the femtosecond laser system [15]. FM is a high reflective flat mirror; CM1 is a curved mirror with ROC = 400 mm; CM2 is a curved mirror with ROC = 600 mm; DM is a flat dichroic mirror; FL is a focusing lens; CL is a collimating lens; C1 and C2 are Yb:KYW crystals; TFP is a thin film polarizer; λ/4 is a quarter wave plate; λ/2 is a half wave plate.

http://dx.doi.org/10.5772/64571

common module of stretcher and compressor based on single diffraction grating, a spectral shaper based on Lyot filter, and a dual-slab regenerative amplifier (RA) with combined gain spectra. The system also includes two Faraday isolators: one for isolation of MO against leaking amplified pulses and the other for extraction of laser pulses from the system after RA. To increase the contrast ratio of output pulses according to pre-pulses and post-pulses, we used a pulse picker based on a second Pockels cell and a few thin film polarizers (TFP) with high quality.

2.1. Mode-locked Yb:KYW oscillator

A schematic design of the Yb:KYW oscillator is shown in **Figure 2**. As a gain material, we used a 3×3×3 mm at 5% Yb^{3+}-doped KGW crystal with antireflection-coated ends both for the pump radiation and for the lasing radiation. The crystal was used in an N_g-cut (N_p-cut) geometry, such that the laser polarization was aligned along the N_p axis (N_m axis), respectively. The pump beam from the 100 μm core diameter fiber output was collimated by an achromatic doublet (CL) with focal length F = 60 mm. Then the beam was focused into the laser crystal (LC) by another achromatic doublet (FL) with focal length F = 60 mm through special dichroic coated mirror (DM1) with transmittance of 95%. By using three chirped mirrors with group-velocity dispersion −1350 fs^2 per single pass, the dispersion in the laser cavity was compensated. The details of the optical layout of the laser are described in Ref. [11]. The concave mirror in the second arm of the cavity was replaced by dichroic coated mirror (DM2) with radius of curvature R = 100 mm and a dumper (d) is mounted additionally. Therefore, the pump beam can transmit through the dichroic mirror DM2 and laser operation can be more stabilized without heating optical mounts of mirror M3.

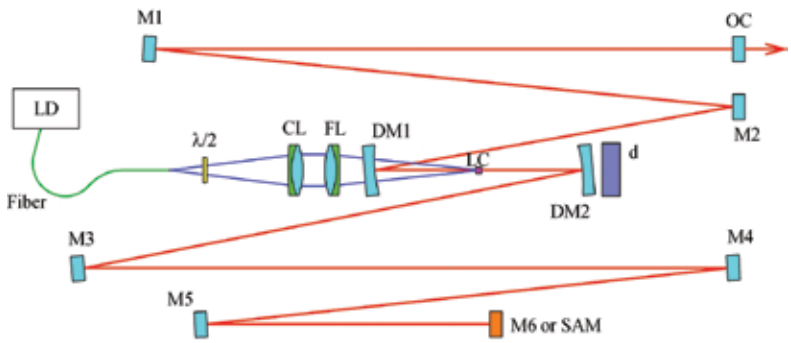

Figure 2. Schematic diagram of the Yb:KYW laser pumped by laser diode (LD) [25]. λ/2 – half wave plate; CL – collimating lens; FL – focusing lens; LC – Yb:KYW laser crystal; DM1, DM2 – spherical dichroic mirror; M1–M6 – cavity mirrors; OC – output coupler; SAM – semiconductor saturable-absorber mirror; d – dumper for blocking and cooling.

As is well known, the transverse size of the pump zone should match with the size of the cavity mode to achieve maximum output power. **Figure 3(a)** shows the schematic drawing to assist in understanding the mode matching between the cavity mode and pump. The pump beam is focused onto the laser crystal as shown in **Figure 3(a)** with black lines and the cavity mode is

depicted as pink color. The position of laser crystal can be defined by the displacement x from the center of the caustic of the beam in the cavity. When the crystal is located in the caustic center of the cavity mode (x = 0 mm), the pump size is larger than the size of cavity mode. Optimal matching of cavity mode and pumped zone in the active media is important for an efficient laser operation. But it is not easy to match the pump size to cavity mode by changing the specification of pump module, because the conventional optics such as fiber and lens are limited in core size and focal length. Instead, mode matching can be easily achieved by displacing the crystal longitudinally along the optical axis. The comparison of the beam profile of pump and cavity mode for both cases of displacement x = 0 mm and 3.5 mm clearly shows this phenomenon as shown in **Figure 3(c)** and **(d)**. The pump profile was obtained by using ZEMAX optical system design software. The cavity mode is assumed to have Gaussian profile and the relevant factors are obtained from LASCAD simulation [12].

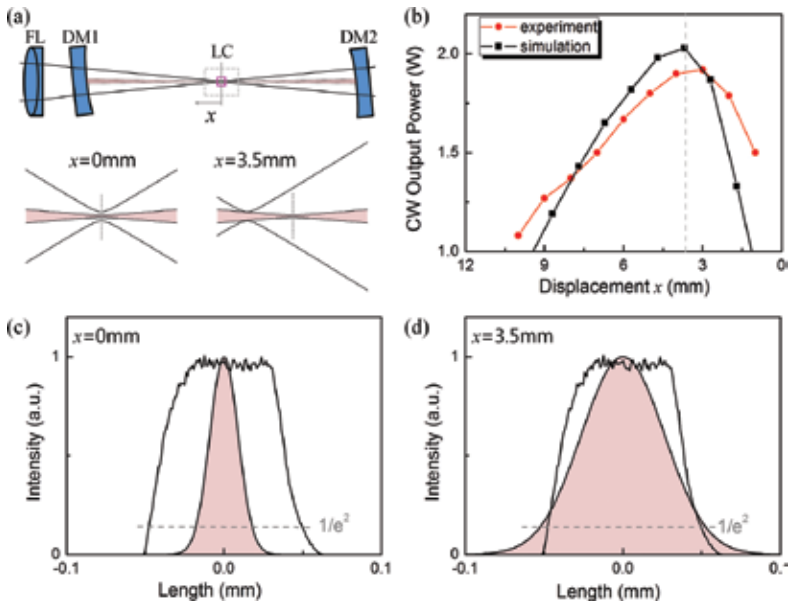

Figure 3. (a) Schematic diagram for the definition of displacement x from the center of the caustic of the beam in the cavity and for the understanding of mode matching. (b) CW output power versus position of laser crystal in the cavity for N_g-cut crystal with OC = 4% of experiment (red) and simulation (black). Comparison of beam profile between pump and cavity mode is shown in the condition of (c) x = 0 mm and (d) x = 3.5 mm [26].

To optimize the position of the crystal, we calculated the CW output power of the resonator as a function of the displacement x as depicted in **Figure 3(b)** with black dots and line by using the LASCAD software. In LASCAD simulation we approximate the top-hat pump spot in focal plane of FL as super-Gaussian distribution in xy plane with diameter 100 μm ($1/e^2$ level). Calculated cavity mode diameter between two curved mirrors DM1 and DM2 significantly changes from diameter 36 μm in a waist to 1.5 mm on the mirror. **Figure 3(b)** shows that the optimal position of the crystal is ~3.5 mm apart from the center of the beam caustic. In order to check the mode matching simulation, we performed the experiment with N_g-cut crystal

http://dx.doi.org/10.5772/64571

oscillator, which was developed previously and in a same condition with simulation [11]. As shown in **Figure 3(b)** with red dots and line, the CW output power is highly dependent on the position of laser crystal and the experimental result coincides well with simulation result. As a note, multimode operation occurred in experiment when the size of the pump beam is larger than TEM_{00} cavity mode and it causes higher CW output power in the displacement region below 3.5 mm.

Not only the position of crystal in the cavity but also the amplification axis of crystal affects the laser operation greatly, because the absorption and emission cross sections of the crystal are quite different according to the orientation of the crystal. In previous work [11], we chose a lasing with $E//N_p$ for antireflection-coated slab crystal because of its broader emission spectrum [6]. We obtained the generator's average power exceeding 1 W at the central wavelength of 1043 nm with a pulse about 90 fs wide. But, according to the literature [13], laser can operate in the shorter wavelength range than 1043 nm by using the different amplification axis of the crystal such as $E//N_m$. For providing effective amplification as a seeding source of CPA femtosecond laser system, the oscillator with shorter wavelength such as 1030 nm is more suitable than the one with 1043 nm [14, 15].

Before going into experiments, we compare the CW output power of the oscillator between N_p- and N_m-polarization with respect to the transmission of output coupler with LASCAD simulation. The corresponding output powers for N_p- and N_m-polarization crystals are shown in **Figure 4(a)** as black and red dots and lines, respectively. From the simulated results, we can conclude that N_m-polarized crystal with 6% output coupler can be used as a candidate for the purpose of seeding source, since only the center wavelength would change with similar output power when we replace the crystal from N_p-polarization (N_g-cut) to N_m-polarization (N_p-cut). And the transmission of 6% of output coupler is chosen due to the output power saturation near 6%.

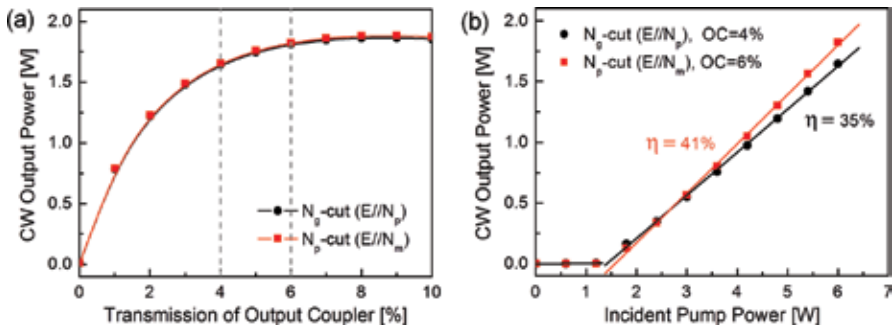

Figure 4. (a) CW output power versus transmission of output coupler for both the N_p- and N_m-polarized crystal. (b) CW output power versus incident pump power for N_p- (OC = 4%) and N_m-polarized crystal (OC = 6%) [26].

Figure 4(b) shows the simulated results according to the replacement from N_p-polarized crystal with 4% output coupler to N_m-polarized crystal with 6% output coupler, in point of the dependence of the average output power on the incident pump power. The slope efficiency

with respect to the incident radiation power is 41% and 35% for each condition. From the simulation results, it is expected to get high output power and high slope efficiency with more suitable center wavelength in the new oscillator.

Based on the simulation results, we conducted the experiment for femtosecond laser based on N_m-polarization Yb:KYW with 6% output mirror and compared the result with the previously reported oscillator based on N_p-polarization Yb:KYW with 4% output mirror in Ref. [11]. An experimental setup of the laser is presented in **Figure 2** as mentioned above. An 8 W high-brightness InGaAs semiconductor injection laser module coupled into optical fiber with a 105 μm core diameter (0.11 NA) and 10 cm length was employed for optical pumping. By using the thermoelectric element (a Peltier cell), the temperature of the laser diode was adjusted for displacing its wavelength to the absorption maximum in the laser crystal. The crystal had a slab design to facilitate efficient heat removal and placed on the optimized position, 3.5 mm apart from the center of the caustic of the beam in the cavity in the longitudinal direction, for size matching of the pump beam and the cavity modes as mentioned. All the laser elements were placed in a compact one-body housing case with 424×214×84-mm size for stable laser operation.

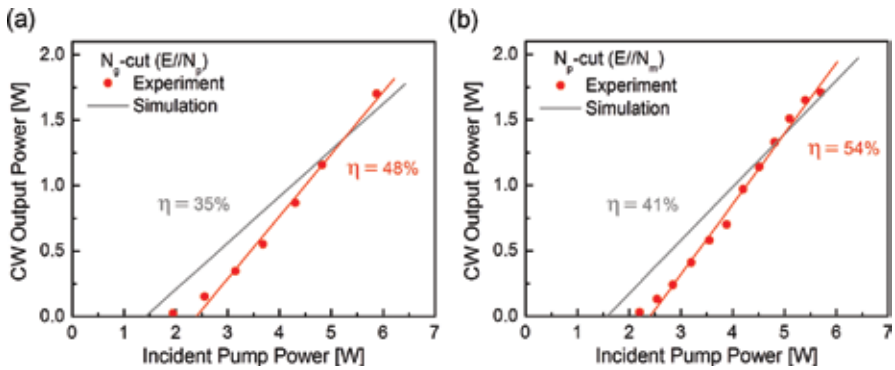

Figure 5. Experimentally observed CW output power versus incident pump power for (a) N_p-polarization (OC = 4%) and (b) N_m-polarization (OC = 6%). Gray lines indicate the calculated values from the LASCAD simulation for comparing with the experimental data [26].

The performance of the laser in the CW regime is shown in **Figure 5** for two cases of (a) the N_p-polarization crystal with 4% output coupler and (b) the N_m-polarization crystal with 6% output coupler. The high slope efficiency of 54% with respect to the incident pump power was achieved with N_m-polarization and the maximum output power exceeded 1.5 W at incident pump power of 6 W. For comparison, simulated CW output powers using LASCAD are also shown in **Figure 5** as grey lines. Computational simulations coincide well with experimental results in general, especially on high incident pump power. The discrepancy in CW output power between experiment and simulation for the low incident pump power can be explained by the characteristics of laser diodes [16]. The center wavelength of diode lasers typically depends on the injection current, operating temperature, and composition. In our case, the operating temperature of the laser diode was adjusted to 36.5°C in high injection current,

http://dx.doi.org/10.5772/64571

corresponding to around 5 W incident pump power in **Figure 5(a)** and **(b)**, for the maximum absorption in the laser crystal. As the injected electric current of laser diode decreases, the pump light shifts toward shorter wavelengths, which results in the decreasing of pump absorption efficiency and low output power of oscillator.

We shall note that for quasi three-level laser media it is difficult to estimate the absorbed pump power experimentally because of the effect of absorption saturation appearing in such media. Therefore we considered the power of launching pump radiation for an estimation of laser efficiency instead of the absorbed power.

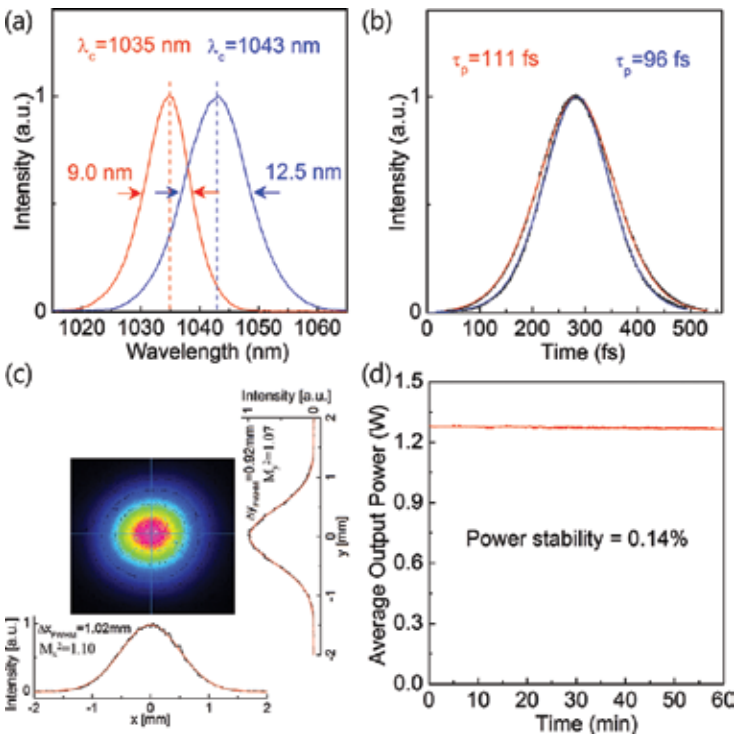

Figure 6. (a) Optical spectra and (b) autocorrelation traces of the 96 fs pulses with center wavelength 1043 nm for N_p-polarization (blue lines) and the 111 fs pulses with center wavelength 1035 nm for N_m-polarization (red lines). (c) Typical spatial pattern of the beam and the corresponding intensity profiles. (d) Measured average output power and its temporal stability [26].

The passively mode-locked regime was realized by replacing a cavity mirror M6 to semiconductor saturable-absorber mirror (SAM) at one end of the resonator in the focal region of a concave mirror (M5) with a radius of curvature R = 300 mm. In **Figure 6(a)** and **(b)**, the measured emission spectra and autocorrelation traces with the fit assuming a sech^2-pulse shape are shown for the N_p- and N_m-polarization as blue and red line, respectively. For N_p-polarization (N_g-cut), 96 fs pulses were generated with the emission spectra centered at

1043 nm. Using N_m-polarization (N_p-cut) crystal, the center wavelength could be changed to 1035 nm with only somewhat longer pulse durations of 111 fs. The time-bandwidth-product of 0.308 is almost close to the Fourier-transform-limited pulse with an intensity profile described by the sech^2 function, and it indicates that dispersion is well compensated and there is no frequency modulation.

Typical spatial pattern of the beam at a distance of 1 m from the output coupler for the new oscillator based on N_m-polarization (N_p-cut) crystal is shown in **Figure 5(c)** with the vertical and horizontal intensity profiles. The cross section is nearly Gaussian with horizontal width 1.02 mm and vertical width 0.92 mm. The M^2 values of the beam are 1.10 in the horizontal plane and 1.07 in the vertical plane, which are fairly close to $M^2 = 1$ for an ideal Gaussian beam.

The thermal lens in the laser crystal did not affect the quality of output beam due to weakness of thermo-optical effects. Our calculations with LASCAD show that the focal lengths of thermal lens are 1273 and 1063 mm for horizontal and vertical directions, respectively, that are much larger than the focal length of focusing mirrors.

Figure 5(d) shows the average output power and its stability of the N_m-polarization oscillator after it was warmed up. We have achieved a maximum average power of 1.27 W at a pulse repetition rate of 87.8 MHz, and it gives a single femtosecond pulse energy greater than 14 nJ. The stability of the output power is to be 0.14% by using the definition such as twice the standard deviation of the measured output power divided by the mean output power.

As a summary, a comparison between the laser performances of the N_p- and N_m-polarization (N_g- and N_p-cut) Yb:KYW materials is given in **Table 1**. Both the relative beam angular stability and relative beam positional stability were measured by using the factors related with angular movement and beam positional movement in accordance with ISO 11670 [17]. The achieved parameters show that the new oscillator with N_m-polarization (N_p-cut) crystal is more stable and powerful with well-defined center wavelength as a seeding source.

	λ_{center} (nm)	$\Delta\lambda$ (nm)	P_{output} (W)	τ_p (fs)	M^2	Power stability (%)	Positional stability (%)	Angular stability (%)
E//N_p,	1043	12.5	0.64	96	1.10 (x)	0.30	0.5 (x)	0.3 (x)
OC = 4%					1.25 (y)		3.2 (y)	1.9 (y)
E//N_m,	1035	9.0	1.27	111	1.10 (x)	0.14	0.1 (x)	0.2 (x)
OC = 6%					1.07 (y)		0.15 (y)	0.3 (y)

Table 1. Comparison between N_p- and N_m-polarization Yb:KYW mode-locked oscillators with 4% and 6% output coupler, respectively.

2.2. Stretcher-compressor

Optical pulse stretcher and compressor are a key subsystem in CPA laser systems [10]. In those systems, the stretcher is used to lengthen optical pulses before the amplification, and the compressor is used to restore original short pulses. In this way, the peak power inside the amplifier cavity can be kept low enough to avoid any damage to the optical element and to

http://dx.doi.org/10.5772/64571

suppress nonlinear distortions on the pulse temporal shape and beam spatial profile due to the self-focusing effect.

Design of stretcher and compressor module in a commercial laser system must provide maximum stretched pulse duration and good output spatial and temporal beam quality in minimum module size. To improve total efficiency and make design of stretcher and compressor more compact, we used in our stretcher-compressor module common transmission diffraction grating and folding mirrors (**Figure 7**).

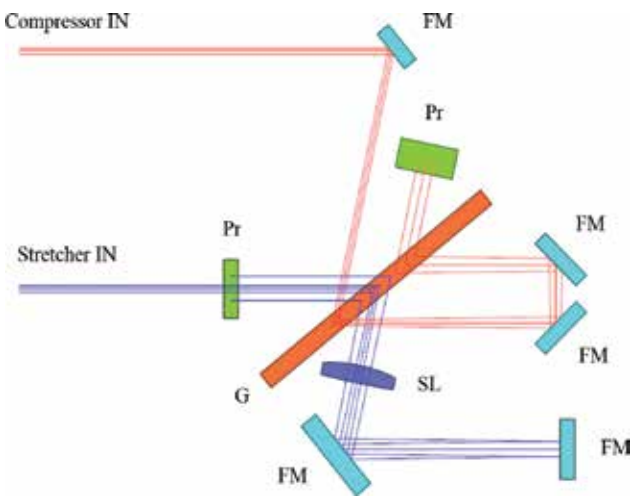

Figure 7. Optical scheme of the stretcher-compressor module based on the transmission diffraction grating (G), spherical lens (SL), right-angle prisms (Pr), and folding mirrors (FM).

In the stretcher and compressor, the beam enters and passes through transmission grating four times. In the stretcher, the beam after first and third passes through diffraction grating is focused and collimated by the spherical lens (SL). To change chirped-pulse duration, we used diffraction grating with two groove densities: N = 1700 mm^{-1} and N = 1500 mm^{-1} and two different spherical lenses with focal length F = 100 mm and F = 200 mm with NA = 0.25 and NA = 0.12, respectively. Using this stretcher-compressor module, we can supply chirped-pulse duration from 50 ps to 300 ps. The compressed pulse duration varies from 230 to 270 fs depending on the optical elements used. Increasing the chirped-pulse duration up to 300 ps using optical elements, the same aperture results in decreasing of spectral pass bandwidth of stretcher up to $\Delta\lambda$ = 14 nm. Spectral clipping introduced by the aperture of optical elements in stretcher affects a recompression pulse duration and its time-bandwidth product.

Increasing the optics aperture is connected with the proportional increase of linear distances in stretcher (spherical aberration introduced by the spherical lens increase with increasing the NA number). Using the diffraction grating with higher groove density to provide more compact design is limited by increasing third-order dispersion.

To check stretcher-compressor module, we used our master oscillator as seed source. We measured initial pulse length and compressed pulse length after the beam passed through the stretcher and compressor. We also measured quality of a beam and total efficiency of the stretcher and compressor. The stretcher-compressor based on 1500 mm^{-1} grating operating with 50 ps chirped-pulse duration provides better degree of recompression and more short output pulse. It is connected with aberration avoiding due to smaller NA number. The measurements made by CCD camera shows that spatial quality of beam did not change after it passed through stretcher and compressor.

Amplification with different pulse durations shows limitation of maximum output pulse energy by Raman scattering excitation and was measured 150 μJ for chirped-pulse duration 50 ps, 300 μJ for 130 ps, and we expected more than 0.5 mJ for 300 ps. Further increase of the pulse energy needs a longer chirped-pulse duration and an increase of the stretcher-compressor module size.

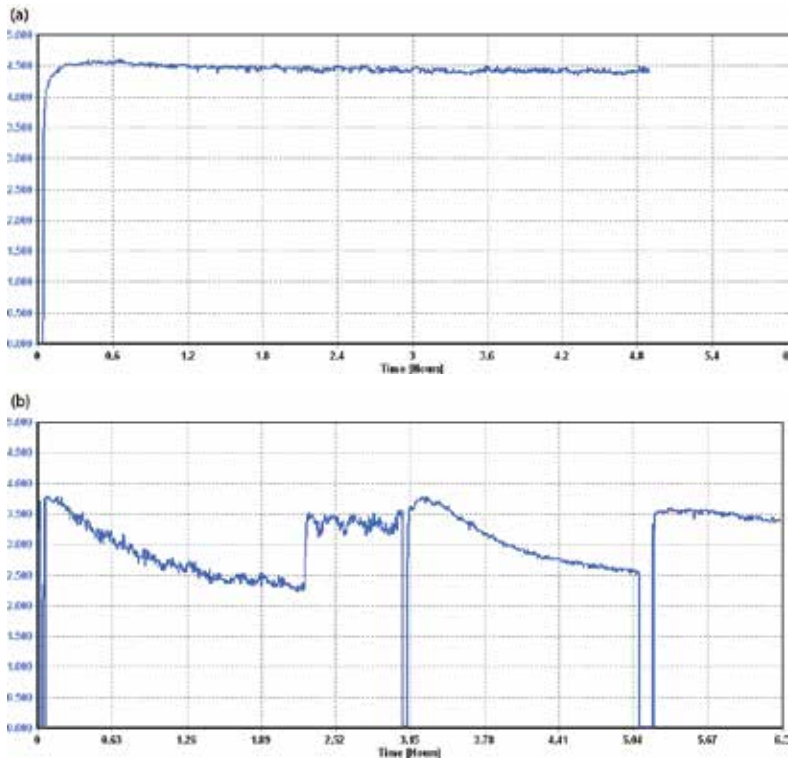

Figure 8. Second harmonic generator output power versus time using thermo stabilized compressor module (a) and nonstabilized one (b).

One of the most important parameters of stretcher-compressor is a temporal stability of compressed pulse duration. Because there is no 100% diffraction grating efficiency, approximately 30% of amplified power is dissipated inside stretcher-compressor module and causes

http://dx.doi.org/10.5772/64571

misalignment of compressor due to thermo expansion of mechanical parts. The requirement for thermomechanical stability of stretcher-compressor elements increases with a decrease in compressed pulse duration. The thermal stabilization of the stretcher-compressor module can significantly improve temporal stability of the compressed pulse. Most dramatically, the effect of temporal detuning of compressor can by observed by the subsequent second harmonic generation. **Figure 8** shows temporal dependence of second harmonic power with water thermo stabilized stretcher-compressor module (a) and without stabilization (b).

In case of no thermo stabilized stretcher-compressor module, fundamental pulse duration increases up to two times with the gradual heating of the module resulting in significant drop of the second harmonic generation efficiency. Thermal stabilization by water cooling the module improves fundamental pulse duration stability and as a result stability of the second harmonic output power.

2.3. Spectral shaping

It is well known that regenerative amplification with high gain leads to the spectral narrowing of amplified pulses [7, 8]. To broaden spectrum in the regenerative amplifier, we tried both extra-cavity and intra-cavity spectral shaping based on the polarization-interference filter (Lyot filter). This technique is well known but it has been used generally for Ti:sapphire lasers [7]. The spectral shaper consists of a birefringent quartz plate placed between two polarizers. To realize optimal spectral shaping, a transmission minimum of the birefringent filter should coincide with maximum gain spectrum and their widths should be close. To fulfill these conditions, a quartz plate with thickness of 8 mm was cut along the optical axis and mounted to the rotation stage to rotate it in two planes for adjusting modulation depth and position of transmission minimum.

2.4. Double-slab laser and amplifier

The maximum average power of solid-state lasers is limited either by the thermal destruction of the active medium or by thermo-optical aberrations [16]. Therefore, one of a few methods of increasing this power in the case of bulk laser media is to increase the active medium length or to use several active elements in the cavity. To increase the average laser power and simultaneously to retain the high spatial quality of the output beam, we used a scheme with two active elements (see also [9, 14, 15]). The optical scheme of a laser amplifier with two active elements made of Yb:KGW crystals with different orientations of optical axes is shown in **Figure 1**. The use of N_p- and N_g-cut crystals, which have different spectral-luminescent characteristics at a corresponding orientation of the polarization vector of generated or amplified beams, makes it possible to widen the gain band and thus generate or amplify more broadband chirped or femtosecond pulses [10]. The crystals were 5 mm long and contained 3% of ytterbium ions, which ensured a good (above 70%) absorption of the pump radiation [18]. Similar to the case of the master oscillator, the pump beam and cavity mode sizes were matched by a longitudinal shift of the active elements. To eliminate possible modulation of the spectrum, the faces of the active elements were antireflection coated and inclined at an angle of ~30′. As pump sources, we used two fiber-coupled laser diode arrays with a maximal output

power of 70 W each. The depolarization of the pump radiation was minimized using a short (30 cm) optical fiber 200 μm in diameter with the numerical aperture NA = 0.22. The pump beams from the fiber output were collimated and focused through dichroic mirrors into the active crystal to a spot with a diameter of about 320 μm, which is close to the diameter of the TEM_{00} cavity mode. This mode was calculated by the well-known ABCD matrix method taking into account the astigmatic thermal lenses induced in the active elements by the pump radiation. Using the LASCAD software, the focal length of these lenses was calculated to be 480–550 mm for the N_p-cut crystal at an incident power of 30 W. These values are in adequate agreement with the literature data [19, 20] and are confirmed by our measurements [18].

We used this laser as a standalone oscillator and as a regenerative amplifier. As an output mirror in this oscillator, we used a thin-film polarizer in combination with a quarter-wave plate, which was rotated to obtain the maximum output power at a given pump power. For electro-optic Q-switching, we used a Pockels cell based on a β-BaB_2O_4 (BBO) crystal and controlled by a special driver. The pulse repetition rate was smoothly changeable from single pulses to 1000 kHz.

The output laser power in the CW regime in the cases of using single active element and two elements simultaneously is shown in **Figure 9** versus the pump power incident on the crystals. The maximum output power was 12.5 and 9 W at a slope efficiency of 47% and 37% for Ng- and Np-cut single crystals, respectively. Note that the output powers for the crystal in which the polarization vector of the laser beam is parallel to the Np axis (E||Np) are higher than for the crystal with E||Nm despite a smaller stimulated emission cross section [9]. This behavior of power can be explained, in our opinion, by different spectral losses in the cavities with crystals emitting at different wavelengths. The maximum output power in the case of two crystals in the cavity was 18.5 W at a pump power of 72 W, which yields the total and slope efficiencies of 25% and 35%, respectively. The laser radiation spectrum was centered at a wavelength of 1035 nm, and its width did not exceed 1 nm.

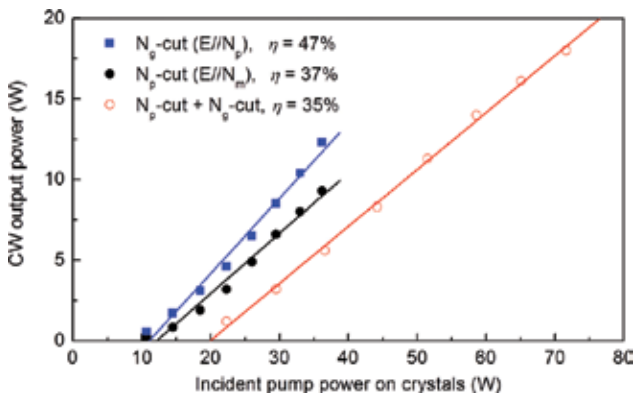

Figure 9. CW output power of laser as a function of incident pump power on crystals in CW mode operation for each single- and dual-slab configuration [15].

http://dx.doi.org/10.5772/64571

Note that the output laser power was maximized in measurements for each pump power by optimal adjustment of the quarter-wave plate. As can be easily shown, this measurement method leads to an underestimation of the slope efficiency. It is this fact that can explain the considerable difference in the slope efficiencies of single- and two-crystal lasers at close total efficiencies (27–30% and 25%, respectively).

The maximum output power obtained in the case of Q-switching reached 16 W at a pulse repetition rate of 100 kHz and 14 W at a repetition rate of 500 kHz (Q-switching time 800 ns). This decrease in the average power with respect to the CW regime can be explained by additional losses introduced by the electro-optic Q-switch. As the Q-switching time decreased to 400 ns, the output power decreased by three times, which obviously occurred because this time was too short for oscillation development. The output pulse duration, determined mainly by a rather long length of the cavity, was 20 ns. The width of the spectrum was 16 nm, which points to a pronouncedly multimode regime. The spectrum had two peaks, at wavelengths of 1035 and 1043 nm, which correspond to the spectral maxima of the gain coefficient for the two used crystals.

We optimized our laser by better alignment of the beam size of pump and laser modes in laser crystals at high pumping levels [21, 22]. This was achieved by moving the mirror CM1 along the optical axis. To suppress thermal losses, the thickness of the laser crystal was also reduced from 2 to 1.2 mm. The optimization results are shown in **Figure 10**. After optimization of the laser, output power increased by 32% from 18.5 to 24.5 W at incident pump power of 110 W.

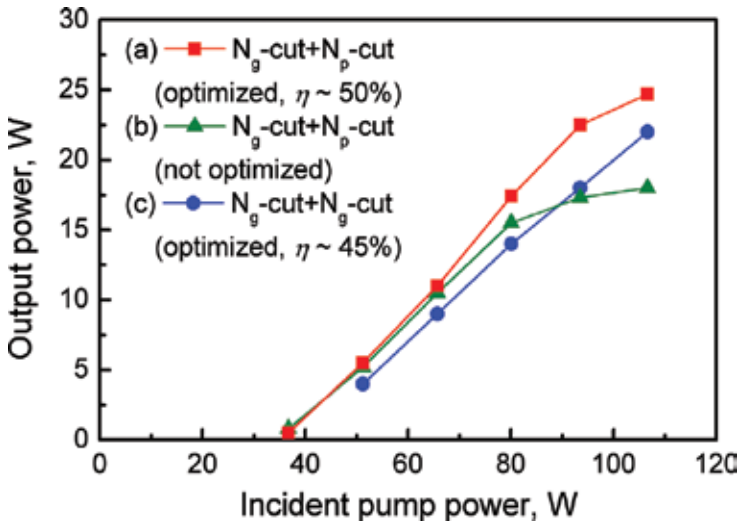

Figure 10. Output power of Q-switched laser versus incident pump power at repetition rate of 200 kHz for different dual-crystal configurations.

Output beam profiles measured using a CCD camera at distance of 1 m from output of compressor was symmetric with beam diameter of 4 mm at e^{-2} intensity level and nearly Gaussian. Increasing of the output power above 15 W resulted in gradual distortion of beam

profile and transformation of beam cross section into the slightly elliptical one as shown in **Figure 5(b)**. However the beam quality parameter M^2 was measured to be below 1.5 even at the laser output power of 22 W as shown in **Figure 11**.

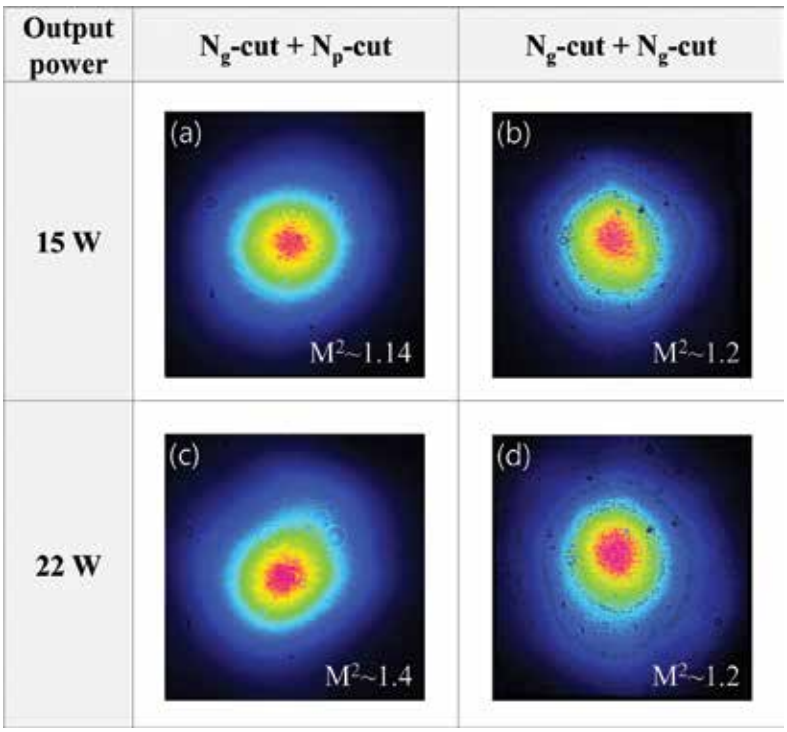

Figure 11. Near-field images and beam qualities M^2 of the laser output for different dual-crystal configurations.

3. Performance of the Yb:KGW femtosecond laser system

When the regenerative amplifier was seeded by stretched pulses, we investigated the output power, spectrum, and pulse shape after compression under different conditions. Our measurements showed that the output power after regenerative amplifier increased up to a value of 21 W when the time gate was increased up to 400 ns and the number of round trips was 24. And then the output power saturated at same value as the time gate increased up to 29 round-trips. It means that the gain is balanced by losses. **Figure 12** shows that the output power is practically linearly dependent on the incident pump power. It means the absence of such parasitic effects restricted gain as amplified spontaneous emission (ASE) and parasitic oscillations. We measured the output power with spectral shaping in addition. There was a power reduction of about 5% when the spectral shaping using a Lyot filter is applied outside the cavity. The compressor and the picker are making a loss, which reduces output power by 25% (15 W).

http://dx.doi.org/10.5772/64571

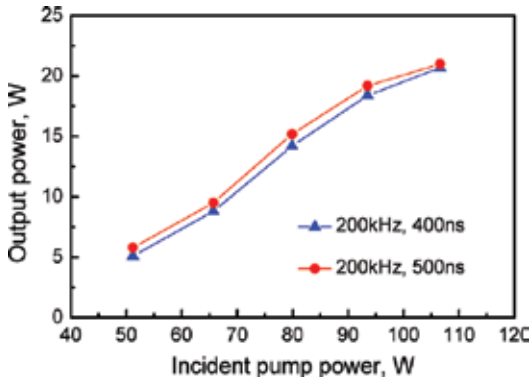

Figure 12. Average output power after RA as a function of incident pump power.

The laser system can operate in the repetition rate range of 50–500 kHz. In this range, the output power is almost not dependent on repetition rate. The single pulse energy was measured to be 300 and 30 μJ at repetition rates of 50 and 500 kHz, correspondently, that is important for microprocessing applications. Maximum pulse energy at 50 kHz was limited by Raman scattering excitation in Yb:KYW crystal that was observed in the experiment [23, 24]. Pulse shape at this repetition rate is distorted phase-modulation of the pulse at the Kerr nonlinearity [24].

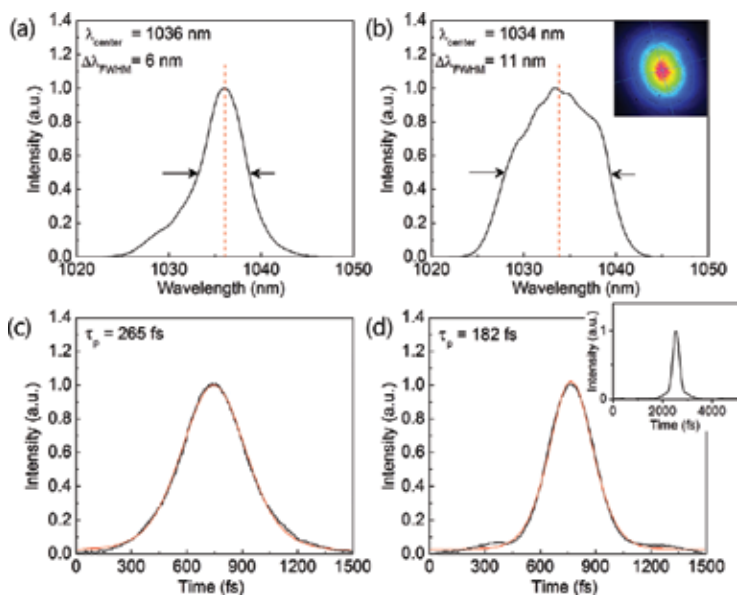

Figure 13. (a, b) Spectra and (c, d) intensity autocorrelation traces (black-experimental data, red-fitting) of output pulses at incident pump power of 67 W and repetition rate of 200 kHz without spectral shaping (a, c) and with spectral shaping (b, d). Insets show the output beam profile (b) and autocorrelation trace in the range of 5 ps (d) [15].

The shape of the output spectrum for equal pump power in both arms of pumping is shown in **Figure 13(a)**. The gain narrowing effect is noticeably well—FWHM spectral width is ~1.5 times narrower compared with the spectrum of master oscillator pulses. Compression provides 265 fs output pulses under this condition as shown in **Figure 13(c)**.

This gain narrowing effect can be suppressed, for example, by making the pump power of Yb:KYW crystals not to be equal [9]. We changed the pump power launched on the N_p-cut and N_g-cut crystals to the ratio of 3:2 [15]. The experimental measurements showed that the spectral width became broader and its shape was modified considerably. In this case, the spectral width was measured to be 11 nm and the pulse length was measured to be 210 fs for assuming sech^2 profile. This method has a drawback that the restriction of pumping power on one crystal results in the restriction of total output power in expense of pulse width. For example the output power dropped 37% in our experimental conditions.

Another way to suppress the spectrum narrowing is to use preliminary spectrum shaping [11] as it was discussed earlier. The example of output spectrum for extra-cavity spectrum shaping by filter Lyot is shown in **Figure 13(b)**. The optical spectrum showed a characteristic "bell" shape with a spectral FWHM bandwidth of 11 nm. Such a bandwidth provides smooth output pulse with width of intensity autocorrelation trace 305 fs that gives the pulse length of τ_{FWHM} = 182 fs for sech^2 pulse profile as shown in **Figure 13(d)**. This pulse length is close to the pulse length of 160 fs defined by aberrations in the stretcher-compressor module. To measure the ultrashort pulse width, we used a PulseCheck autocorrelator (APE GmbH). The inset of **Figure 13(d)** shows that there is no noticeable peak beyond the range of 1.5 ps.

Inserting a spectrum shaper inside the cavity of regenerative amplifier, we obtained approximately the same spectral width but less output power of about 20%. It is connected with accumulated effect of intra-cavity losses by Lyot filter inside the cavity. Thus combination of Lyot filter outside the cavity as a spectral shaper and identical pump power for two slabs in the dual-slab regenerative amplifier provides optimal condition of output power and pulse length.

Beam quality M^2 of output beam was below 1.2 at output power <12 W that allows the beam focusing to small spot size of 5–10 μm. High average output power, with more than tens of μJ, and beam quality are important for industrial microprocessing applications.

4. Microhole drilling for processing drawing dies using ultrafast Yb:KGW laser

Laser micromachining techniques are currently used due to the broad applications across the manufacturing sectors. Among the major applications, laser microhole drilling and cutting have much attention. For microhole drilling, the conventional fabrication method, lithography, which requires advanced facilities and numerous multiple steps, is limited in material type and geometry. Currently used drilling and cutting with nanosecond (ns) or longer pulsed laser are always accompanied with contamination to the surrounding material, melt zone, and

http://dx.doi.org/10.5772/64571

recast layer. Although the geometrical precision could be improved by using ns laser techniques, the quality and precision achievable are still limited due to the subsequently uncontrolled deposition of the melt. Due to the high energy input and thermally induced stress, drilling and cutting using picosecond pulsed laser still have disadvantages, e.g. cracks and heat-affected zone in the surrounding area. Not only the accuracy but also the reliability of the process is affected. For ultrafast lasers, energy deposition occurs on a timescale that is short compared to atomic relaxation processes. Ultrafast lasers suppress thermal diffusion and thus reduce heat-affected zone.

When processing transparent materials with ultrafast laser, the high intensity of focal volume induces multiphoton or tunnel ionization, and then subsequent electron heating or avalanche ionization, which gives rise to the efficient absorption of light. This phenomenon is observed by the nonlinear nature of the ultrafast laser interaction with the transparent materials. This generates the unique capability of transparent material processing using ultrafast laser.

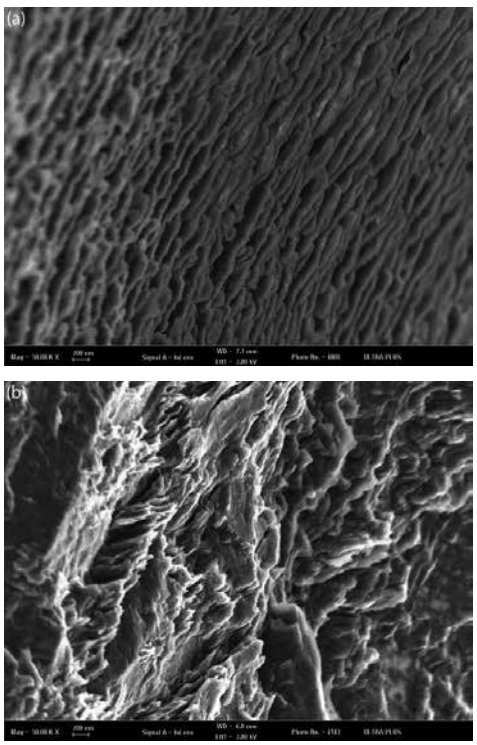

Figure 14. Scanning electron microscope (SEM) views of the structure on bearing land in drawing dies (a) using femtosecond (fs) laser and (b) using nanosecond (ns) laser.

Its promising application is drawing dies-hole drilling. Wire drawing is a deformation and metalworking process used to reduce the cross-section of a wire by pulling the wire through a drawing die. For drawing very fine wire, a single crystal diamond die is used. The drawing die consists of three zones: cone-shape entrance, bearing land, and back relief. The die bearing

determines the size of the wire. As demand for microwire increases across the manufacturing sectors, large scale machines are currently used to produce wire of microlevel, but it is not economical in an industry. Micromachining with ultrafast laser, which made the hole size small, has been reported. Smooth surfaces, also, are generally preferred for precision machining. **Figure 14** shows the SEM view of the bearing surface of drilled hole in dies. The comparison with fs and ns laser drilling results shows the advantage of fs laser drilling. **Figure 14(a)** shows a ripple for which spacing is generally <200 nm. The orientations of the ripple structures are parallel to each other. Similar ripple structure has been observed in various materials for fs laser drilling. Uneven and rough structures are shown in **Figure 14(b)**. It is clear that the material removal during the dies-hole drilling is accomplished by the formation of melt. Compared with two methods, micromachining with ultrafast laser creates much cleaner and smoother hole.

Ultrafast laser micromachining is an emerging technology for high-precision and cold-ablation material processing. For its advantages and potential uses, suitable ultrafast laser and laser operating parameters such as wavelength, repetition rate, average power, pulse duration, spot size, beam quality, and sample moving speed must be selected to achieve desired high-quality micromachining. In the near future, ultrafast laser micromachining will be used in various sectors including sub-micron material processing, surface structuring, photonics devices, biomedical devices, microfluidics, displays, and solar applications.

5. Conclusion

In conclusion, a room-temperature, diode-pumped, dual-crystal Yb:KGW laser operating as a Q-switched oscillator or regenerative amplifier has been developed where the gain bandwidth was extended by using N_g-cut + N_p-cut or N_g-cut + N_g-cut configuration. It was shown that fine-tuning the mode sizes in the crystals in the resonator with high pump power is important to obtain the maximal output power since thermal effects change the operation point in the stability zone and mode matching conditions. It was demonstrated simply by shifting the position of the end mirror along optical axis in the resonator. Optimization of the laser resonator increased the output power from 18 to 24 W in case of Q-switched oscillator and from 17 to 21 W in case of regenerative amplifier. Such optimization of laser resonator improves not only output power but also stability of laser operation, especially for N_g-cut + N_g-cut crystal configuration, that is manifest in reduction of output power fluctuations.

The use of this regenerative amplifier enabled to create compact, high average power, high brightness, diode-pumped femtosecond Yb:KGW laser system. This laser, which utilized a CPA MOPA laser scheme, consisted of master oscillator, regenerative amplifier, and stretcher-compressor module. It was capable of delivering 15 W of average output power with a pulse duration down to 182 fs high in a nearly diffraction limited output beam (M^2~1.2) at pulse repetition rates of 50–500 kHz.

This level of output power and quality of a laser beam are practically the same as the output power of Yb:KGW/Yb:KYW thin-disk lasers with medium level of output power [6, 9].

http://dx.doi.org/10.5772/64571

However laser heads based on volume laser media are considerably easier and cheaper compared with those based on thin-disk configuration. Subsequent development of multi-crystal laser approach will be able to increase output power on the level of high-power thin-disk lasers.

The achieved level of radiation parameters allows to successfully use this femtosecond laser for ultrafast micromachining in various applications including sub-micron material processing, surface structuring, creating photonics devices, biomedical devices, microfluidics, displays, and solar applications.

Acknowledgements

Parts of this chapter are reproduced from authors' previous publications [15, 25, 26].

Author details

Guang-Hoon Kim[1*], Juhee Yang[1], Byunghak Lee[1], Bosu Jeong[1], Sergey Chizhov[1], Elena Sall[1], Vladimir Yashin[2] and Uk Kang[1]

*Address all correspondence to: ghkim@keri.re.kr

1 Advanced Medical Device Research Division, Korea Electrotechnology Research Institute, Ansan-si, Republic of Korea

2 State Optical Institute, St. Petersburg, Russia

References

[1] Dausinger F., Lichtner F., and Lubatschowski H. (2004) Femtosecond Technology for Technical and Medical Applications. Berlin: Springer.

[2] Diels J.-C. and Rudolph W. (2006) Ultrashort Laser-Pulse Phenomena: Fundamentals, Techniques, and Applications on Femtosecond Time Scale. Boston: Academic Press.

[3] Fermann M. E., Galvanauskas A., and Sucha G. (2003) Ultrafast Lasers: Technology and Applications. New York: Marcel Dekker.

[4] Kuleshov N. V., Lagatsky A. A., Podlipensky A. V., Mikhailov V. P., and Huber G. (1997) Pulsed laser operation of Yb-doped $KY(WO_4)_2$ and $KGd(WO_4)_2$. Opt. Lett. 22: 1317–1320.

[5] Liu H., Nees J., Mourou G., Biswal S., Spuehler G.J., Keller U., and Kuleshov N. V. (2002) Yb:KGd(WO_4)$_2$ chirped-pulse regenerative amplifiers. Opt. Commun. 203: 315–321.

[6] Nickel D., Stolzenburg C., Giesen A., and Butze F. (2004) Ultrafast thin-disk Yb:KY(WO_4)$_2$ regenerative amplifier with a 200-kHz repetition rate. Opt. Lett. 29: 2764.

[7] Barty C., Korn G., Raksi F., Rose-Petruck C., Squier J., Tian A., Wilson K., Yakovlev V., and Yamakawa K. (1996) Regenerative pulse shaping and amplification of ultrabroadband optical pulses. Opt. Lett. 21: 219–221.

[8] Raybaut P., Balembois F., Druon F., and GeorgesP. (2005) Numerical and experimental study of gain narrowing in ytterbium-based regenerative amplifiers. IEEE J. Quantum Electron. 41: 415–426.

[9] Buenting U., Sayinc H., Wandt D., Morgner U., and Kracht D. (2009) Regenerative thin disk amplifier with combined gain spectra producing 500 mJ sub 200 fs pulses. Opt. Express 17: 8046–8050.

[10] Strickland D., and Mourou G. (1985) Compression of amplified chirped optical pulses. Opt. Commun. 56: 219–221.

[11] Kim G. H., Kang U., Heo D., Yashin V. E., Kulik A. V., Sall' E. G., and Chizhov S. A. (2010) A compact femtosecond generator based on an Yb:KYW crystal with direct laser-diode pumping. J. Opt. Technol. 77: 225–229.

[12] Software package for LASer Cavity Analysis and Design (LAS-CAD). 1996–2015 LAS-CAD GmbH, Germany, www.las-cad.com.

[13] Brunner F., et al. (2000) Diode-pumped femtosecond Yb:KGd(WO_4)$_2$ laser with 1.1-W average power Opt. Lett. 25: 1119.

[14] Buettner A., Buenting U., Wandt D., Neumann J., and Kracht D. (2010) Ultrafast double-slab regenerative amplifier with combined gain spectra and intracavity dispersion compensation. Opt. Express 18(21): 21973–21980.

[15] Kim G. H. Yang J., Chizhov S. A., Sall E. G., Kulik A. V., Yashin V. E., Lee D. S., and Kang U. (2012) High average-power ultrafast CPA Yb:KYW laser system with dual-slab amplifier Opt. Express 20: 3434–3442.

[16] Koechner W. (2006) Solid-state Laser Engineering. New York: Springer.

[17] International Standard ISO 11670:2003: Lasers and Laser-related Equipment – Test Methods for Laser Beam Parameters – Beam Positional Stability. This standard was last reviewed in 2015.

[18] Kim G. H., Yang J., Lee B., Sall E. G., Chizhov S. A., Yashin V. E., and Kang U. (2015) Investigation of diode-pump absorption efficiency and thermo-optical effects in a high-power Yb:KGW laser. Quantum Electron. 45: 211–215.

[19] Biswal S., O'Connor S. P., Bowman S. R. (2005) Thermo-optical parameters measured in ytterbium-doped potassium gadolinium tungstate. Appl. Opt. 44: 3093–3097.

[20] Chenais S., Balembois F., Druon F., Lucas-Leclin G., and Georges P. (2004) Thermal lensing in diode-pumped ytterbium lasers – part I: theoretical analysis and wavefront measurements. IEEE J. Quantum Electron. 40: 1217–1234.

[21] Kim G. H., Yang J., Chizhov S. A., Sall E. G., Kulik A. V., Yashin V. E., Kang U. (2013) High brightness Q-switched oscillator and regenerative amplifier on dual-crystal Yb:KGW laser. Laser Phys. Lett. 10: 125004.

[22] Kim G. H., Yang J., Chizhov S. A., Sall E. G., Kulik A. V., Yashin V. E., Kang U. (2014) High-power directly diode-pumped femtosecond Yb:KGW lasers with with optimized parameters. Proc. of SPIE, 8959: 8959B-1–89591B-8.

[23] Kim G. H., Yang J. H., Lee D. S., Yashin V. E., Kulik A. V., Sall E. G., Chizhov S. A., Kang U. (2012) High power and high efficiency lasers on crystals Yb:KYW with end pumping operating in CW and pulsed regimes. Quantum Electron. 42: 292–297.

[24] Kim G. H., Yang J. H., Yashin V. E., Kulik A. V., Sall E. G., Chizhov S. A., Kang U. (2013) Power limitation and pulse distortions in Yb:KGW laser system with chirped pulse amplification. Quantum Electron. 43: 725–730.

[25] Kim G. H., Yang J., LeeD. S., KulikA. V., Sall'E. G., ChizhovS. A., YashinV. E., and KangU. (2012) Directly diode-pumped femtosecond laser based on an Yb:KYW crystal. Proc. SPIE 8247: 82471C.

[26] Kim G. H., Yang J., Sall E., Chizhov S., Kulik A., Lee D. S., Kang U., Yashin V. (2012) Development of compact femtosecond Yb: KYW oscillators: simulation and experiment. J. Korean Phys. Soc. 61: 365–370.

Chapter 3

Yb:YAG-Pumped, Few-Cycle Optical Parametric Amplifiers

Hanieh Fattahi

Additional information is available at the end of the chapter

http://dx.doi.org/10.5772/64438

Abstract

In this chapter, the principle, design, and characteristics of high-efficiency, short-pulse-pumped, few-cycle optical parametric chirped-pulse amplification (OPCPA) systems are reviewed. To this end, the feasibility of two techniques to increase the conversion efficiency of few-cycle OPCPA systems is demonstrated and discussed. The techniques result in 2.5 mJ, 7.5 W pulses and correspond to a pump-to-signal conversion efficiency of 30%. The broadband amplified spectrum supports 5.7 fs. Finally, the feasibility of extending the amplified spectrum to a near-single-cycle regime by using the combination of different crystals and phase matching is shown.

Keywords: optical parametric chirped-pulse amplification, Yb:YAG thin-disk laser, attosecond pulse, femtosecond laser

1. Introduction

The new generation of femtosecond technology based on short-pulse-pumped optical parametric chirped-pulse amplification (OPCPA) [1] holds promise for scaling the peak power and average power of few-cycle pulses simultaneously. This progress would benefit a number of fields, notably attosecond science [2, 3] by allowing to scale attosecond pulse generation at higher photon energy and higher flux.

In OPCPA, the amplified bandwidth is not limited by the energy level structure of a laser medium or gain narrowing [4], as is the case in laser amplifiers [5]. Therefore, OPCPA appears to be the method of choice for the production of ultrashort pulses (down to the few-cycle regime) at high peak and average power. Employing short pulses (several-ps to sub-ps) to

pump an OPCPA allows higher peak intensity in the nonlinear medium as the damage threshold intensity of materials scales with the inverse square root of the pulse duration [6]. The high pump intensity makes it possible to achieve the required gain in a shorter crystal, which leads to greater amplification bandwidth.

Further advantage with a short crystal is that the effect of transverse walk-off is reduced, the temporal contrast can be enhanced, and stretchers and compressors can be simpler. However, the crystal length does not decrease as rapidly as the pulse duration, so the temporal walk-off relative to the pulse duration increases for short pulses. A simple analytical analysis shows that the optimum pump-pulse duration to achieve a high conversion efficiency and a broadband gain is around 1 ps [7].

Nevertheless, all these advantages of short-pulse-pumped OPCPA remain useless without an efficient, reliable, and powerful pump source. Such pump lasers are required to deliver high-energy near-1-ps pulses with near-diffraction-limited beam quality at repetition rates in the kHz to MHz range.

Heretofore, due to the lack of suitable pump lasers, the few-cycle OPCPA delivered either high-energy pulses at a low repetition rate [8, 9] or low-energy pulses at a high repetition rate [10]. Nowadays, Yb-doped lasers in the thin-disk, fiber or slab geometries [1, 11–15] are capable of delivering high-energy, high average power pulses with ps-pulse duration. Among these laser technologies, the recent advances in Yb:YAG thin-disk lasers have started to fulfill the criteria for suitable pump sources for OPCPA systems and hold promise to change the current state of the art of OPCPA systems to few-cycle pulses with higher energy and average power [1, 16].

This chapter is devoted to the recent progress in Yb:YAG-pumped, few-cycle OPCPA systems. In Section 1, a brief overview on the fundamentals of OPCPA is presented. In Sections 2 and 3, novel techniques for increasing the conversion efficiency are discussed. In Section 4, a technique for extension of the amplification bandwidth is discussed.

In a medium with second-order nonlinearity, a high-energy photon (called pump) can decay to two newly generated photons with lower frequencies (called seed and idler). In the presence of initial seed photons, the decay of pump photons is stimulated and consequently more photons at the seed frequency are generated. The seed photons after amplification are named signal and the process is called optical parametric amplification (OPA). The frequency of the generated signal and idler photons is defined by the conservation of energy. However, the amplification bandwidth can be increased by fulfilling conservation of momentum between pump, signal, and idler pulses, which can be tuned by the type, thickness, and temperature of the nonlinear medium and also the geometry of the three interacting beams.

To obtain a strong pump-to-signal and idler energy conversion, the spatial and temporal overlap between seed and pump pulses in the nonlinear medium should be maximized. The optimum temporal overlap between the pump and seed pulses can be ensured by temporal stretching of the seed pulses to the temporal window of pump pulses. This technique is the combination of chirped-pulse amplification (CPA) [17] and OPA, hence called optical parametric chirped-pulse amplification.

http://dx.doi.org/10.5772/64438

In addition to the above-mentioned parameters, the conversion efficiency in OPA or OPCPA systems also depends on the thickness of the nonlinear medium, peak intensity of the pump pulses, and the initial seed energy. Conversion efficiency scales up by increasing the thickness of the nonlinear medium as long as the phase-matching condition (conservation of momentum) between the three interacting beams is satisfied. At higher pump peak intensity to induced nonlinear polarization in the nonlinear medium is stronger and therefore larger amplification is achieved. Moreover, by increasing the seed-to-pump energy ratio, the conversion efficiency at lower amplification gain can be achieved.

The optimization of the pump-to-signal conversion efficiency of multicycle OPCPA systems has been the subject of several studies [18–22]. In the next two sections, the feasibility and realizability of two techniques to increase the conversion efficiency of few-cycle OPCPA systems are discussed.

2. Recycling the pump energy

In optical parametric amplification, the behavior of the gain over the length of the nonlinear medium can be divided into three main regions (**Figure 1(a)**). In the beginning, the energy of the amplified signal has an exponential growth due to the generation of the idler field that enhances the amplification process (region A). In region B, the gain drops gradually as the pump energy is reduced, and the growth of the signal power becomes approximately linear. When the pump beam has been locally depleted at some point in time and space, back conversion sets in and further reduces the gain. In region C, back conversion dominates, and the signal power drops. In the case of pulses with Gaussian spatiotemporal profile, the depletion mainly occurs at the center of the pulse, where the intensity is highest. Therefore, the back conversion already starts before the complete depletion of the pump. Because back conversion depends on both signal and idler beams, it can be reduced by removing the idler between the stages of a multistage OPCPA.

To explore this option, three different designs (as shown in **Figure 1(b)**) are simulated and compared using the SISYFOS code [23]. In all designs, the amplification takes place in a type-I BBO crystal, where the angle between the Optical axis and the signal is 22°, and the noncollinear angle between the pump and the signal in the tangential phase-matching geometry is 2.7°. The pump have a Gaussian beam and pulse shape, and the seed have the Gaussian beam shape and a super-Gaussian spectrum of order 4, ranging from 600 to 1100 nm and linearly chirped to 1.1 ps pulse duration. Higher-order nonlinear effects and parasitic processes were not taken into account.

Figure 1(c) compares the three simulated OPCPA systems. The first configuration (Design 1 in **Figure 1(b)**) consists of a single OPCPA stage using a 2 mm thick BBO crystal, with 7 mJ of pump energy at a peak intensity of 80 GW/cm^2, which results in a conversion efficiency of 14%.

The second design (Design 2 in **Figure 1(b)**) has two stages, and the idler beam is removed between the two stages. This reduces back conversion in the second stage and allows operation

in a regime with stronger pump depletion. Temporal and spatial overlap of the beams could be readjusted between the stages, and a further advantage with the two-stage design is that the phase-matching of the crystals can be tuned slightly differently to optimize the total bandwidth. The crystal lengths for the two stages are 1.2 and 0.7 mm, respectively. The second stage is pumped by the residual pump energy from the first stage resulting in a conversion efficiency of 34%.

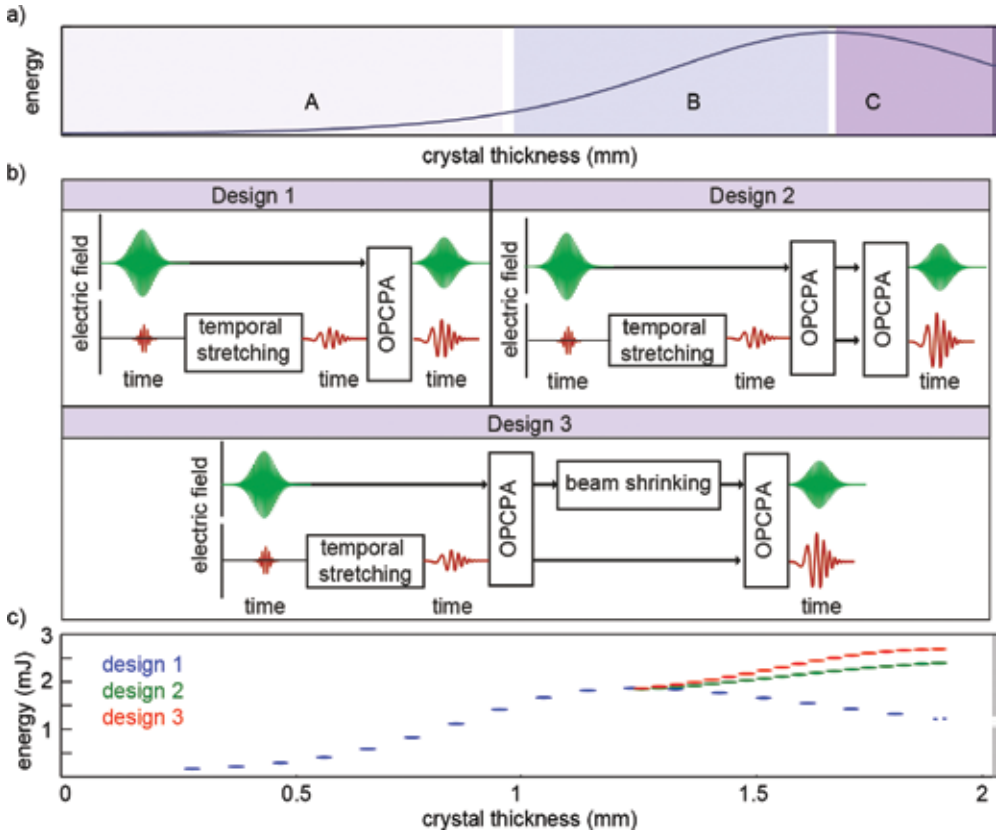

Figure 1. (a) Qualitative behavior of OPCPA amplified energy over the length of the nonlinear medium. (b) Three OPCPA designs are discussed in the main text. Design 1 consists of one OPCPA stage. Designs 2 and 3 consist of two OPCPA stages, where the residual pump energy after the first OPCPA stage is reused in the second stage. In Design 3, the pump after the first amplification stage is resized to increase the pump peak intensity. (c) Calculated amplified signal energy over the crystal length for the three different designs.

The third configuration (Design 3 in **Figure 1(b)**) is a two-stage OPCPA system similar to the second design except that the pump-beam size between the two stages is reduced to compensate the reduction in the pump intensity after the first stage of amplification and therefore the efficiency in the third design reaches 39%.

All three designs are capable of supporting the ultrabroad amplification bandwidth necessary for a few-cycle pulse durations. The detailed parameters of the simulations are shown in

Table 1. In what follows, the experimental realization of the third design is demonstrated and discussed. The third design is chosen as it supports the highest conversion efficiency in the above-mentioned study.

	Design 1	**Design 2**		**Design 3**	
	1st stage	**1st stage**	**2nd stage**	**1st stage**	**2nd stage**
L (mm)	2	1.2	0.7	1.2	0.7
E amp (mJ)	1	1.8	2.4	1.8	2.7
ϕ_p (mm)	2.5	2.5	–	2.5	2
ϕ_s (mm)	2.5	2.5	–	2.5	D^*_{amp}
Efficiency (%)	14	26	14	26	21
Overall efficiency (%)	14	34		39	

D^*_{amp}: the diameter of the amplified beam.

Table 1. Parameters used in simulations: L_c, crystal thickness; $E_{s\,\text{amp}}$, amplified signal energy; ϕ_p, pump-beam diameter at full width at half maximum; ϕ_s, seed beam diameter at FWHM.

2.1. System description

2.1.1. Front end

The experimental OPCPA setup (as shown in **Figure 2**) consists of a Ti:Sa-based oscillator and amplifier followed by a broadband nonlinear seed generation scheme, a pump laser, a temporal jitter compensation system, three OPCPA stages, and a chirped-mirror compressor [24]. The Yb:YAG regenerative amplifier [25], optically synchronized with the OPCPA seed [26], delivers 16 mJ, 1.6 ps pulses at full width at half maximum (FWHM) at 3 kHz repetition rate and its frequency doubled output is used for pumping the OPCPA. However, due to the long optical beam-path difference between seed and pump pulses, timing fluctuations occur due to air turbulence, mechanical vibrations of optical components, temperature drifts, and the finite stability of the front end, which need to be compensated by an active stabilization system. The timing jitter in our system is reduced to a level of 24 fs (root mean square) by using an active stabilization system based on spectrally resolved cross-correlation between the stretched seed and the pump pulse [27].

The broadband OPCPA seed was generated by using a small portion of the output of the Ti:Sa multipass amplifier (Femtolasers GmbH), providing a spectral bandwidth of 60 nm (FWHM) centered at 790 nm. These pulses, containing 30 μJ of energy, focused on a 15 cm long hollow core fiber (HCF) with an inner diameter of 120 μm filled with 4.5 bar of krypton. The pressure of krypton in the HCF and the group delay dispersion (GDD) of the input pulse were optimized to obtain the maximum spectral broadening, covering a spectral range from 500 to 1050 nm.

With this combination of parameters, an overall throughput of 10 μJ pulse energy in a near-diffraction-limited output beam containing the broad spectrum was achieved (**Figure 3(a)**).

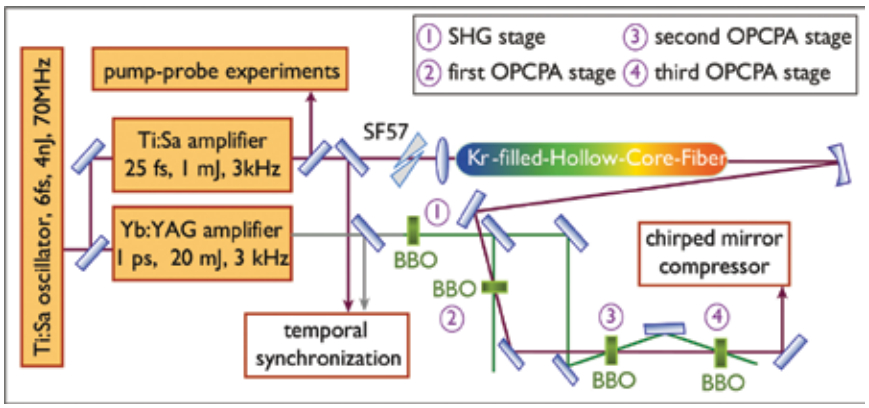

Figure 2. Block diagram of the OPCPA system. The OPCPA broadband seed pulses are generated from a Ti:Sa regenerative amplifier. The output of a Yb:YAG thin-disk amplifier, after frequency doubling, is used to pump the three OPCPA stages. Finally, a chirped-mirror compressor is used for pulse compression of the broadband amplified pulses.

In order to measure the amount of introduced material dispersion, which needs to be compensated after the final OPCPA stage, the broadband seed was sent through the entire beam path without any pump. Pulse dispersion was caused over merely 5.5 mm beam path in BBO, 4 mm path length in SF57 glass, and over 10 m propagation in air. The stretched seed pulses were characterized by a multishot, second harmonic generation (SHG)-XFROG device incorporating a 20 μm thick BBO crystal cut at 29° as the nonlinear medium, while a fraction of the multipass amplifier's output provided the reference beam. From these measurements, a second-order spectral phase of 1433 fs^2 evaluated at 850 nm was retrieved. This is in excellent agreement with the GDD introduced by the above components, evaluated as 1403 fs^2. The pulse duration of the seed pulses assuming a Gaussian fit for the retrieved time structure is 1.1 ps (FWHM), which ensures a sufficiently good temporal matching between the seed and pump pulses in the OPA stages.

For frequency doubling of the pump laser, a BBO crystal was used. Its high nonlinearity allowed the use of a relatively short crystal keeping the accumulated B-integral in the system negligible. Using a BBO crystal of 1.5 mm length, a conversion efficiency as high as 70% with a good beam quality was obtained. The high SHG efficiency confirms the excellent beam quality and clean output pulses of the regenerative amplifier. However, in order to definitely avoid problems related to the B-integral in the OPCPA stages, a 1 mm BBO crystal for the SHG was chosen, which resulted in a conversion efficiency of 57%.

2.1.2. OPCPA stages and pulse compression

The OPCPA setup consists of three stages. We added an OPCPA-based preamplifier stage in the experiment in order to boost the seed energy before the two power amplifier stages. This

http://dx.doi.org/10.5772/64438

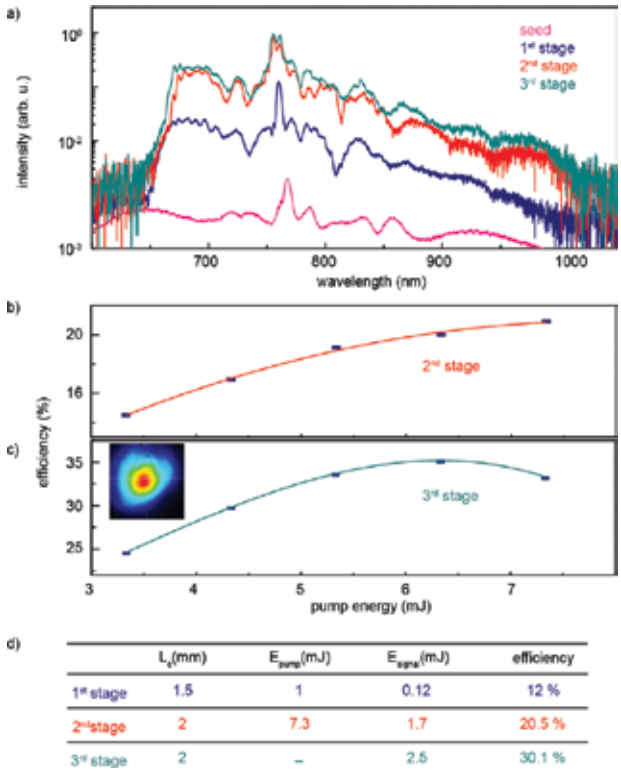

	L_c(mm)	E_{pump}(mJ)	E_{signal}(mJ)	efficiency
1st stage	1.5	1	0.12	12 %
2nd stage	2	7.3	1.7	20.5 %
3rd stage	2	–	2.5	30.1 %

Figure 3. (a) The seed spectrum and the amplified spectra of three OPCPA stages, normalized to the output energy of each stage. (b) and (c) Conversion efficiencies after the second and third stages, respectively. The conversion efficiency is defined as the net increase in signal energy divided by the input pump energy of stage two. (d) The detailed parameters of each OPCPA stage. The total efficiency after each stage is defined as the net increase in signal energy after the stage divided by the total pump energy of the OPCPA chain. Inset: amplified beam profile after the third stage [7].

stage is necessary to drive the following stages into saturation [7]. Therefore, 1 mJ of the frequency doubled output of the thin-disk amplifier was used to pump a 1.5 mm BBO crystal, and an amplified energy of 120 μJ and a 350 nm broad spectrum were achieved in the first stage (**Figure 3(a)**). Here, the OPCPA crystal length was chosen to minimize the superfluorescence at the third stage [28].

The following two stages were designed for reaching the highest possible pump-to-signal conversion efficiency by controlling the idler energy and recycling the pump energy. Up to 7.3 mJ of the pump energy with the peak intensity of 80 GW/cm^2 at 515 nm was used for the second OPCPA stage that employed a 2 mm thick BBO crystal. In this stage, an amplified pulse energy of 1.77 mJ was obtained. The thickness of the crystal at this stage is adjusted to stop amplification slightly below the saturation while preserving a good residual pump-beam quality.

Subsequently, the size of the remaining pump beam was reduced to increase the peak intensity to 80 GW/cm^2 in the third amplification stage. Here, by employing a 2 mm thick BBO crystal, the amplified energy reached 2.5 mJ. In the last two OPCPA stages, an optical-to-optical

conversion efficiency of >32% was achieved (**Figure 3(b)** and **(c)**), which to the best of our knowledge is the highest reported conversion efficiency for few-cycle OPCPA systems [9, 10, 29, 30]. No measurable superfluorescence background was observed when blocking the signal beam in front of the first stage.

The simulated boost efficiency in our design study is in good agreement with the experimental results. Quantitative comparison shows, however, that higher conversion efficiencies were yielded for a shorter crystal in the simulation than in the experiment. We relate the deviation from the theoretical prediction to a slight ellipticity in our pump beam, caused by the compressor of the Yb:YAG amplifier, which limited the effective interaction area between pump and signal beams.

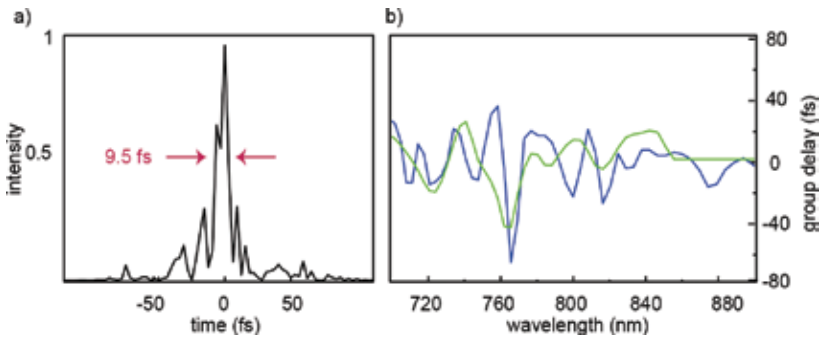

Figure 4. (a) Retrieved temporal intensity of the compressed pulses after 12 reflections in a double-angle chirped-mirror compressor measured by SH-FROG. The pulse is compressed to 9.5 fs and holds Fourier transform limit of 5.7 fs. (c) The calculated GD of retrieved spectral phase for the pumped (blue curve) and unpumped (green curve) OPCPA chains.

The 350 nm broad amplified signal measured with the Si-based spectrometer supports a transform-limited pulse duration of 5.7 fs. Preliminary compression, by using 12 reflections on double-angle chirped mirrors with −30 fs^2 GDD per reflection, resulted in a pulse duration of 9.5 fs (FWHM). The compressor had a total throughput of 80%. The retrieved temporal intensity profile and retrieved residual group delay (GD) of the pulses are shown in **Figure 4(a)** and **(b)**. Our analytical study shows that the pulse can be compressed to 7 fs by adding the GD of a 0.5 mm thick fused silica to the measured GD of the pulse. However, to investigate the origin of the fine oscillation in the retrieved GD, a frequency resolved optical gating (FROG) measurement of the whole OPCPA chain was performed, but this time without any pumping. The comparison between two cases in **Figure 4(b)** shows that oscillations were enhanced by amplification but did not originate from the OPCPA phase [31]. The peak of the GD is at 760 nm, which coincides with the wavelength of Ti:Sa amplifier's pulses and the peak in the spectral intensity of the seed pulses after the HCF. Therefore, it can be concluded that the measured residual higher-order chirp is due to the self-phase modulation in the HCF, OPCPA phase, and the residual oscillations in group delay dispersion of the double-angle chirped-mirror compressor [32, 33]. The higher-order dispersion and the satellite pulses can be compensated

http://dx.doi.org/10.5772/64438

by using specially designed chirped mirrors for this system along with the implementation of spectral smoothing techniques, such as cross-polarized wave generation [34] after the HCF.

The demonstrated highly efficient compact OPCPA system delivers broadband pulses with 2.5 mJ energy supporting a two-cycle pulse at a repetition rate of 3 kHz. Our simple OPCPA design shows that, by extraction of the idler energy and optimization of the pump peak intensity, a higher conversion efficiency can be achieved. The output of the system ensures to be compressible to its two-cycle transform limit by using specially designed chirped mirrors. The system also has the capability to operate with a stabilized carrier envelope phase (CEP) by stabilizing the Ti:Sa oscillator. These features make the reported OPCPA system a suitable driver for high harmonic generation (HHG) [35].

In the next section, an alternative method to achieve high conversion efficiency as well as uniform amplified spectrum is discussed.

3. Controlling the deposition of pump energy

In this section, the realizability of a second novel technique that allows the simultaneous increase in the spectral bandwidth and optical conversion efficiency of OPCPA systems is discussed. This approach is based on a patent application by Deng and Krausz [36].

In the conventional OPCPA systems, similar to the one described in Section 2, the seed-pulse duration is designed to be a fraction of pump-pulse duration in order to maximize the energy conversion. Here as the seeds are strongly chirped, the temporal intensity profile of the pump pulses has to be nearly constant to ensure uniform amplification for the entire seed spectrum. Therefore, for pump pulses with Gaussian temporal profile, the seed pulses have to be considerably shorter than the pump pulses. Consequently, the pump energy is not consumed efficiently and the relative seed-to-pump pulse duration ratio will be a compromise between the amplification bandwidth and the conversion efficiency.

These deficiencies can be overcome if OPCPA seed pulses are linearly stretched to several times longer than the pump pulses. Subsequently, different fraction of seed pulses can be temporally overlapped with pump pulses and are amplified in different OPCPA stages.

This technique enables the controlled deposition of pump energy in the subsequent temporal/spectral locations along the chirped seed pulse [36]. Furthermore, by controlling the amplification gain in each stage, the spatiotemporal profile of the pump pulses can be shaped into a flat-top pulse. By tuning the phase-matching angle of the crystal to the central wavelength of the seed pulse, the ultimate amplified spectrum can be shaped and a broader amplified bandwidth is gained. In addition, by reusing the pump energy after each amplification stage, the total conversion efficiency is increased.

3.1. Theoretical analysis

Figure 5 shows simulation results for three different OPCPA designs. The simulation's input parameters are similar to the ones presented in Section 2.

In the first design, the residual pump energy after the first amplification stage is used to pump the second stage and ultimately the residual pump energy after the second stage is used to pump the third stage.

Due to the Gaussian shape of the pump in time and space, the energy extraction takes place primarily in the middle of the pump. Therefore, the wings are mostly left unaffected with a signature of energy back conversion at the center, due to the fact that this part of the pump possesses the highest peak intensity. In this design, the OPCPA pump-to-signal conversion efficiency is increased to 43% compared to the OPCPA system demonstrated in Section 2 (**Figure 5(b)** and **(c)**).

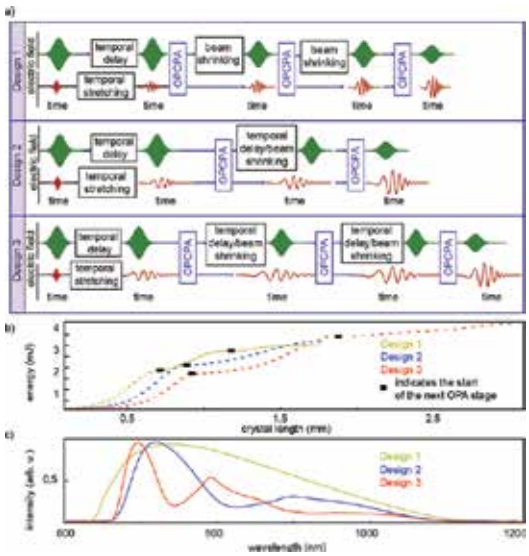

Figure 5. (a) Three designs are discussed in the main text. Design 1 consists of three OPCPA stages, where the residual pump energy after each amplification stage is reused in a subsequent OPCPA stage. Design 2 consists of two OPCPA stages. Here, the seed pulses are temporally stretched to twice the pump-pulse duration, and the residual pump energy after the first OPCPA stage is reused in the second stage. In Design 3, the seed pulses are temporally stretched to triple of the pump-pulse duration, and the residual of the pump energy is reused after each amplification stage. (b) Calculated amplified signal energy over the crystal length and their corresponding spectra (c) for the three different designs [7].

In the second design, the seed pulses are stretched temporally to twice the pump-pulse duration. The blue part of the seed spectrum is amplified in the first OPCPA stage by adjusting the temporal overlap between pump and seed pulses. Subsequently, the pump pulses after the first stage are reused to amplify the red part of the spectrum at the second stage. In this design, the pump-to-signal conversion efficiency reaches 45% indicating the good pump-energy extraction while the beam quality of the amplified signal is maintained (**Figure 5(b)** and **(c)**).

The 45% conversion efficiency achievable from the second design is not drastically different from the 38.6% efficiency achievable from the case where the seed and pump pulses have the

http://dx.doi.org/10.5772/64438

same pulse duration (as discussed in Section 2) as the pump pulses after the first amplification stage in both cases maintain a good spatiotemporal profile.

The gain and the shape of the amplified spectrum can be further optimized by adjusting the phase-matching angles of the crystal in each stage to tune the amplification for the selected part of the spectrum, which is not investigated in this study.

In the third design, the seed pulses are stretched three times the pump pulses and amplified in three subsequent OPCPA stages, while the residual pump energy of the preceding stage is used to pump the subsequent stage. The bluest frequencies of the seed spectrum are amplified in the first stage, while the reddest frequency components are amplified in the third OPCPA stage. The pump-to-signal conversion efficiency in this design reaches 57%, which is a noticeably higher value compared to the other designs (**Figure 5(b)** and **(c)**). The spectral narrowing for Designs 2 and 3 is caused by a suboptimal stretching factor of the input signal and phase-matching angle of the crystal. The optimizations of these parameters are cumbersome in simulation but straightforward in an experimental setup.

3.2. Experimental setup

The seed pulses of the OPCPA system described in Section 2 are stretched after the first amplification stage by using an 8 mm thick SF57 plate at Brewster's angle. The blue frequencies of the seed spectrum were amplified to 4 W by adjusting the temporal delay between the seed and pump pulses and adjusting the phase-matching angles of the BBO crystal (blue curve in **Figure 6(a)**). In the next OPCPA stage, the amplification is moved to the second half of the seed spectrum gaining 6 W of the total amplification (**Figure 6(a)**, pink curve).

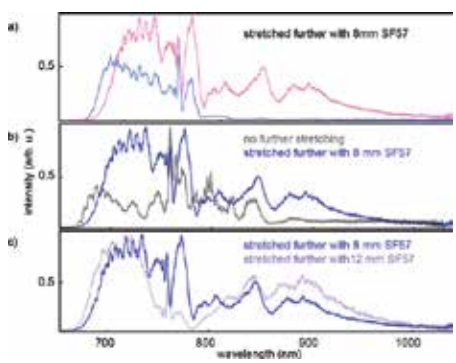

Figure 6. (a) The experimental demonstration of Design 2. The seed pulses are heavily stretched by using an 8 mm thick SF57 plate. The higher frequencies in the spectrum are amplified first (blue curve). The residual of the pump energy is used to amplify the lower frequency components of the spectrum (pink curve). (b) The gray curve shows the amplified spectrum in the similar OPCPA system without any spectral stacking (gray curve) compared to the amplified spectrum shown in (a) (blue curve). (c) Further stretching of the seed pulses by using a 12 mm thick SF57 plate results in appearing of a hole in the amplified spectrum (purple curve) [7].

The same setup, after removing the bulk stretcher, resulted in 6.2 W of amplification after the third stage. As shown in **Figure 6(b)**, the amplified spectrum of the stacked OPCPA is more

uniform due to the even amplification gain. The red wing of the spectrum carries more energy in the stacked OPCPA compared to the amplified spectrum achieved from the system discussed in Section 2. Moreover, the spectral spike at 780 nm is heavily suppressed. **Figure 6(c)** shows amplified spectrum for a similar system but with a larger stretching factor. Here, after stretching the seed pulses using a 12 mm thick SF57 plate, 5 W of the average power was obtained. It can be seen that the amplified spectrum contains a hole, leaving the 8 mm thick SF57 plate, the optimum thickness for temporal stretching of the seed pulses.

Temporal stretching of the signal pulses to twice the pump-pulse duration, demonstrated in this section experimentally, did not show further increase in the OPCPA conversion efficiency compared to the scheme realized in Section 2. This similarity in the conversion efficiency is due to the fact that the spatiotemporal quality of the residual pump pulses after one amplification stage is preserved for both cases.

However, it is shown analytically that the further temporal stretching of seed pulses results in the increase in the conversion efficiency, as the spatiotemporal quality of the remaining pump pulses after two amplification stages is preserved just for the case of heavily chirped input seed.

4. Gain bandwidth engineering

The bandwidth of the amplified spectra, as discussed in the previous sections, can be extended further by using different crystals or a crystal with different phase-matching angles. The combination of BBO and LiB_3O_5 (LBO) crystals can be used to extend the amplified spectrum to longer frequencies, as the BBO crystal does not support amplification for spectral components above 1.1 μm. The amplified spectrum in both crystals supports near-single-cycle pulses, which is not unobtainable with solely either of them.

To this end, the broadened seed spectrum generated in the HCF subsequently focused on a 4 mm $Y_3Al_5O_{12}$ (YAG) crystal to extend the spectrum to 1400 nm and is amplified in an OPCPA chain similar to the system described in Section 2. Combinations of LBO and BBO crystals at different OPCPA stages are used to increase the amplification bandwidth. The first OPCPA stage was optimized to amplify a broad spectral range from 750 to 1400 nm up to 50 μJ energy in a 2 mm LBO crystal. In the second stage, a 2 mm BBO crystal was employed. The amplified spectrum measured in this stage, using an Si-based spectrometer, spans from 670 to 1100 nm and contained 1.1 mJ energy. Finally at the third stage, 1.8 mJ energy was obtained in a 3 mm LBO crystal.

The amplified spectra at each OPCPA stage, normalized to their energy, are shown in **Figure 7**. The amplified spectrum obtained after the third stage supports 4.3 fs transform-limited pulses (FWHM). The preliminary pulse compression was performed by using a set of chirped-mirror compressor designed for spectral wavelength of 700–1300 nm. **Figure 7(b)** shows the pulse compression to 9 fs measured with an SH-FROG containing a 10 μm BBO crystal. The retrieved spectrum from the FROG measurement is in a good agreement with a

spectrum measured after the third OPCPA stage. Pulse compression to its Fourier transform limit would require a specially designed chirped-mirror compressor for compensating the higher-order chirp.

The conversion efficiency of the system can be optimized further by using a longer crystal in the last OPCPA stage without relinquishing the amplified spectral bandwidth.

As shown in this section, the utilization of different well-selected nonlinear crystals extends the OPCPA gain bandwidth substantially. The realized three-stage OPCPA system, using one BBO and two LBO crystals, delivers 1.8 mJ pulses with a Fourier transform limit of 4.5 fs. The system supports shorter pulse duration than an all-LBO three-stage OPCPA system with 5.3 fs (FWHM) pulses. The reported extension of the amplified spectral bandwidth is crucial for experiments that rely on high-energy, single-cycle pulses.

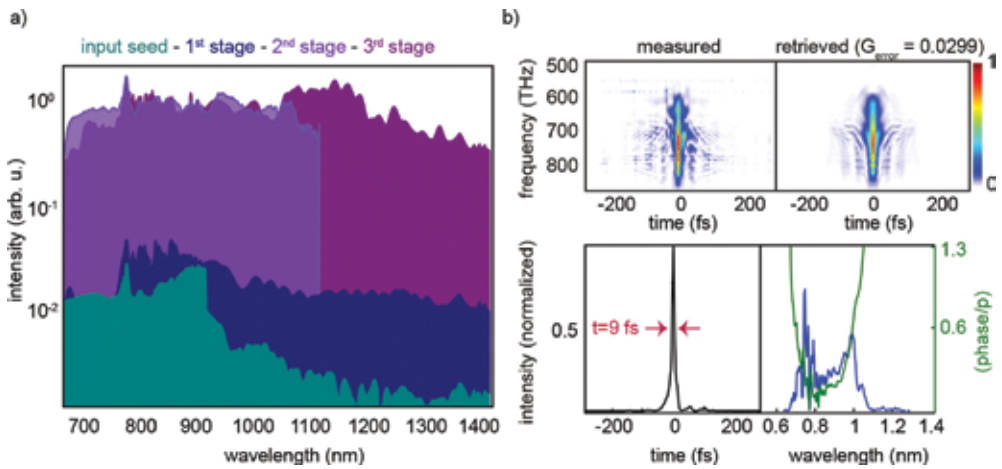

Figure 7. (a) Amplified spectra in a three-stage OPCPA system. A 2 mm LBO crystal is used to amplify the spectral components from 750 to 1400 nm in the first OPCPA stage. In the second stage, the spectral components from 680 to 1100 nm were amplified in a 2 mm BBO crystal and finally in the last stage a 3 mm LBO crystal is used to boost the amplification to 1.8 mJ. (b) Measured and retrieved SH-FROG traces (top) and the retrieved spectrum and temporal profile of the pulses (bottom) of the OPCPA system [7].

5. Summary

In this chapter, three few-cycle OPCPA systems operating at the near-infrared spectral range and pumped by the second harmonic generation of a Yb:YAG thin-disk amplifier were reviewed. The feasibility of increasing the conversion efficiency of the system by reusing the pump energy after each amplification stage, in the subsequent OPCPA stages, was demonstrated. It was shown that by controlled deposition of pump energy in different parts of the seed spectrum, high conversion efficiency along with a smooth amplified spectrum can be achieved. Furthermore, the feasibility of TW-level monocycle OPCPA systems was studied by

using different crystals in different amplification stages. In addition to the presented systems, different harmonics of the Yb:YAG amplifier can be used to pump few-cycle pulses in visible or mid-infrared spectral range [16].

6. Outlook

The capabilities of the current high harmonic generation sources, based on CPA Ti:Sa technology, are limited to energies around a few hundred eV and to pulse durations of several tens of attoseconds. This limitation originates from a deficiency of the current laser technology that can either provide pulses with ultrahigh (petawatt) peak powers at relatively low repetition rates or moderate peak power (gigawatt) pulses at kHz repetition rates. Scaling attosecond pulses to high repetition rates and photon energies as high as several keV demands few-cycle laser systems with high peak and average power, which is beyond the performance of the current laser technology.

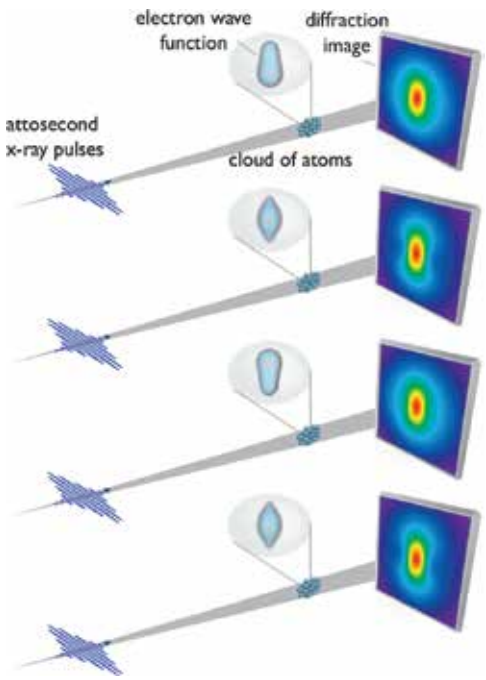

Figure 8. Attosecond X-ray diffraction: as a coherently induced charge oscillation takes place in an atom or molecule, an incident X-ray pulse takes a diffraction snapshot of the electron distribution at the time of interaction; changing the time delay between the source of the excitation and the attosecond pulse allows for the temporal evolution of the charge density to be directly measured in time and space. The figure represents the simulated dynamic of hydrogen atoms when they are exposed to 100-as, X-ray pulses and are excited into the 1S-2P coherent superposition state. As shown, the electron dynamic can be reconstructed by means of attosecond X-ray diffraction spectroscopy [3].

http://dx.doi.org/10.5772/64438

OPCPAs are scalable in terms of peak and average power and directly benefit from the availability of turn-key, industrial-grade ps-pump lasers. For more than two decades, powerful, cost-effective ps pump sources have been unavailable. Nowadays, diode-pumped ytterbium-doped lasers in the thin-disk geometry are able to deliver 1 ps scale pulses at kilowatt-scale average power, in combination with terawatt-scale peak powers. By merging these two existing technologies, and comprising OPCPAs driven by ytterbium-based pump lasers, the new generation of femtosecond technology will combine terawatt-scale peak powers with kilowatt-scale average powers in ultrashort optical pulse generation opening new path in the generation of isolated attosecond pulses with higher flux and photon energies.

The increased photon flux will greatly expand the applicability of attosecond spectroscopy to scrutinizing phenomena where current-generation sources delivered signal near or below the noise level, whereas shorter wavelengths provide direct access to electronic motions on increasingly shorter length scales from nanostructures toward atomic dimensions.

The availability of attosecond X-ray pulses could lead to resolve the spatiotemporal motion of electrons in their ultimate resolution, picometer-attosecond resolution, via attosecond X-ray diffraction spectroscopy (**Figure 8**).

Acknowledgements

I wish to thank Prof. Ferenc Krausz for fruitful discussions about the material of this chapter.

Author details

Hanieh Fattahi

Address all correspondence to: hanieh.fattahi@mpq.mpg.de

Max-Planck Institut für Quantenoptik, Garching, Germany and Department für Physik, Ludwig-Maximilians-Universität München, Garching, Germany

References

[1] H. Fattahi, H. G. Barros, M. Gorjan, T. Nubbemeyer, B. Alsaif, C. Y. Teisset, M. Schultze, S. Prinz, M. Haefner, M. Ueffing, A. Alismail, L. Vámos, A. Schwarz, O. Pronin, J. Brons, X. T. Geng, G. Arisholm, M. Ciappina, V. S. Yakovlev, D. E. Kim, A. M. Azzeer, N. Karpowicz, D. Sutter, Z. Major, T. Metzger, and F. Krausz, "Third-generation femtosecond technology," Optica 1, 45–63 (2014).

[2] M. Hentschel, R. Kienberger, C. Spielmann, G. A. Reider, N. Milosevic, T. Brabec, P. Corkum, U. Heinzmann, M. Drescher, and F. Krausz, "Attosecond metrology," Nature 414, 509–513 (2001).

[3] F. Krausz and M. Ivanov, "Attosecond physics," Rev. Mod. Phys. 81, 163–234 (2009).

[4] A. Dubietis, G. Jonušauskas, and A. Piskarskas, "Powerful femtosecond pulse generation by chirped and stretched pulse parametric amplification in BBO crystal," Opt. Commun. 88, 437–440 (1992).

[5] C. Le Blanc, P. Curley, and F. Salin, "Gain-narrowing and gain-shifting of ultra-short pulses in Ti: sapphire amplifiers," Opt. Commun. 131, 391–398 (1996).

[6] M. Lenzner, J. Krüger, S. Sartania, Z. Cheng, C. Spielmann, G. Mourou, W. Kautek, and F. Krausz, "Femtosecond optical breakdown in dielectrics," Phys. Rev. Lett. 80, 4076–4079 (1998).

[7] H. Fattahi, "Third-generation femtosecond technology," Springer Theses (Springer International Publishing, Cham, 2015).

[8] D. Herrmann, L. Veisz, R. Tautz, F. Tavella, K. Schmid, V. Pervak, and F. Krausz, "Generation of sub-three-cycle, 16 TW light pulses by using noncollinear optical parametric chirped-pulse amplification," Opt. Lett. 34, 2459–2461 (2009).

[9] N. Ishii, L. Turi, V. S. Yakovlev, T. Fuji, F. Krausz, A. Baltuska, R. Butkus, G. Veitas, V. Smilgevicius, R. Danielius, and A. Piskarskas, "Multimillijoule chirped parametric amplification of few-cycle pulses," Opt. Lett. 30, 567–569 (2005).

[10] M. Schultze, T. Binhammer, G. Palmer, M. Emons, T. Lang, and U. Morgner, "Multi-μJ, CEP-stabilized, two-cycle pulses from an OPCPA system with up to 500 kHz repetition rate," Opt. Express 18, 27291–27297 (2010).

[11] F. Röser, T. Eidam, J. Rothhardt, O. Schmidt, D. N. Schimpf, J. Limpert, and A. Tünnermann, "Millijoule pulse energy high repetition rate femtosecond fiber chirped-pulse amplification system," Opt. Lett. 32, 3495–3497 (2007).

[12] P. Russbueldt, T. Mans, G. Rotarius, J. Weitenberg, H. D. Hoffmann, and R. Poprawe, "400W Yb:YAG Innoslab fs-amplifier," Opt. Express 17, 12230–12245 (2009).

[13] L. E. Zapata, H. Lin, A.-L. Calendron, H. Cankaya, M. Hemmer, F. Reichert, W. R. Huang, E. Granados, K.-H. Hong, and F. X. Kärtner, "Cryogenic Yb:YAG composite-thin-disk for high energy and average power amplifiers," Opt. Lett. 40, 2610–2613 (2015).

[14] O. H. Heckl, J. Kleinbauer, D. Bauer, S. Weiler, T. Metzger, and D. H. Sutter, "Ultrafast Thin-Disk Lasers," 93–115 (2016) DOI: 10.1007/978-3-319-17659-8_5.

[15] H. Fattahi, A. Alismail, H. Wang, J. Brons, O. Pronin, T. Buberl, L. Vámos, G. Arisholm, A. M. Azzeer, and F. Krausz, "High-power, 1-ps, all-Yb:YAG thin-disk regenerative amplifier," Opt. Lett. 41, 1126–1129 (2016).

[16] Y. Deng, A. Schwarz, H. Fattahi, M. Ueffing, X. Gu, M. Ossiander, T. Metzger, V. Pervak, H. Ishizuki, T. Taira, T. Kobayashi, G. Marcus, F. Krausz, R. Kienberger, and N. Karpowicz, "Carrier-envelope-phase-stable, 1.2 mJ, 1.5 cycle laser pulses at 2.1 μm," Opt. Lett. 37, 4973–4975 (2012).

[17] D. Strickland and G. Mourou, "Compression of amplified chirped optical pulses," Opt. Commun. 55, 447–449 (1985).

[18] M. Guardalben, J. Keegan, L. Waxer, V. Bagnoud, I. Begishev, J. Puth, and J. Zuegel, "Design of a highly stable, high-conversion-efficiency, optical parametric chirped-pulse amplification system with good beam quality." Opt. Express 11, 2511–2524 (2003).

[19] L. J. Waxer, V. Bagnoud, I. A. Begishev, M. J. Guardalben, J. Puth, and J. D. Zuegel, "High-conversion-efficiency optical parametric chirped-pulse amplification system using spatiotemporally shaped pump pulses," Opt. Lett. 28, 1245–1247 (2003).

[20] L. Yu, X. Liang, L. Xu, W. Li, C. Peng, Z. Hu, C. Wang, X. Lu, Y. Chu, Z. Gan, X. Liu, Y. Liu, X. Wang, H. Lu, D. Yin, Y. Leng, R. Li, and Z. Xu, "Optimization for high-energy and high-efficiency broadband optical parametric chirped-pulse amplification in LBO near 800 nm," Opt. Lett. 40, 3412–3415 (2015).

[21] P. Wnuk, Y. Stepanenko, and C. Radzewicz, "Multi-terawatt chirped pulse optical parametric amplifier with a time-shear power amplification stage." Opt. Express 17, 15264–15273 (2009).

[22] J. Moses, C. Manzoni, S.-W. Huang, G. Cerullo, and F. X. Kaertner, "Temporal optimization of ultrabroadband high-energy OPCPA," Opt. Express 17, 5540–5555 (2009).

[23] G. Arisholm, "General numerical methods for simulating second-order nonlinear interactions in birefringent media," J. Opt. Soc. Am. B 14, 2543–2549 (1997).

[24] R. Szipocs, K. Ferencz, C. Spielmann, and F. Krausz, "Chirped multilayer coatings for broadband dispersion control in femtosecond lasers." Opt. Lett. 19, 201–203 (1994).

[25] T. Metzger, "High-repetition-rate picosecond pump laser based on a Yb:YAG disk amplifier for optical parametric amplification," PhD thesis (2009).

[26] C. Teisset, N. Ishii, T. Fuji, T. Metzger, S. Köhler, R. Holzwarth, A. Baltuska, A. Zheltikov, and F. Krausz, "Soliton-based pump-seed synchronization for few-cycle OPCPA." Opt. Express 13, 6550–6557 (2005).

[27] A. Schwarz, M. Ueffing, Y. Deng, X. Gu, H. Fattahi, T. Metzger, M. Ossiander, F. Krausz, and R. Kienberger, "Active stabilization for optically synchronized optical parametric chirped pulse amplification," Opt. Express 20, 5557–5565 (2012).

[28] S. Adachi, N. Ishii, T. Kanai, A. Kosuge, J. Itatani, Y. Kobayashi, D. Yoshitomi, K. Torizuka, and S. Watanabe, "5-fs, multi-mJ, CEP-locked parametric chirped-pulse amplifier pumped by a 450-nm source at 1 kHz," Opt. Express 16, 14341–14352 (2008).

[29] M. Puppin, Y. Deng, O. Prochnow, J. Ahrens, T. Binhammer, U. Morgner, M. Krenz, M. Wolf, and R. Ernstorfer, "500 kHz OPCPA delivering tunable sub-20 fs pulses with

15 W average power based on an all-ytterbium laser," Opt. Express 23, 1491–1497 (2015).

[30] J. Rothhardt, S. Demmler, S. Hädrich, J. Limpert, and A. Tünnermann, "Octave-spanning OPCPA system delivering CEP-stable few-cycle pulses and 22 W of average power at 1 MHz repetition rate," Opt. Express 20, 10870–10878 (2012).

[31] F. Tavella, Y. Nomura, L. Veisz, V. Pervak, A. Marcinkevius, and F. Krausz, "Dispersion management for a sub-10-fs, 10 TW optical parametric chirped-pulse amplifier," Opt. Lett. 32, 2227–2229 (2007).

[32] V. Pervak, I. Ahmad, M. K. Trubetskov, A. V. Tikhonravov, and F. Krausz, "Double-angle multilayer mirrors with smooth dispersion characteristics," Opt. Express 17, 7943–7495 (2009).

[33] D. Franz, H. Fattahi, V. Pervak, M. Trubetskov, E. Fedulova, N. Karpowicz, Z. Major, and F. Krausz, "Investigation of temporal compression of few-cycle pulses from an ultrabroadband, multi-mJ optical parametric amplifier," in "Conf. Lasers Electro-Optics—Int. Quantum Electron. Conf." (2013), p. CFIE_P_3.

[34] T. Buberl, A. Alismail, H. Wang, N. Karpowicz, and H. Fattahi, "Self-compressed, spectral broadening of a Yb:YAG thin-disk amplifier," Opt. Express 24, 10286–10294 (2016).

[35] W. Schweinberger, A. Sommer, E. Bothschafter, J. Li, F. Krausz, R. Kienberger, and M. Schultze, "Waveform-controlled near-single-cycle milli-joule laser pulses generate sub-10 nm extreme ultraviolet continua," Opt. Lett. 37, 3573–3755 (2012).

[36] Y. Deng and F. Krausz, "Method and device for optical parametric chirped pulse amplification," WO/2013/020671 PCT/EP2012/003283, 14.02.2013, 01.08.2012 (2013).

Section 2

Laser-produced Soft X-Ray Sources

Chapter 4

Brilliance Improvement of a Laser-Produced Soft X-Ray Plasma

Tobias Mey

Additional information is available at the end of the chapter

http://dx.doi.org/10.5772/64149

Abstract

The brilliance of a laser-produced soft X-ray source is enhanced for gaseous target concepts. In contrast to solid or liquid target materials, these sources are clean and versatile but provide a comparably low conversion efficiency of laser energy into EUV and soft X-ray radiation. The basic idea is to induce supersonic effects in the gas jet, leading to a local increase of the particle density, and thus, to a larger number of possible emitters. Typically, the target gas is expanded into a vacuum environment and the density rapidly drops in all directions. In the present approach, a low pressure helium atmosphere is used to generate shock waves in the supersonic nozzle flow. Passing through these structures, the target gas is recompressed, and the particle density is raised. By focusing the laser beam into such regions, a higher number of gas atoms can be ionized resulting in a brighter and smaller plasma.

Keywords: soft X-ray, laser-produced plasma, supersonic jet, barrel shock

1. Introduction

Photons of the soft X-ray spectral region (≈ 0.1–10 nm) have very small absorption lengths in all kinds of material due to the strong interaction with matter [1]. This fact together with the short wavelength qualifies this radiation as a tool for structuring and the analysis with nanometer resolution. An important application is the next-generation lithography that further reduces the achievable feature size in computer chip production [2, 3]. Surface analysis becomes extremely precise by means of reflectometry and scatterometry [4–6] and also the binding state of molecules can be studied by spectral investigations [7–9]. Microscopy with radiation at wavelengths in the water window (λ = 2.3–4.4 nm) allows highly resolved direct

imaging of samples in aqueous environments [10–12]. Mostly, these applications are realized at large-scale facilities, such as synchrotron sources or free-electron lasers. However, the demand for beam time is always too large to be satisfied by these institutions, and thus, people endeavor to transfer experiments to their laboratories. This constitutes the need of compact beam sources as can be realized by the principle of laser-produced plasmas (LPP) that is the subject of this chapter.

In order to classify and compare the radiation of different soft X-ray beam sources, the brilliance *Br* is a commonly used quantity that is the number of photons within a narrow spectral range $\Delta\lambda/\lambda$ emitted into a solid angle Ω from an area A within the time scale τ (typically the wavelength range $\Delta\lambda$ is defined to be 0.1% of the central wavelength λ) [1]:

$$Br = \frac{N_{ph}}{\tau \cdot A \cdot \Omega \cdot \Delta\lambda / \lambda}. \tag{1}$$

The value of *Br* is given in the unit 1/(s·mm²·mrad² · 0.1%BW) with 0.1%BW indicating the bandwidth of 0.1%. A distinction is made between the peak brilliance, where τ denotes the pulse duration, and the average brilliance, where τ is the inverse of the repetition rate.

In comparison to synchrotrons and free-electron lasers, the brilliance of laser-produced plasma sources is several orders of magnitude lower. However, there are strategies to increase their brilliance which involve, e.g., higher power densities of the generating laser pulse. On the other hand, the density of the target material has a strong impact on the achievable number of soft X-ray photons too, whereas basically the source brilliance scales with the density. Thus, the brightest plasmas can be achieved with solids. Respective target materials are deposited on rotating cylinders [13] or quickly moving tapes [14], which provide repetition rates of up to 1 kHz. Prominent elements are gold or tin for the production of radiation at a wavelength of 13.5 nm, which is applied in EUV lithography [15]. Furthermore, there are sources employing cold gases in a solid phase, such as an argon filament that emits soft X-rays in the wavelength range 2–5 nm [16]. Achievable plasma sizes with solid targets are comparably small and on the order of several tens of μm (full-widths at half-maximum, FWHM).

A plasma of similar brilliance and extent is obtained with liquid targets, e.g., xenon [17], methanol [18], or tin [15]. A fluid jet [19] provides high target densities but might lead to size and brightness fluctuations. Going one step further to individual microscopic droplets [20], the advantage is the mass limitation such that the entire target material is converted into a highly ionized plasma state, supporting source stability. However, the drawback of solid and liquid target concepts is the inevitable production of fast particles and ions with kinetic energies of up to several hundred keV [21], which severely damage optics in the beam path. There are mitigation strategies to slow down the debris material such as repeller fields [22] or localized gas jet shields [23], but still the collector optics has a limited lifetime [2]. Contrarily, gaseous targets are almost free from debris [24]. Short gas pulses with durations of μs to ms are expanded from a pressure of several 10 bar into vacuum by a piezomechanical or electromagnetic nozzle, resulting in a supersonic jet. Different target gases feature individual spectra

http://dx.doi.org/10.5772/64149

of the resulting radiation, ranging from emitters with characteristic spectral lines (low atomic number, e.g., nitrogen) to broadband emitters (high atomic number, e.g., xenon) [25]. However, here, the conversion efficiency from laser energy into soft X-ray energy is comparably low due to the low density of the target material. Furthermore, achievable plasma sizes of several 100 μm are large. For metrology or scientific applications, though, these sources are very attractive due to their high cleanliness and versatility [8, 26].

In this study, a brilliance enhancement of laser-produced plasmas is demonstrated for gaseous jet targets, making use of supersonic effects. First, the theoretical background is provided to describe the physical properties of laser-produced plasmas as well as the gas dynamics of the related jet target. Experimental techniques are introduced that are employed to characterize the plasma and the gas jet. The effect of supersonic shocks within the target gas is investigated in both ways, theoretically and experimentally, revealing a significant brilliance enhancement for plasmas generated in respective shock regions. This chapter is based on a previous publication by Mey et al. [25] and has been revised and extended partly.

2. Physical properties of a plasma

Initially, the laser beam that irradiates the target material creates ions by multiphoton absorption, tunneling, or field ionization [27]. The resulting free electrons are accelerated by the strong electric field leading to inverse bremsstrahlung and avalanche ionization. A hot dense plasma state is generated. In competition to the heating processes, deionization takes place in terms of diffusion and recombination [27]. Depending on the electron temperature, a continuum of electromagnetic radiation is produced due to bremsstrahlung and recombination of free electrons with ions. Additionally, bound–bound transitions within the ions contribute narrow lines to the emission spectrum. A corresponding scheme is depicted in **Figure 1**.

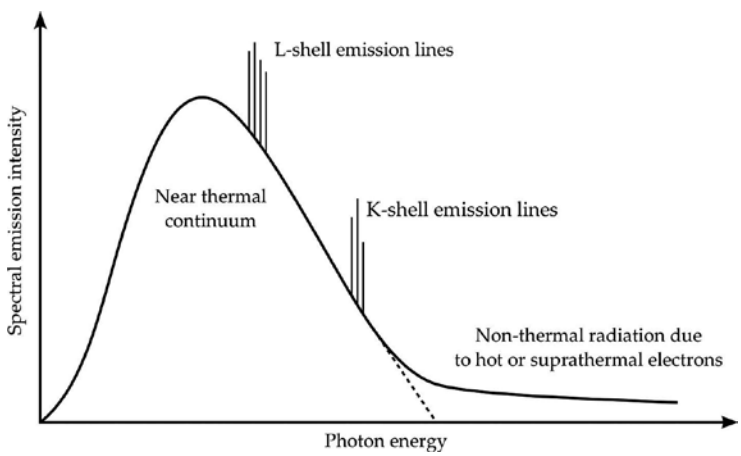

Figure 1. Scheme of the emission spectrum of a hot dense plasma.

The thermodynamics within a hot dense plasma can be approximated by the idealized state of a thermal plasma that is characterized by a single electron temperature T and a corresponding Maxwell velocity distribution. Within that simplification, the plasma may be treated as a blackbody that emits radiation with a continuous spectrum. The assumption that photons are emitted carrying discrete quanta of energy, with energy proportional to frequency, leads to the spectral energy density [1]

$$Br = 3.146 \times 10^{11} \left(\frac{k_B T}{\mathrm{eV}} \right)^3 \frac{\left(\frac{\hbar\omega}{k_B T} \right)^3}{e^{\frac{\hbar\omega}{k_B T}} - 1} \frac{Photons}{mm^2\, mrad^2 s\ (0.1\% BW)} \tag{2}$$

here, given in units of the brilliance with Planck's constant $\hbar$ and the photon frequency ω. Typical electron temperatures for gas targets irradiated by nanosecond laser pulses are 20–200 eV [28, 29]. The corresponding spectral maxima of the Planck distribution are found at the photon wavelengths 2.2–22.0 nm with peak brilliances of 3.6×10^{15} to 3.6×10^{18} 1/(s mm^2 mrad^2). In fact, a laser-produced plasma is far away from thermodynamic equilibrium and a thermal plasma rather is an upper limit for the spectral power density. However, mostly a two-temperature model is already sufficient to adequately describe the continuum radiation by a hot dense plasma, which is then called near-thermal plasma [1]. In addition to the thermal electrons, a suprathermal component is introduced which is raised by nonlinear interactions such as resonant absorption. When these electrons undergo bremsstrahlung or recombination, they give rise to a high photon energy tail in the emission spectrum as indicated in **Figure 1**. Line radiation is emitted when electrons change their energy state within an ion from an outer to an inner electron shell. The resulting photon energy corresponds to the transition energy of the electron as described by Moseley's law, which is an extension of the Rydberg formula [30]

$$\frac{1}{\lambda} = \frac{R_\infty}{1 + m_e / m_{nuc}} \left(Z_{at} - S_{sh} \right)^2 \left(\frac{1}{n_1^2} - \frac{1}{n_2^2} \right) \tag{3}$$

with the Rydberg constant R_∞, the nuclear mass m_{nuc}, and the atomic number Z_{at}. The constant S_{sh} describes the shielding due to electrons between the core and the considered electron. Furthermore, n_1 and n_2 are the principal quantum numbers of the initial and final states of the electron. In plasmas of species with low atomic numbers like nitrogen ($Z_{\mathrm{at}} = 7$), comparatively few free electrons are produced and the emitted radiation is dominated by single spectral lines. In contrast, elements with high atomic numbers such as xenon ($Z_{\mathrm{at}} = 54$) yield much more free electrons, resulting in a spectrum of numerous closely packed lines and a significant thermal contribution.

Another important plasma parameter is the electron plasma frequency [1]

http://dx.doi.org/10.5772/64149

$$\omega_p = \left(\frac{e^2 n_e}{\epsilon_0 m_e} \right)^{1/2} \tag{4}$$

at which the free electrons tend to oscillate (where e is the electron charge, n_e is the electron density, m_e is the electron mass, and ϵ_0 is the vacuum permittivity). As a consequence, an incident electromagnetic wave can propagate in the plasma only if its frequency ω is greater than ω_p and it is totally reflected if $\omega = \omega_p$. This yields a critical electron density [1]

$$n_c = \frac{\epsilon_0 m_e \omega^2}{e^2} \tag{5}$$

which is $n_c = 1 \times 10^{23}$ cm^{-3} for a common Nd:YAG laser beam with a wavelength of 1064 nm. Thus, when the plasma reaches the critical electron density, it cannot further be heated to pose a limit especially on solid and liquid target concepts. In order to mitigate that limitation, a less intense prepulse can be used to heat the target material and decrease its density precedent to the main pulse [31].

3. Gas dynamics of jet targets

Supersonic gas jets employed as targets inherently exhibit strong density gradients. Here, the basics of supersonic nozzle flows and related shock phenomena are described theoretically, mainly based on [32, 33]. As a result, density estimations of the target gas are provided corresponding to the experimental situation at a laser plasma source.

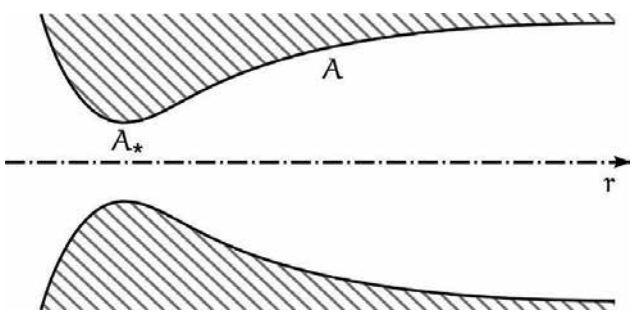

Figure 2. Sketch of a de Laval nozzle. A denotes the local cross-sectional area with the minimum value A_* at its throat position.

Let us first consider the example of a compressible fluid that expands through a convergent-divergent nozzle, a so-called de Laval nozzle as shown schematically in **Figure 2**. In gas dynamics, the basic equations to describe that problem are the conservation laws of mass and energy, formulated for compressible and isentropic flows. It can be shown that these relations

lead to the well-known area relation between the local cross-sectional area A, the throat area A_*, and the local Mach number M [33]

$$\frac{A}{A_*} = \frac{1}{M}\left[\frac{2}{\kappa+1}\left(1+\frac{\kappa-1}{2}M^2\right)\right]^{\frac{\kappa+1}{2(\kappa-1)}}. \tag{6}$$

Here, $\kappa = c_p/c_v$ is the ratio of specific heats (c_p at constant pressure and c_v at constant volume) and the Mach number M is defined as the ratio between the local flow velocity and the local speed of sound. In the present example of a convergent-divergent nozzle, a gas is accelerated in the convergent part according to the continuity equation. If the critical Mach number $M_* = 1$ is reached at the throat, this results in supersonic velocities $M > 1$ in the divergent part, and the thermal energy of the gas is efficiently converted into directed kinetic energy. Concurrently, the gas density decreases according to the relation [32]

$$\frac{\rho}{\rho_0} = \left(1+\frac{\kappa-1}{2}M^2\right)^{-\frac{1}{\kappa-1}} \tag{7}$$

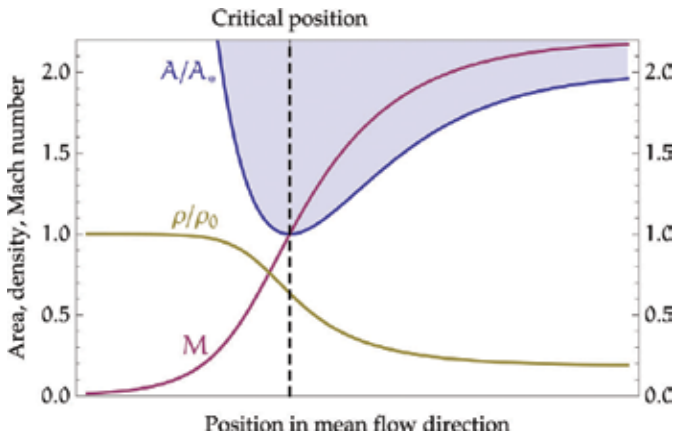

Figure 3. State functions of a flow in a de Laval nozzle: density ρ in terms of its stagnation value ρ_0, Mach number M and the local cross-sectional area A reaching A_* at its throat position. A diatomic gas with $\kappa = 7/5$ is assumed.

The shape of the cross-sectional area A/A_* of a typical de Laval nozzle is shown in **Figure 3** together with the resulting distribution of density ρ/ρ_0 (ρ_0 stagnation density) and Mach number M under the assumption of a diatomic gas with $\kappa = 7/5$. Utilizing a supersonic gas jet as a target for laser-produced plasmas requires large particle densities for high conversions efficiencies of laser energy into soft X-ray energy. Thus, a compromise needs to be found between a directed, but rarefied flow at high Mach numbers and divergent but denser flow at low Mach numbers. This can be achieved by adapting the nozzle geometry [34].

http://dx.doi.org/10.5772/64149

Within this work, shock waves, as they can be observed in supersonic flows, are employed to further optimize the particle density in a jet target. Within very short distances on the order of the mean-free path of the molecules, this phenomenon leads to an increase in density, pressure, and temperature while the Mach number decreases. Based on the conservation laws of mass, momentum, and energy, it is possible to derive equations that relate the initial values of those properties with the conditions right behind a shock wave. Here, it is sufficient to consider the change of the initial density ρ and the Mach number M in the case of a normal shock relative to the flow direction. After passing through the shock structure, these properties are denoted as $\hat{\rho}$ and $\widehat{M}$, as indicated in **Figure 4**. The corresponding shock relations read [32]

$$\frac{\hat{\rho}}{\rho} = \frac{(\kappa+1)M^2}{2+(\kappa-1)M^2} \tag{8}$$

$$\widehat{M} = 1 - \frac{M^2-1}{1+\frac{2\kappa}{\kappa+1}(M^2-1)}. \tag{9}$$

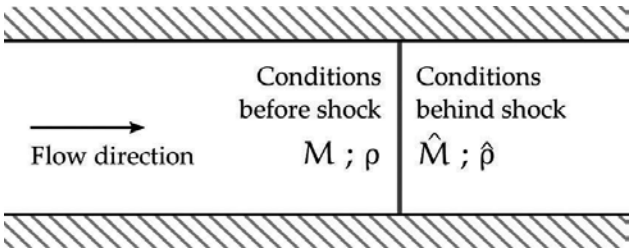

Figure 4. Normal shock structure in a supersonic flow. Gas passing through the shock experiences a decrease from the initial Mach number M to $\widehat{M}$ and an increase in density from ρ to $\hat{\rho}$.

Basically, high Mach numbers lead to a strong compression of the fluid when passing through a shock. However, relation (8) defines an upper limit for the density ratio that can be achieved in connection with a shock wave. This limit is approached if $M \to \infty$, and for diatomic gases it is $\frac{\hat{\rho}}{\rho} \to 6$ ($\kappa = 7/5$). At the same time, the Mach number behind the shock decreases to $\widehat{M} \to 1/7$. Shock waves appear, e.g., when obstacles perturb a supersonic flow or vice versa, or when objects travel with Mach numbers $M > 1$ through a gas at rest. In the case of a supersonic jet that expands from a stagnation pressure p_0 into an atmosphere with a sufficiently large background pressure p_b, shock waves can also be observed. At a certain distance to the nozzle exit, the collision between the jet particles and the surrounding gas particles leads to a shock structure, which is called barrel shock (see **Figure 5**). With respect to that situation, Muntz et al. introduced the rarefaction parameter [35]

$$\zeta = d_* \frac{\sqrt{p_0 \cdot p_b}}{T_0} \tag{10}$$

where d_* is the throat diameter of the nozzle and T_0 denotes the stagnation temperature. This parameter describes the interaction between jet and background particles, i.e., how strong the expansion flow is influenced by the surrounding gas. Muntz et al. propose a differentiation of the occurring flow into three regimes [35]:

- Scattering regime $\zeta \leq \zeta_s$

  Molecules of the background gas interact with the freely expanding jet by diffusion only, no distinct shock waves evolve.

- Transition regime $\zeta_s < \zeta < \zeta_c$

  Thick lateral shock waves develop and confine an undisturbed core of the jet that is surrounded by a mixing zone of jet and background particles.

- Continuum regime $\zeta_c \leq \zeta$

  The fully evolved barrel shock structure is present, as shown in **Figure 5**. The inner barrel shock waves and the Mach disk spatially delimit the influence of the background gas.

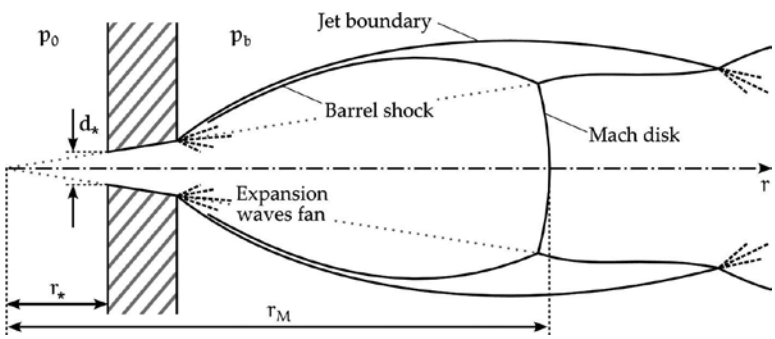

Figure 5. Typical structure of a barrel shock as apparent at supersonic jets in the presence of a background gas. Here, a fluid is expanded from a high pressure p_0 through the conically diverging nozzle into an ambient atmosphere of relatively low pressure p_b. The depicted shock system represents the continuum regime. Adapted from [36].

In the continuum regime, the extent of the shock structure scales with the nozzle pressure ratio p_0/p_b. In particular, within the range $15 < p_0/p_b < 17{,}000$, the distance $l_M = r_M - r_*$ between the nozzle throat and the Mach disk is given by [37]

$$l_M = 0.67 \cdot d_e \sqrt{\frac{p_0}{p_b}} \tag{11}$$

http://dx.doi.org/10.5772/64149

where d_e is the exit diameter of the orifice. It should be noted that this relation has been derived for nozzles with a constant diameter, i.e., for a nondivergent geometry.

In the following, estimations are made for a gas jet with barrel shock structures as it is under experimental investigation in this work too. Nitrogen expands from a pressure of $p_0 = 11$ bar into a helium atmosphere with a pressure of $p_b = 170$ mbar through a conically diverging nozzle (thickness $l_n = 1$ mm, throat diameter $d_* = 300$ µm, and exit diameter $d_e = 500$ µm). At rest, both gases are at room temperature $T_0 = 293$ K. In a simplification, a source flow is assumed corresponding to the dotted cone in **Figure 5** with its apex in a distance of $r_* = 1.5$ mm to the nozzle's throat. According to Eq. (11), the Mach disk appears 2.7 mm behind the nozzle throat, i.e., $r_M = 2.7$ mm. The dimensionless area of the assumed source flow is expressed in terms of the distance r to the virtual source as $A/A_* = (r/r_*)^2$. Solving Eqs. (6) and (7) results in the state functions ρ/ρ_0 and M along the symmetry axis of the nozzle from throat position to the Mach disk, i.e., in the range 1.5 mm < r < 4.2 mm. The conditions directly behind the Mach disk are determined by the shock relations (8) and (9). For r > 4.2 mm, the flow is assumed to be incompressible (ρ = const.) since the Mach number has decreased sufficiently below $M = 1$. Thus, subsequent behavior of M is approximated by the continuity equation $M(r) = \widehat{M} \cdot (r/r_M)^2$.

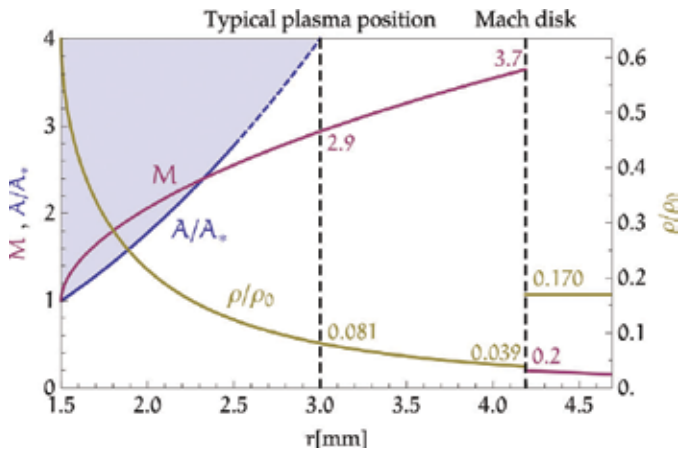

Figure 6. State functions along the symmetry axis of a barrel shock: density ρ in terms of its stagnation value ρ_0, and Mach number M. The solid blue line for A/A_* represents the cross-sectional area of the orifice, whereas the dashed blue line indicates the subsequent conical source flow.

The corresponding state functions $\rho(r)/\rho_0$ and $M(r)$ are depicted in **Figure 6** with respect to the distance r to the virtual source. Usually, the nozzle is operated with a background pressure on the order of $p_b \leq 10^{-4}$ mbar and the plasma is generated in a distance of 500 µm to the nozzle exit. The conditions at the usual plasma position, before and behind the Mach disk, are given in the diagram. It is revealed that due to the shock a two times higher density is achieved in a larger distance to the nozzle as compared to the typical plasma position. In practice, the density increase is even higher since plasma production takes place a few 100 µm besides the symmetry

axis of the nozzle. Here, without ambient gas the jet is even more rarefied and with ambient gas the shock structure is present.

4. The laser-produced soft X-ray source

The setup of a standard soft X-ray source based on gas targets is used [8]. It basically consists of a piezoelectrically operated Proch–Trickl gas valve [38] mounted on a vacuum chamber, and a driving Nd:YAG laser that emits radiation at the fundamental wavelength of 1064 nm with a pulse energy of 800 mJ and a pulse duration of 6 ns (InnoLas SpitLight 600), see **Figure 7**. The intensity profile of the unfocused laser beam, measured by a CCD camera (Lumenera Lu160M), reveals a beam diameter of 5.9 mm (determined through $1/e^2$ decay), corresponding to a mean power density of 4.9×10^8 W/cm^2. Plasma production takes place as soon as a critical power density of $\approx 10^{12}$ W/cm^2 is reached in the focused beam at a sufficiently large particle density [39]. This initiates the first ionization of the target gas followed by avalanche ionization, creating large numbers of free electrons.

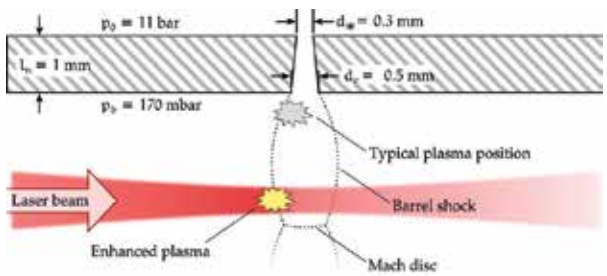

Figure 7. Pinhole camera images of the plasma at a stagnation pressure of p_0 = 11 bar for various background pressures p_b as given below the individual figure. The average of 30 single shots is shown.

The target gas is expanded through a divergent nozzle of conical shape. Over a length of l_n = 1 mm, its diameter increases from the throat diameter d_* = 0.3 mm to the exit diameter d_e = 0.5 mm. The nozzle is opened for a period of 1 ms, generating an underexpanded supersonic jet that expands from stagnation pressure p_0 = 11 bar into vacuum, i.e., the background pressure p_b is as low as 10^{-4} mbar. The laser is focused into the gas as soon as the jet flow is steady. The position where the plasma is produced is located in a distance of 500 μm, i.e., one diameter d_e behind the nozzle exit (see the typical plasma position indicated in **Figure 8**). Although the density is highest at the nozzle exit, the plasma should not be generated closer to the nozzle because of growing degradation effects. By employing different target species, various spectra can be obtained in the EUV and soft X-ray range. Noble gases with high atomic numbers such as xenon, argon, or krypton are broadband emitters, while oxygen or nitrogen each produces several narrow lines. The corresponding spectra can be found in **Figure 9**, produced by a system comparable to that described above and captured with a soft X-ray spectrometer, which is described in detail in [8]. Here, nitrogen is used in combination with a titanium filter,

http://dx.doi.org/10.5772/64149

resulting in a monochromatic emittance at λ = 2.88 nm in the water window, corresponding to the transition $1s^2 - 1S2p$ of the valence electron of the N^{5+} ion [40].

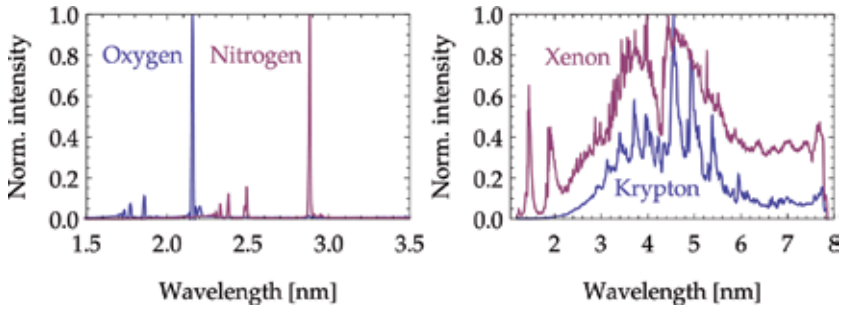

Figure 8. Photograph of experimental setup for plasma generation. The laser beam is focused by a lens into the vacuum chamber and generates the plasma right below the gas nozzle, which appears here in bluish color in the center of the chamber.

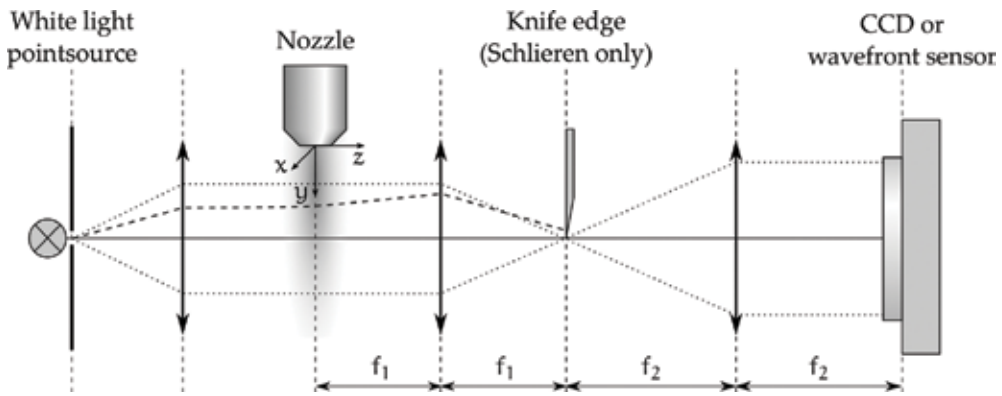

Figure 9. Principle of plasma generation employing jet targets: typically the plasma is generated close to the nozzle under vacuum conditions. Applying a background pressure p_b induces the barrel shock structure, which enhances plasma generation due to a local density increase.

In the approach pursued in this work, the background pressure p_b is increased to several tens of mbar in order to generate a barrel shock in the supersonic jet. For this purpose, helium is utilized as a background gas due to its high transmissivity of photons generated by the plasma. In addition, the optical path length of the resulting soft X-rays through helium is minimized by differential pumping. Another advantage of using helium as a surrounding gas is its large first ionization energy (24.6 eV) compared to that of nitrogen (14.5 eV) [41]. Thus, the critical power density to drive ionization by the incident laser beam is higher for helium, which ensures that only the target species nitrogen is ionized. Right behind the shock system generated in the jet, the particle density increases. In this manner, regions involving high densities of the target gas are obtained at comparably large distances from the nozzle. Thus,

the plasma can be generated further away from the nozzle exit, and degradation effects are minimized.

5. Gas jet and soft X-ray diagnostics

In order to characterize the supersonic gas jet and the evolving shock structure, two different methods are employed: the Schlieren technique for highly resolved qualitative imaging of density gradients and wavefront measurements with a Hartmann–Shack sensor in order to quantify the density distribution, but at a lower resolution. Both methods are described in detail in Sections 5.1 and 5.2.

The plasma is imaged by a pinhole camera and the number of the resulting soft X-ray photons is determined with a calibrated photodiode. A description of these tools follows in Section 5.3.

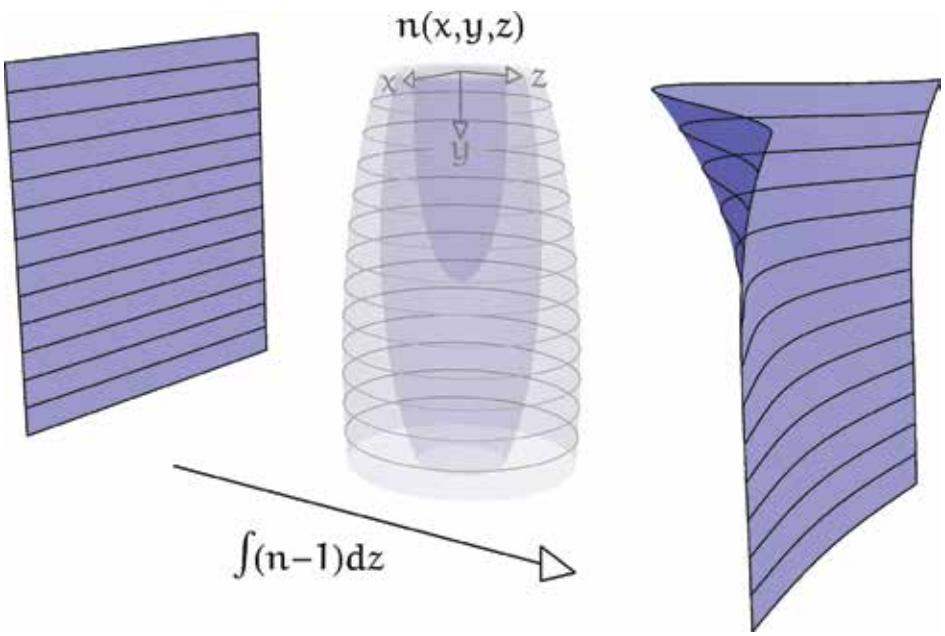

Figure 10. Characteristic emission spectra of various target gases, captured with a soft X-ray spectrometer.

5.1. Schlieren imaging

Schlieren imaging is a common technique in fluid dynamics that enables the qualitative measurement of density gradients [42]. The experimental setup is schematically shown in **Figure 10**. A pinhole with a diameter of 100 μm is illuminated by white light, and a focusing lens collimates the resulting beam, which then travels in the *z*-direction through the gas distribution of the jet target. The *xy*-plane at $z = 0$ is imaged by a 4f setup to a CCD camera

http://dx.doi.org/10.5772/64149

(Lumenera Lu160M) and captured with an exposure time of 50 μs. The camera is synchronized with the gas jet at a repetition rate of 10 Hz. Here, imaging lenses with focal lengths of f_1 = 160 mm and f_2 = 300 mm are used. A knife edge is moved close to the focal spot in between the two lenses, eliminating half of the spatial frequencies in the Fourier plane. The orientation of the blade determines which component of the density gradient will become visible. For example, as depicted in **Figure 10**, a knife edge aligned with the x-axis generates contrast proportional to the gradient of the refractive index $\partial n/\partial y$ corresponding to the density gradient $\partial \rho/\partial y$. Note, however, that in the Schlieren images shown below, the knife edge is aligned with the y-axis, so that density gradients within the jet are visualized in radial direction, thus emphasizing the barrel shock.

5.2. Wavefront monitoring

A Hartmann-Shack wavefront sensor [43, 44] is used to obtain quantitative information on the density distribution in the supersonic gas jet [34]. The experimental setup is mostly the same as that depicted in **Figure 10** for Schlieren imaging. However, the knife edge is removed and the CCD camera is replaced by the wavefront sensor. An initially plane wavefront of a test beam that travels through the target gas is deformed due to the spatial variation of the refractive index $n(x, y, z)$. The sensor splits the test beam into many subbeams by an array of microlenses, each producing a spot on a CCD camera (Lumenera Lu160M). The position of the spots contains the information of the local wavefront gradient. Thus, the deformation of the wavefront can be recovered. The spatial resolution Δx of a measured wavefront is equal to the pitch of the microlens array of 150 μm divided by the magnification factor f_2/f_1 = 1.88 of the 4f setup, yielding Δx = 80 μm.

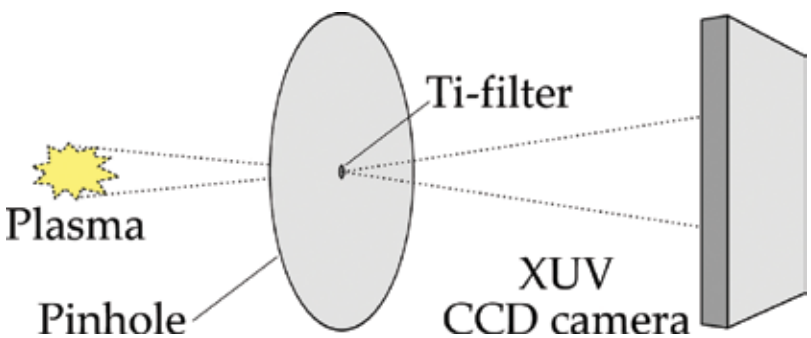

Figure 11. Experimental setup for Schlieren and wavefront measurements. The dotted lines represent the path of unrefracted light. The dashed line indicates a light ray that is refracted by varying distribution of gas density below the nozzle, thus hitting the knife edge and darkening the image. In order to monitor wavefront deformations, the CCD camera is replaced by a Hartmann–Shack sensor and the knife edge is removed.

The particle density distribution $N(x, y)$ in the nozzle plane $z = 0$ is recovered from a measured shape $w(x, y)$ of a deformed wavefront as follows. The test beam integrates $n(x, y, z)$ over the propagation direction z of the light beam, resulting in a difference $w(x, y)$ in the optical path, as illustrated in **Figure 11**. Now, it is assumed that in a plane corresponding to a constant $y = y_0$, $n(x, y_0, z)$ is approximated by a rotationally symmetric Gaussian shape with a maximum value $n_0(y_0) = n(0, y_0, 0)$. Then, the deformation of the wavefront reads

$$\begin{aligned} w(x,y) &= \int \left[n(x,y,z) - 1 \right] dz \\ &= \int \left[n_0(y) - 1 \right] \cdot \exp\left(-\frac{x^2}{2\sigma(y)^2} \right) \cdot \exp\left(-\frac{z^2}{2\sigma(y)^2} \right) dz \\ &= \left[n_0(y) - 1 \right] \cdot \sqrt{2\pi}\, \sigma(y) \cdot \exp\left(-\frac{x^2}{2\sigma(y)^2} \right). \end{aligned}$$

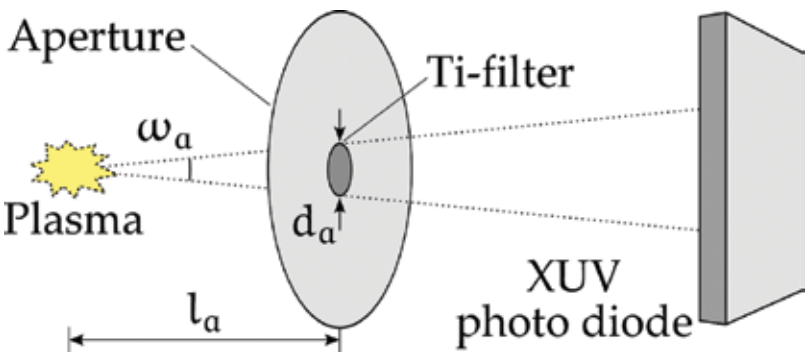

Figure 12. Wavefront deformation induced by the gas jet. The distribution of the optical density $n(x, y, z)$ increases the optical path length, resulting in the indicated wavefront deformation.

The standard deviation $\sigma(y)$ of $n(x, y, z)$ is determined from the shape of the measured deformation of the wavefront $w(x, y)$ by a Gaussian fit. The distribution of the refractive index in the plane $z = 0$ containing the jet axis is recovered by

$$n(x,y,0) - 1 = \frac{w(x,y)}{\sqrt{2\pi}\sigma(y)}. \tag{12}$$

Conversion of the refractive index $n(x, y, 0)$ into a particle density N is done by using the Lorentz-Lorenz formula [45]

$$\frac{n^2 - 1}{n^2 + 2} = \frac{4}{3}\pi\alpha N \tag{13}$$

http://dx.doi.org/10.5772/64149

where α, the polarizability of the considered gas particles, is derived using the values n = 1.0002974 and $N = 2.69 \times 10^{19}$ cm^{-3} for nitrogen under normal conditions [41] (at a temperature of 273.15 K and a pressure of 1013.25 mbar). In these calculations, the surrounding helium atmosphere is neglected because of its low refractive index that amounts to only a few percent as compared to that of the nitrogen jet.

5.3. Plasma characterization

Qualitatively, the plasma is characterized by a pinhole camera system as sketched in **Figure 12**. It consists of a phosphor-coated CCD camera (Lumenera Lu160M with three layers of phosphor P43 with a grain size of ≈ 1 μm) in combination with a titanium-filtered pinhole (100 μm diameter, Ti-layer 200 nm thick). This way, the intensity distribution of radiation at the wavelength λ = 2.88 nm is captured. Here, the luminescent area A is approximated by an ellipsoidal shape with the semiaxes a and b. Then, $A = \pi\, a\, b$, where a and b are defined as the full-widths at half-maximum of the intensity in the x- and y-directions. The uniformity of the plasma is characterized by its eccentricity $\varepsilon = \sqrt{a^2 - b^2}/a$. Examples of the intensity images are shown in **Figure 17** in combination with the corresponding Schlieren images of the gas jet for the case of both, gas issuing into vacuum and gas issuing into a background gas and thus forming a barrel shock.

Quantitatively, the peak brilliance Br of the plasma is derived by

$$Br = \frac{N_{ph}}{\tau\, \Omega A} \tag{14}$$

with the pulse duration τ, the solid angle Ω, and the source area A. The number of photons N_{ph} with a wavelength of λ = 2.88 nm is determined by a calibrated XUV photodiode (International Radiation Detectors, AXUV100), which is equipped with a titanium filter (thickness 200 nm, applied to a nickel mesh with a transmissivity of 0.89). As shown in **Figure 13**, only these photons reach the detector that propagate within a cone confined by a circular aperture with diameter d_a in a distance l_a to the plasma. Thus, the solid angle is defined by the corresponding opening angle $\omega_a = 2 \tan d_a/(2l_a)$ of the cone [46]

$$\Omega = 4\pi \sin^2 \sin^2 \frac{\omega_a}{4}. \tag{15}$$

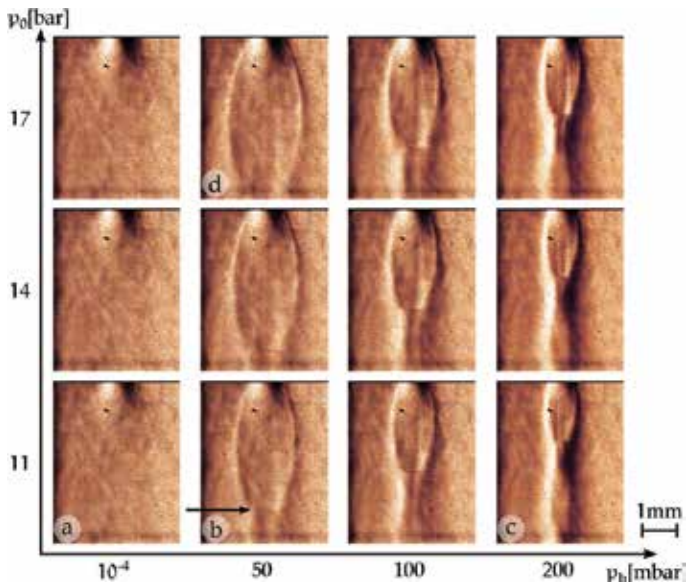

Figure 13. Principle of plasma characterization by pinhole camera.

In good approximation, the lifetime of the plasma is assumed to be $\tau = 6$ ns, which equals the duration of the exciting laser pulse. Finally, the luminescent area A is determined with a pinhole camera as described above.

6. Experimental results

First, the gas jet and the effect of a background pressure on the resulting flow structure are investigated using the techniques described in the previous section. The derived results are compared to theoretical relations discussed in Section 3. Subsequently, the effect of the barrel shock on the plasma generation is explored and the brilliance improvement of the soft X-ray source is quantified.

6.1. Characterization of the target gas jet

Depending on the stagnation and background pressure, the gas jet may form various shapes, which are discussed in the following. In previous studies of laser-produced soft X-ray sources, the nozzle was operated in the range $p_0 = 11$–17 bar at a background pressure of $p_b = 10^{-4}$ mbar, i.e., practically without any background gas. In this case, the emerging flow is in the scattering regime and does not show any discontinuities. Independently of p_0, the density distribution has a maximum value at the nozzle exit and rapidly falls off in all directions. The corresponding Schlieren images are taken with the knife edge aligned with the y-axis and can be found in **Figure 14** for the pressure range $p_0 = 11$–17 bar.

http://dx.doi.org/10.5772/64149

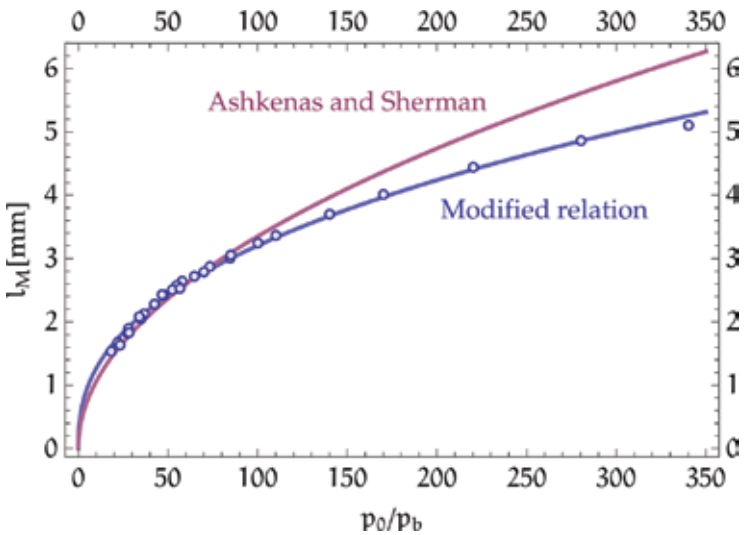

Figure 14. Principle of plasma characterization by diode measurement.

With rising background pressure, particle collisions increasingly affect the gas jet and retard its free expansion. At a certain distance from the nozzle, this results in a shock that is directly connected to a local decrease of the Mach number M. At the same time, the local particle density increases. This becomes evident in regions of the Schlieren images that show strong changes in intensity, implying high-density gradients. As can be seen, e.g., in **Figure 14(b)**, the shape of the resulting shock structure resembles a barrel, why it is referred to as a barrel shock. In the downstream direction, the barrel shock is terminated by the Mach disk, which is indicated in the Schlieren image by an arrow. In the present Schlieren pictures, the Mach disk is reproduced only weakly because the knife edge was aligned perpendicular to the disk and only density gradients parallel to the disk were detected.

Increasing p_b, as from **Figure 14(b)–(c)**, results in a confinement of the gas flow toward the nozzle axis—the lateral shocks approach each other and the Mach disk moves upstream. In contrast to this, increasing p_0 has the opposite effect, i.e., the radius of the barrel shock and the width σ of the density distribution increase and the Mach disk moves downstream, see **Figure 14(b)–(d)**. These two opposite effects allow generation of the same shock structure at different combinations of the pressures, provided that the ratio p_0/p_b stays constant.

From the Schlieren images as shown in **Figure 14**, the distance l_M between the Mach disk and the nozzle throat is derived for pressure ratios in the range $18 \le p_0/p_b \le 340$. In **Figure 15**, the resulting data set is compared to the empirical relation (11)

$$l_M = 0.67 \cdot d_e \left(\frac{p_0}{b_b} \right)^{1/2} \tag{16}$$

which has been derived by Ashkenas and Sherman [37] for a nondivergent nozzle. Apparently, the experimental results deviate from the depicted curve, especially for large pressure ratios. Most likely, this can be attributed to a different nozzle geometry as in the present situation. Here, a divergent orifice initially guides the supersonic expansion of the gas before it expands freely into the helium atmosphere. For that case, a relation of the form

$$l_M = d_e \left(\frac{p_0}{p_b} \right)^a \tag{17}$$

reveals good agreement with the measured shock distances as it is evident in **Figure 15**. By a least-squares fit routine, the exponent is derived to $a = 0.4034$.

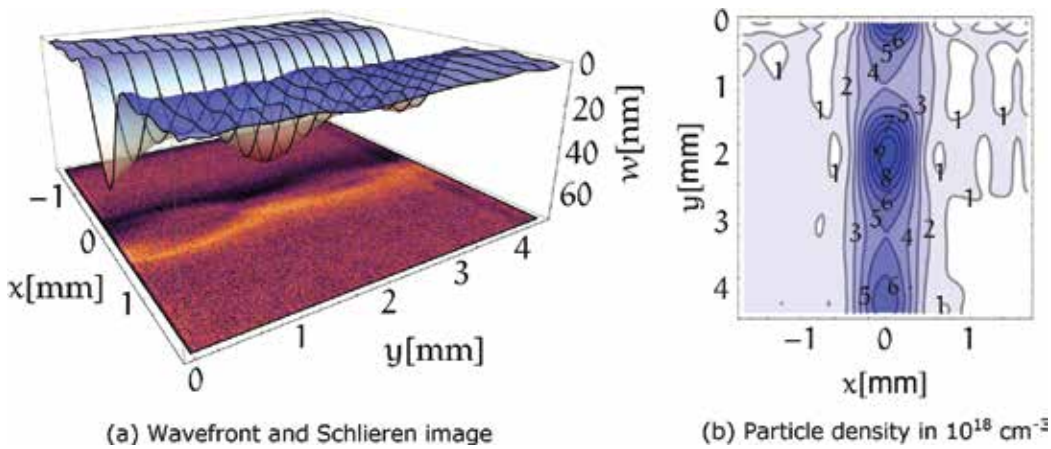

Figure 15. Schlieren images indicating the supersonic flow structure of an N_2 jet as a function of stagnation and background pressure (flow direction: top → bottom). (a) Scattering regime, no internal structures evolve; (b) continuum regime with barrel shock structure, the Mach disk is indicated by the arrow; (b) → (c) shock structure contracts for increasing background pressure; (b) → (d) shock structure inflates for increasing stagnation pressure.

In **Figure 16**, wavefront and Schlieren measurements are compared with each other for a stagnation pressure of $p_0 = 11$ bar and a background pressure of $p_b = 170$ mbar. The results of both techniques are well consistent. The particle density $N(x, y)$ shows the mean gas distribution inside the jet. In the downstream direction, along the nozzle axis, N first decreases to $N_{min} = 4.0 \times 10^{18}$ cm^{-3} and then increases again up to a maximum value of $N_{max} = 9.8 \times 10^{18}$ cm^{-3}. Subsequently, the wave-like behavior of the particle density is repeated at lower density values. The observed maxima coincide approximately with the positions where the lateral shocks interfere, forming a Mach disk.

http://dx.doi.org/10.5772/64149

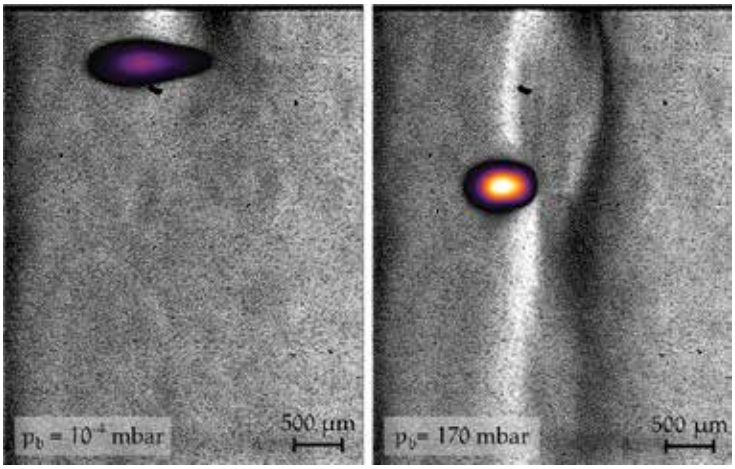

Figure 16. Distance between Mach disk and nozzle exit for various pressure ratios. The points are derived from the Schlieren images, the violet curve represents the empirical relation (11) from Ashkenas and Sherman [37] and the blue curve represents the modified relation given in Eq. (17) with $a = 0.4034$.

Employing the relations of gas dynamics introduced in Section 3, a rough theoretical estimate of the particle density ahead and behind the Mach disk is now compared to the results obtained with the wavefront sensor. Corresponding to the experimental situation, the density distribution along the symmetry axis of the gas jet is shown in terms of its stagnation value ρ_0 as shown in **Figure 6**. There, a normal shock induces a density increase from $\rho_{min} = 0.039\ \rho_0$ to $\rho_{max} = 0.170\ \rho_0$ in a distance of $l_M = 2.7$ mm to the nozzle throat. For the current pressure ratio of $p_0/p_b = 64.7$, this coincides with the position of the Mach disk.

In order to derive absolute density values, the stagnation density ρ_0 of the nitrogen jet is required. Following the ideal gas law, $p_0 = \rho_0\ R_{sp}\ T_0$ results in $\rho_0 = 12.65$ kg/m^3 with the specific gas constant for nitrogen $R_{sp,N_2} = 296.8$ J/(kg · K) [41], the temperature $T_0 = 293$ K, and pressure $p_0 = 11$ bar inside the vessel. Finally, particle densities ahead and behind the Mach disk are evaluated with the molecular mass of nitrogen $m_{N_2} = 4.653 \times 10^{-26}$ kg [41]. A comparison between the theoretical estimation and the measured values is given in **Table 1**.

	Theoretical estimate	**Measurement**
N_{min} (10^{18} cm^{-3})	10.6	4.0
N_{max} (10^{18} cm^{-3})	46.1	9.8

Table 1. Particle density ahead (N_{min}) and after (N_{max}) the barrel shock, given on the symmetry axis of the jet. Comparison between theoretical estimate and measurement.

The estimated values are of the same order of magnitude but larger than the experimental results. This discrepancy can be attributed to the spatial resolution of the wavefront sensor that is not able to resolve the high density value right behind a shock. Furthermore, the estimate

provides an upper limit of the particle density since in a simplification a conical source flow has been assumed. In fact, the stream lines of the flow are bended in lateral direction, stronger than the cone geometry presumes. Consequently, this results in a higher rarefaction of the gas and the typical bulbous barrel shock. This explains why values of the estimated particle densities, both of the maximum and the minimum, are higher than the corresponding measured values.

6.2. Characterization of the plasma enhancement

The effect of an increase in target gas density on the plasma generation is illustrated in **Figure 17** for a stagnation pressure of p_0 = 11 bar. Taking advantage of the barrel shock, obviously the brightness of the plasma is raised, whereas its size has decreased in the direction of the incident laser beam. Due to the increased target density, there are more emitters of soft X-ray radiation in the same volume. Besides, the absorption of laser energy is raised. Thus, the power density of the beam decreases more rapidly below its critical value and no further atoms are ionized. This confines the size of the plasma in the beam direction and explains its smaller size. Another mechanism causing the reduced size might be plasma defocusing [47]. Due to an increased plasma density, a stronger defocusing effect can be expected, limiting the ionization region. During the experiments, it turned out that generation of a plasma right below the Mach disk, where the density is expected to be at a maximum, is not the optimal position. It was found that even brighter and smaller plasmas occur when the laser is focused onto the edge of the jet at a location slightly above the Mach disk and after the barrel shock (see **Figure 17**). This behavior may be caused by reabsorption of soft X-rays by the surrounding nitrogen particles.

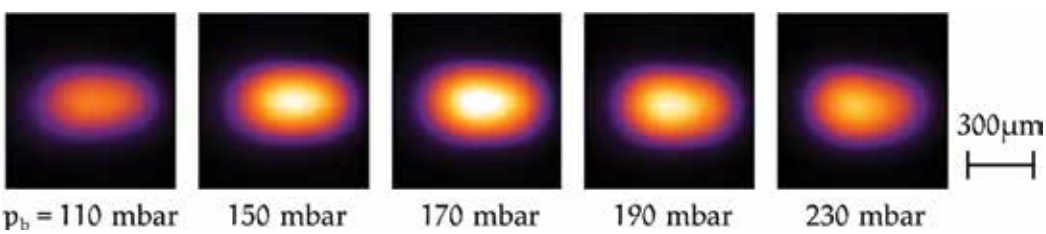

Figure 17. (a) Combination of quantitative wavefront and qualitative Schlieren image of the N_2 jet expanding from p_0 = 11 bar into an He atmosphere with p_b = 170 mbar. (b) Density distribution $N(x, y)$ of the N_2 jet in the plane z = 0, which results from the wavefront as described in Section 5.2.

The barrel shock is enclosed by a thin supersonic compressed layer, which becomes thicker at the Mach disk [36], leading to increased reabsorption. In order to study the brilliance improvement depending on the location of plasma generation with respect to shock structures in the jet, the latter were varied by changing the background pressure at a constant stagnation pressure (p_0 = 11 bar). By lowering p_b, the radius of the barrel shock is increased; conversely, with increasing p_b, the radius of the barrel shock decreases. Thus, with the location of the focus of the laser beam fixed, its relative location with respect to high-density regions behind the shock is changed. In **Figure 18**, intensity distributions of the plasma are shown for various

http://dx.doi.org/10.5772/64149

background pressures p_b. In this case, the location of plasma generation is kept constant. An optimum value is found at $p_b = 170$ (see also **Figure 17**).

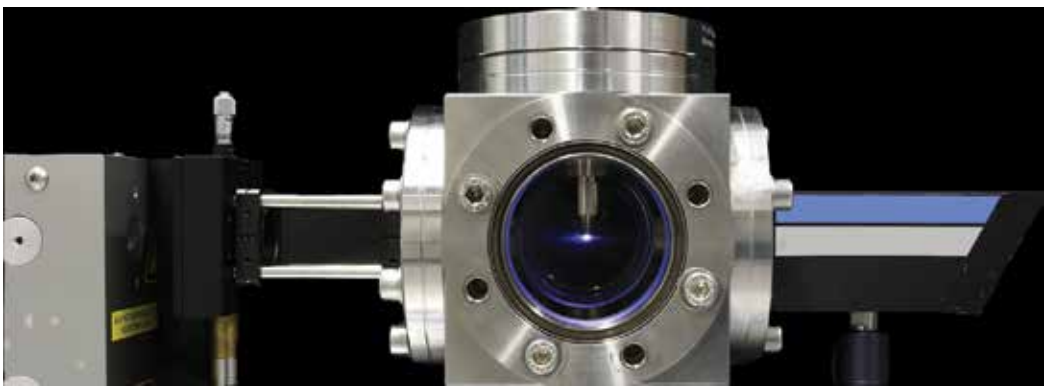

Figure 18. Pinhole camera images of the plasma superimposed on the Schlieren images of gas jet at $p_0 = 11$ bar. Left: under vacuum conditions $p_b = 10^{-4}$ mbar. Right: with ambient He atmosphere at $p_b = 170$ mbar. Both plasma images are an average of 30 single shots.

Unexpectedly, increasing both p_0 and p_b while preserving the pressure ratio p_0/p_b, does not lead to a considerable further increase in the brilliance of the source. Approaching high-pressure values ($p_0 = 17$ bar), quite the reverse happens: the plasma appears even darker. It can be assumed that, in fact, more soft X-ray photons are generated since the target density is increased. However, the density of the background gas is increased as well, which leads to higher reabsorption of the generated photons. The latter effect seems to dominate the former. It is expected that further efforts in differential pumping can shorten the path length of the soft X-rays through the outer helium gas so that the brilliance of the source can further be increased.

Now, parameters characterizing the plasma in the optimal case are compared with those of a plasma produced near the nozzle exit with a jet in the scattering regime. In both cases, the same stagnation pressure of $p_0 = 11$ bar is considered. Regarding the shape of the resulting plasma, which is represented by its luminescent area, it can be seen that the radiating area is reduced by a factor of 0.71 to $A = 0.063$ mm^2, and its eccentricity decreases slightly from $\varepsilon = 0.91$ to $\varepsilon = 0.80$ when a barrel shock is present. This results in a better brilliance and improves the coherence properties due to a smaller source size and a more uniform shape. The number of photons emitted per pulse and solid angle from the nitrogen plasma at a wavelength of $\lambda = 2.88$ nm is raised by a factor of 7.1 to a value of 1.2×10^{13} sr^{-1}. Based on these values, the peak brilliance can be computed. One finds an improvement by a factor of 10 to a value of $Br = 3.15 \times 10^{16}$ photons/(mm^2 mrad^2 s). This clearly demonstrates the advantage of utilizing the density increase across a barrel shock system. An overview of the characteristic parameters of the plasma is given in **Table 2**.

	Without barrel shock	With barrel shock	Factor
Radiating area (mm^2)	0.088	0.063	0.71
Eccentricity [1]	0.91	0.80	0.88
Photons/(solid angle · pulse) (sr^{-1})	1.66×10^{12}	1.18×10^{13}	7.10
Peak brilliance (mm^{-2} $mrad^{-2}$ s^{-1})	3.15×10^{15}	3.15×10^{16}	10.0

Table 2. Comparison of plasma emission characteristics at λ = 2.88 nm obtained with a nitrogen jet issuing into vacuum (no barrel shock) and into a background gas (with barrel shock).

7. Conclusion

Laser-produced plasmas based on gas targets serve as versatile and nearly debris-free soft X-ray sources at a table-top size. In this chapter, a method has been shown by which the brilliance of gas targets can be improved. To this end, a background pressure is applied to the gas jet that leads to a strong recompression of the target particles. For the example of an underexpanded supersonic nitrogen jet, the resulting barrel shock has been qualitatively visualized by the Schlieren photography. The corresponding density distribution was obtained by a quantitative Hartmann-Shack measurement. Measured values of the shock location and particle densities are of the same order of magnitude as those of a first estimate that was partly based on correlations. The size of the resulting plasma is reduced by a factor of 0.71 and its shape becomes more uniform, thus improving the coherence properties of the source. At the same time, the number of photons per solid angle at λ = 2.88 nm is raised by a factor of 7.1. In this manner, the brilliance of the source is increased by a factor of 10.0 to $Br = 3.15 \times 10^{16}$ photons/(mm^2 $mrad^2$ s). Even greater increases may be obtained by using hydrogen as the background gas since H_2 shows a 13 times lower absorption of the generated X-rays compared to He [48]. However, for safety reasons H_2 has not been employed here. A further increase in the plasma's brilliance is to be expected with increasing the stagnation and background pressure. An essential condition for achieving this is an improvement in the differential pumping system in order to lower the reabsorption of the soft X-rays by the background gas.

Acknowledgements

The author kindly acknowledges support by Deutsche Forschungsgemeinschaft within Sonderforschungsbereich 755 "Nanoscale photonic imaging." Furthermore, the author acknowledges the permission to reproduce material [25], which has been previously published by IOP Publishing & Deutsche Physikalische Gesellschaft under CC BY-NC-SA license.

Author details

Tobias Mey

Address all correspondence to: tobias.mey@llg-ev.de

Laser-Laboratorium Göttingen e.V., Göttingen, Germany

References

[1] Attwood D. Soft X-Rays and Extreme Ultraviolet Radiation. Cambridge: Cambridge University Press; 1999.

[2] Bakshi V, editor. EUV Lithography. SPIE Press; Bellingham, Washington, USA. 2008. 702 pp.

[3] Wu B, Kumar A. Extreme ultraviolet lithography: a review. Journal of Vacuum Science & Technology B. 2007; 25: 1743–1761. DOI: 10.1116/1.2794048

[4] Scholze F et al. New PTB beamlines for high-accuracy EUV reflectometry at BESSY II. Soft X-Ray and EUV Imaging Systems. .Proc. SPIE 4146. 2000; 72. DOI: 10.1117/12.406678

[5] Scholze F, Laubis C. Use of EUV scatterometry for the characterization of line profiles and line roughness on photomasks. In: Mask and Lithography Conference (EMLC), 24th European Conference; 2008.

[6] Banyay M, Juschkin L. Table-top reflectometer in the extreme ultraviolet for surface sensitive analysis. Applied Physics Letters. 2009; 94(6): 063507. DOI: 10.1063/1.3079394

[7] Chen JG. NEXAFS investigations of transition metal oxides, nitrides, carbides, sulfides and other interstitial compounds. Surface Science Reports. 1997; 30: 1–152. DOI: 10.1016/s0167-5729(97)00011-3

[8] Peth C, Barkusky F, Mann K. Near-edge X-ray absorption fine structure measurements using a laboratory-scale XUV source. Journal of Physics D. 2008; 41: 105202. DOI: 10.1088/0022-3727/41/10/105202

[9] Stöhr J. NEXAFS Spectroscopy (Springer Series in Surface Sciences). Springer; Berlin Heidelberg, Germany. 2003.

[10] Da Silva LB et al. X-ray laser microscopy of rat sperm nuclei. Science. 1992; 258: 269–271. DOI: 10.1126/science.1411525

[11] Berglund M et al. Compact water-window transmission X-ray microscopy. Journal of Microscopy. 2000; 197: 268–273. DOI: 10.1046/j.1365-2818.2000.00675.x

[12] Hertz HM et al. Laboratory X-ray microscopy for high-resolution imaging of environmental colloid structure. Chemical Geology. 2012; 329: 26–31. DOI: 10.1016/j.chemgeo.2011.07.012

[13] Barkusky F et al. Direct photoetching of polymers using radiation of high energy density from a table-top extreme ultraviolet plasma source. Journal of Applied Physics. 2009; 105: 014906. DOI: 10.1063/1.3054565

[14] Haney SJ et al. Prototype high-speed tape target transport for a laser plasma soft-x-ray projection lithography source. Applied Optics. 1993; 32: 6934–6937. DOI: 10.1364/ao.32.006934

[15] Wagner C, Harned N. EUV lithography: lithography gets extreme. Nature Photonics. 2010; 4: 24–26. DOI: 10.1038/nphoton.2009.251

[16] Peth C et al. XUV laser-plasma source based on solid Ar filament. Review of Scientific Instruments. 2007; 78: 103509. DOI: 10.1063/1.2801882

[17] Hansson BAM. Characterization of a liquid-xenon-jet laser-plasma extreme-ultraviolet source. Review of Scientific Instruments. 2004; 75: 2122–-2129. DOI: 10.1063/1.1755441

[18] Vogt U et al. High-resolution spatial characterization of laser produced plasmas at soft x-ray wavelengths. Applied Physics B. 2004; 78: 53–58. DOI: 10.1007/s00340-003-1338-9

[19] Jansson PAC et al. Liquid-tin-jet laser-plasma extreme ultraviolet generation. Applied Physics Letters. 2004; 84: 2256–2258. DOI: 10.1063/1.1690874

[20] Richardson M et al. High conversion efficiency mass-limited Sn-based laser plasma source for extreme ultraviolet lithography. Journal of Vacuum Science & Technology B. 2004; 22: 785–790. DOI: 10.1116/1.1667511

[21] Wieland M et al. EUV and fast ion emission from cryogenic liquid jet target laser-generated plasma. Applied Physics B. 2001; 72: 591–597. DOI: 10.1007/s003400100542

[22] Bakshi V, editor. EUV Sources for Lithography. SPIE Press; Bellingham, Washington, USA. 2006.

[23] Rymell L, Hertz HM. Debris elimination in a droplet-target laser-plasma soft x-ray source. Review of Scientific Instruments. 1995; 66: 4916–4920. DOI: 10.1063/1.1146174

[24] Rakowski R et al. Characterization and optimization of the laser-produced plasma EUV source at 13.5 nm based on a double-stream Xe/He gas puff target. Applied Physics B. 2010; 101: 773–789. DOI: 10.1007/s00340-010-4327-9

[25] Mey T et al. Brilliance improvement of laser-produced soft x-ray plasma by a barrel shock. New Journal of Physics. 2012; 14: 073045. DOI: 10.1088/1367-2630/14/7/073045

[26] Fiedorowicz H et al. Compact laser plasma EUV source based on a gas puff target for metrology applications. Journal of Alloys and Compounds. 2005; 401: 99–103. DOI: 10.1016/j.jallcom.2005.02.069

[27] Morgan CG. Laser-induced breakdown of gases. Reports on Progress in Physics. 1975; 38: 621–665. DOI: 10.1088/0034-4885/38/5/002

[28] Fiedorowicz H et al. Investigation of soft X-ray emission from a gas puff target irradiated with a Nd:YAG laser. Optics Communications. 1999; 163: 103–-114. DOI: 10.1016/s0030-4018(99)00100-5

[29] Müller M et al. Emission properties of ns and ps laser-induced soft X-ray sources using pulsed gas jets. Optics Express. 2013; 21: 12831. DOI: 10.1364/oe.21.012831

[30] Mayer-Kuckuk T. Atomphysik. Teubner Verlag; Stuttgart, Germany. 1997.

[31] Komori H et al. EUV radiation characteristics of a CO_2 laser produced Xe plasma. Applied Physics B. 2006; 83: 213–218. DOI: 10.1007/s00340-006-2172-7

[32] Wieghardt K. Theoretische Strömungslehre. Universitätsverlag; Göttingen, Germany 2005.

[33] Spurk J, Aksel N. Strömungslehre. Berlin: Springer; 2010.

[34] Peth C et al. Characterization of gas targets for laser produced extreme ultraviolet plasmas with a Hartmann-Shack sensor. Review of Scientific Instruments. 2004; 75: 3288–3293. DOI: 10.1063/1.1791314

[35] Muntz EP et al. Some characteristics of exhaust plume rarefaction. AIAA Journal. 1970; 8: 1651–1658. DOI: 10.2514/3.49856

[36] Rebrov AK. Free jets in vacuum technologies. Journal of Vacuum Science & Technology A. 2001; 19: 1679–1987. DOI: 10.1116/1.1382649

[37] Ashkenas H, Sherman FS. The structure and utilization of supersonic free jets in low density wind tunnels. In: Proceedings of the Fourth Symposium on Rarefied Gas Dynamics; 1966. pp. 84–105.

[38] Proch D, Trickl T. A high-intensity multi-purpose piezoelectric pulsed molecular beam source. Review of Scientific Instruments. 1989; 60: 713. DOI: 10.1063/1.1141006

[39] Phuoc TX. Laser spark ignition: experimental determination of laser-induced breakdown thresholds of combustion gases. Optics Communications. 2000; 175: 419–423. DOI: 10.1016/s0030-4018(00)00488-0

[40] Moore CE. Selected tables of atomic spectra, atomic energy levels and multiplet tables — N IV, N V, N VI, N VII. National Standard Reference Data Series, NSRDS-NBS3 (Sect. 4). Washington, D.C. 1971.

[41] Haynes WM, editor. CRC Handbook of Chemistry and Physics, 94th ed. CRC Press; Boca Raton, Florida 2013.

[42] Settles G. Schlieren & Shadowgraph Techniques. Springer; Berlin Heidelberg, Germany 2006.

[43] Hartmann J. Bemerkungen über den Bau und die Justierung von Spektrographen. Zeitschrift für Instrumentenkunde. 1900; 20: 47.

[44] Platt BC, Shack R. History and principles of Shack-Hartmann wavefront sensing. Journal of Refractive Surgery. 2001; 17: 573–577.

[45] Born M, Wolf E. Principles of Optics: Electromagnetic Theory of Propagation, Interference and Diffraction of Light. Cambridge University Press; Cambridge, UK. 1999.

[46] Bronstein IN et al. Taschenbuch der Mathematik. Europa-Lehrmittel; Haan-Gruiten, Germany.2013.

[47] Auguste T et al. Defocusing effects of a picosecond terawatt laser pulse in an underdense plasma. Optics Communications. 1992; 89: 145–148. DOI: 10.1016/0030-4018(92)90148-k

[48] Henke BL et al. X-ray interactions: photoabsorption, scattering, transmission, and reflection at E = 50-30,000 eV, Z = 1-92. Atomic Data and Nuclear Data Tables 1993; 54: 181–342. DOI: 10.1006/adnd.1993.1013

Chapter 5

High-Brightness Solid-State Lasers for Compact Short-Wavelength Sources

Akira Endo

Additional information is available at the end of the chapter

http://dx.doi.org/10.5772/64147

Abstract

Various types of compact short-wavelength sources are emerging in the region from EUV to hard X-ray and further to gamma ray. These high-energy photons are usually accessible in a large-scale facility such as SR or FEL, and the compactness of these new technologies provides new possibilities for broader applications in dedicated laboratories or factories. Laser-produced plasma is used for soft X-ray laser and high average power EUV sources for lithography. Laser Compton short-wavelength sources are now entering into practical applications in medical imaging. The performance of these sources critically depends on the laser driver performance. This chapter describes the recent progress of high-brightness, short-pulse solid-state laser technology in close relation to these new compact short-wavelength sources. Pulsed picosecond thin disc laser progress is reviewed with kW average power specifications. Cryogenic laser is reported for the advantage of higher beam quality in large-pulse energy operation.

Keywords: thin disc laser, cryogenic laser, plasma EUV source, laser Compton X-ray source

1. Introduction

A rapid progress is recently observed in the field of compact extreme-ultraviolet (EUV) and X-ray sources with high brightness and small footprint enough to be installed in laboratories in educational and research institutions, manufacturing facilities, hospitals, and other suitable sites [1]. This may advance scientific and technical disciplines in practical applications by complementing large-scale synchrotron radiation and free-electron laser sources. Applications span a wide range from biomedical, semiconductor, fundamental and applied

research, environmental engineering to industrial nondestructive testing. Component technology progress is one of the key factors in these advancements of the compact EUV through hard-X-ray sources. These key elements are instrumentation, optics, detectors, data management and processing, and one of the most significant factors is the progress of high average power, short-pulse solid-state lasers.

Semiconductor industry has been struggling in the past two decades to establish a technological system of extreme-ultraviolet lithography as the ultimate scheme, and the establishment of reliable, high average power (>100 W) 13.5 nm source has been always the most critical challenge. The basic architecture is now realized as the LPP (laser-produced plasma) EUV source, in which the conditioning of the mist target from a liquid tin droplet is essential for higher conversion efficiency and perfect recovery of the injected tin atoms [2]. The mist formation is performed by a diverging shock wave inside the microdroplet, which is driven by an impulse generated by an irradiation of picosecond solid-state laser pulse of mJ level pulse energy. The system repetition rate is typically 100 kHz, and the laser average power is more than 100W. The size of the droplet is 10 μm in diameter, and the required laser beam quality and stability must meet the requirements.

Lasing was reported in the EUV spectrum region by efficient excitation of dense plasma columns at 100 Hz repetition rate using a tailored pump pulse profile of a 1 J picosecond cryogenic Yb:YAG laser [3]. The average power of the 1 J picosecond laser is 100 W. The tabletop soft-X-ray laser average power is 0.1 mW at λ = 13.9 nm and 20 μW at λ = 11.9 nm from transitions of Ni-like Ag and Ni-like Sn, respectively. Lasing on several other transitions with wavelengths between 10.9 and 14.7 nm was also reported. The efficient X-ray laser operation was realized by an optimized pump pulse design as a nanosecond prepulse followed by two picosecond pulses to create higher density plasma of Ni-like ions of higher temperature for higher gain in longer time and in larger space. The high average power of these compact soft X-ray lasers promises to enable various applications requiring high photon flux with coherence.

Laser Compton X-ray source has been established as a compact, high-brightness short-wavelength source. The basic principle is similar to an undulator emission, and a high-intensity laser field is used as the modulating electromagnetic field. The laser Compton X-ray source is demonstrated as a compact short-wavelength imaging approach combined with the phase contrast method of biosamples. Single-shot imaging is critical for many practical applications, and the required specification depends on the usable laser pulse with some threshold parameters because all other component technologies are well matured. The optimization of the laser Compton hard X-ray source by single-shot base is already studied in detail [4, 5]. Experimental results well agreed with theoretical predictions. Highest peak brightness is obtained in the configuration of counterpropagating laser pulse and electron beam bunch, in the minimum focusing area before nonlinear threshold [6, 7]. A single-shot phase contrast bioimaging was demonstrated in the hard X-ray region [8]. The employed laser was a picosecond CO_2 laser of 3 J pulse energy [9], but the laser system was not an easy and compact one for further broad applications in various laboratories and hospitals. The Extreme Light Infrastructure–Nuclear Physics (ELI–NP) facility will have a brilliant γ-beam of 10^4 photons/s/eV, ≤0.5% bandwidth,

http://dx.doi.org/10.5772/64147

with $E\gamma < 19.5$ MeV, which is obtained by the laser Compton method from an intense electron beam (Ee > 700 MeV) produced by a warm linac [10]. The main purpose is to provide an opportunity for the production of radioisotopes for medical research. The repetition rate is 100 Hz with a 1 J, picosecond Yb:YAG laser. A standard laser Compton X ray source is under construction as the STAR project at the University of Calabria (Italy) to generate monochromatic tunable, ps-long, polarized X-ray beams, ranging from 20 to 140 keV. The X-rays will be devoted to experiments of material science, cultural heritage, advanced radiological imaging with microtomography capabilities [11]. An S-band RF gun produces electron bunches at 100 Hz, boosted up to 60 MeV by a 3 m long S-band cavity. It is critical to use a high-brightness linac of low emittance and high pointing stability to focus higher charge bunch to a smaller spot size down to 10 μm. The allowed spatial stability is a few μm. The research and development of the X-ray generation laser is the key technology for higher and stable X-ray generation. The Yb:YAG laser is ideal for a compact, high pulse energy picosecond pulse and should be synchronized to the RF system in less than picosecond time jitter.

Compact short-wavelength sources are emerging due to the progress of extreme ultraviolet lithography (EUVL) in semiconductor industry. The EUVL has been intensively developed in the field of various component technologies, for example, Mo/Si high reflectivity mirror at 13.5 nm wavelength, new types of resist of higher sensitivity at this wavelength, and plasma-based 100 W class stable EUV sources. Further increase of average power is expected for large-scale manufacturing to kW level and shorter wavelength to 6.7 nm where a higher reflectivity mirror seems available. The necessity to evaluate an alternative approach is recently proposed based on high repetition rate free electron laser (FEL), to avoid a risk of the source power limit by the plasma-based technology. The possibility is indicated to realize a high repetition rate (superconducting) FEL to generate a multiple kW 13.5 nm light. It is important to note that the present FEL pulses are characterized typically as 0.1 mJ pulse energy, 100 fs pulse duration, and 1 mm beam diameter, and generated in the SASE mode. The beam fluence is higher than the ablation threshold of typical resists, and the beam has a higher spatial coherence, which leads to speckle patterns. The beam is composed of many short spikes with high peak intensities [12]. Seeding an FEL with an external coherent source has been studied together with SASE operation to increase the brightness and pointing/energy stability compared to SASE mode. An efficient seeding method was established by using UV wavelength laser in which the seed laser modulates the electron beam into coherent bunching at the harmonics of the seed laser wavelength. The bunching is intensified in another undulator for coherent FEL action, and the method is named as high-gain higher harmonic generation (HGHG). A successful demonstration is reported from FERMI as a double stage-seeded FEL with a fresh bunch injection technique [13]. The fresh bunch scheme was demonstrated as the FEL radiation produced by one HGHG stage acts as an external seed for a second HGHG stage. A 10 Hz demonstration was reported in the EUV wavelength region. The development of higher repetition rate FEL requires new optical laser developments to meet the needs of laser-induced FEL seeding. Conventional copper accelerating cavities operate up to tens to hundreds of hertz, but superconducting (SC) cavities, allow a much higher repetition rate of up to few megahertz. FLASH at DESY has a maximum repetition rate of 1 MHz within a burst structure (electron bunch train) of 800 μs at 10 Hz. Future linear accelerator designs plan an SC linear accelerator

capable of a continuous repetition rate of up to 1 MHz. This presents major challenges for the design and operation of laser-seeded FELs in both burst and continuous mode. At lower repetition rates, conventional Ti:Sapphire lasers are currently used for laser-induced FEL seeding at, for example, FERMI FEL-1. The future requirements of a tunable, high repetition rate laser with sufficient pulse energy can be met with optical parametric chirped-pulsed amplification (OPCPA). A tunable OPCPA is demonstrated at 112 W in burst mode. The center wavelength is located in the wavelength region of 720–900 nm. The repetition rate is 100 kHz and the pulse energy is 1.12 mJ with 30 fs pulse duration. The OPCPA pumping laser power limits the scalability of the OPCPA output, and it was demonstrated for a 6.7–13.7 kW (burst mode) thin-disk OPCPA-pump amplifier, increasing the possible OPCPA output power to many hundreds of watts. Furthermore, the third and fourth harmonic generation experiments are performed for the FEL seeding purpose [14].

Recent solid-state laser progress is closely related to the demands in the field of laser microablation in industry. Fiber laser is advancing in the high repetition rate, short-pulse operation mode in the subpicosecond pulse length. Significant progress has been made on the scaling of the performance of subpicosecond fiber laser systems in the past decade. The current limitation exists in the achievable peak power and average power of a linear amplifier. The maximum of the available average power in a single fiber laser is determined by the mode instabilities. Several hundred watts is the typical maximum power, depending on the properties of the fiber and other system parameters. The pulse energy is ultimately limited by the extractable energy of the fiber, nonlinear pulse distortions, and damage issues. Four coherently combined fiber amplifiers were reported as a single CPA system [15]. The average power was 530 W and combined pulse energy was 1.3 mJ. It is expected to realize higher system parameters from a beam combined fiber laser, especially in higher average power in pulsed mode. The beam quality was excellent and the beam combination efficiency was as high as 93%. It is expected that with the coherent combination concept and further progress in fiber laser technology, average powers in the range of 1 kW and pulse energy of 10 mJ are realistic parameters in the future. A 10 J, 10 kHz femtosecond laser system is under conceptual design by a coherent combination of 10,000 fibers as the extension of the coherent combining scheme for high repetition rate PW laser [16].

Another promising laser is the InnoSlab laser, which is a thin slab laser cooled from both surface and is reported as a Yb:YAG InnoSlab amplifier with femtosecond pulses of <3 mJ pulse energy with a repetition rate of 100 kHz. The chirped pulse amplification is essential to achieve high average power generation in the power amplifier stage. The laser system is consisted of a 10 mW seed laser with a pulse repetition rate of 100 kHz to MHz, and a preamplifier stage, and a high power InnoSlab amplifier which is followed by a grating pulse compressor. This laser system is ideal for OPCPA pumping and micromaterial processing [17]. The highest average power picosecond laser was reported from a thin-disk multipass laser amplifier, delivering 1.4 kW with pulses of 4.7 mJ pulse energy and duration of 8 ps at 300 kHz repetition rate [18]. The beam quality factor was better than M2 = 1.4. The experiments showed that the thin-disk multipass amplifier can scale pulse energy and average output power independently in the repetition rates between 300 and 800 kHz. Frequency doubling by means of an LBO

http://dx.doi.org/10.5772/64147

crystal led to 820 W of average power at a wavelength of 515 nm with 1170 W of incident IR power which corresponded to a conversion efficiency of 70% and an SHG pulse energy of 2.7 mJ. By sum-frequency generation between the beams at 1030 and 515 nm in a second LBO crystal, an average UV power of 234 W (780 μJ of pulse energy) was generated at the wavelength of 343 nm with a conversion efficiency of 32%. The output powers in the green and UV spectral region are limited by thermal effects and the apertures of the crystals employed. Future work may try to use shorter seed pulses as well as to increase the output power by implementing a higher number of passes in the amplifier and the pump module and by increasing the pump power. For the higher harmonic generation, crystals with larger apertures and an improved temperature control is critical to further improve the performance.

Carbon fiber-reinforced plastic (CFRP) is the most promising light material in aircraft or similar machines. CFRP was processed with the kW picosecond laser with 8 ps pulses and an average output power of up to 1.1 kW at a pulse repetition rate of 300 kHz with a maximum pulse energy of 3.7 mJ. Heat accumulation influences are studied for the processing quality in high average power operation [19]. The pulse overlapping and repetitive scans are studied for the heat accumulation effect in the report. The study indicates an estimation of optimized feed rates and maximum scan speeds. The kW picosecond thin disc laser demonstrated its applicability in the cutting application of a 2 mm CFRP with a high cutting speed of 0.9 m/min and smaller thermal damage less than 20 μm. These lasers, such as fiber, InnoSlab, and thin disc, have been proving solutions for high beam quality, short-pulse generation in the high average power regime in the past two decades. An alternative approach was reported by a cryogenically cooled Yb:YAG by demonstration to have significant potential for efficient near-diffraction-limited high average power lasers [20]. A single-pass amplifier was reported with 250 W output power, 54% optical-optical efficiency, M2= 1.1 and a power oscillator with 300 W output power demonstrated 64% optical-optical efficiency, and M2= 1.2. In each case, the laser systems were based on end-pumped laser rod gain modules cryogenically cooled in liquid nitrogen cryostats. The single-pass amplifier is a simple way, compared to fiber or thin disc, to boost the power of a laser oscillator. The output power in the experiments was limited only by the incident pump power. The cryogenically cooled, bulk Yb:YAG four-pass amplifier was operated at 100 kHz repetition rate [21]. The amplified optical pulses were 2.5 mJ pulse energy with <20 ps pulse length before compression and the spectrum for 3.6ps in transform limited duration. The measured power stability was less than 0.5% in half an hour full power operation. A flat-top spatial profile was measured with near-diffraction-limited beam divergence. This compact amplifier is ideal for pumping of OPCPA. This chapter describes recent progress of high average power, picosecond thin-disc laser from the research and development of the HiLASE project during 2012–2015. HiLASE R&D laser center is a technological infrastructure in Dolní Břežany near Prague in the Czech Republic, which was founded in a close connection to the ELI activity. Major effort is to develop lasers for high-tech application, in which the short-wavelength generation is one of the dominant ones. HiLASE focuses on the development of kW-class thin-disk-based picosecond and subpicosecond lasers from mJ to sub-1-J pulse energy. Laser pulses are emitted at repetition rates from 1 to 100 kHz with prospective upgrade up to 1 MHz near fundamental wavelength. In order to cover the broadest application potential

of the lasers, it was also initiated high-power harmonic frequency generation and high-power mid-IR picosecond system consisting of an OPG followed by double OPA systems (**Figure 1**).

Figure 1. Building of the HiLASE R&D Centre in Dolní Břežany, Czech Republic.

2. High repetition rate picosecond Yb:YAG thin disc-laser in LPP EUV source

Continuous shrinking of the microcircuit is the natural law for lower cost, higher yield, short time to the market in the semiconductor industry. The microlithography has been the central manufacturing technology, and the continuous shrinking of the wavelength is the principal architecture. The proposal of the application of EUV wavelength appeared long before the perspective of the light source itself. The shift of source technology to the ArF excimer is followed by immersion technology and the ArF laser is the long-life light source technology. The EUV lithography is now entering into the mass production phase in the 22 nm node, and the wavelength is 13.5 nm (92.5 eV) supported with Mo/Si high reflectivity mirrors. 13.5 nm wavelength is the first generation of ionizing radiation in the mass production of semiconductor industries. The laser-produced plasma (LPP) EUV source has been established as the basic architecture of the EUV source technology, after one decade of focused research and engineering. The present concern is the stability and cleanness of the source itself and further engineering is continued [22]. The EUV light source is essentially incoherent spherical emission from highly ionized Tin plasma. The source is composed of three parts, namely driving laser, plasma generation/exhaust, and EUV light collector. A large Mo/Si collector mirror has peak reflectivity at 13.5 nm with 2% bandwidth. It is located close to the high-power plasma source and the extension of the lifetime is the most critical engineering concern. It is reported in a recent conference that the power available at the intermediate focus (IF) in the field is 125 W, and a test source is operated in a company laboratory aiming at 250 W [23]. A typical configuration of the LPP EUV source for high volume manufacturing (HVM) is shown in **Figure 2**, where a train of 100 kHz Sn droplet is injected and irradiated by a solid-state laser prepulse

http://dx.doi.org/10.5772/64147

(purple), dispersed into a mist bunch, and irradiated by a CO_2 laser main pulse (red). A discharge pumped EUV source is now employed for metrology purpose in less than 100 W level. The typical configuration is shown to the right of the LPP system. A small laser pulse initiates Sn vapor for main discharge from a rotating disc immersed in Sn liquid [24]. It is called as laser-assisted discharge plasma (LDP).

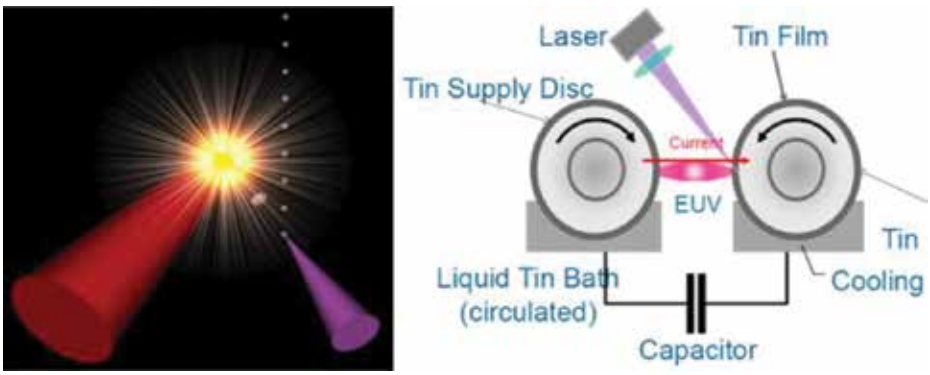

Figure 2. Configuration of double pulse method in LPP (left) and LDP (right) EUV sources.

The initial state of the injected Sn droplet is liquid phase of 10–20 μm diameter in the LPP system, and the direct laser irradiation results in a lower conversion efficiency (CE) and messy split of liquid Sn inside the chamber. The solution is the double-pulse method, as the initial pulse converts the liquid Sn droplet into nanocluster bunch (mist) for better laser absorption and ionization. An experiment demonstrated that the prepulse is much efficient in the case of picosecond pulse length compared to the nanosecond one. **Figure 3** shows the experimental results reported in a conference [25].

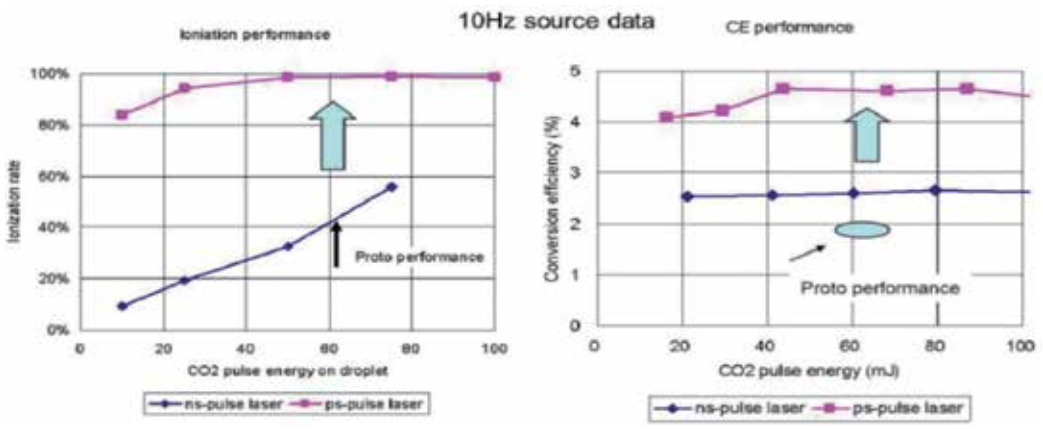

Figure 3. Ionization rate of Sn and CE depending on the pulse length of pre-pulse. Left: Ionization rate. Right: Conversion efficiency (CE).

The picosecond laser has typical parameters as pulse energy more than mJ, pulse length is 10 ps or less, and focusing diameter is a few times larger than the droplet diameter of 10–20 μm. The average power is more than 100 W at the repetition rate of 100 kHz. The laser specification is not easily covered by any commercial products and must be specifically developed. Thin-disc laser is suitable for the required specification among other types of advanced lasers such as fiber or thin slab with its larger beam diameter. HiLASE project was dedicated in a research and development of kW class picosecond thin-disc lasers in the period of 2012–2015. One of the laser beamlines is PERLA (Pearl) C, which is aimed to realize a compact, stable 500 W picosecond thin-disc laser with 100 kHz repetition rate [26]. The research and development of the laser system is briefly described in the following.

Design of the laser comes from the thin-disk laser concept. **Figure 4** shows the configuration of the thin-disc laser module with a parabolic mirror that collimates and images the pump radiation from laser diodes. The parabolic mirror images several times the unabsorbed pumping radiation with a set of roof mirrors. The thermal lensing is limited minimum due to the axial thermal flow from the gain medium to the water cooled heat sink. The nonlinear effects in the solid-state medium (self-phase modulation, B-integral) are controlled at low level in the multiple optical passes in the thin disc. The cooling is efficient due to the small thickness of the disc. The typical discs are characterized by the gain thickness as 100–300 μm and the disc diameter as 8–30 mm. Special optical design is required to compensate the low single-pass amplification gain together with pump absorption. Regenerative amplifier is selected for medium-power amplifier, and multipass amplifier is designed for higher average power or higher pulse energy amplifier. Regenerative amplifiers allow very compact and robust laser systems. High-power regenerative amplifier concept is based on a ring cavity, which is in fact a new approach. High average power and high repetition rate regenerative amplifiers usually suffer from Pockels cell issues. A new kind of large aperture BBO Pockels cell was developed to overcome this obstacle (**Figure 4**). A kW-class regenerative amplifier with a ring cavity is a novel approach in the field of picosecond thin disk lasers.

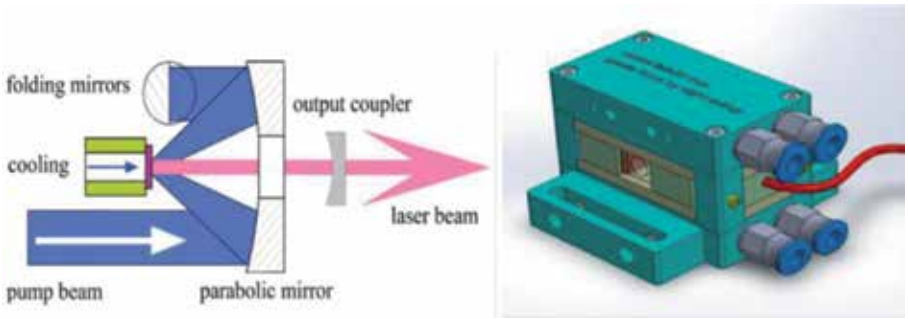

Figure 4. Left: Concept of efficient pumping (blue beam) of thin-disk lasers. Right: in-house developed large-aperture and water-cooled BBO Pockels cell.

Various solid-state materials are applied in thin disc modules, and the Yb:YAG is the most favored one due to high quality in fabrication and picosecond pulse generation. Yb:YAG is

http://dx.doi.org/10.5772/64147

studied for more than two decades in its growing, cutting, and polishing, and its thermomechanical characteristic is well fitted for picosecond and subpicosecond pulse generation. One of the disadvantages of the thin-disc laser is the bonding technology of large diameter thin Yb:YAG disc to the heatsink basement to be robust in high-temperature and high optical fluence environment. Several bonding methods are available to 10 mm diameter and further new techniques are still tested for higher reliability. In the present stage, HiLASE Centre uses two types of bonding methods, namely soldering to a copper-tungsten heatsinks and bonding to a diamond substrate. The diamond substrate is advantageous for its higher thermal conductivity for lower disc temperature under high pumping fluence. Popular pumping source is a laser diode with 940 nm center wavelength where the absorption has a broader bandwidth. Yb:YAG has a narrower but high-peak absorption wavelength at 968.8 nm, which is called as zero-phonon line, and a specific laser diode at this wavelength is used for efficient pumping. The quantum defect decreases from 8.7% with 940 nm pumping to 5.9 % with zero-phonon line pumping. Zero-phonon line pumping is also better in its suppression of nonlinear phonon relaxation in the Yb:YAG medium. The resulting steady-state disc temperature is kept lower compared to 940 nm pumping, and better stability of the amplification and higher output pulse energy is the positive result [27]. Pump diodes should have bandwidth <1 nm. Since the absorption line near 968.8 nm is very narrow, the diodes are stabilized by volume Bragg gratings (**Figure 5**).

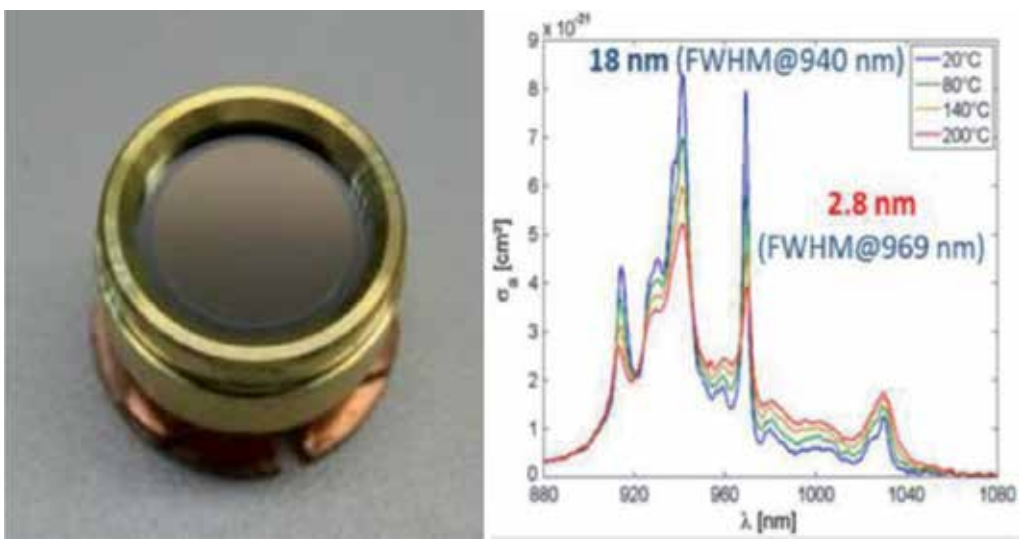

Figure 5. Left: Diamond-heat spreader-bonded thin disc. Right: Absorption cross section of Yb:YAG.

The high repetition rate beamline PERLA C operates at 100 kHz and provides picosecond pulses from 1 to >4 mJ in a compressed pulse. The seeder of the laser system is a commercially available Yb-doped fiber laser from Fianium. The pulse length is 12 ps at 50 MHz repetition rate, and the pulse energy is 6 nJ with 20 nm broad bandwidth. The pulses are stretched to 0.5 ns pulse length by a small Bragg grating. The pulse bandwidth is filtered to 2.2 nm by the

bandwidth of the grating, and the bandwidth limited pulse length is less than 2 ps. The seeder pulses are amplified by a semiconductor optical amplifier (SOA) and a single-mode fiber amplifier before injection into a regenerative amplifier. The advantage of the SOA is its electric controllability of the gain time window and used as a pulse picker to reduce the repetition rate from 50 to 1 MHz. The average power is 300 mW before the regenerative amplifier.

The regenerative amplifier is composed of a single Yb:YAG module with a standing wave cavity for 100 W operation (**Figure 6**). The total footprint is compact as 900 × 1200 mm including a pulse compressor. The pump spot size of the thin disc is 2.7 mm in diameter with cavity length of 2 m. A double Pockels Cell system optically switches the input and output pulses. The size of the BBO crystal is 8 × 8 mm^2. The crystal holder is engineered to avoid damages to the BBO by piezo ringing in high repetition rate switching. The maximum available BBO aperture is 12 × 12 mm^2, and the repetition rate is 1 MHz and the voltage is 10 kV. As described earlier, the pumping is by zero-phonon line continuous fiber-coupled laser diodes. The maximum amplified pulses are 1.2 mJ of energy at 100 kHz repetition rate with M2 = 1.3 beam quality

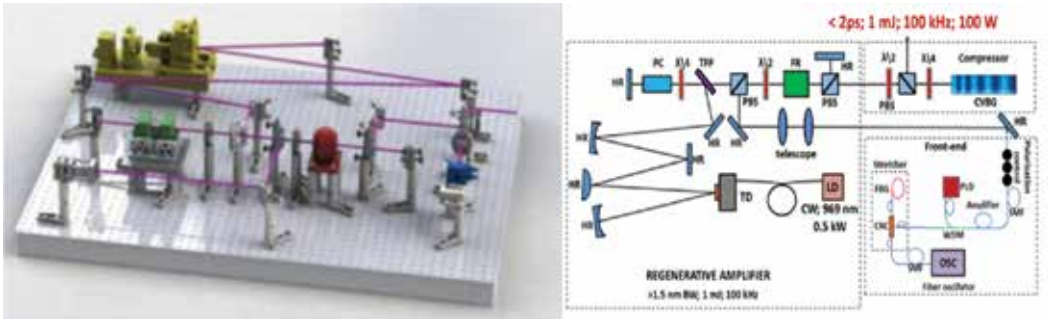

Figure 6. Left: 100 W regenerative amplifier. Right: Optical scheme including a CVBG pulse compressor (HR, highly reflective mirror; TD, thin disk; LD, pump laser diodes; PC, Pockels cell; TFP, thin-film polarizer; FR, Faraday rotator; PBS, polarizing beam splitter; CVBG, chirped volume Bragg grating; $\lambda/2$ and $\lambda/4$, half- and quarter-wave plates; SMF, single-mode fiber; PLD, pump laser diode; WDM, multiplexer; CRC, circulator; FBG, fiber Bragg grating; OSC, oscillator).

This is critically important for precise irradiation like prepulse in an LPP EUV source. Pulses are compressed by a chirped volume Bragg grating (CVBG) compressor, which is a very robust, compact, and easy to align bulk compressor with 8 × 8^2 mm aperture. The CVBG compressor was tested for long time operation and demonstrated a reliable pulse compression of high average power pulse train with >85 % diffraction efficiency under optimized cooling condition. Compressed pulses measured by intensity autocorrelation (**Figure 7**, right) have temporal width 1.6 ps ($sech^2$). The pulse-to-pulse energy stability measured over 4 million pulses was better than 1.7%, and the long-term average power stability measured over 1 h was <1.5 % (RMS value). Better housing and active stabilization can even improve the stability.

http://dx.doi.org/10.5772/64147

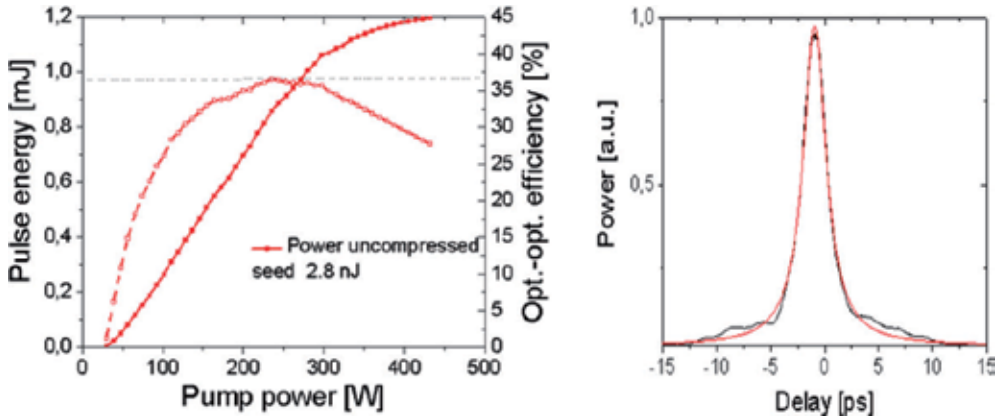

Figure 7. Left: 1.2 mJ of the output pulse energy at 100 kHz repetition before compression has been achieved from the 100 W PERLA C in a nearly diffraction-limited beam. Right: the pulses were compressed to 1.6 ps (FWHM) by a CVBG as shown by the intensity autocorrelation trace.

A higher average power regenerative amplifier was developed with a ring cavity (**Figure 8**). The amplifier is switched by a reliable Pockels cell, which is in-house design for 10 × 10 mm^2 aperture with effective cooling. The fundamental spatial mode operating cavity is designed for a 5.2 mm pump spot and the cavity contains a single diamond-bonded Yb:YAG thin disc. The disc is zero-phonon line-pumped by VBG-stabilized fiber-coupled diodes. Laser cavity was tested in the CW regime to evaluate the thermal distortion. 550 W output was observed with almost 50% optical-optical efficiency and >4 mJ was achieved in a 100 kHz pulse train with a nearly diffraction-limited output beam (**Figure 8**).

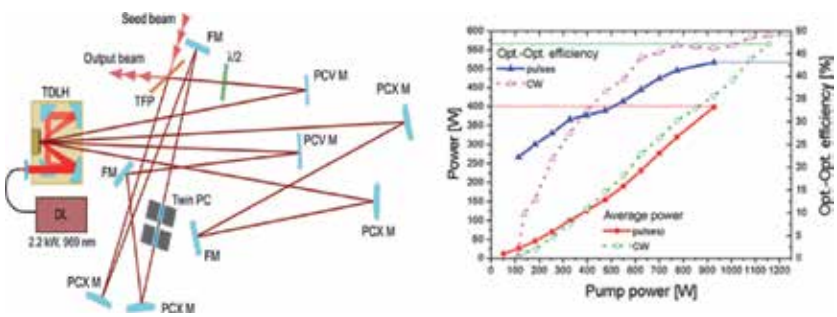

Figure 8. Left: ring cavity of the 500 W PERLA C laser system. FM, folding mirror; PCX M, planoconvex mirror; PCV M, planoconcave mirror; TFP, thin-film polarizer; PC, Pockels cell; TDLH, thin-disc laser head; DL, pump diodes; $\lambda/2$, half-waveplate. Right: performance of the 500 W ring cavity in CW and pulse mode (PERLA C).

3. High average power wavelength conversion of picosecond solid-state lasers

The extreme ultraviolet lithography is now in an introductory phase in semiconductor industry. The EUVL has been developed in the field of various component technologies such as Mo/Si high reflectivity mirror at 13.5 nm wavelength, new types of resist of higher sensitivity at this wavelength, and plasma-based 100 W class stable EUV sources. Further increase in average power is expected for large-scale manufacturing to kW level and shorter wavelength to 6.7 nm where a higher reflectivity mirror seems available. The present source architecture is the laser-produced plasma (LPP) and is recently considered in its practical scaling limitation in average power in the range of kW. Free electron laser has been emerging as the new short-wavelength source in the EUV to X-ray region in the past decade. The present generation is based on lower repetition rate operation for scientific applications, but the next generation is aiming at high repetition rate for high average power. Several research papers are discussing on the possibility of high repetition rate FEL by superconducting RF cavity technology for the generation of more than kW average power at 13.5 nm wavelength [28, 29]. The present FEL is operated in the SASE mode, in which the pulses are generated in undulator and composed of many short-pulse length spikes. The typical pulse parameters are 0.1 mJ pulse energy, 100 fs pulse length, and the beam diameter is 1 mm. The beam fluence is higher than the ablation threshold of a resist [30], and the high spatial coherence results in much higher localized peak fluence on the resist. The interaction mechanism is now in a basic study to overcome these effects compared to the present LPP-generated 100 kHz, mJ EUV pulses with no coherence and longer pulse length as 10 ns.

The scaling of the FEL technology to kW average power level requires the photocathode operation in higher repetition rate in industrial environment together with optical technology to optimize the FEL beam for lithography application and scaling to the 6.7 nm wavelength region.

The first consideration is the industrial operation of photocathode at >MHz repetition rate. The bunch charge is typically 1 nC. Metal photocathode is robust, but the quantum efficiency (QE) is lower for higher charge generation. Several semiconductor cathodes were studied for higher efficiency to reduce the requirement for the driver laser average power in the repetition rate mode. The Advanced Photo-Injector (APEX) experiment in Lawrence Berkley National Laboratory is working to realize a high repetition rate at MHz, high-brightness photocathode. The photocathode is a normal conducting, 187 MHz RF cavity in the CW mode, and designed for short bunches as 1–10 ps of 750 keV energy up to 1 nC charges. Several semiconductor cathode materials are tested for better beam emittance for various operational conditions. CsK_2Sb is irradiated by SHG of Yb fiber pulses, and Cs_2Te is irradiated by 4HG. Both semiconductor cathodes have nearly 1% quantum efficiency. The laser pulse energy is 0.5 μJ with the MHz repetition rate, and the average power is 0.5 W [31]. Cu and Mg photocathodes were studied for use in an RF photocathode. The gun was manufactured by a technique of hot isostatic pressing with diamond polishing and tested under a peak electric field of 57 MV/m. The quantum efficiency of the Cu cathode was 10^{-4}, while Mg cathode achieved a high QE of

http://dx.doi.org/10.5772/64147

up to 10^{-3} under 262 nm laser-light illumination. The QE of the Mg cathode under 349 nm laser-light illumination was measured to be 2.2×10^{-5}. The experimental setup and the results of the photocathode QE measurement are shown in **Figure 9** [32].

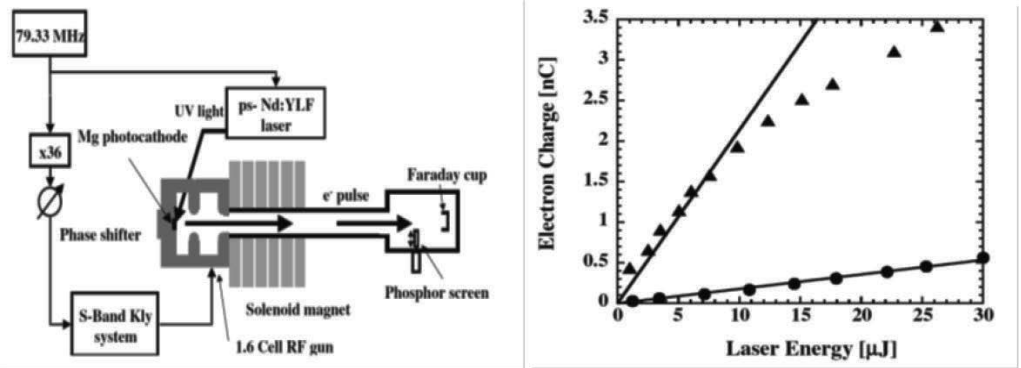

Figure 9. Left: Experimental setup of photocathode QE measurement. Right: Electron charge vs. input laser energy (266 nm) from Mg photocathode, • is for before laser cleaning.

It is concluded that 5 μJ, 266 nm, picosecond pulse is enough for Mg photocathode operation and the required average power at the MHz repetition rate is 5 W. Cu photocathode is proven to be robust material and usable by a 50 W 4HG picosecond laser. The progress of the laser technology is now making the metal photocathode again usable for the emerging requirement for long-life industrial application.

The other consideration is the reduction of the temporal microspikes in the SASE FEL pulses. Coherence is characterized in a report on the FLASH operation at 8.0 nm wavelength [33]. The single FEL femtosecond beam is passed through double pinholes for diffraction pattern, and the measured transverse coherence length is 6.2 ± 0.9 μm in the horizontal and 8.7 ± 1.0 μm in the vertical directions. The mutual coherence function K is given as 0.42, and a measurement of K by a laser plasma source is 3.2×10^{-9}. It is concluded from these measurements that a beam spatial homogenization is required at EUV wavelength by using total reflection. Temporal coherence was also reported by using a split and delay unit. The coherence time of the pulses produced in the same operation conditions of FLASH was measured to be 1.75 fs. The measured coherence time has a value, which corresponds to about 65.5 ± 0.5 wave cycles ($c\tau/\lambda$). It is well known that the SASE FEL pulses are composed of many small spikes and random spectrum due to SASE process. It is reported that the averaged spectrum has a 1.4% bandwidth typically, which is favorable for the Mo/Si EUV multilayer mirror at 13.5 nm (bandwidth 2%). It is necessary to smooth the temporal spikes to avoid random EUV flux change in the resist absorption process. The requirement is similar to most FEL applications, and we must consider efficient seed technology for MHz repetition rate operation.

It is desirable to increase the brightness and pointing/energy stability compared to SASE mode. An efficient seeding method was established by using a UV wavelength laser, in which the seed laser modulates the electron beam into coherent bunching at the harmonics of the seed

laser wavelength. The bunching is intensified in another undulator for coherent FEL action, and the method is called as high-gain higher harmonic generation (HGHG). FERMI is the leading institute in this specific technology, and it is reported on the double-stage-seeded FEL with the fresh bunch injection technique [13]. The main limitation for the direct extension of the HGHG to shorter wavelength is the required small electron beam energy spread and higher average power seed laser source. The fresh bunch scheme is the solution for this problem, in which the FEL radiation is initially produced in an earlier stage undulator and used as the seeder for shorter wavelength generation (**Table 1**).

	Fermi FEL-2	**EUV FEL**
Seed wavelength (nm)	260	324
1nd FEL (nm)	32	40.5
2nd FEL (nm)	10.8	13.5

Table 1. Comparison of wavelengths for HGHG operation in FERMI FEL-2 and EUV FEL.

The external seed laser was the third harmonic of a Ti:Sapphire laser with a duration of ~180 fs (FWHM) and up to 20 μJ energy per pulse. Its transverse size in the modulator was made larger than the electron beam size to ensure as uniform as possible electron beam energy modulation. Once the same laser energy is required for MHz EUV FEL, 20 W average power is required for 324 nm with 180 fs at MHz repetition rate. There are two approaches to generate such laser pulses, the first is based on the MHz repetition rate Ti:Sapphire laser with 100 μJ level pulses, and the second one is based on OPCPA.

The short-pulse, short-wavelength laser technology is now advancing to realize the specification described here in a compact box, due to the new suitable laser configuration as thin-disc laser and an efficient wavelength conversion method.

An ultrafast thin-disc multipass laser amplifier demonstrated the advantage recently by delivering 1.4 kW of average output power with 4.7 mJ pulse energy and duration of 8 ps at a repetition rate of 300 kHz [18]. The beam quality factor was better than M2 = 1.4. The experiments show that the thin-disc multipass amplifier can scale pulse energy and average output power independently for the investigated repetition rates between 300 and 800 kHz. Frequency doubling by means of an LBO crystal generated 820 W SHG average power at the wavelength of 515 nm with 1170 W of incident IR power, which corresponds to a conversion efficiency of 70% and an SHG pulse energy of 2.7 mJ. By sum-frequency generation between the beams at 1030 and 515 nm in a second LBO crystal, an average UV power of 234 W (780 μJ of pulse energy) was generated at the wavelength of 343 nm THG with a conversion efficiency of 32%.

A wavelength conversion experiment was performed in the HiLASE project to evaluate the high average power generation of picosecond harmonics, namely, SHG (515 nm) and FHG (257.5 nm), in LBO and BBO/CLBO crystals, respectively [34]. The pumping of the crystals was performed by the PERLA C Yb:YAG thin-disc laser operating at 100 kHz and 60 W average power with 4 ps pulse duration. The average output power of 6 W DUV was achieved in CLBO

http://dx.doi.org/10.5772/64147

at a spectral bandwidth of 0.2 nm and the FHG/fundamental conversion efficiency was 10%. The basic optical configuration is shown in **Figure 10** together with a photo. The input beam (upper left) is reflected by two motorized mirrors controlled by a beam stabilizer ensuring pointing stability better than 20 μrad (RMS). The following half-wave plate and polarizer is used for energy tuning. The beam is frequency doubled in an LBO at 50°C and 10 mm long, cut for the critically phase-matched generation at $\theta = 90°$ and $\phi = 12.8°$, and antireflection coated for 1030 and 515 nm. The second harmonic beam passes two dichroic mirrors and is injected into an argon-filled box with a BBO or CLBO crystal. To ensure a stable long-term functioning of the crystals the temperature was kept at 150°C. The experimental results are shown in **Figure 11**. It is visible that the 4HG/SHG conversion in the CLBO crystal has 30% higher efficiency than in the BBO crystal. The next step of the experiment is to increase the pumping power to 500 W to confirm the linearity of the conversion efficiency for 50 W FHG output power.

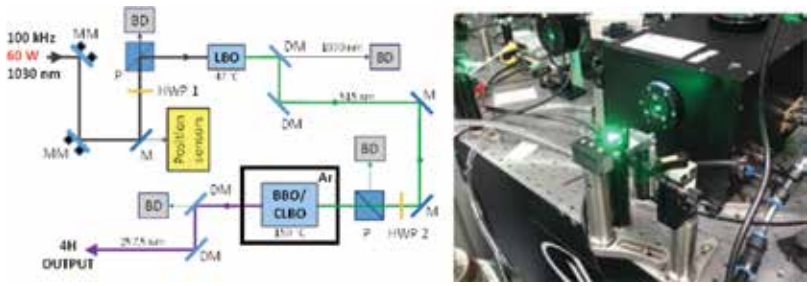

Figure 10. Optical configuration of the SHG and FHG, and SHG light is introduced into a box filled with argon.

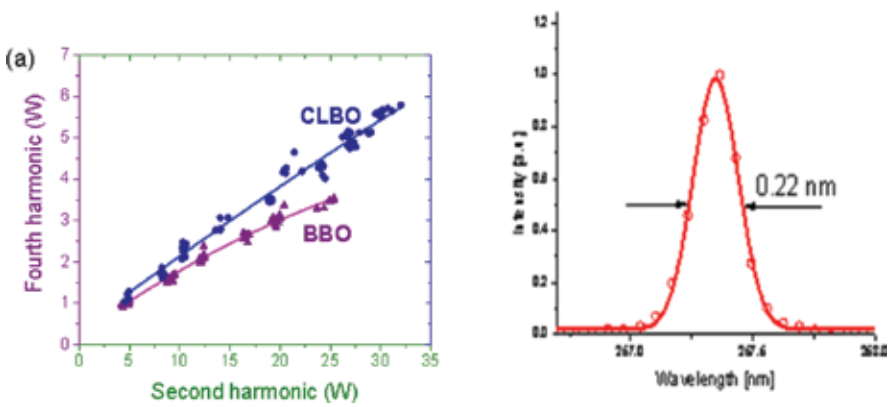

Figure 11. Left: Fourth harmonic output power dependence on the second harmonic in BBO (AR coated) and CLBO (uncoated) crystals. Right: Relevant FHG spectra from CLBO.

A small part of the beam is absorbed in the crystal and converted into heat that leads to temperature gradients in the crystal in the high average power wavelength conversion. This causes partial phase mismatch and reduces the conversion efficiency. It is estimated that the fundamental power absorption at the 60 W input is <20 mW in the 10 mm long LBO crystal. The total absorbed power may be higher due to the fact that a green laser beam has higher absorption than the fundamental beam [35]. The absorption in the antireflective coating increases the temperature, which causes the mismatch more than the bulk absorption [36].

A tunable, 112 W optical parametric chirped-pulse amplifier (OPCPA) was demonstrated for FEL seeding in a burst mode with center frequencies ranging from 720 to 900 nm, pulse energies up to 1.12 mJ, and a pulse duration of 30 fs at a repetition rate of 100 kHz [14]. The results demonstrated the feasibility of 112 W femtosecond OPCPA in a burst mode with a duty cycle of 8×10^{-3}, where no heating effects were observed. It was indicated from the measurements of absorption coefficients of BBO and LBO and calculations, the feasibility of much higher powers up to 1 kW in continuous mode was expected. Absorption causes a spatially and temporally varying temperature distribution in the sample. This leads to local changes of the refractive index and results in the development of a thermal lens. Especially in anisotropic crystals, this has consequences on increased phase mismatch in optical parametric processes with a conversion efficiency decrease. In the case of anisotropic crystal in electro-optical devices such as Pockels cells, the thermally induced depolarization reduces the contrast ratio. Though the absorption of the anisotropic crystal in these applications is usually very low, the related effects can be significant with input powers at the kilowatt level. In order to estimate the influence of thermal effects and taking it into account in the optical system design, the comprehensive knowledge of material absorption at the operation wavelength is unavoidable. An extended photothermal method was demonstrated for the quantitative determination of laser-induced wavefront deformations, which enables the separation of bulk and surface contributions to absorption in the more complex case of optically anisotropic crystalline media [36]. Experimental setup is shown in **Figure 12**. The wavefront deformations of the test beam (light source) are measured and used for absorption evaluations. The results show that the absorption is highest at the AR-coated KTP surface of input side (**Figure 13**, left), while it is higher at the surface of the output side of noncoated KTP (**Figure 13**, right). This photothermal method is usable in the real OPCPA for a better cooling system installation.

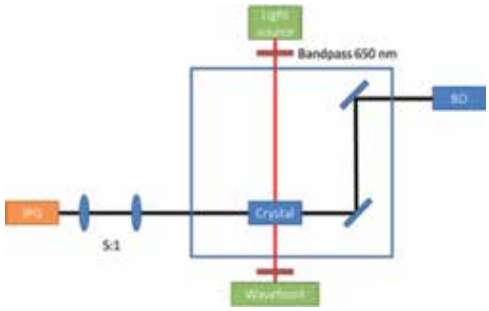

Figure 12. Setup of the photothermal method by crossed beam measurement. Wavefront measurement is performed by a Hartmann-Shack sensor.

http://dx.doi.org/10.5772/64147

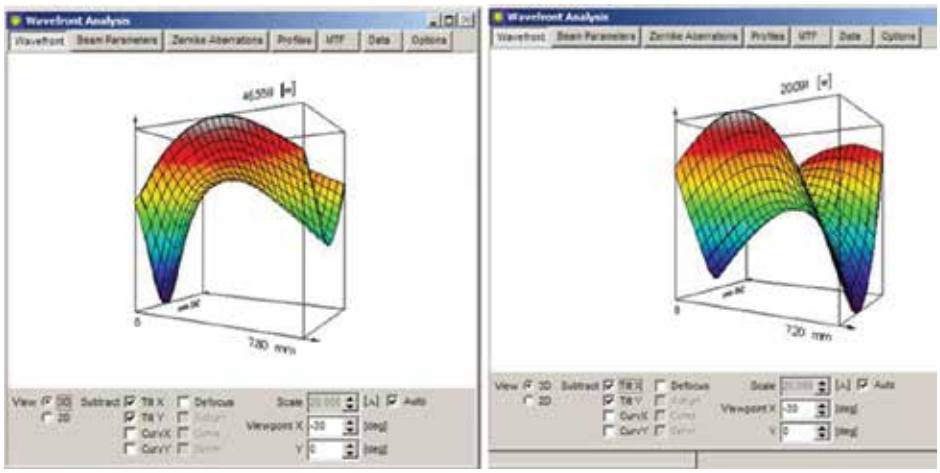

Figure 13. Wavefront deformation measurement results for AR-coated (left) and noncoated KTP samples. Blue indicates the largest wavefront deformation. The heating laser beam comes into the crystal horizontally from the left, while the probe beam passes vertically to the readers.

4. Cryogenic laser technology for high pulse energy picosecond amplifier

The basic principle of the laser Compton short-wavelength source is similar to an undulator emission, and high-intensity laser field is used as the modulating electromagnetic field. Basic principle of the laser Compton X-ray source is well studied, and a single-shot imaging is critical for many practical applications. The required specification is explained as the laser pulse must exceed some threshold parameters. It is known that the highest peak brightness is obtained in the case of counterpropagating laser pulse and electron beam bunch, in the minimum focusing area before nonlinear threshold. **Figure 14** describes the schematic of the laser Compton interaction between the electron beam and the laser.

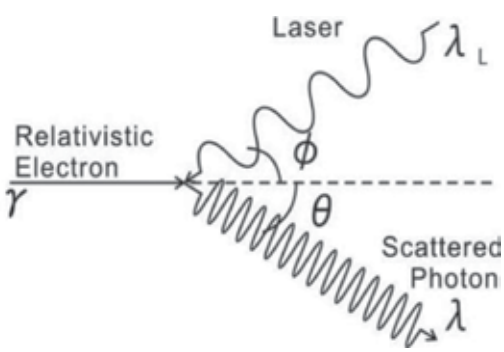

Figure 14. Schematic of the laser Compton scattering process.

The general formula of obtainable X-ray photon flux N_0 is calculated in the counter collision by the following expression:

$$N_0 \propto (\sigma_c \, Ne \, Np) / (4\pi r^2)$$

where σ_c is the Compton cross section (6.7×10^{-25} cm^2), Ne is the total electron number, Np is the total laser photon number, and r is the interaction area radius. It is predicted that an increase in Ne and Np, and the reduction in r results in the increase in the photon flux N_0. The practical limitation of these operations are the instrumental condition of electron beam emittance in higher charge, M2 of laser beam at higher pulse energy, and optimization for reduced focusing diameter r. It is possible to assume these parameters as 1 nC charge with 3 ps pulse duration to be focused down to 10 μm at 38 MeV voltage. Another limitation is the maximum of single-pulse laser intensity to reach the nonlinear threshold of the higher harmonics generation in the X ray region. The nonlinear Compton threshold is characterized by the laser field strength

$$a0 = eE/m\omega LC$$

where parameters E, ωL, and C correspond to the amplitude of the laser electric field, laser frequency, and the speed of light, respectively. The laser field strength is a function of the laser wavelength. The nonlinear threshold a_0 is given around 0.6 which corresponds to 1 J pulse energy in 1 ps pulse duration at 10 μm focusing intensity in the solid-state laser wavelength. The threshold laser energy for a single-shot imaging is similar to this critical laser pulse energy in the expected tight focus condition. The laser technology was not matured to realize such parameters simultaneously in the past, and usual approach was to increase the repetition rate of the event to increase the effective obtainable X-ray photon average flux in the affordable imaging time period such as <millisecond for bioimaging. The first approach is the pulsed laser storage in an optical enhancement cavity for laser Compton X-ray sources [37]. It is described in the experimental report that "the enhancement factor P inside the optical cavity was 600 (circulating laser power was 42 kW), in which the Finess was more than 2000, and the laser beam waist of 30 μm (2σ) was stably achieved using a 1 μm wavelength Nd:Vanadium mode-locked laser with repetition rate 357 MHz, pulse width 7 ps, and average power 7 W." The second approach is the multipass optical cavity, in which the laser Compton generation focus exists inside the multipass cavity. The minimum focusing diameter is limited due to the requirement of the cavity design. SHG picosecond pulse of 0.2 J pulse energy is circulated 32 times to collide electron bunches [38].

An approach is undertaken by the thin-disc laser technology to generate 1 J, picosecond high beam quality pulses at 100 Hz repetition rate in the Max Born Institute, Berlin, Germany. The development is based on a ring cavity concept combined with chirped pulse amplification (CPA) [39]. The regenerative amplifier produced more than 300 mJ energy when pumped with the maximum available pump power of 1.7 kW. The regenerative amplifier is followed by a large aperture ring amplifier that increases the pulse energy further to 600 mJ. This ring

http://dx.doi.org/10.5772/64147

amplifier consists of a Pockels cell and a set of polarizers for the in- and out-coupling, two amplifier heads and a spatial filter in between. The amplifier heads are equipped with 750 μm thick Yb:YAG (7%) discs of 25 mm diameter. Each disc is pumped by 1 ms long pulses of 4 × 1.5 kW. Booster amplifier for 1 J pulse is based on the large aperture ring amplifier design without internal Pockels cell. The amplifier discs were pumped by diode modules that deliver 6 kW peak power out of a 2 mm fiber. Each amplifier is equipped with two of these pump modules, which together provide about twice the pump power compared to the large aperture ring amplifier. The booster amplifier is changed from former multipass configuration to a large aperture ring amplifier. The result is a multiple amplifier stage configuration with many thin-disc laser modules.

Cryogenic laser technology is suitable for the generation of large-pulse energy in a laser configuration of lower stages. A cryogenic thick-disc Yb:YAG laser was reported as 1 J was generated at 100 Hz repetition rate [3]. The picosecond CPA laser was developed for driving high average power soft X-ray lasers. This is one of the greatest breakthroughs in the history of high-energy solid-state laser, and it is described in the report on the configuration and operation as "Seed pulses of 100 mJ energy were produced by the laser frontend and amplified to 1.5 Joules pulse energy by the five-pass power amplifier which consists of two Yb:YAG disks mounted in vacuum on a single cryo-cooling head. The Yb:YAG disks are bonded on all lateral sides with a Cr:YAG cladding to eliminate feedback of spontaneous emission into the active region to prevent amplified spontaneous emission (ASE) losses and transverse parasitic lasing. Cryogenic cooling of Yb:YAG to liquid nitrogen temperature increases the heat conductivity and reduces the saturation fluence, allowing for efficient high energy pulse generation at high repetition rates. High capacity cooling was accomplished by flowing cryogenic liquid coolant through the laser head. Each disk was pumped with 1.5 ms duration, 4 kW pulses from a λ = 940 nm laser diode array. At the maximum pump power, 1.5 J laser pulses were obtained. These pulses were compressed by a dielectric grating pair producing 1 J, 5 ps FWHM duration pulses at 100 Hz repetition rate." The repetition rate is recently increased to 500 Hz and the picosecond pulse energy is 1 J, and the resulting average power is 500 W. Temporally pulse-shaped laser pulses were focused into a ~5 mm long, 30 μm FWHM wide line on a solid target using cylindrical optics. The beam quality is indicated by the focusing specification. The resulting plasma was in the Ni-like stage, and strong collisional excitation leads to a large transient population inversion on the $4d1S_0 \rightarrow 4p1P_1$ transition of Ni-like ions at wavelengths ranging from 10.9 to 18.9 nm.

Cryogenic solid-state laser is preferred for power scalability with better beam quality, especially in higher pulse energy mode, and improvement of efficiency at the cost of longer pulse length [40]. Yb:YAG is the most tested material due to its low quantum defect and still broadband absorption in low temperatures. Various thermal optical properties are reported for base materials as YAG (ceramic and single crystal), GGG, GdVO4, and Y_2O_3 on the thermal conductivity, thermal expansion, refractive index, absorption cross section, emission cross section, and fluorescence lifetime in the cryogenic condition.

One of the key features of the cryogenic laser is its better beam quality. A quantitative evaluation is important for a practical laser design for dedicated applications and a measure-

ment was performed on the wavefront distortion caused by the thermal origin in a cryogenic Yb:YAG crystal in the temperature range 250–130 K in nonlasing condition [41]. The wavefront aberration was evaluated by a wavefront sensor. The measurement results showed a significant reduction of the wavefront aberration in lower temperature. The thermal defocus was concluded as originated to the thermal lensing effect together with electronically induced change of the refractive index by the excitation of ion activators (electronic lensing). The dominant reason of the aberration was found as the thermal lensing in the experimental condition as 6.3 kW/cm^2 pumping intensity and pumping repetition rate of 100 Hz. The Strehl ratio was observed to be improved in the lower temperature even the absorbed energy was increased. The experiment showed the advantage of the cryogenic technology in terms of efficiency and beam quality.

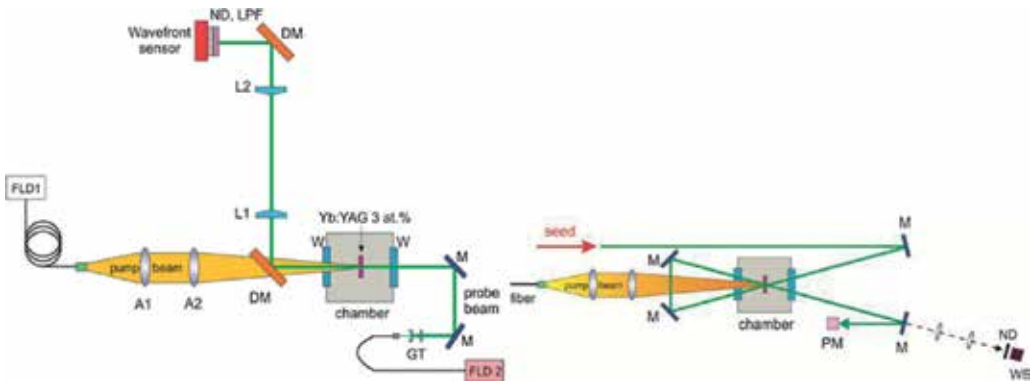

Figure 15. LEFT: Experimental configuration of the aberration measurement. FLD1, fiber-coupled pump diode at 936.6 nm; FLD2, fiber-coupled probe beam laser diode at 1065 nm; GT, Galilean telescope; W, windows; M, turning mirrors; DM, dichroic mirrors; A1, 2, achromatic doublets with focal lengths of 100 and 250 mm, respectively, L1, 2, lenses with a focal length of 250 mm; ND, neutral density filters; LPF, longpass filter with cutoff wavelength at 1050 nm. Right: Multipass amplification configuration. WS, wavefront sensor; PM, power meter.

The experimental setup used for the measurement of the wavefront aberrations in a cryogenically cooled Yb:YAG slab is shown in **Figure 15** (left). The right side figure shows the configuration of multipass amplification from the 100 mJ level input. A Yb:YAG crystal is mounted in a copper holder in a closed-loop pulse tube cryostat (Q Drive). The cooling capacity is 12 W at 100 K. The crystal was supplied from Crytur, Czech Republic, and the specification was thickness 2 mm, diameter 10 mm, and doping concentration 3 at%. A fiber-coupled laser diode (DILAS) pumped the crystal from one side. The peak wavelength was 936.9 nm, and the peak intensity was 6.3 kW/cm^2. Two achromatic doublet lens of focal length 100 and 250 mm imaged the 1 mm core of the fiber with NA 0.22 to the Yb:YAG surface. The resulting pump spot size was 2.5 mm (1/e2) in super-Gaussian intensity distribution. **Table 2(a)** summarizes the absorbed energy per pump pulse at each temperature. The absorbed energy increases by about 19 % if the temperature decreases by 120 K from initial 250 K. The absorbed power and thus generated heat is higher with decreasing temperature, and the aberrations are lower because of higher thermal conductivity, lower dn/dT, and lower expansion

http://dx.doi.org/10.5772/64147

coefficient. Theoretical thermal decay time constants were calculated according to the formula $t_T = r_p^2/4\kappa$, where r_p is the radius of the pump, and κ is the thermal diffusion coefficient, which is defined as $k/(\rho cp)$ where k is the thermal conductivity, ρ is the mass density, and cp is the specific heat. The estimated values are shown in **Table 2(b)** for the thermal relaxation time constants for different temperature conditions in 3 at% doped Yb:YAG as an estimation from data for 2 and 4 at% doped crystals. The thermal decay time is around 31 ms at 150 K, which is three times longer than the time interval between pumping at 100 Hz. This value is 93 ms at 250 K.

(a)

Temperature (K)	Absorbed energy (mJ)	Absorbed energy (%)
250	128	41.3
210	137	44.3
170	145	46.8
130	152	49.0

(b)

Temperature (K)	Thermal decay time for 3 at% Yb:YAG crystal (ms)
250	93
200	60
150	31

Table 2. (a) Absorbed energy per pump pulse by the 2 mm thick, 3 at% doped Yb:YAG slab pumped by energy of 310 mJ at a wavelength of 936.6 nm for different temperatures of the cooling finger. (b) Calculated thermal decay time for 3 at% Yb:YAG crystal.

Cryogenic cooling is usually applied in booster amplifiers with more than one pass of the seed beam through the active medium in order to efficiently extract the stored energy. Therefore, it is assumed to evaluate four beam passes, and the measured wavefront with subtracted tilt and defocus was four times multiplied to calculate the real Strehl ratio in multipass amplification. The calculated Strehl ratio was 0.96 at 130 K and decreased to 0.93 at 250 K as shown in **Figure 16**. The practical Strehl ratio to obtain the same pulse energy decreases at higher temperature to obtain the same pulse energy in lower gain. The measurement indicates the linearity of the Strehl ratio to the temperature decrease, and it is expected further increase in the beam quality is possible in lower temperature of about less than 130 K.

In the last part of this chapter, a large aperture cryogenic laser is evaluated. The performance of a gas-cooled multislab laser is recently reported from the DiPOLE project within the Central Laser Facility (CLF RAL STFC), UK. The development is aiming at an efficient high pulse energy diode-pumped solid-state laser (DPSSL) architecture based on cryogenic gas-

cooled, multislab ceramic Yb:YAG amplifier technology. A prototype amplifier is delivering up to 10.8 J pulse energy at 1030 nm wavelength with 10 Hz repetition rate. The optical-optical conversion efficiency is 22.5% [42]. The long-term energy stability was observed as 0.85% RMS with 7 J pulse energy for 48 h operation (2 million shots). An extension of the cryogenic technology is now under test in the DiPOLE 100 to confirm the cryogenic concept at 100 J, 10 Hz region (kW average power). The present laser system is built for the HiLASE project and will deliver 100 J temporally shaped ns pulses at 10 Hz with a fully integrated control system. A second system is also under development for the high-energy density (HED) beamline of the European XFEL project.

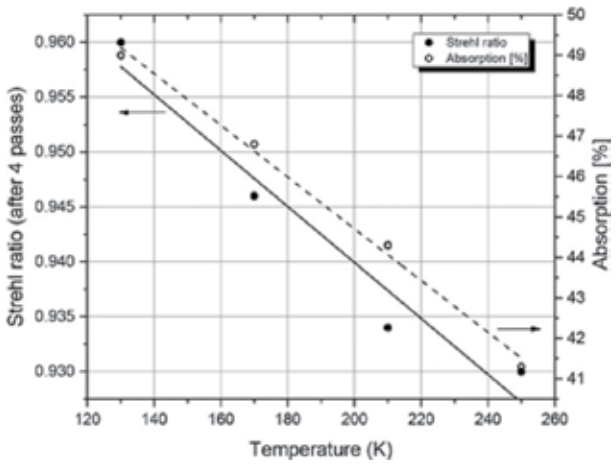

Figure 16. Strehl ratio for the four passes of the probe beam through the Yb:YAG slab and absorbed pump power per single pass as a function of temperature. Lines represent a linear fit with slopes of -6×10^{-4}/K and −0.064%/K, respectively.

The 10 J amplifier architecture is based on the multislab approach. The gain medium is composed of four circular Yb:YAG slabs with two different Yb doping levels as 1.1 and 2.0 at % to confirm a uniform temperature distribution among each slab. The diameter of the circular slab is 45 mm with a 5 mm thickness, and the pump area is square of 23 × 23 mm^2. The pump beam is supplied from 939 nm diodes in stack with a pumping time duration of 700 μs at 10 Hz. The Yb:YAG circular slab is cladded with a 5 mm wide Cr:YAG absorber with 6 cm^{-1} absorption coefficient. This is effective to prevent amplified spontaneous emission (ASE) and parasitic oscillations. A cryogenic He flow cools the slab and keeps the temperature as 150–170 K. The pressure of the He flow is 10 bar. **Figure 17** shows the optical arrangement for amplification. A seed beam is injected into the amplifier through a dichroic mirror and then image relayed by a spatial filter (f = 1 m) to a back reflector and reflected back to the amplifier module. One spatial filter locates on each side of the amplifier head. Each pass is composed by a set of separate mirrors. A deformable mirror is placed in the amplifier after the third pass for the aberration compensation. After seven passes, the beam is extracted from the amplifier with pulse energy increased to 9 J with a size of 21 mm × 21 mm^2.

http://dx.doi.org/10.5772/64147

Numerical modeling of the multislab amplifier is conducted in the HiLASE project to ensure the scaling of the cryogenic technology for further increased parameter region in pulse energy, repetition rate, and better beam quality. Comsol Multiphysics software was chosen to model the thermal and stress effects in the amplifiers [43]. The sources of heat were calculated in the ASE code [44]. The axial surfaces of the slabs are assumed to be cooled only by flowing helium gas at 160 K. The slab was assumed to have no thermal contact with its 2 cm thick Invar holder; and all heat is removed by convection through the faces. From the temperature and stress maps of the slab, the optical path difference (OPD) and birefringence depolarization losses were calculated for a single slab according to a prior approach. The gradual decrease of cooling efficiency in the direction of gas flow, caused by He heating, results in the loss of left-right symmetry of the temperature, stress, depolarization, and OPD maps.

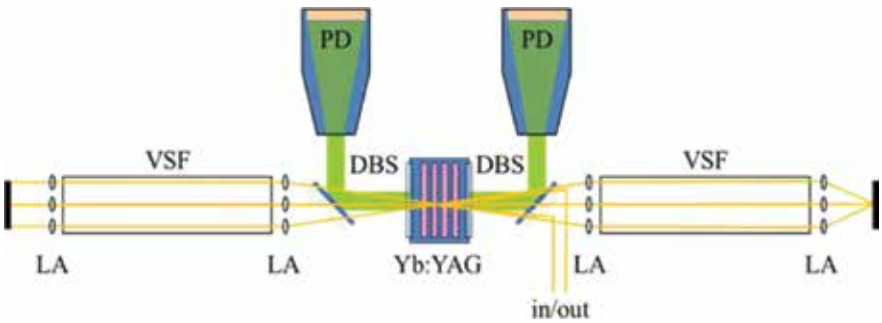

Figure 17. Schematic of the 10 J cryogenic multislab amplifier. It consists of Yb:YAG ceramic slabs in the laser head, dichroic beam splitters (DBSs), lens arrays (LAs), vacuum spatial filters (VSFs), and homogenized pump diode laser modules (PDs).

It is planned to increase the repetition rate of the 10 J amplifier to 100 Hz by keeping the basic performance. Once the operation is as expected, the cryogenic laser offers a technological stage for a single module to generate picosecond multipulses of a few joules of energies, for a single-shot imaging Compton source.

5. Conclusion

Recent progress of thin-disc lasers is promising to realize a high-brightness pumping source of laser plasma or laser Compton short-wavelength sources. Further progress is possible by an advanced cryogenic technology with its higher thermal conductivity. These laser progresses are contributing in the practical applications in short-wavelength imaging and material processing. Picosecond thin-disc laser technology is now in the stage of 1 kW level with >100 kHz repetition rate. Further research and developments are aiming at 1 kW with kHz repetition rate (1 J, ps, kHz), pulse length reduction into subpicosecond region with MHz repetition rate (mJ, fs, MHz), and increase in the average power to 10 kW region. These challenges require further improvements of the achieved technology bases and evaluation of new schemes.

Cryogenic technology is now offering an option for these challenges in the solid-state laser technology.

Acknowledgements

The author appreciates kind collaboration of many researchers in HiLASE Centre in Czech Republic, Waseda University, and Gigaphoton Inc., in Japan. Dr. M. Smrz is especially acknowledged for his excellent work in the 100 kHz thin-disc picosecond laser, Dr. H. Turcicova and Dr. O.Novak for their high average power wavelength conversion, and Dr. P. Sikocinski for his aberration measurement in cryogenic Yb:YAG. Dr. Sakaue is highly appreciated for his experimental and theoretical work in the Laser Compton and FEL seeding research and Dr. T. Yanagida for his pioneering work of tin droplet atomization by a picosecond laser. Experimental work of this chapter is cofinanced by the state budget of the Czech Republic (project HiLASE: Superlasers for real world: LO1602). This work is also supported by the Czech Science Foundation (GACR) under project GA16-12960S.

Author details

Akira Endo

Address all correspondence to: endo@fzu.cz

1 Research Institute for Science and Engineering, Waseda University, Tokyo, Japan

2 HiLASE Centre, Institute of Physics AS CR, Dolní Břežany, Czech Republic

References

[1] Assoufid, L. and Naulleau, P. (2016) Topical Meeting, Compact (EUV & X-ray) Light Sources, OSA High-Brightness Sources and Light-Driven Interactions Congress, 20–22 March 2016, Hilton Long Beach, Long Beach, California, USA

[2] Mizoguchi, H. Nakarai, H. Abe, T. Nowak, K.M. Kawasuji, Y. Tanaka, H. Watanabe, Y. Hori, T. Kodama, T. Shiraishi, Y. Yanagida, T. Soumagne, G. Yamada, T. Yamazaki, T. Okazaki, S. and Saitou, T. (2015) "Performance of one hundred watt HVM LPP-EUV source," Proceedings of SPIE 9422-11

[3] Reagan, B.A. Berrill, M. Wernsing, K.A. Baumgarten, C. Woolston, M. and Rocca, J.J. (2014) "High-average-power, 100-Hz-repetition-rate, tabletop soft-X-ray lasers at sub-15-nm wavelengths," Phys. Rev. A 89, 053820

[4] John, R.W (1998) "Brilliance of X rays and gamma rays produced by Compton back scattering of laser light from high energy-electrons," Laser Particle Beams 16, 115–127

[5] Endo, A. Yang, J. Okada, Y. Yanagida, T. Yorozu, M. and Sakai, F. (2001) "Characterization of the monochromatic laser Compton X-ray beam with picosecond and femtosecond pulse widths," Proceedings SPIE 4502, pp. 100–108

[6] Babzien, M. Ben-Zvi, I. Kusche, K. Pavlishin, I.V. Pogorelsky, I.V. Siddons, D.P. and Yakimenko, V. (2006) "Observation of the second harmonic in Thomson scattering from relativistic electrons," Phys. Rev. Lett. 96, 054802

[7] Kumita, T. Kamiya, Y. Babzien, M. Ben-Zvi, I. Kusche, K. Pavlishin, I.V. Pogorelsky, I.V. Siddons, D.P. Yakimenko, V. Hirose, T. Omori, T. Urakawa, J. Yokoya, K. Cline, D. and Zhou, F (2008) "Observation of the nonlinear effect in relativistic Thomson scattering of electron and laser beams," Laser Phys. 16, 267–271

[8] Oliva, P. Carpinelli, M. Golosio, B. Delogu, P. Endrizzi, M. Park, J. Pogorelsky, I. Yakimenko, V. Williams, O. and Rosenzweig, J (2010) "Quantitative evaluation of single-shot inline phase contrast imaging using an inverse Compton x-ray source," Appl. Phys. Lett. 97, 134104

[9] Pogorelsky, I.V. Babzien, M. Pavlishin, I. Stolyarov, P. Yakimenko, V. Shkolnikov, P. Pukhov, A. Zhidkov, A. and Platonenko, V.T. (2006) "Terwatt CO2 laser; a new tool for strong field research," Proceedings of SPIE, 6261, 18

[10] Ur.C.A. Balabanski, D. Cata-Danil, G. Gales, S. Morjan, I. Tesileanu, O. Ursescu, D. Ursu, I. and Zamfir, N.V. (2015) "The ELI–NP facility for nuclear physics," Nucl. Instrum. Method B 355, 198–202

[11] Bacci, A. Palmer, D. Serafini, L. Torri, V. Petrillo, V. Tomassini, P. Puppin, E. Alesini, D. Anania, M. Bellaveglia, M.P. Bisesto, F. Pirro, G.Di. Esposito, A. Ferrario, M. Gallo, A. Gatti, G. Ghigo, A. Spataro, B. Vaccarezza, C. VillaF. Cianchi, A. Agostino, R.G. Borgese, G. Ghedini, M. Martire, F. Pace, C. Levato, T. Dauria, G. Fabris, A. and Marazzi, M. (2014) "The STAR Project," Proceedings of IPAC2014, WEPRO115A

[12] Endo, A. Sakaue, K. Washio and M. Mizoguchi, H. (2014) "Optimization of high average power FEL for EUV lithography application," Proceedings of FEL2014, FRA04

[13] Allaria, E. Castronovo, D. Cinquegrana, P. Craievich, P. Dal Forno, M. Danailov, M.B. D'Auria, G. Demidovich, A. De Ninno, G. Di Mitri, S. Diviacco, B. Fawley, W.M. Ferianis, M. Ferrari, E. Froehlich, L. Gaio, G. Gauthier, D. Giannessi, L. Ivanov, R. Mahieu, B. Mahne, N. Nikolov, I. Parmigiani, F. Penco, G Raimondi, L. Scafuri, C. Serpico, C. Sigalotti, P. Spampinati, S. Spezzani, C. Svandrlik, M. Svetina, C. Trovo, M. Veronese, M. Zangrando, D. and Zangrando, M. (2013) "Two-stage seeded soft-X-ray free-electron laser," Nature Photon. 7, 913–918

[14] Höppner, H. Hage, A. Tanikawa, T. Schulz, M. Riedel, R.Teubner, U. Prandolini, MJ. Faatz, B. and Tavella, F. (2015) "An optical parametric chirped-pulse amplifier for seeding high repetition rate free-electron lasers," New J. Phys. 17, 053020

[15] Klenke, A. Breitkopf, Kienel, S.M. Gottscha, T. Eidam, T. Hädrich, S. Rothhardt, J. Limpert, J. and Tünnermann, A. (2013) "530 W, 1.3 mJ, four-channel coherently combined femtosecond fiber chirped-pulse amplification system," Opt. Lett. 38, 2283–2285

[16] Brocklesby, W.S. Nilsson, J. Schreiber, T. Limpert, J. Brignon, A. Bourderionnet, J. Lombard, L. Michau, V. Hanna, M. Zaouter, Y. Tajima, T. and Mourou, G. (2014) "ICAN as a new laser paradigm for high energy, high average power femtosecond pulses," Eur. Phys. J. Special Topics 223, 1189–1195

[17] Mans, T.R. Graf, R. Dolkemeyer, J. Schnitzler, C (2014) "Femtosecond Innoslab amplifier with 300 W average power and pulse energies in the mJ regime," Proceedings of SPIE 8959-43

[18] Negel, J.P. Loescher, A. Voss, A. Bauer, D. Sutter, D. Killi, A. Ahmed, M.A. and Graf.T, (2015) "Ultrafast thin-disk multipass laser amplifier delivering 1.4 kW (4.7 mJ, 1030 nm) average power converted to 820 W at 515 nm and 234 W at 343 nm," Opt. Exp. 23, 21064

[19] Freitag, C. Wiedenmann, M. Negel, J.P. Loescher, A. Onuseit, V. Weber, R. Ahmed, M.A. Thomas Graf, T. (2015)" High-quality processing of CFRP with a 1.1-kW picosecond laser," Appl. Phys. A 119, 1237–1243

[20] Ripin, D.J. Ochoa, J.R. Aggarwal, R.L. Fan, T.Y. (2005) "300-W Cryogenically Cooled Yb:YAG Laser," IEEE J. Quantum Electron, QE-41, 1274–1277

[21] Zapata, L.E. Reichert, F. Hemmer, M. Kaertner, F.X. (2016) "250 W average power, 100 kHz repetition rate cryogenic Yb:YAG amplifier for OPCPA pumping," Opt. Lett. 41, 492–495

[22] Endo, A. Lithography, Chapter 9 (2010) "CO_2 laser produced Tin plasma light source as the solution for EUV lithography," edited by Michael Wang, InTech, Janeza Trdine 9, 51000 Rijeka, Croatia

[23] Pirati, A. Peeters, R. Smith, D.A. Lok, S. Noordenburg, M. Es, R. Verhoeven, E. Meijer, H. Minnaert, A. Horst, W. Meiling, H. Mallmann, J. Wagner, C. Stoeldraijer, J. Fisser, G. Levasier, L. Finders, J. Zoldesi, C. Stamm, U. Boom, H. Brandt, D.C. Brown, D.J. and Fomenkov, I.V. (2016) "EUV lithography performance for manufacturing: status and outlook," Proceedings of SPIE 9776-10

[24] Teramoto, Y. Santos, B. Mertens, G. Kops, R. Kops, M. Wezyk, A. Bergmann, K. Yabuta, H. Nagano, A. Ashizawa, N. Shirai, T. Nakamura, K. and Kasama, K. (2016) "High-radiance LDP source: Clean, reliable, and stable EUV source for mask inspection," Proceedings of SPIE 9776-22

[25] Mizoguchi, H. Saitou, T. Yamazaki, T. Okazaki, S. Nakarai, H. Abe, T. Kodama, T. Yanagida, T. Hori, T. Nowak, K.M. Kawasuji, Y. Tanaka, H. Shiraishi, Y. Watanabe, Y.

Yamada, T. and Soumagne, G. (2014) "Sub-hundred Watt operation demonstration of HVM LPP-EUV source," Proceedings of SPIE 9048-22

[26] Smrž, M. Miura, T. Chyla, M. Muzik, J. Nagisetty, S.S. Novák, O. Turcicova, H. Linnemann, Huynh, J. Severová, P. Sikocinski, P. Endo, A. and Mocek, T. (2016) "Progress in kW-class picosecond thin-disk lasers development at the HiLASE," Proceedings of SPIE 9726-43

[27] Smrž, M. Miura, T. Chyla, M. Nagisetty, S. Novák, O. Endo, A. and Mocek, T. (2014) "Suppression of nonlinear phonon relaxation in Yb:YAG thin disk via zero phonon line pumping," Opt. Lett. 39, 4919–4922

[28] Schneidmiller, E.A. , Vogel, V.F. Weise, H. and Yurkov, M.V. (2011) "A kilowatt-scale free electron laser driven by L-band superconducting linear accelerator operating in a burst mode," International Workshop on EUV and Soft X-ray Sources, November 7–9, 2011, Dublin, Ireland

[29] Hosler, E.R. Wood, O.R. Barletta, W.A. Mangat, P.J., Preil, M.E. (2015) "Considerations for a free-electron laser-based extreme-ultraviolet lithography program," Proceedings of SPIE, 9422-12

[30] Chalupský, J. Juha, L. et.al. (2007) "Characteristics of focused soft X-ray free-electron laser beam determined by ablation of organic molecular solids," Opt. Exp. 15, 6036

[31] Filippetto D. Byrd, J. Chin, M. Cork, C. Santis, S.De. Feng, J. Norum, W.E. Doolittle, L. Papadopoulos, C. Portmann, G. Quintas, D.G. Sannibale, F. Stuart, M. Wells, R. and Zolotorev, M. (2011) "Low energy beam diagnostic for APEX, the LBNL VHF photoinjector," Proceedings of 2011 Particle Accelerator Conference, WEP222

[32] Nakajyo, T. Yang, J. Sakai, F. and Aoki, Y. (2003) "Quantum efficiencies of Mg photocathode under illumination with 3rd and 4th harmonics Nd: LiYF4 laser light in RF gun," Jpn. J. Appl. Phys. 42 1470–1474

[33] Singer, A. Sorgenfrei, F. Mancuso, A.P. Gerasimova, N. Yefanov, O.M. Gulden, J. Gorniak, T. Senkbeil, T. Sakdinawat, A. Liu, Y. Attwood, D. Dziarzhytski, S. Mai, D.D. Treusch, R. Weckert, E. Salditt, T. Rosenhahn, A. Wurth, W. and Vartanyants, A. (2012) "Spatial and temporal coherence properties of single free electron laser pulses," Opt. Exp. 20, 17480

[34] Turcicova, H. Nowak, O. Smrz, M. Miura, T. Endo, A. and Mochek, T. "Deep ultraviolet (257.5 nm and 206 nm) picosecond pulses produced a high-power 100 kHz solid-state thin-disk laser," Proceedings of SPIE 9893-1

[35] Riedel, R. Rothhardt, J. Beil.K, Gronloh, B. Klenke, A. Höppner, H. Schulz, M., Teubner, Kränkel, U.C. J.Limpert, J. Tünnermann, A. Prandolini, M.J. F. and Tavella, F. (2014) "Thermal properties of borate crystals for high power optical parametric chirped-pulse amplification," Opt. Exp. 22, 17607.

[36] Stubenvoll, M. Schäfer, B. Mann, K. and Novak, O. (2016) "Photothermal method for absorption measurements in anisotropic crystals," Rev. Sci. Instrum. 87, 023904, Proceedings of SPIE 9726-43

[37] Sakaue, K. Araki, S. Fukuda, M. Higashi, Y. Honda, Y. Sasao, N. Shimizu, H. Taniguchi, T. Urakawa, J. and Washio, M. (2011) "Development of a laser pulse storage technique in an optical super-cavity for a compact X-ray source based on laser-Compton scattering," Nucl. Instru. Meth. A 637, S107–S111

[38] Courjaud, A. Tropheme, B. Falcoz, F. Eric, P. Mottay, E.P. and Riboulet, G. (2015) "High power lasers for gamma source," Proceedings of SPIE 9342-23

[39] Jung, R. Tümmler, J. Nubbemeyer, T. and Will, I. (2015) "Two- Channel thin-disk laser for high pulse energy," Advanced Solid State Lasers Conference© OSA 2015, AW3A.7.

[40] Fan, T.Y. Ripin, D.J. Aggarwal, R.L. Ochoa, J.R. Chann, B. Tilleman, M. and Spitzberg, J. (2007) "Cryogenic Yb3+-Doped Solid-State Lasers," IEEE J. Quantum Electron. QE-13, 448–458

[41] Sikocinski, P. Novak, O. Smrz, M. Pilar, J. Jambunathan, V. Jelínková, H. Endo, A. Lucianetti, A. and Mocek, T. (2016) "Time-resolved measurement of thermally induced aberrations in a cryogenically cooled Yb:YAG slab with a wavefront sensor," Appl.Phys.B. April 2016, 122:73

[42] Mason, P.D. Banerjeea, S. Ertela, K. Phillipsa, P.J. Thomas, J. Butchera, T.J. Smitha, J.M. Vidoa, M.D. Tomlinsona, S. Oleg Chekhlova, O. Shaikha, W. Blakea, S. Holligana, P. Divoky, M. Pilar, J Hernandez-Gomeza, C. Justin, R. Greenhalgha, S. and Colliera, J.L. (2015) "DiPOLE100: A 100 J, 10 Hz DPSSL using cryogenic gas cooled Yb:YAG multi slab amplifier technology," Proceedings of SPIE 9513 02-1

[43] Slezak, O. Lucianetti, A. Divoky, M. Sawicka, M. and Mocek, T. (2013) "Optimization of wavefront distortions and thermal-stress induced birefringence in a cryogenically-cooled multislab laser amplifier," IEEE J. Quantum Electron, QE 49, 960–966

[44] Sawicka, M. Divoky, M. Novak, J. Lucianetti, A. Rus, B. and Mocek, T. (2012) "Modeling of amplified spontaneous emission, heat deposition, and energy extraction in cryogenically cooled multislab Yb3+:YAG laser amplifier for the HiLASE Project," J. Opt. Soc. Am. B 29, 1270–1276

Section 3

Large-scale High-power Laser Systems

Chapter 6

Multiterawatt Hybrid (Solid/Gas) Femtosecond Systems in the Visible

Leonid D. Mikheev and Valery F. Losev

Additional information is available at the end of the chapter

http://dx.doi.org/10.5772/63972

Abstract

A novel hybrid (solid/gas) approach to the development of femtosecond high-intensity laser systems operating in the visible is presented in this chapter. Behind this approach is a combination of a solid-state front end relying on widespread and highly developed techniques for femtosecond pulse generation in the near infrared with a photochemically driven boosting amplifier operating in the visible spectral range. Historical background of developing photochemically pumped gas lasers on broad bandwidth electronic transitions in molecules and physical principles of their operation are briefly summarized as well. The architecture and the design issues of the hybrid femtosecond systems relying on the amplification of the second harmonic of Ti:sapphire front ends in the photodissociation XeF(C-A) power-boosting amplifiers driven by the VUV radiation from electron-beam-to-VUV-flash converters are described, as well as breakthrough results of proof-of-principle experiments demonstrating a high potential of the hybrid approach. Wavelength scaling of laser-matter interaction is shortly discussed to demonstrate advantages of shorter driver wavelengths for some applications with main emphasis placed on recombination-pumped soft X-ray lasers.

Keywords: hybrid femtosecond systems, visible spectral range, photochemically driven laser media, laser-matter interaction

1. Introduction

Significant progress in the development of all-solid-state femtosecond laser systems relying on chirped-pulse amplification (CPA) technique has resulted in reaching petawatt (PW) peak powers [1] and focused intensities as high as 10^{22} W/cm^2 [2] that provides great opportunities for experimental studies in the area of the extreme high-field science. The all-solid-state

laser systems providing pulses shorter than 100 fs are based on the Ti:sapphire and optical parametric chirped-pulse amplification (OPCPA) technologies.

Presented in this chapter are milestones and main results obtained in the course of the realization of a novel hybrid (solid/gas) approach to the development of femtosecond systems that, unlike the all-solid-state systems operating in the near-infrared (NIR) region, allow for producing super-intense optical pulses in the blue-green spectral range. This approach aims to marry robust solid-state laser technologies highly developed for femtosecond pulse generation and amplification in the NIR spectral range with advantages of photochemically driven gaseous gain media of the visible range.

Most extensive development of the photochemical method of pumping gaseous active media dates back to the 1960s–1990s of the last century (see [3–5] and references cited therein). Being applied to optical excitation of gas lasers on electronic molecular transitions by radiation from such unconventional pump sources as high-temperature electrical discharges and strong shock waves in gas, This method resulted in emerging a new class of gaseous active media for lasers emitting in the spectral range extending from the NIR to UV with a high output energy increasing in proportion to the active volume and pump energy. Among a variety of molecules lasing upon optical excitation, there are three broadband active media (XeF(C-A), Kr_2F, and Xe_2Cl), which offer a number of characteristics extremely attractive for the amplification of femtosecond optical pulses up to ultrahigh peak powers. The gaseous nature and visible spectrum of emission of these media promise important virtues of the hybrid systems. First of all, the gaseous nature of these media is characterized by low nonlinear refractive index allowing amplification of optical pulses with much higher intensities as compared with solid media. Secondly, the visible spectrum of emission requires nonlinear frequency upconversion of a seed pulse generated in the NIR spectral region by a solid-state front end, thereby providing efficient temporal cleaning of the ultrashort optical pulse and the high temporal contrast ratio of an output pulse, which is of primary importance for a number of high-field experiments.

The main motivation for the development of hybrid systems in the visible is favorable drive frequency scaling of laser-matter interaction in a number of high-field applications. Of overriding importance is the dramatic improvement of the recombination soft X-ray laser excitation in an optical field ionized (OFI) plasma with drive frequency.

2. Photochemical lasers

The photochemical method of gaseous active media pumping by radiation from broadband optical sources originates from the development of the high-power photodissociation laser in metastable iodine atoms ($\lambda = 1.315$ μm) (for example, see [6–8]), resulted in variety of remarkable results: 1 MJ of output energy in a single beam [9], 2 and 30 kJ in a short laser pulse obtained, respectively, with flash lamp [10] and surface discharge [11] optical pumping. The breakthrough results obtained in the course of the iodine photodissociation laser development stimulated extensive studies of the potentialities of the gaseous active media optical pumping

and the search for new active media for high-power optically driven lasers in many laboratories around the world.

It is important to stress the major impact of untraditional pumping sources on the photochemical method development, such as high-current open discharges initiated with exploding wires or sliding sparks, as well as strong shock waves driven by detonation of chemical explosives [4]. These pumping sources, initiated directly in laser working mixtures, had no shell separating them from an active medium that removes limitations on energy deposition into the pumping sources and makes it possible to utilize the radiation in any spectral range, including the UV and VUV, where the most intense absorption bands of the overwhelming majority of molecules are located. As compared with ordinary flash lamps, these pumping sources have much higher brightness temperature reaching 30–35 kK.

The main emphasis in these studies was placed on molecular transitions that, unlike atoms, do not require complete population inversion of the electronic states participating in the laser transition and enable a fairly simple depletion of the lower laser levels due to vibrational relaxation and/or dissociation of the lower state. The application of such optical sources has led to emerging new class of gas lasers emitting in the spectral range from the NIR to UV regions due to the development of a variety of photochemical excitation techniques relying on the photolysis and direct optical excitation of molecular gases, as well as secondary photochemical reactions (see [3–5] and references cited therein).

One of the most remarkable results obtained in the course of these studies is the optical excitation of lasing on broadband bound-free $Kr_2F(4\ ^2\Gamma\text{-}1,2\ ^2\Gamma)$, $Xe_2Cl(4\ ^2\Gamma\text{-}1,2\ ^2\Gamma)$, and XeF(C-A) transitions in the visible. These active media are very sensitive to the internal losses because they have much lower small-signal gain as compared with excimers emitting in the UV spectral range on the B-X transition due to the large width of their luminescence spectra and long radiative lifetime of the excited states. For this reason, e-beam or fast discharge pumping of these active media turned out to be ineffective since electron excitation technique is based on plasmochemical reactions involving ionized and highly excited atoms and molecules that are characterized by strong absorption in the visible [12]. For example, laser action from electron-beam-excited Kr_2F and Xe_2Cl active media was observed only in the afterglow of the pump pulse when the transient absorption is significantly reduced [13]. The photochemical technique, relying on reactions of neutrals excited to low-lying energetic states, free of the shortcomings associated with transient absorption. This makes optical pumping to be superior to electron excitation in the efficiency of producing laser action on the aforementioned transitions.

Due to extremely broad gain bandwidth supporting pulses of shorter than 10 fs, these active media are of practical interest for amplifying femtosecond optical pulses to ultrahigh peak powers [4, 5, 14, 15]. The main spectroscopic characteristics of the transitions are listed in the **Table 1**. One of most important parameters is the saturation fluence accounting for the maximum energy extraction per surface unit of an amplifier output aperture. This parameter, ranging from 0.05 J/cm^2 for XeF(C-A) to 0.2 J/cm^2 for Kr_2F due to rather long radiative lifetime of the upper laser states, promises peak power, I_{out}, of up to ~10 TW per square cm of an output aperture in a 25 fs pulse. At the same time, the gas active media are easily scalable to large volumes with wide aperture (several hundred cm^2) to reach PW level of output peak power.

Moreover, the combined use of two media with spectrally shifted emission bands (Kr_2F with XeF(C-A) or Xe_2Cl) in an amplifier chain makes promising for the amplification of even shorter optical pulses due to twofold broadening a gain bandwidth (**Figure 1**) and spectrally inhomogeneous gain saturation.

Transition	**XeF(C-A)**	**$Kr_2F(4^2\Gamma\text{-}1,2^2\Gamma)$**	**$Xe_2Cl(4^2\Gamma\text{-}1,2^2\Gamma)$**
λ_{max}, nm	480	420	510
$\Delta\lambda$, nm	70	80	100
τ_{FT}, fs	5	3	4
τ_{sp}, ns	100	180	250
σ_{st}, cm^2	10^{-17}	2.3×10^{-18}	2.8×10^{-18}
ε_{sat}, J/cm^2	0.05	0.2	0.15
I_{out} ($\tau = 25$ fs), TW/cm^2	2	8	6

λ_{max} is the wavelength of the gain maximum.
$\Delta\lambda$ is the gain bandwidth.
τ_{FT} is the transform-limited pulse width (for Gaussian profile).
τ_{sp} is the spontaneous lifetime.
σ_{st} is the stimulated emission cross-section.
ε_{sat} is the saturation fluence.
I_{out} is the estimated maximum peak power density related to a laser amplifier output aperture.

Table 1. Characteristics of broadband active media.

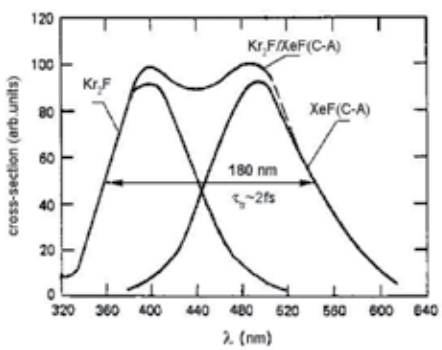

Figure 1. Emission spectrum for the mixed Kr_2F/XeF(C-A) system.

An important advantage of gaseous active media resides in the much lower value of the nonlinear index of refraction as compared with solid-state materials, which allows amplification of optical pulses at much higher intensities than in condensed gain media. For the first time, hybrid architecture employing a gaseous active medium was realized in the system comprising a dye femtosecond oscillator and e-beam or fast discharge-driven boost amplifier on the UV B-X transitions of ArF, XeCl, KrF, and XeF rare-gas-halide excimer molecules. The

highest peak power obtained in the hybrid systems of this type reached ~1 TW in a 310 fs pulse [16]. However, gain bandwidth on the B-X transition does not exceed 2 nm in full width at half-maximum (FWHM) corresponding to the spectrally limited pulse width of ~50 fs. With spectral gain narrowing in amplifiers, it is difficult to count on the possibility of producing pulses shorter than 0.1 ps at the TW level of peak power. Moreover, due to the short spontaneous lifetime of the B state and rather narrow spectral bandwidth, these transitions exhibit as low as 1 mJ/cm^2 saturation fluence, which corresponds to the output intensity of 10^{-2} TW/cm^2 in a 0.1 ps pulse, requiring too large output aperture to produce multiterawatt output peak power.

Compared with the B-X transition, the broadband photochemical media are characterized by more than an order of magnitude larger gain bandwidth and saturation fluence allowing for several TW/cm^2 to be obtained in hybrid systems comprising these active media. In addition, unlike to the electron-impact excitation, the optical pumping, which is practically free of transient absorption within the laser transition spectral band, makes the entire transition bandwidth to be accessible for the femtosecond pulse amplification. These active media are briefly reviewed in the subsequent sections.

2.1. XeF(C-A) active medium

A schematic energy diagram of the upper and lower XeF laser levels is shown in **Figure 2**. Behind the optical pumping XeF active medium is the photolysis of XeF_2 vapor in the spectral range of <204 nm to produce XeF excimers mainly in the B state [17–19]. The C state, lying lower than the B state, is populated due to collisional relaxation of the latter in the presence of a buffer gas. Depending on composition of working mixture, laser action is observed on the B-X (353 nm) or C-A (480 nm) transition [20]. Broad gain bandwidth on the C-A transition ($\Delta\lambda$ = 70 nm [21]) is accounted for by the repulsive nature of the A state. On the other hand, repulsive character of the lower A state provides its virtually instantaneous depopulation and ensures population inversion independently on the presence of buffer gas.

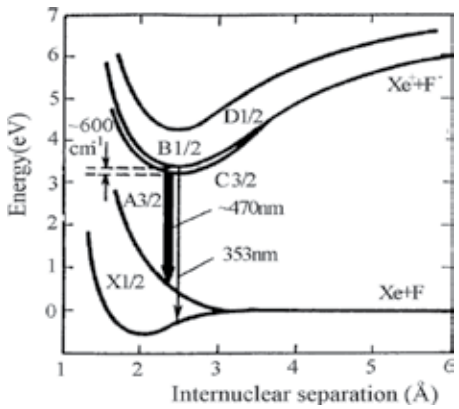

Figure 2. The potential curves of low-lying energetic states of the XeF excimer molecule.

Lasing in the photochemically driven XeF active medium was obtained for the first time in 1977 on the *B-X* transition with an exploding wire as a pump source [22]. Later on, in a series of papers, laser action on XeF(B-X) and XeF(C-A) was reported upon optical pumping by broadband VUV radiation from exploding wires [20, 23], surface discharges [24–27], formed-ferrite flash [28, 29], and strong shock waves [30], as well as by the Xe_2 spontaneous emission at 172 nm excited by an electron beam [31–33]. These studies have led to a number of significant achievements. Among them are high output energies attaining as much as 1 kJ and 170 J in the UV region with the strong shock wave [30] and surface discharge optical pumping [24], respectively, as well as 120 J and 10 J obtained in the visible under optical pumping by radiation from surface discharges operating in the single shot [24] and 1 Hz repetitive rate [27] modes respectively.

Studies of the XeF(C-A) laser showed that, besides minor transient absorption discussed above, the optical pumping XeF(C-A) active medium has an additional advantage over the electron-impact excitation, which consists in the much weaker competition of the B-X transition. The point is that upon optical excitation, relative populations of the closely lying B and C states are determined by the thermodynamic equilibrium at a buffer-gas temperature that is close to the room temperature, while, upon e-beam and fast discharge pumping, the main role in the energy exchange between these states is played by secondary electrons, which have a temperature of ~1 eV characteristic of this pumping. In the optically driven active medium, the electron concentration is negligibly low, thereby providing an efficient laser action on the C-A transition.

From the viewpoint of femtosecond pulse amplification, the pump technique relying on the e-beam-driven spontaneous emission of Xe_2 excimers is of particular concern because, along with surface discharge optical pumping, it paved a new way for the development of the hybrid (solid/gas) femtosecond systems in the blue-green region. With the use of this technique to pump the XeF(C-A) laser, as high as 6 J of output energy was reported in [33].

Finally, it is essential to note that one of the most important conclusions gained from the optically driven XeF(C-A) laser studies is that at a proper composition of the active medium its broad amplification band is not practically modified by transient absorption making the entire transition bandwidth to be accessible for the femtosecond pulse amplification. A drawback of the XeF(C-A) active medium is that it must be replaced in a laser chamber after each shot because of the photodecomposition of the parent XeF_2 molecules.

2.2. Xe_2Cl active medium

Among the broad bandwidth photochemically driven active media listed in **Table 1**, Xe_2Cl is of special interest because initial working mixture is not consumed throughout pump flash allowing for operation in the repetitive mode without replacing the working gas mixture after each shot. Moreover, as compared with the XeF(C-A) transition, this active medium has a much longer radiative lifetime of the upper state, which was measured to be 245 ns [34].

This active medium, as well as Kr_2F discussed below, is currently studied to a much lesser extent as compared with XeF. First observation of lasing in the Xe_2Cl triatomic excimer was

reported in 1980 upon e-beam pumping [35]. This was followed in 1985 by successful operation of the Xe_2Cl laser optically pumped by the VUV radiation at 137 nm from the open discharge initiated by an exploding wire [36]. Behind the laser action is the reaction of optically excited molecular chlorine with Xe to form XeCl(B) excimers that then recombine with xenon into Xe_2Cl^* emitting in the blue-green region with a fluorescence quantum yield experimentally measured to be ~75%, with respect to the absorbed pumping photons [37].

However, the application of this technique for the femtosecond pulse amplification is of little practical significance since, due to the narrow Cl_2 absorption bandwidth at 137 nm, an efficiency of the Xe_2Cl pumping by the thermal pump source is expected to be low. Moreover, to take advantage of repetitive pulse mode of operation, it requires the development of a powerful large-area pumping source radiating in the short-wave part of the VUV spectral range in a repetitive pulse regime.

On the other hand, as was shown in [38], more promising is the excitation of the active medium in mixtures of Xe and $C1_2$ vapor due to the photoassociation process

$$Xe + Cl + h\nu \rightarrow XeCl(B,C)$$

at the wavelength of a XeCl laser (308 nm) followed by the three-body XeCl(B,C) recombination with xenon to form $Xe_2Cl(4\ ^2\Gamma)$. Production of Cl atoms is provided by the same pump pulse of the XeCl laser via photodissociation of $C1_2$. In the mixtures of Xe and Cl_2 at pressures of 1–2 bar and 1–2 Torr, respectively, the quantum efficiency for the energy transfer from XeCl(B,C) to $Xe_2Cl(4\ ^2\Gamma)$ is close to 100% due to the extremely high rate constant (1.3×10^{-30} $cm^6\ s^{-1}$ [39]) of the XeCl(B,C) recombination with xenon. The main loss process in the pump mechanism considered here is the $C1_2$ photodissociation to accumulate a sufficient number of Cl atoms and thereby ensure a high enough absorption of pump photons in the longitudinal geometry of excitation. Nevertheless, the overall efficiency for the conversion of the pump energy into the energy stored in the Xe_2Cl active medium is estimated to be as high as 5% at the pump intensity of 5 MW/cm^2 in a 100 ns pump pulse. According to Ref. [38], this mechanism of pumping can be of great practical importance, since it enables to produce a small-signal gain in the Xe_2Cl active medium, which is expected to be even higher than that obtained in the XeF(C-A) amplifier to be discussed later. Moreover, molecular chlorine is not consumed upon optical excitation because chlorine atoms, generated in the Cl_2 photodissociation, recombine back to the molecular state at a time scale of 1 ms. This makes it far easier to operate a Xe_2Cl femtosecond amplifier in the pulse repetition regime.

For the sake of completeness, it should be noted that the gain on the Xe_2Cl laser transition excited due to photoassociation at 308 nm was observed for the first time in chlorine-doped solid [40] and liquid [41] xenon. However, unlike gaseous active media, realization of the femtosecond pulse amplifier based on this technique is a serious technological problem.

2.3. Kr_2F active medium

Emission band of Kr_2F at 420 nm is spectrally shifted relative to emissions of XeF(C-A) at 480 nm and Xe_2Cl at 490 nm that enables twofold broadening of the amplification band (**Figure 1**) with the use of two different active media in an amplifier chain.

The Kr_2F excitation mechanism relies on the KrF_2 photodissociation absorption in the VUV spectral range around 164 nm [42] to produce KrF(B) excimers. The utilization of KrF(B) in secondary processes is different, depending on the composition and pressure of the working mixture. For example, in low-concentration Xe admixtures, exchange processes take place, resulting in XeF(B) formation with a yield close to 100% and laser action at 353 nm upon pumping by radiation from exploding wire [42]. Being mixed with Kr at a pressure of ~1 bar, KrF(B) forms $Kr_2F(4\,^2\Gamma)$ excimers in three-body recombination collisions [43].

It was found that the laser action in Kr_2F^* also occurs if, instead of Kr, nitrogen is admixed to the working mixture. This observation was attributed to the formation of KrN_2F^* four-atomic excimers that produce Kr_2F^* in exchange reactions with Kr atoms generated upon photochemical decomposition of KrF_2 vapor by VUV pump radiation [43]. Note that, despite a complex Kr_2F^* formation mechanism, which involves three stages of chemical transformations in mixtures with nitrogen (at one of the stages, products of photochemical processes react with each other), the Kr_2F^* yield is rather high providing ~70% of KrF(B) molecules to be transformed into Kr_2F^* excimers [43]. Lasing in Kr_2F at 450 nm was observed upon optical pumping of KrF_2:N_2 = 1:1500 Torr and KrF_2:CF_4:Kr = 1:300:1200 Torr gas mixtures by the VUV radiation from an open discharge initiated by an exploding wire [44].

The most detailed results of experimental investigations of above considered broadband active media and a complete bibliography on the works can be found in Refs. [3, 20, 45].

3. Hybrid systems with XeF(C-A) amplifiers

Among the gaseous active media with broad amplification band, XeF(C-A) is the most widely studied. That is why this transition was the first to study the hybrid approach with the use of the broadband excimer molecules. Studies of the femtosecond pulse amplification on the XeF(C-A) transition were pioneered by demonstration of 1 TW peak power due to the direct amplification of 250 fs seed pulses from a mode-locked dye laser in the e-beam-driven active medium [15]. However, application of electron-beam excitation to the XeF(C-A) active medium faces serious difficulties associated with the above mentioned transient absorption and competition of B-X and C-A transitions due to strong mixing of closely lying *B* and *C* states of the XeF excimer by electrons. As it was discussed above, transient absorption results in the afterglow gain formation. Strong B-C states mixing causes C-state depopulation via ASE depletion of the B-state which has two orders of magnitude higher stimulated emission cross section for the B-X transition compared with that for the C-A transition. Using five-component mixture comprising F_2, NF_3, Xe, Kr, and Ar has circumvented this problem due to formation of Kr_2F excimers strongly absorbing emission at the wavelength of the B-X transition (353 nm). As discussed above, optical pumping of this active media is free of both of these shortcomings.

3.1. Hybrid systems based on surface discharge-driven XeF(C–A) amplifiers

Beginning with the proposal of femtosecond pulse amplification in the optically driven XeF(C-A) active medium [14], experimental studies in the field of the hybrid (solid/gas) technology started with the development of the XeF(C-A) amplifier optically driven by the VUV radiation from large-area multichannel surface discharges (see [5] and references cited therein). For this purpose, two versions of the photochemically driven XeF(C-A) amplifier based on the surface discharge as an optical pump source have been built at the P.N. Lebedev Physical Institute (LPI, Moscow, Russia) and at the Lasers Plasmas and Photonic Processes (LP3) Laboratory (Marseille, France) (**Figure 3**). They differ from each other by an output aperture (3×11 and $5 \times 18\ cm^2$, respectively), discharge initiation technique, and pump energy. Pumping sources are based on the multichannel surface discharges initiated along the side walls of rectangular half a meter long dielectric chambers filled with a mixture of XeF_2 vapor, argon, and nitrogen at 1 atm. The pumping scheme, in which two planar sources pump an active medium placed between them, provides spatially homogenous excitation of the medium. Moreover, rectangular aperture of the designed amplifiers offers a simple approach to the development of the multipass optical scheme for energy extraction from XeF(C-A) active medium characterized by rather low values of small-signal gain upon optical pumping. In a multipass scheme of the "wedge-trap configuration," a seed pulse runs between two tilted intracell mirrors allowing for up to 45 double passes through the active medium to be realized.

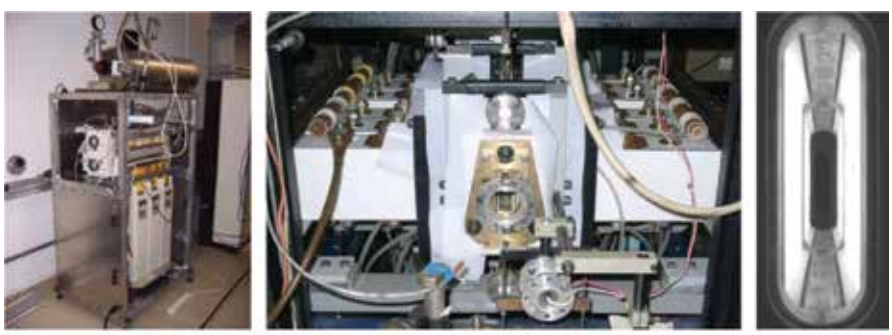

Figure 3. Photographs of the XeF(C-A) amplifiers built at (a) LP3 and (b) LPI. (c) Inside view of the amplifier cell with multichannel surface discharges fired along its side walls.

Operating performances of the XeF(C–A) amplifier, which were measured at the LP3 Laboratory with the use of a hybrid Ti:sapphire/optical-parametric-amplifier front end system, demonstrated a total multipass gain factor of 10^2, corresponding to a small-signal gain of $2 \times 10^{-3}\ cm^{-1}$, with spectrally and spatially homogeneous amplification.

More details and a complete bibliography on the operating characteristics of the laser amplifier and pump sources relying on the multichannel surface discharge are summarized in [5].

3.2. Hybrid systems based on XeF(C-A) amplifiers pumped by the VUV radiation of e-beam converter

The promising results obtained in the course of the studies of the surface discharge pumped XeF(C-A) amplifiers motivated the development of an alternative pump technique based on the conversion of e-beam energy to the VUV radiation, which is expected to be more practical from the viewpoint of the XeF(C-A) amplifier scaling. The main principle of laser action upon pumping by the e-beam excited xenon emission was introduced for the first time in [31] to pump a XeF(B-X) laser operating in the UV region. Later on, this technique was applied to pump a multijoule XeF(C-A) laser in the visible [33].

To study this approach, two hybrid fs systems, THL-30 with a design peak power of ~10 TW and THL-100 designed for 50–100 TW peak power, have been built at the LPI and Institute of High-Current Electronics (IHCE, Tomsk, Russia), respectively. Both of these systems comprise Ti:sapphire front ends (Avesta Project Ltd), frequency doublers, prism pair stretcher, and power-boosting XeF(C-A) amplifiers driven by e-beam-to-VUV-flash converters made at the IHCE.

3.2.1. THL-30 hybrid system

Photos of the front end and XeF(C-A) amplifier incorporated into the THL-30 hybrid system are presented in **Figure 4**. **Figure 5** shows the cross sectional schematic diagram of the XeF(C-A) amplifier. The e-beam converter (2) of cylindrical form is filled with pure xenon at a pressure of 3 bars. Emission of Xe_2^* is excited by four 120 cm long × 15 cm wide radially converging beams of electrons accelerated up to 450 keV in the vacuum diode (1) and injected into the converter through 40 μm Ti foils. The laser cell (3) consists of a 12 × 12 × 128 cm square cross-sectional tube with arrays of 10 rectangular CaF_2 windows (12 × 12 cm) sealed on its side walls. The cell containing XeF_2/N_2 mixture at 0.25–1 bar is housed into the e-beam converter along its axis. In this configuration, the laser cell is thus immersed into the xenon. The distance of 7.5 cm between the Ti foil and CaF_2 windows is chosen to assure that the electrons issued from the e-beams are stopped in the converter at the xenon operating pressure of 3 bars. The e-beams excite the xenon over a 250 ns pulse to produce Xe_2^* fluorescence at 172 nm with a ~30% average fluorescence efficiency [33]. The Xe_2^* radiation is transmitted through arrays of CaF_2 windows into the laser cell to photodissociate XeF_2. The e-beam energy deposited into xenon

Figure 4. THL-30: Photographs of the Ti:sapphire front end (left) and XeF(C-A) amplifier (right).

is measured to be 2.5–3 kJ, which yields a small signal gain of (1.5–2.5) × 10^{-3} cm^{-1} in the laser cell [46, 47].

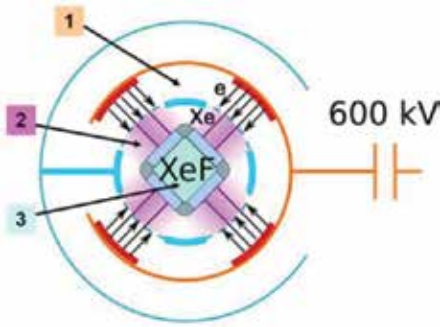

Figure 5. Cross-sectional schematic diagram of the XeF(C-A) amplifier: (1) vacuum diode, (2) e-beam converter, and (3) photolytic laser cell.

Seed pulses with 50 fs duration and 5 mJ energy at 475 nm are produced in the solid-state front end consisting of a Ti:sapphire oscillator operating at 950 nm, regenerative and multipass amplifiers, and KDP frequency doubler spectrally matching the front end to the boosting XeF(C-A) amplifier. Nonlinear frequency upconversion also allows for temporal cleaning of seed pulses injected into the final gas amplifier.

Before the final amplification, the seed pulses are negatively chirped to 1 ps with the use of a prism-pair arrangement. Besides avoiding nonlinear pulse distortion in the amplifier, seed pulse stretching is required to exceed the rotational reorientation time of the XeF(C) molecules, which is estimated to be about 0.8 ps [48, 49]. If the seed pulse is linearly polarized and shorter than the above value, saturation of only a portion of all excited XeF molecules is possible (because of random molecular orientation), thus limiting energy extraction from the amplifier. Down-chirped pulses can be then recompressed due to the positive group velocity dispersion in bulk glass and/or chirped mirrors.

A multipass optical scheme for energy extraction from the active medium has a 3D "wedge-trap" configuration formed by two pairs of tilted intracell mirrors providing the displacement of a beam in two mutually orthogonal directions.

In test experiments, an output energy of 0.25 J has been extracted from the amplifier seeded with a 4 mJ pulse [46, 47], indicating that 5 TW peak power can be obtained in THL-30. Presently, this system is mainly used for the development of key technologies purposed for the implementation in the THL-100 system to be discussed below in more detail.

3.2.2. THL-100 hybrid system

Architecture of THL-100 laser is substantially similar to that described above for the THL-30 hybrid system. Its optical scheme is shown in **Figure 6**.

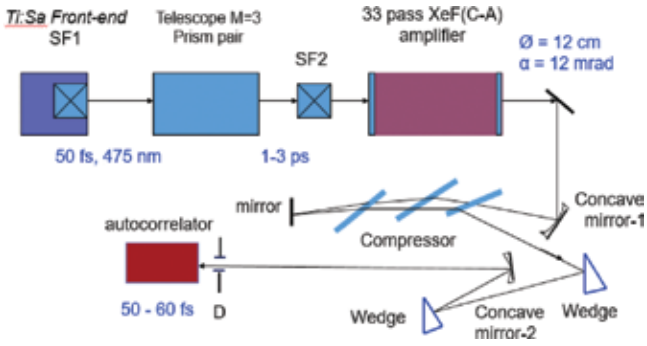

Figure 6. Optical scheme of THL-100 laser system. Ti:Sa front end—Start-480M; SF1 and SF2—vacuum spatial filters; compressor—4-cm-thick fused silica plates at Brewster angle; D—260 μm diaphragm; concave mirror-1—F = 7.5 m; concave mirror-2—F = 12 m.

3.2.2.1. Front end

The front end (Start-480M manufactured by "Avesta Project Ltd") shown in **Figure 7a** consists of a Ti:sapphire master oscillator pumped by a CW pump laser (Verdy-8) at a wavelength of 532 nm, grating stretcher, regenerative and two multipass amplifiers pumped by repetitively pulsed lasers (SOLAR Laser Systems) at a wavelength of 532 nm, spatial filter after the final amplifier, grating compressor, and generator of the second harmonic. The output energy of 20 mJ is produced in a 50 fs pulse at the wavelength of the second harmonic (~475 nm) [50]. The front end operates in the single pulse mode and with a repetition rate of 10 Hz. The output beam of 2.5 cm diameter is directed to the prism pair arrangement (**Figure 7b**) with negative group velocity dispersion, which allows a seed pulse to be stretched. It consists of a mirror telescope with a magnification M = 3, two fused silica prisms allowing a 75-mm-diameter beam to pass, and the mirrors for beam transportation between the prisms in the forward and backward directions. The maximum distance that can be realized between the prisms is 9.6 m, corresponding to the 2.4 ps pulse duration. After the prism pair, the laser beam is directed into the XeF(C-A) amplifier.

Figure 7. (a) Femtosecond Ti:sapphire front end. (b) Prism pair arrangement.

3.2.2.2. Photodissociation XeF(C-A) amplifier

Figure 8 shows a photograph of the XeF(C-A) amplifier. Its principle of operation and the design is similar to the above described XeF(C-A) amplifier of THL-30 laser system. However, it has its differences: the e-beam converter is driven by six electron beams instead of four and its pump energy is four times higher. The amplifier includes two high-voltage pulse generators operating at $U_0 = 90$ kV or 95 kV charging voltage, a vacuum electron diode, gas chamber with a foil support structure, which filled with xenon, and laser cell with two mirror units for multipass amplification of the laser beam. The design and specifications of the XeF(C-A) amplifier are described in detail in [47, 51–54].

Figure 8. General view of the XeF(C-A) amplifier.

An electron accelerator generates six 100 cm long × 15 cm wide electron beams with a maximum energy of 550 keV (at $U_0 = 95$ kV) at the total diode current of 250 kA in a 150 ns (FWHM) pulse. Bunches are injected into the chamber filled with xenon at a pressure of 3 bar. The electron beam energy is converted to the VUV radiation of Xe_2^* excimers at a wavelength of 172 nm with an efficiency of 30–40%. Inside the gas chamber along its axis is the hexagon laser cell (**Figure 9a**), on the side faces of which there are a total of 54 windows made of CaF_2. The windows with size of 12 × 12 cm and 2 cm thick are set in grooves on the rubber gasket (Viton) and sealed by means of clamping flanges. The windows are arranged opposite grates with foil, through which the electron beam is injected into the gas chamber. This provides the best geometric coupling of the cell with laser pump source. The output aperture of the laser cell has a diameter of 24 cm. Both ends of the laser cell are sealed with fused silica windows with a diameter of 30 cm. Inside the cell, there are two mirror units that provide multiple passage of the seed pulse through the active region. Each unit has 16 mirrors of different diameters arranged along its perimeter. The mirror reflection coefficient is 99.5–99.7%. The laser cell is filled with a gas mixture consisting of 0.25–0.5 bar high purity nitrogen and 0.1–0.4 Torr XeF_2 vapor. **Figure 9b** shows an internal view of the laser chamber with the mirror unit at the rear end. To maximize the efficiency of conversion of the electron beam energy into the VUV radiation, the high purity (99.9997%) xenon is used and the e-beam converter gas chamber is evacuated to a pressure of 10^{-4} Torr. As xenon purity decreases due to exposure of the electron

beams to the structural elements of gas chamber, its purification is carried out by a filtering device "Sircal MP-2000."

Figure 9. (a) Laser cell of the XeF(C-A) amplifier. (b) Inside view of the laser cell with the mirror unit.

3.2.2.3. Experimental techniques

The active medium of the XeF(C-A) amplifier is created under the action of the VUV radiation at a wavelength of 172 nm. XeF excimer molecules are formed in the B-state via XeF_2 photodissociation. The upper state of the XeF(C-A) laser transition is formed as a result of the relaxation of the XeF(B) molecules in collisions with the molecules of the N_2 buffer gas. Amplification of the seed pulses was carried out in a multipass optical scheme (33 passes). The laser beam entering into the XeF(C-A) amplifier was made slightly divergent, so that during amplification, it was steadily increased in diameter from 20 mm (inlet) to 62 mm (the penultimate mirror), making a double round-trip along the inside perimeter of the laser cell. The penultimate convex mirror directed the beam to a flat mirror 100 mm in diameter, located on the optical axis. After reflection from this mirror, the beam propagated along the optical axis of the cell reaching 120 mm in diameter at the amplifier output.

Small-signal gain distribution over the laser chamber cross section was measured at four passes through the active medium of the XeF(C-A) amplifier with the help of the Sapphire-488 CW semiconductor laser (488 nm). In addition, the total small-signal gain, G, was measured in the 33 pass amplification scheme. For measuring the power of amplified spontaneous emission (ASE) of the XeF(C-A) amplifier, the output radiation without a seed pulse was focused by concave mirror with a focal length of 22 m on an aperture with diameter 1.1 mm, behind which a filter and calibrated photodiode were located.

Seed pulses of 50 fs duration from the front end were pre-lengthened to 1–2.4 ps in the prism pair with negative group velocity dispersion. After amplification, the down-chirped laser pulses were recompressed in a double pass of a collimated beam with a diameter of 20 cm through three 4-cm-thick fused silica plates at the Brewster angle. Energy losses in the compressor did not exceed 2%. To measure the pulse duration, the central part of the beam (with the help of two fused silica wedges and a spherical mirror with diameter of 90 mm and focal length of 12 m) was assigned to the autocorrelator ASF-20–480 through an aperture with a diameter of 260 μm.

3.2.2.4. Experimental results

The gain characteristics of the active medium (viz. value and spatial distribution of the small-signal gain) depending on the initial composition of the working mixture were examined using 4-passes amplification of the probe laser. The optimal composition of the gas mixture (0.25 Torr XeF_2 and 190 Torr nitrogen) corresponding to the maximum value of the unsaturated total gain ($G = (5–6) \times 10^3$) was found as a result of a compromise between the uniformity of the radial distribution of the small-signal gain and its maximum lying in the peripheral region of the laser cell, where the main part of the beam trajectories is located. It should be noted that the heterogeneity of the small-signal gain distribution over the chamber cross section had almost no effect on the uniformity of the beam intensity, as the diameters of the laser beam and laser cell differ by almost an order of magnitude.

In the test mode, when the maximal pump energy (at $U_0 = 95$ kV) of the VUV radiation was 240 J, the energy of output radiation attained 1 J at amplification of a 1 ps seed pulse with an energy of 1.8 mJ. At the level of 0.7 J output energy, the pulse duration after the bulk fused silica compressor was measured with and without activation of the XeF(C-A) amplifier. In both cases, the pulse width was measured to lie in the range of 50–60 fs (**Figure 10a**). This indicates that a peak power of 14 TW was reached at the output of the laser system [47].

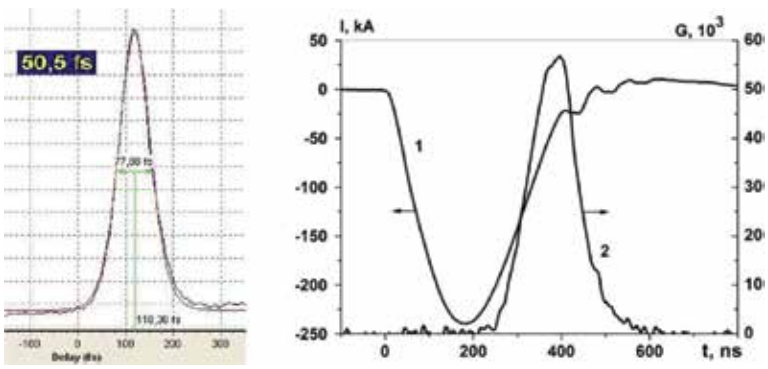

Figure 10. (a) Autocorrelation function of the output pulse with an energy of 0.7 J (in the $Sech^2$ approximation). (b) The time behavior of the diode current (1) and total gain (2). $U_0 = 95$ kV.

The ASE power from the XeF(C-A) amplifier, which was measured in the angle of 0.5 mrad with the seed pulse blocked, turned out to be as low as 0.7 W. At the 14 TW peak power obtained in the above experiments, this ASE power corresponds to the temporal contrast ratio of 2×10^{13}. Since the temporal contrast at the 10^{10} level is now routine to obtain in Ti:sapphire systems, and taking into account the nonlinear frequency doubling required to spectrally match the Ti:sapphire front end to the XeF(C-A) boosting amplifier, the temporal contrast of the hybrid (solid/gas) systems seems to be determined only by the ASE of the XeF(C-A) amplifier and is expected to reach 10^{12}–10^{13} at a peak power of about 100 TW.

For further improvements of the THL-100 operating performances, the XeF(C-A) amplifier pump system has been upgraded [51, 52] to increase the maximum VUV pump energy up to

300 J at $U_0 = 95$ kV. As a result, the total small-signal gain at 33 passes was enhanced up to (5–6) × 10^4. **Figure 10b** shows the temporal behavior of the diode current (1) and total small-signal gain (2) at 33 passes through the active medium. **Figure 11** shows the dependence of the small-signal gain in arbitrary units vs the partial pressures of nitrogen and XeF_2 vapor.

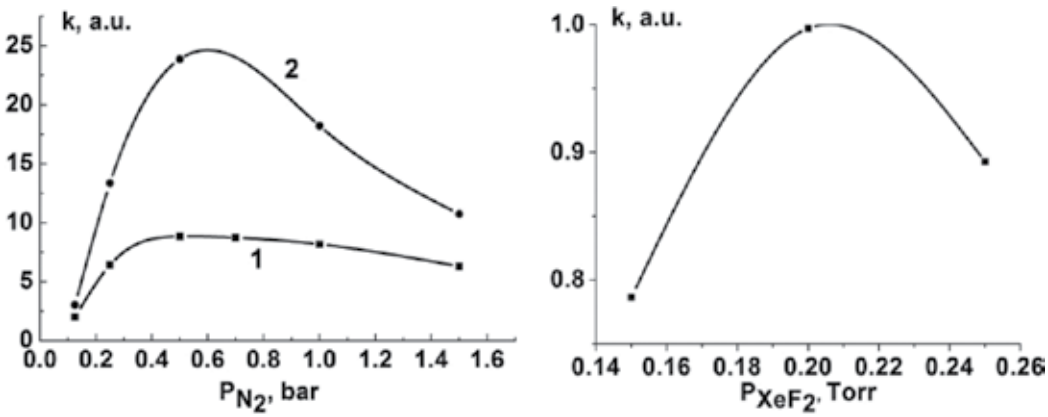

Figure 11. (a) Dependence of the small-signal gain vs the nitrogen pressure, $p(XeF_2) = 0.25$ Torr, 1—$U_0 = 90$ kV, 2—$U_0 = 95$ kV. (b) Dependence of the small-signal gain vs the XeF_2 pressure, $p(N_2) = 0.5$ bar, $U_0 = 90$ kV.

Amplification of a chirped pulse in the XeF(C-A) amplifier was carried out with the use of the laser mixture containing 0.2 Torr XeF_2 and 0.5 bar nitrogen at $U_0 = 95$ kV. An output energy of 2.5 J was reached when a 2.4 ps seed pulse with an energy of about 1 mJ in a super-Gaussian beam was injected into the XeF(C-A) amplifier [51]. An autograph of the output laser beam on a photographic paper sheet is shown in **Figure 12**. The energy obtained in this experiment promises a peak power as high as ~50 TW to be attained in the visible after pulse recompression to the initial duration of 50 fs.

Figure 12. Imprint of the output laser beam with 2.5 J energy.

4. Wavelength scaling of laser-matter interaction

The visible spectrum of the hybrid femtosecond systems based on the XeF(C-A) amplifiers allows for the λ-scaling laser-matter interaction to be studied. Just to illustrate the role of laser-driver wavelength in laser-matter interaction we shall mention briefly some of applications in which the shorter laser wavelength provides advantages due to favorable wavelength scaling with special emphasis placed on the possible realization of a recombination soft X-ray laser operating in the "water window". The examples considered below do not cover all the applications in which the shorter laser wavelength may be favorable as compared with near IR solid-state femtosecond systems. Nevertheless, they show that the extension of laser wavelength to the visible region allows for wider experimental conditions to be realized providing different laser-matter interaction parameters and better understanding of the underlying physics.

4.1. Laser wake-field acceleration

Laser-driven plasma wake-field acceleration (LWFA) capable of producing high-energy electron beams is widely studied both theoretically and experimentally. In plasma-based acceleration, an intense laser beam drives large amplitude plasma waves via the ponderomotive force. The plasma wave can support very high longitudinal electric fields trapping and accelerating electrons. LWFA experiments have demonstrated acceleration gradients >100 GV m^{-1} enabling electrons to be accelerated well beyond GeV energy on a distance of about 1 cm using a 100 TW-class laser [55].

The electron energy gain ΔE is proportional to the acceleration length, L_{acc}, and longitudinal electric field, E_z, averaged over the acceleration length: $\Delta E = eE_zL_{acc}$. Among the factors limiting the effective acceleration length, laser diffraction, electron dephasing, and pump depletion are the most important. In experiments, the limiting role of the first factor is usually mitigated due to relativistic self-guiding or by using a preformed plasma channel. Electron dephasing originates from the difference of electron and plasma-wave propagation velocities. As a result, highly relativistic electrons, accelerated up to a velocity approaching the speed of light, outrun the accelerating phase region of the plasma wave propagating with a phase velocity, v_p, that is close to the laser pulse group velocity v_g and less than the electron velocity. Electrons are accelerated until their phase slips by one-half the plasma-wave period. In the most promising and efficient high-intensity limit corresponding to a nonlinear wake-field acceleration, referred to the blow-out, bubble, or cavitation regime, the radial ponderomotive force expels all the plasma electrons outward to create a electron density structure resembling a spherical ion cavity behind the laser pulse. Coulomb forces pull the electrons back to the axis in about a plasma period at the rear of the cavity to be trapped and accelerated by the wake-field until they reach the cavity center where they diphase. The acceleration length strongly depends on the plasma-wave phase velocity, which is close to the laser pulse group velocity, v_g, obeying the plasma dispersion low: $v_g = d\omega/dk \approx c(1-\omega_p^2/\omega_0^2)^{1/2}$ with ω_0 and ω_p being the laser and plasma frequencies, respectively. Due to the plasma dispersion, shorter wavelength laser pulses propagating with higher group velocity provide longer dephasing length, L_d. Accord-

ing to the estimations made in [51] with pump depletion taken into account, the dephasing length, given by $L_d \approx 4ca_0^{1/2}\,(\omega_0^2/3\omega_p^3)$ with $a_0 = eA/m_ec^2$ being the relativistically normalized laser amplitude, scales as ω_0^2 showing that shorter laser wavelengths are highly beneficial from the viewpoint of an increase in the acceleration length.

The detailed consideration [56] based on the phenomenological 3D theory for LWFA in the blowout regime, valid at laser power, P, exceeding the critical power $P_c = 17(\omega_0^2/\omega_p^2)$ [GW] for relativistic self-focusing, predicts the electron energy gain

$$\Delta E\left[\mathrm{GeV}\right] = 1.7\left(P\left[\mathrm{TW}\right]/100\right)^{1/3}\left(10^{18}/n_p\left[\mathrm{cm}^{-3}\right]\right)^{2/3}(0.8/\lambda_0[\mu\mathrm{m}])^{4/3}$$

where n_p is the plasma density, and λ_0 stands for the laser wavelength. This indicates that the λ-scaling of LWFA could be of great practical interest. Practically, the same λ-scaling has been obtained in Ref. [57]. However, it should be noted that the gain in energy is achieved at the expense of reducing the number of accelerated electrons, which is proportional to the laser wavelength [56, 57].

4.2. High-order harmonic generation

High-order harmonic generation (HHG) is nowadays widely used to generate spatially and temporally coherent short-wavelength radiation when an intense optical field interacts with a gas or solid target. HHG can provide a single burst or train of attosecond pulses, which allow for ultrafast dynamics of electrons in atoms, molecules, or even solids to be explored [58]. (For a detailed review of experimental and theoretical developments in HHG, see, e.g., [58, 59].)

According to the generally accepted semiclassical three-step model of HHG in gases, the highest possible photon energy (cutoff energy, E_{cutoff}) in the high harmonic spectrum that can be generated from a single atom or ion is predicted by the universal law $E_{cutoff} = I_p + 3.17U_p$ [60]. Here, I_p is the ionization potential and $U_p = 9.33 \times 10^{-14}\, I_0\lambda_0^2$ is the ponderomotive energy, which is the cycle-averaged kinetic energy of an electron in the laser electric field of intensity I_0 and wavelength λ_0. The λ_0^2 dependence of U_p implies that the use of long excitation wavelengths should result in extending the harmonic cutoff energy further into the X-ray region. On the other hand, conversion efficiency of HHG in gases strongly depends on laser wavelength. The λ-scaling at constant laser intensity has revealed the dependences of HHG efficiency to be between λ_0^{-5} and λ_0^{-6}, which have been obtained experimentally and from numerical simulations [61–63]. General scaling analysis of HHG efficiency as a function of drive laser parameters and material properties is given in [64], which predicts the scaling of the HHG efficiency with the driving wavelength to be λ_0^{-5} at the cutoff and λ_0^{-6} at the plateau region for fixed harmonic wavelength. The severe wavelength dependence of the HHG efficiency is associated with the single-atom dipole response and phase matching. Shorter driver wavelengths are advantageous for both of these factors, if the final objective is not to produce as high-energetic photons as possible. The experimental results obtained in Ref. [65] for different noble gases confirm

this wavelength scaling and show two orders of magnitude higher HHG intensity in the energy range of 20–70 eV with 400 nm pulses as compared with 800 nm laser driver.

However, HHG in gases has fundamental physical restrictions arising from the limitation on the laser intensity since plasma generation, caused by strong ionization of the gaseous medium at intensities above 10^{16} W/cm^2, results in phase mismatch, thereby suppressing harmonic generation [66]. This limitation is not present in the case of HHG from solid. According to the oscillating plasma mirror model [67], the laser field produces a relativistic oscillation of the overcritical plasma surface with the laser frequency, inducing incident pulse modulation that gives rise to the high-order harmonics in the spectrum of the reflected emission due to a transient Doppler frequency upshift. (For more detailed analysis of the basic generation mechanisms lying behind HHG from solids, see, e.g., [59, 68, 69].)

Using particle-in-cell (PIC) simulation to accurately model the HHG with a plasma target, Teubner and Gibbon [59] have obtained the laser-to-harmonic conversion efficiency, η_H, in the laser intensity range $I_0 = 10^{17}$–10^{19} W/cm^2. Summarized by an empirical relation for high harmonic orders ($N = \lambda_0/\lambda_H >> 1$, where λ_H stands for harmonic wavelength), the results of the numerical simulation take the form [54]:

$$\eta_H \approx 9'10^{-5}(I_0\lambda_0^{\,2} / 10^{18}\,\mathrm{W\ cm^{-2}\mu m^2})^2 \left(N/10\right)^{-\alpha}$$

with α depending on the laser intensity and ranging from $\alpha = 6$ at $I_0 = 10^{17}$ W/cm^2 to $\alpha = 3.5$ at $I_0 = 10^{19}$ W/cm^2 at $\lambda_0 = 1$ μm. On the basis of this empirical scaling, the authors came to the conclusion that shorter wavelength lasers are highly beneficial from the viewpoints both of extending to shorter-wavelength harmonics and harmonic efficiency enhancement. The wavelength scaling of the same form but with $\alpha = 5$ independent of laser intensity was argued with the use of 1D-PIC code in the earlier paper of Gibbon [70]. The analysis made in [59] of a variety of experimental results obtained with different laser wavelengths confirms the prediction of the strong harmonic yield increase with laser frequency. This makes powerful blue-green hybrid systems to be very promising as the drivers for generation of soft X-ray harmonics well within the water-window spectral range.

4.3. Soft X-ray lasers

Development of coherent X-ray sources is motivated by a variety of their applications in science and technology. X-ray lasers offer new capabilities in understanding the nanoscale structure of complex materials, including biological systems, and X-ray matter under extreme conditions. One of the greatest challenges is the high-resolution 3D holographic microscopy of a wide range of biological objects in the living state. For this purpose, coherent ultrafast X-ray sources of high power are required. One of the most important milestones for the high contrast X-ray imaging of living biological structures in a natural aqueous environment is the "water window" lying between the K absorption edges of carbon (4.37 nm) and oxygen (2.33 nm), where carbon is highly opaque, while water is largely transparent. A primary challenge of X-ray exposure is the realization of "diffraction-before-destruction" approach allowing for

diffraction patterns to be obtained on time scales shorter than the onset of radiation damage of samples. This approach has been successfully demonstrated in studies of biological samples with the use of X-ray free electron lasers (XFEL) producing femtosecond pulses of high intensity (For example, see [71]).

There has been remarkable progress in the development of XFELs that hold the great promise for user experiments ranging from atomic physics to biological structure determination. Despite the fact that these lasers are powerful tools in studies of matter structure and physics of light-matter interaction, they have limited accessibility because of their high cost and large-scale. This makes the current search for alternative X-ray sources of laboratory scale to be of great importance.

Presently, there are two main approaches to the development of compact ultrashort-pulsed sources of coherent soft X-ray: above considered HHG by gas and solid targets, as well as the generation of coherent X-ray radiation in the laser plasma. The first one is characterized by low-intensity soft X-ray radiation, insufficient for the realization of holographic imaging methods. The laser plasma enables generation of lasing in the soft X-ray region with beam performances close to those of XFELs [72].

Actually, only collisional and recombination schemes of active media excitation to produce soft X-ray in a laser plasma are of practical interest. The first of them was realized in a laser plasma with high electron temperature, providing a population inversion on transitions between excited states of ions, which typically lie in the range 10–50 nm [72]. The most promising way to extend the spectral range of the X-ray lasers deeper into the X-ray region, including the "water window," lies in the further developing recombination scheme of excitation of transitions to the ground state of recombining fully stripped ions.

The first observation of the amplification on the transition to the ground state dates back to 1983 [73] when hydrogen-like lithium ions were excited in the laser plasma produced due to optical field ionization (OFI) by the UV radiation from a subpicosecond KrF laser. Later that year, this observation was confirmed in different experimental conditions [74–76]. The OFI approach to excitation of recombination soft X-ray lasers is particularly attractive since it produces fully stripped ions on a time scale of one period of the incident laser electric field and enables formation of cold electrons with low residual energy (for a linearly polarized laser pulse) providing favorable conditions for high-rate three-body recombination. Residual energy is proportional to the square of a pump laser wavelength and can be reduced by using a short-wavelength driver pulse.

An electron removed from an atom due to OFI interacts with the plane polarized laser field and acquires quiver energy of the coherent electron oscillation in the field and energy of electron drift along the laser field direction [77, 78]. For ultrashort pulses, the quiver energy is returned to the wave, and it does not contribute to residual energy. Most of the electrons are ionized within a narrow interval near the crest of the oscillating electric field because of the exponential dependence of the ionization rate on the electric field amplitude. Classically, the average drift energy, ε, of an electron depends on the phase mismatch, $\Delta\phi$, between the phase at which the electron is freed and the crest of the electromagnetic wave:

$$\varepsilon = 2\varepsilon_q \sin^2 \Delta\phi$$

where ε_q is the quiver energy ($\varepsilon_q = e^2E_0^2/4m_e\omega^2$ with E_0 and ω being the peak amplitude and angular frequency of the laser electric field $E = E_0 \sin\omega t$, respectively). Thus, the residual energy of electrons produced by OFI can be much lower than the electron quiver energy, and, secondly, shorter wavelength ionizing lasers are beneficial to achieve gain in the recombination scheme.

To demonstrate advantages of short-wavelength pumping, λ-scaling of the recombination excitation efficiency for the transitions to ground state was experimentally and numerically studied by different groups [76, 78, 79]. Numerical simulations of the small-signal gain on the $4s_{1/2}$–$3p_{3/2}$ transition at 23.2 nm in Ar^{7+} show that 400 nm pump laser radiation allows an increase in the small-signal gain on the $4s_{1/2}$–$3p_{3/2}$ transition at 23.2 nm in Ar^{7+} by more than an order of magnitude as compared with 800 nm pumping [80].

Simulation of the recombination gain formation on the 2 → 1 transition at 3.4 nm in H-like CVI pumped with a 400 nm pump laser has been performed in [81]. It was shown that the recombination gain as high as 180 cm^{-1} can be achieved on this transition using the driving pulse duration of 20 fs with peak intensity of 8×10^{18} W/cm^2 and 10 μm diameter focal spot. The key factor playing important role in the recombination mechanism of pumping is the non-Maxwellian nature of the distribution function after OFI [79, 81], which is strongly peaked near the zero electron energy. Ultrashort pumping time (<100 fs) is required to minimize heating and Maxwellization of electron energy distribution at the time scale of three-body recombination.

Less encouraging results have been obtained in Ref. [82], indicating that there are a number of issues, which have to be investigated experimentally for better understanding of the physical processes lying behind the optical production of recombination plasmas. This requires the development of ultrashort (20–50 fs) multiterawatt lasers in the UV or visible range as pumping sources.

5. Conclusions

Development of the photochemical method for exciting active media has resulted in the emerging of the new class of gas lasers in the spectral range extending from the NIR to UV regions. The most remarkable achievements of these studies belong to the visible range where no alternatives are available so far for the excitation of broadband gaseous active media (XeF(C-A), Xe_2Cl, and Kr_2F) that would not be strongly modified by transient absorption. This pave the way for the development of hybrid (solid/gas) laser systems towards petawatt peak power in the blue-green spectral region due to their broad amplification bandwidths, able to support as short as 10 fs pulses, and their relatively high saturation fluences (0.05–0.2 J cm^{-2}), promising as high as 10 TW peak power to be obtained from square cm of an output aperture.

To demonstrate the high potential of the hybrid approach relying on the optically driven broadband active media in the visible, two femtosecond hybrid systems are now under development with the aim of conducting proof-of-principle experiments: THL-30 at LPI, designed for about 5 TW of output peak power, and THL-100 at IHCE, designed to be ten times more powerful. Behind these systems is the amplification of the second harmonic of Ti:sapphire front ends in the power-boosting XeF(C-A) amplifiers driven by the e-beam-to-VUV flash converters. In the pilot experiments performed in the THL-100 system, peak power of 14 TW has been attained in the 50 fs pulse at the output energy of 0.7 J. After upgrading pumping source, an energy output has been enhanced up to 2.5 J in the 2.4 ps pulse before its recompression promising a peak power of 50 TW to be obtained. Besides spectral matching between a solid-state frond-end and gas XeF(C-A) amplifier, the nonlinear frequency upconversion results in efficient temporal cleaning of the ultrashort optical pulse, thereby providing a high contrast ratio for the output blue-green pulses produced by a hybrid laser chain. This was confirmed by the results of ASE measurements in the XeF(C-A) amplifier of the THL-100 system, which argue that a contrast ratio of 10^{12}–10^{13} is feasible in the blue-green hybrid femtosecond systems with a peak power of about 100 TW.

By the example of LWFA, HHG, and recombination soft X-ray lasers, it was shown that, in some cases, application of shorter wavelength lasers (as compared to Ti:sapphire lasers operating in the NIR) for laser-matter interaction may be advantageous and extends the frontiers of experimental ability to provide deeper insight into the physical mechanisms of the laser-matter interaction. One of the greatest challenges is the development of recombination-pumped soft X-ray lasers that have potential to extend SXRL spectral range towards "water window" and beyond.

Actually, the above-discussed blue-green hybrid concept can be considered as an alternative to the direct nonlinear upconversion of intense NIR laser radiation to the visible with the use of second harmonic generation (SHG) technique. However, to the best of our knowledge, the highest peak power reached so far in the visible with SHG does not exceed 4 TW, producing the peak intensity in a focal spot diameter of about 3 μm as low as 3×10^{18} W/cm^2 because of poor beam quality [83]. Achieving higher parameters in Ti:sapphire laser systems with SHG meets serious technical problems arising from a variety of nonlinear effects in crystals at high intensities leading to a significant spatiotemporal degradation of beam quality [84]. Moreover, a broad spectrum of femtosecond pulses and strong nonlinear wave front distortion require application of very thin (0.5–1 mm) nonlinear crystals of large diameter (>10 cm). The technology of such crystals manufacture is not yet available. Nevertheless, a large ongoing effort is presently devoted to overcome these difficulties in SHG and to reach hundreds of TW at wavelength of the second harmonic [85, 86]. The hybrid (solid/gas) laser technology is free of these problems because peak powers of 0.1–1 TW are required for a seed pulse generated by the solid-state front end in order to extract most of the energy stored in the final gaseous amplifier.

At the same time, it is necessary to say that the hybrid systems relying on the photochemically driven boosting amplifiers are inferior to the all-solid-state systems from the view point of a pulse-repetition rate reaching 1 kHz at moderate output peak powers. The hybrid systems

operating in the visible could be of interest for the use in low repetition rate experiments, which require an output peak power of tens and hundreds of TW. In the case of the Xe_2Cl active medium, repetition rates up to 10 Hz seems to be attainable with proper engineering.

Acknowledgements

The work was supported by the Russian Foundation for Basic Research (Grant No. 15-19-10021).

Author details

Leonid D. Mikheev[1,2*] and Valery F. Losev[3,4]

*Address all correspondence to: mikheev@sci.lebedev.ru

1 P.N. Lebedev Physical Institute, Russian Academy of Sciences, Moscow, Russia

2 National Research Nuclear University MEPhI (Moscow Engineering Physics Institute), Moscow, Russia

3 Institute of High Current Electronics, Siberian Branch, Russian Academy of Sciences, Tomsk, Russia

4 National Research Tomsk Polytechnic University, Tomsk, Russia

References

[1] Danson C, Hillier D, Hopps N, Neely D. Petawatt class lasers worldwide. High Power Laser Sci. Eng. 2015;3:e3. doi:10.1017/hpl.2014.52

[2] Bahk S-W, Rousseau P, Planchon TA, Chvykov V, Kalintchenko G, Maksimchuk A, Mourou GA, Yanovsky V. Characterization of focal field formed by a large numerical aperture paraboloidal mirror and generation of ultra-high intensity (10^{22} W/cm^2). Appl. Phys. B. 2005;80:823–832. doi:10.1007/s00340-005-1803-8

[3] Zuev VS, Mikheev LD. Photochemical Lasers. Chur: Harwood Acad. Publ; 1991. 103 p.

[4] Mikheev LD. Photochemical lasers on electronic molecular transitions. Quantum Electron. 2002;32:1122–1132. doi:10.1070/QE2002v032n12ABEH002355

[5] Mikheev LD, Tcheremiskine VI, Uteza OP, Sentis ML. Photochemical gas lasers and hybrid (solid/gas) blue-green femtosecond systems. Progr. Quantum Electron. 2012;36:98–142. doi:10.1016/j.pquantelec.2012.03.004

[6] Basov NG, Zuev VS. Short-Pulse Iodine Laser. Il Nuovo Cimento. 1976;31B:129–151.

[7] Brederlow G, Fill E, Witte KJ. The High-Power Iodine Laser. Berlin Heidelberg: Springer-Verlag GmbH; 1983. 183 p. doi:10.1007/978-3-540-39491-4

[8] Zuev VS, Ka1ulin VA. Scientific foundations of powerful photodissociation lasers (history of research in the 1960s at the Division of Quantum Radiophysics of the P N Lebedev Physics Institute). Quantum Electron. 1997;27:1073–1080. doi:10.1070/QE1997v027n12ABEH001112

[9] Zarubin PV. Academician Basov, high-power lasers and the antimissile defence problem. Quantum Electron. 2002;32:1048–1064. doi:10.1070/QE2002v032n12ABEH002348

[10] Brederlow G, Brodmann R, Eidmann K, Nippus M, Petsch R, Witkowski S, Volk R, Witte KJ. Performance of the Asterix III high power iodine laser. IEEE J. Quantum Electron. 1980;QE 16:122–125. doi:10.1109/JQE.1980.1070441

[11] Kirillov GA, Murugov VM, Punin VT, Shemyakin VI. High-power laser system Iskra-V. Laser Part. Beams. 1990;8:827–831. doi:10.1017/S0263034600009198

[12] Tittel FK, Marowsky G, Wilson WL, Smiling M. Electron beam pumped broad-band diatomic and triatomic excimer lasers. IEEE J. Quantum Electron. 1981;QE 17:2268–2281. doi:10.1109/JQE.1981.1070705

[13] Tang KY, Lorents DC, Huestis DL. Gain measurements on the triatomic excimer Xe_2Cl. Appl. Phys. Lett. 1980;36:347–349. doi:10.1063/1.91498

[14] Mikheev LD. Possibility of amplification of a femtosecond pulse up to the energy 1 kJ. Laser Part. Beams. 1992;10:473–478. doi:10.1017/S0263034600006716

[15] Hofmann T, Sharp T, Dane B, Wisoff P, Wilson W, Tittel F, Szabó G. Characterisation of an ultrahigh peak power XeF(C-A) excimer laser system. IEEE J. Quantum Electron. 1992;QE 28:1366–1375. doi:10.1109/3.135279

[16] Simon J. Ultrashort light pulses. Rev. Sci. Instrum. 1989;60:3597–3624. doi:10.1063/1.1140516

[17] Tellinghuisen P, Tellinghuisen J, Coxon JA, Velazco JE, Setser DW. Spectroscopic studies of diatomic noble gas halides. IV. Vibrational and rotational constants for the X, B, and D states of XeF. J. Chem. Phys. 1978;68:5187–5198. doi:10.1063/1.435583

[18] Bibinov NK, Vinogradov IP, Mikheev LD, Stavrovskii DB. Determination of spectral dependence of the absolute quantum yield of XeF(B,C,D) excimer formation upon photolysis of XeF_2. Sov. J. Quantum Electron. 1981;11:1178–1181. doi:10.1070/QE1981v011n09ABEH008227

[19] Kono M, Shobatake K. Photodissociative excitation processes of XeF_2 in the vacuum ultraviolet region 105–180 nm. J. Chem. Phys. 1995;102:5966–5978. doi:10.1063/1.469331

[20] Mikheev LD, Stavrovskii DB, Zuev VS. Photodissociation XeF laser operating in the visible and UV regions. J. Rus. Las. Res. 1995;16:427–475. doi:10.1007/BF02581226

[21] Brashears HC, Setser DW. Transfer and quenching rate constants for XeF(B) and XeF(C) state in low vibrational levels. J. Chem. Phys. 1982;76:4932–4946. doi:10.1063/1.442839

[22] Basov NG, Zuev VS, Mikheev LD, Stavrovskii DB, Yalovoi VI. Stimulated emission due to the $B(1/2)$–$X^2\Sigma^+$ transition in the XeF molecule formed by photodissociation of XeF_2. Sov. J. Quantum Electron. 1977;7:1401. doi:10.1070/QE1977v007n11ABEH008201

[23] Basov NG, Zuev VS, Kanaev AV, Mikheev LD, Stavrovskii DB. Laser action due to the bound-free C(3/2)–A(3/2) transition in the XeF molecule formed by photodissociation of XeF_2. Sov. J. Quantum Electron. 1979;9:629. doi:10.1070/QE1979v009n05ABEH009058

[24] Zuev VS, Kashnikov GN, Mamaev SB. XeF laser with optical pumping by surface discharges. Quantum Electron. 1992;22:973–979. doi:10.1070/QE1992v022n11ABEH003645

[25] Knecht BA, Fraser RD, Wheeler DJ, Zietkiewich CJ, Mikheev LD, Zuev VS, Eden JG. Compact XeF (C → A) and iodine laser optically pumped by a surface discharge. Opt. Lett. 1995;20:1011–1913. doi:10.1364/OL.20.001011

[26] Knecht BA, Fraser RD, Wheeler DJ, Zietkiewich CJ, Mikheev LD, Zuev VS, Eden JG. Optical pumping of the XeF(C-A) and iodine 1.315-μm lasers by a compact surface discharge system. Opt. Eng. 2003;42:3612–3621. doi:10.1117/1.1751133

[27] Yu L, Liu J, Ma L, Yi A, Huang C, An X, Li H, Chen G. 10 J energy-level optically pumped XeF(C–A) laser with repetition mode. Optics Lett. 2007;32:1087–1089. doi:10.1364/OL.32.001087

[28] Gross RWF, Schneider LE, Amimoto ST. XeF laser pumped by high-power sliding discharges. Appl. Phys. Lett. 1988;53:2365–2367. doi:10.1063/1.100231

[29] Sentis ML, Tcheremiskine VI, Delaporte PC, Mikheev LD, Zuev VS. XeF(C-A) laser pumped by formed-ferrite open discharge radiation. Appl. Phys. Lett. 1997;70:1198–1200. doi:10.1063/1.118529

[30] Anisimov SV, Ermilov YuA, Kashnikov GN, Kazanskii VM, Mikheev LD, Nesterov RO, Stavrowskii DB, Theremiskine VI, Zemskov EM, Zuev VS. Spectrally selective time resolved actinometry of VUV radiation of a moving gas-dynamic discontinuity. Laser Phys. 1994;4:416–418.

[31] Eden JG. XeF(B → X) laser optically excited by incoherent Xe_2^* (172-nm) radiation. Opt. Lett. 1978;3:94–96. doi:10.1364/ol.3.000094

[32] Bischel WK, Nakano HH, Eckstrom DJ, Hill RM, Huestis DL, Lorents DC. A new blue-green laser in XeF. Appl Phys. Lett. 1979;34:565–567. doi:10.1063/1.90868

[33] Eckstrom DJ, Walker HC, Jr. Multijoule performance of the photolytically pumped XeF (C-A) laser. IEEE J. Quantum Electron. 1982;QE 18:176–181. doi:10.1109/JQE.1982.1071517

[34] McCown AW, Eden JG. Ultraviolet photoassociative production of XeCl(*B*,*C*) molecules in Xe/Cl_2 gas mixtures: Radiative lifetime of $Xe_2Cl(4\ ^2\Gamma)$. J. Chem. Phys. 1984;81:2933–2938. doi:10.1063/1.448042

[35] Tittel FK, Wilson WL, Stickel RE, Marowsky G, Ernst WE. A triatomic Xe2Cl excimer laser in the visible. Appl. Phys. Lett. 1980;36:405–407. doi:10.1063/1.91533

[36] Basov NG, Zuev VS, Kanaev AV, Mikheev LD. Stimulated emission from an optically pumped Xe_2Cl laser. Sov. J. Quantum Electron. 1985;15:1289–1290. doi:10.1070/QE1985v015n09ABEH007742

[37] Zuev VS, Kanaev AV, Mikheev LD. Determination of the absolute quantum efficiency of the luminescence of Xe_2Cl^* in Cl_2–Xe mixtures. Sov. J. Quantum Electron. 1987;17:884–885. doi:10.1070/QE1987v017n07ABEH009473

[38] Mikheev LD. Evaluating the prospects of exciting the Xe_2Cl active medium by laser radiation for amplifying femtosecond pulses. Quantum Electron. 2005;35:984–986. doi:10.1070/QE2005v035n11ABEH013027

[39] Quiñones E, Yu YC, Setser DW, Lo G. Decay kinetics of XeCl(*B*,*C*) in Xe and in mixtures of Xe with Kr, Ar, Ne, and He. J. Chem. Phys. 1990;93:333–344. doi:10.1063/1.459605

[40] Okada F, Apkarian VA. Electronic relaxation of Xe_2Cl in gaseous and supercritical fluid xenon. J. Chem. Phys. 1991;94:133–144. doi:10.1063/1.460387

[41] Wiedeman L, Fajardo ME, Apkarian VA. Cooperative photoproduction of $Xe_2^+Cl^-$ in liquid Cl_2/Xe solutions: Stimulated emission and gain measurements. Chem. Phys. Lett. 1987;134:55–59. doi:10.1016/0009-2614(87)80013-1

[42] Zuev VS, Isaev IF, Kanaev AV, Mikheev LD, Stavrovskii DB, Shchepetov NG. Lasing as a result of a *B*–*X* transition in the excimer XeF formed as a result of photodissociation of KrF_2 in mixtures with Xe. Sov. J. Quantum Electron. 1981;11:221–222. doi:10.1070/QE1981v011n02ABEH005884

[43] Zuev VS, Kanaev AV, Mikheev LD, Stavrovskii DB. Investigation of luminescence in the 420 nm range as a result of photolysis of KrF_2 in mixtures with Ar, Kr, and N_2. Sov. J. Quantum Electron. 1981;11:1330–1335. doi:10.1070/QE1981v011n10ABEH008468

[44] Basov NG, Zuev VS, Kanaev AV, Mikheev LD, Stavrovskii DB. Stimulated emission from the triatomic excimer Kr_2F subjected to optical pumping. Sov. J. Quantum Electron. 1980;10:1561–1562. doi:10.1070/QE1980v010n12ABEH010282

[45] Mikheev LD. Use of photoprocesses with charge transfer to excite active laser media. J. Sov. Las. Res. 1990;11:288–304. doi:10.1007/BF01120629

[46] Aristov AI, Grudtsin YaV, Zubarev IG, Ivanov NG, Konyashchenko AV, Krokhin ON, Losev VF, Mavritskii AO, Mamaev SB, Mesyats GA, Mikheev LD, Panchenko YuN, Rastvortseva AA, Ratakhin NA, Sentis M, Starodub AN, Tenyakov SYu, Uteza O, Tcheremiskine VI, Yalovoy VI. Hybrid femtosecond laser system based on photochemical XeF(C-A) amplifier with an aperture of 12 cm. Optica Atmosfery i Okeana J. 2009;22:1024–1029 (in Russian).

[47] Alekseev SV, Aristov AI, Grudtsyn YaV, Ivanov NG, Koval'chuk BM, Losev VF, Mamaev SB, Mesyats GA, Mikheev LD, Panchenko YuN, Polivin AV, Stepanov SG, Ratakhin NA, Yalovoi VI, Yastremskii AG. Visible-range hybrid femtosecond systems based on a XeF(C–A) amplifier: state of the art and prospects. Quantum Electron. 2013;43:190–200. doi:10.1070/QE2013v043n03ABEH015096.

[48] Hofmann T, Sharp TE, Dane CB, Wisoff P, Wilson WL, Jr, Tittel FK, Szabó G. Characterisation of an Ultrahigh Peak Power XeF(C-A) Excimer Laser System. IEEE J. Quantum Electron. 1992;QE 28:1366–1375. doi:10.1109/3.135279

[49] Sharp TE, Hofmann Th, Dane CB, Wilson WL, Tittel FK, Wisoff PJ, Szabó G. Ultrashort-laser-pulse amplification in a XeF(C-A) excimer amplifier. Opt. Lett. 1990;15:1461–1463. doi:10.1364/OL.15.001461

[50] Alekseev SV, Ivanov MV, Ivanov NG, Losev VF, Mesyats GA, Mikheev LD, Panchenko YN, Ratakhin NA. Modernization of THL-100 hybrid femtosecond laser system. Izvestiya Vysshikh Uchebnykh Zavedenii, Seriya Fizika. 2014;57(12/2):101–105 (in Russian).

[51] Alekseev SV, Ivanov MV, Ivanov NG, Losev VF, Mesyats GA, Panchenko YN, Ratakhin NA. Parameters of the THL-100 hybrid femtosecond laser system after modernization. Russ. Phys. J. 2015;58:1087–1092. doi:10.1007/s11182-015-0616-4

[52] Abdullin EN, Ivanov NG, Losev VF, Morozov AV. Production of a large cross-section electron beam in electron diode with rod reverse current conductors. Laser and Particle Beams. 2013;31:697–702. doi:10.1017/S026303461300075X

[53] Alekseev SV, Ivanov NG, Kovalchuk BM, Losev VF, Mesyats GA, Mikheev LD, Panchenko YN, Ratakhin NA., Yastremsky AG. Terawatt laser hybrid THL-100 system based on the photodissociation XeF(C-A) amplifier. Optica Atmosfery i Okeana J. 2012;25:221–225 (in Russian).

[54] Alekseev SV, Aristov AI, Ivanov NG, Kovalchuk BM, Losev VF, Mesyats GA, Mikheev LD, Panchenko YuN, Ratakhin NA. Multi-terawatt femtosecond hybrid system based on a photodissosiation XeF(C-A) amplifier in the visible range. Quantum Electron. 2012;42:377–378. doi:10.1070/QE2012v042n05ABEH014902

[55] Leemans WP, Gonsalves AJ, Mao H-S, Nakamura K, Benedetti C, Schroeder CB, Tóth CS, Daniels J, Mittelberger DE, Bulanov SS, Vay J-L, Geddes CGR, Esarey E. Multi-GeV

Electron beams from capillary-discharge-guided subpetawatt laser pulses in the self-trapping regime. Phys. Rev. Lett. 2014;113:245002. doi:10.1103/PhysRevLett.113.245002

[56] Lu W, Tzoufras M, Joshi C, Tsung FS, Mori WB, Vieira J, Fonseca RA, Silva LO. Generating multi-GeV electron bunches using single stage laser wakefield acceleration in a 3D nonlinear regime. Phys. Rev. ST AB 2007;10:061301. doi:10.1103/PhysRevSTAB.10.061301

[57] Gordienko S, Pukhov A. Scalings for ultra relativistic laser plasmas and quasimonoenergetic electrons. Phys. Plasmas 2005;12:043109. doi:10.1063/1.1884126

[58] Eden JG. High-order harmonic generation and other intense optical field–matter interactions: review of recent experimental and theoretical advances. Prog. Quantum Electron. 2004;28:197–246. doi:10.1016/j.pquantelec.2004.06.002

[59] Teubner U, Gibbon P. High-order harmonics from laser-irradiated plasma surfaces. Rev. Mod. Phys. 2009;81:445–479. doi:10.1103/RevModPhys.81.445

[60] Krause JL, Schafer KJ, Kulander KC. High-order harmonic generation from atoms and ions in the high intensity regime. Phys. Rev. Lett. 1992;68:3535–3538. doi:10.1103/PhysRevLett.68.3535

[61] Yakovlev VS, Ivanov M, Krausz F. Enhanced phase-matching for generation of soft X-ray harmonics and attosecond pulses in atomic gases. Opt. Express 2007;15:15351–15364. doi:10.1364/OE.15.015351

[62] Tate J, Auguste T, Muller HG, Salières P, Agostini P, DiMauro LF. Scaling of wave-packet dynamics in an intense midinfrared field. Phys. Rev. Lett. 2007;98:013901. doi:10.1103/PhysRevLett.98.013901

[63] Colosimo P, Doumy G, Blaga CI, Wheeler J, Hauri C, Catoire F, Tate J, Chirla R, March AM, Paulus GG, Muller HG, Agostini P, DiMauro LF. Scaling strong-field interactions towards the classical limit. Nat. Phys. 2008;4:386–389. doi:10.1038/nphys914

[64] Falcão-Filho EL, Gkortsas VM, Gordon A, Kärtner FX. Analytic scaling analysis of high harmonic generation conversion efficiency. Opt. Express 2009;17:11217–11229. doi:10.1364/OE.17.011217

[65] Falcão-Filho EL, Lai C-J, Gkortsas V-M, Huang S-W, Chen L-J, Hong K-H, Kärtner FX. Scaling of high harmonic generation efficiencies with 400-nm and 800-nm driver pulses. In: Proceedings of Conference on Lasers and Electro-Optics and Quantum Electronics and Laser Science Conference (CLEO/QELS-2010); 16–21 May 2010; San Jose, California United States: IEEE; paper JThI4. doi:10.1364/CLEO.2010.JThI4

[66] Chen M-C, Arpin P, Popmintchev T, Gerrity M, Zhang B, Seaberg M, Popmintchev D, Murnane MM, Kapteyn HC. Bright, coherent, ultrafast soft X-ray harmonics spanning the water window from a tabletop light source. Phys. Rev. Lett. 2010;105:173901. doi:10.1103/PHYSREVLETT.105.173901

[67] Lichters R, Meyer-ter-Vehn J, Pukhov A. Short-pulse laser harmonics from oscillating plasma surfaces driven at relativistic intensity. Phys. Plasmas 1996;3:3425–3437. doi: 10.1063/1.871619

[68] Thaury C, Quéré F. High-order harmonic and attosecond pulse generation on plasma mirrors: basic mechanisms. J. Phys. B: At. Mol. Opt. Phys. 2010;43:213001. doi: 4075/43/21/213001

[69] Baeva T, Gordienko S, Pukhov A. Theory of high-order harmonic generation in relativistic laser interaction with overdense plasma. Phys. Rev. E. 2006;74:046404. doi: 10.1103/PhysRevE.74.046404

[70] Gibbon P. Harmonic generation by femtosecond laser-solid interaction: a coherent "Water-Window" light source?. Phys. Rev. Lett. 1996;76:50–53. 10.1103/PhysRevLett. 76.50

[71] Redecke L, et al. Natively inhibited *Trypanosoma brucei* cathepsin B structure determined by using an X-ray laser. Science. 2013;339:227–230. doi:10.1126/science.1229663

[72] Suckewer S, Jaeglé P. X-ray laser: past, present, and future. Laser Phys. Lett. 2009;6:411–436. doi:10.1002/lapl.200910023

[73] Nagata Y, Midorikawa K, Kubodera S, Obara M, Tashiro H, Toyoda K. Soft-x-ray amplification of the Lyman-alpha transition by optical-field-induced ionization. Phys. Rev. Lett. 1993;71:3774–3777. doi:10.1103/PhysRevLett.71.3774

[74] Nagata Y, Midorikawa K, Kubodera S, Obara M, Tashiro H, Toyoda K, Kato Y. Production of an extremely cold plasma by optical-field-induced ionization. Phys. Rev. A. 1995;51:1415–1419. doi:10.1103/PhysRevA.51.1415

[75] Korobkin DV, Nam CH, Suckewer S, Goltsov A. Demonstration of soft X-ray lasing to ground state in Li III. Phys. Rev. Lett. 1996;77:5206–5209. doi:10.1103/PhysRevLett. 77.5206

[76] Goltsov A, Morozov A, Suckewer S, Elton R, Feldman U, Krushelnick K, Jones T, Moore C, Seely J, Sprangle P, Ting A, Zigler A. Is efficiency of gain generation in LiIII 13.5-nm laser with 0.25-μm subpicosecond pulses the same as with 1 μm?. IEEE J. Sel. Top. Quantum Electron. 1999;5:14531459. doi:10.1109/2944.814984

[77] Corkum PB, Burnett NH, Brunel F. Above-Threshold Ionization in the Long-Wavelength Limit. Phys. Rev. Lett. 1989;62:1259–1262. doi:10.1103/PhysRevLett.62.1259

[78] Penetrante BM, Bardsley JN. Residual energy in plasmas produced by intense subpicosecond lasers. Phys. Rev. A 1991;43:3100–3113. doi:10.1103/PhysRevA.43.3100

[79] Ditmire T. Simulations of heating and electron energy distributions in optical field ionized plasmas. Phys. Rev. E. 1996;54:6735–6740. doi:10.1103/PhysRevE.54.6735

[80] Spence DJ, Hooker SM. Simulations of recombination lasing in Ar^{7+} driven by optical field ionization in a capillary discharge waveguide. Opt. Commun. 2005;249:501–513. doi:10.1016/j.optcom.2005.01.031

[81] Avitzour Y, Suckewer S. Feasibility of achieving gain in transition to the ground state of C VI at 3.4 nm. J. Opt. Soc. Am. B 2007;24:819–828. doi:10.1364/JOSAB.24.000819

[82] Pert GJ. Scaling relations for the design of a recombination laser using tunneling ionization. J. Phys. B: At. Mol. Opt. Phys. 2009;42:225401. doi:10.1088/0953-4075/42/22/225401

[83] Toth R, Kieffer JC, Fourmaux S, Ozaki T, Krol A. In-line phase-contrast imaging with a laser-based hard x-ray source. Rev. Sci. Instrum. 2005;76:083701. doi: 10.1063/1.1989407

[84] Begishev IA, Kalashnikov M, Karpov V, Nickles P, Schönnagel H. Limitation of second-harmonic generation of femtosecond Ti:sapphire laser pulses. J. Opt. Soc. Am. B. 2004;21:318–322. doi:10.1364/JOSAB.21.000318

[85] Mironov S, Lozhkarev V, Ginzburg V, Khazanov E. High-efficiency second-harmonic generation of superintense ultrashort laser pulses. Appl. Opt. 2009;48:2051–2057. doi: 10.1364/AO.48.002051

[86] Ginzburg VN, Lozhkarev VV, Mironov SYu, Potemkin AK, Khazanov EA. Influence of small-scale self-focusing on second harmonic generation in an intense laser field. Quantum Electron. 2010;40:503–508. doi:10.1070/QE2010v040n06ABEH014126

Chapter 7

Nuclear-Induced Plasmas of Gas Mixtures and Nuclear-Pumped Lasers

Mendykhan U. Khasenov

Additional information is available at the end of the chapter

http://dx.doi.org/10.5772/63823

Abstract

We briefly describe the basic processes of formation and relaxation of nuclear-induced plasmas of gas mixtures, especially the processes of inverse population creation in nuclear-pumped lasers (NPL). A review of the work to create and research nuclear-pumped lasers is in progress: on transitions of atoms and atomic ions and on molecular transitions. An increased focus is on the gas media, which we also study on WWR-K nuclear reactor and DC-60 ion accelerator. The studies on emission of heteronuclear ionic molecules of inert gases are also reviewed.

Keywords: laser, ionizing pumping, mechanism of population, recombination, direct excitation

1. Introduction

Direct conversion of nuclear energy into light energy is of great interest as it provides for application of compact and energy-intensive nuclear energy sources to create high-power generators of coherent and incoherent optical radiation. Nuclear energy pumping into active laser medium was first proposed with the appearance of first lasers [1, 2]. At present, the research on nuclear-pumped lasers (NPL) has progressed to the stage where design and engineering developments of continuous and pulse nuclear laser equipment for various purposes have become possible, that is integrated units based on nuclear engineering and physics, quantum electronics, physics of low-temperature plasma, optics, gas dynamics, and other areas of science and technology [3].

Nuclear-pumped lasers have potential in a wide range of applications, especially in cases requiring high-power and compact lasers to be placed on autonomous remote facilities. The most promising areas of nuclear-pumped laser application are as follows: laser thermonuclear fusion, long-distance transmission of radiant energy and information, rocket laser engine, laser isotope separation and photochemistry, stratospheric ozone layer recovery, and space junk removal. Considerable interest in this area research is also associated with significant difference between the mechanisms of level population during nuclear pumping and population processes in conventional gas-discharge lasers. Application of nuclear energy for active laser medium pumping can be considered not as the way to create high-power laser, but as the way to obtain energy from nuclear reactor. This necessitates consideration of fundamentally new equipment—a reactor laser designed to spatially combine nuclear laser active medium and nuclear reactor core. This approach opens up opportunity to generate qualitatively new energy.

Attempts to achieve laser action during pumping of condensed media with nuclear radiation did not yield positive results. The main obstacle on the road of creating condensed media NPLs is their radiation damage: radiation defects of crystal lattice in solid-state laser, radiolysis, and gas bulb generation on the tracks of nuclear particles in liquid lasers. Presently known gas NPLs [3] radiate in spectral range 391–5600 nm in about 50 atomic transitions of Xe, Ar, Kr, Ne, C, N, Cl, O, I, Hg; Cd^+, Zn^+, Hg^+ ions, CO molecules, and N_2^+ molecular ion.

2. Methods and sources of gas excitation by nuclear reaction products

NPLs include active media that are excited directly using nuclear radiation, or with the use of intermediate nuclear-optical converters. There are three basic sources of nuclear radiation, which can be used to pump NPLs or convert nuclear energy into light energy on transitions of atoms and molecules:

1. nuclear explosions,
2. radioactive isotopes,
3. neutron radiation of nuclear reactors.

Using the γ-ray radiation from nuclear explosion as the pump source was apparently done for the first time in VNIIEF (All-Union Scientific Research Institute of Experimental Physics) in 1971 [3]. Xenon emitted as Xe_2* excimer molecules was used as an active media. Experiments on xenon excimer laser pumping (λ ~ 170 nm) were done in a testing area in Nevada in 1973 [4]. Experiments to develop NPLs using nuclear explosive devices were carried out up until 1987 when underground test ban was introduced.

Optical radiation of gases excited by radioactive nucleus decay products (^{210}Po, ^{238}Pu, ^{239}Pu, ^{241}Am, etc.) was studied before to create gas scintillators [5, 6]. Radioactive isotopes usage for laser pumping [7] or pre-ionization in electric discharge lasers [8, 9] is limited by lower power density deposited in gas (up to 0.6 W/cm^3). The main volume of works on NPL active media

search and study of their parameters was performed on stationary and pulsed nuclear reactors. Nuclear reactors are the source of neutron and γ-radiation. Neutrons were used to pump lasers, as in this case the energy input to laser medium is several times higher than due to γ-radiation. Direct pumping of active media is usually carried out not by neutron radiation but by nuclear reaction products with thermal neutrons (**Table 1**).

Reaction (energy of reaction, MeV)	Natural composition of isotopes	Kinetic energy of reaction products, MeV	Cross-section of reaction for thermal neutrons, barns
^{3}He(n,p)T, (0,76)	^{4}He(100%)+^{3}He(1,4°10^{-4}%)	p—0,57; T—0,19	5400
^{10}B(n,α)^{7}Li, (2,35)	^{11}B (80,1)% +^{10}B (19,9%)	^{4}He—1,5; ^{7}Li—0,85	3837
^{6}Li(n,T)^{4}He (4,7)	^{6}Li (7,5%)+^{7}Li (92,5%)	T—2,7; ^{4}He—2,0	945
^{235}U(n,ff)FF (167)	^{238}U(99,28%)+^{235}U(0,72%)	Fragments: light—99; heavy—68	582

Table 1. Nuclear reactions [10] for NPL pumping.

When nuclear reactors are used as neutron sources, two basic types of laser-medium excitation are utilized:

1. a gaseous isotope or compound thereof (^{3}He, $^{235}UF_6$, $^{10}BF_3$) is a component part of the laser medium,
2. internal surface of the gas-filled laser cell is coated with a thin layer of isotope (^{10}B, ^{6}Li, ^{235}U) or compound thereof ($^{235}UO_2$, $^{235}U_3O_8$).

In the case of volumetric source of pumping using ^{3}He, the non-uniformity of pumping comes from the absorption of slow neutrons in ^{3}He and from the reduction of energy contribution in area near the wall, owing to removal of reaction products to the walls of the cell, in case of $^{235}UF_6$—fission fragments energy loss on the walls of the cell. Results of computation of the total energy deposition and spatial distribution of the deposited energy depending on ^{3}He pressure and diameter of cylindrical cell are given in [11, 12], while [13] shows the results of computation for $^{235}UF_6$-He at different pressure of mixture and content. In Ref. [14], authors show summary of results of experimental and theoretical studies dedicated to definition of energy contribution in NPL cells. Three experimental methods were considered: pressure shock method, interferometric method, and string calorimeter method. The cell size and path length of nuclear reaction products in the gas mixture determines spatial non-uniformity at surface pumping source use. Various calculation models for spatial distribution of energy deposition, influence of non-uniformity of uranium-containing layers, and analysis of experimental data on determination of uranium fission fragments energy loss in gas medium are given in [3].

Due to high ^{3}He and ^{10}B neutron-absorption cross-section, loading laser devices using ^{3}He or ^{10}B on the walls can significantly affect reactivity charge of nuclear reactor and even lead it to subcritical state. A laser cell containing ^{235}U also serves as a fuel element of reactor. This has

triggered an idea of laser reactor, which must spatially combine active laser medium and nuclear reactor core [2, 15]. Initially considered option included uranium-235 hexafluoride serving as uranium-containing medium, the only uranium compound existing in gas phase at moderate temperatures. However, the use of $^{235}UF_6$ complicated due to the chemical aggressiveness of uranium hexafluoride and products of radiolysis. Laser radiation absorption by UF_6 molecules, high speed of quenching of excited atoms and molecules in collisions with UF_6, electron attachment to molecules of UF_6 also prevents the use of uranium hexafluoride as a component of the laser mixture [16]. At present, the most realistic designs are heterogeneous reactor lasers using thin-film uranium fuel [17, 18]. The core of this reactor laser is a specific quantity of laser cells with uranium layers appropriately placed in a neutron moderator matrix. With appropriate selection of components, the conditions for the reactor-laser operation are provided without utilizing additional fuel (uranium). The number of laser cells may vary from a few 100 to 1000, the total weight of uranium from 5 to 70 kg, and characteristic linear dimensions are 2–5 m [3, 18].

Studies in recent years were set out to explore opportunity to load uranium in active laser mixture in the form of fine dust with a particle size of 100–500 nm substantially lower than the path length of fragments [19]. In this case, it is possible to minimize energy loss in the fuel and substantially improve the efficiency and uniformity of pumping. It is necessary to ensure the transparency of such a mixture at the lasing wavelength. Theoretically, it is possible by arranging the dust particles in the form of periodic structure with a mutual distance comparable to laser wavelength, that is, in the form of dust crystals.

2.1. Basic processes of formation and relaxation of nuclear-induced plasmas of gas mixtures

Currently, direct nuclear pumping is implemented in gas media in which the populating of lasing levels occurs in a low-temperature plasma formed by ionizing radiation, in nuclear-induced plasmas. This section describes the basic processes of formation and relaxation of such plasma, in relation to active media of lasers with nuclear pumping and conversion of nuclear energy into the energy of spontaneous gas emission. The most complete information about the processes in plasma of active media of gas lasers with nuclear pumping is contained in monographs [3, 20].

Initial stage of ionization processes in gas media. Gas medium ionization occurs by various types of radiation: uranium fission fragments and transuranium elements, fast electrons, protons and tritons, lithium nuclei, α-particles, γ-quanta. Ionization in γ-radiation of gas is induced by fast electrons produced in the process of Compton scattering, photoeffect, and effect of electron-positron pair formation. In the initial stage of ionization process, primary ionization during the immediate interaction of charged particles and secondary ionization in interaction of media atoms with electrons formed as a result of primary ionization.

The process of ionization of an atom may be viewed as a binary collision of oncoming charged particle and one of the electrons of the atom's shell [21]. Due to the large difference in masses of heavy charged particles and the electron, only a comparatively small percentage of fragment energy can be transferred to the orbital electron. The spectrum of electrons produced by ionization of heavy particles is softer compared with the spectrum produced by ionization of

http://dx.doi.org/10.5772/63823

gas by fast electrons [22, 23]. The average energy of electrons formed in neon as a result of ionization by fission fragments is 40 eV and fast electrons 150 eV [22]. In the case of fission fragments, the secondary electron may provide additional one or two acts of ionization on average, while in the case of fast electrons, it is from 5 to 10 [23].

However, differences in the effects on gas media by different types of ionizing particles are not substantial, because the ultimate result is a combined effect of primary and secondary ionization. It follows from calculations in that the electron energy distribution and energy formation of electron-ion pair in the gas does not depend on the type of charged particles [24, 25]. The same conclusion can be drawn from the luminescent properties of plasma and gas NPLs output parameters, which do not depend on the type of charged particles, but depend on the power and duration of pumping [18].

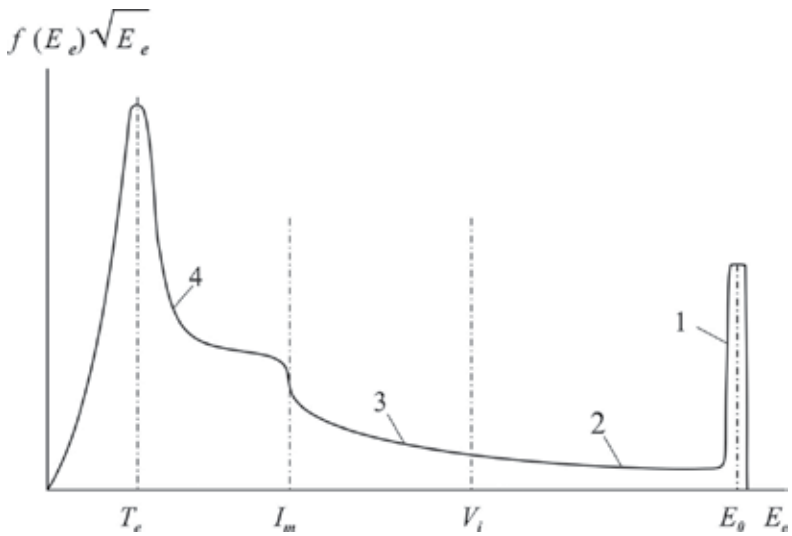

Figure 1. Electron energy distribution in the ionized gas. 1—primary electrons of source; 2—electrons of ionization cascade; 3—electrons in the inelastic excitation region; 4—thermal and subthreshold electrons.

Usually, the calculation and analysis of parameters of nuclear-induced plasmas, development of laser action and NPLs radiation, ionization of gas medium are assumed to be homogeneous. One of the features of nuclear-induced plasma is associated with the formation of tracks when passing through dense gas of heavy charged particles [26, 27]. Depending on parameters of gas media, transverse dimensions of the tracks are 1–10 μm, and the track lifetime or the time to establish uniform ionization through diffusion is 0.1–1 μs [28]. Nonuniformity of ionization associated with track structure of plasma will be most noticeable in the following cases:

- at ionization by fission fragments and other heavy ions,
- in dense gases with high atomic weight,
- at a very low degree of ionization, when there is no overlapping of tracks.

Fluctuations of plasma component concentrations induced by the track structure may have some effect on NPL characteristics excited by fission fragments, if population of upper levels is due to the fast charge process, for example, in laser on a mixture of He-Cd [28]. The influence of plasma track structure on recombination processes will be insignificant, as the track lifetime is much less than the characteristic time of recombination processes [29, 30]. Tracks' overlapping occurs at high pumping power densities; therefore, the track structure of plasma disappears. Estimates show that the overlap of tracks in atmospheric pressure helium occurs at excitation power densities ~2 W/cm^3 [29].

Ionization of gas at the initial stage is carried out directly by charged particles and secondary electrons. A picture of the electron energy distribution in the gas is shown in **Figure 1**, where f_e is the energy distribution function of the electrons, and E_e is the electron energy.

The entire electron energy range can be divided into three regions [24]:

1. The region of ionization cascade $V_i < E_e < E_0$ (E_0 is the particle initial energy, V_i is the ionization potential of the gas atoms and molecules), in which the electrons energy is sufficient for ionization of gas particles.

2. In elastic excitation region $I_m < E_e < V_i$ (I_m is the minimal threshold of electron or vibrational excitations), in which the energy of the electrons is reduced, primarily due to excitation of electron and vibrational states of the gas particles.

3. In the subthreshold region ($E_e < I_m$), electrons lose energy in small "portions" due to elastic collisions with gas particles, thus creating electron thermalization. In subthreshold region, the electrons are involved in the processes that are important in population kinetics and NPL levels' deactivation. These processes include the following: the electron-ion recombination, quenching of excited states, processes of attachment to electronegative gas, excitation, and ionization in collisions with gas particles in excited states.

At $E_e > I_m$, the function of electron energy distribution differs greatly from Maxwell distribution. Electrons in this region do not participate in recombination processes and this region supplies electrons in the subthreshold region. The electrons of inelastic region excitation and ionization cascade possibly play a major role in population of 3p levels of neon [30, 31].

2.2. Kinetics of plasma processes at nuclear pumping of gas mixtures

In quantum system, the gain (absorption) factor of the medium is described by [32]:

$$\alpha = \sigma(N_2 - N_1 \frac{g_2}{g_1}) \tag{1}$$

where indexes (1, 2) refer to upper level 2 and lower 1, N—level population, g—statistical weight of levels. The cross section of stimulated transition:

http://dx.doi.org/10.5772/63823

$$\sigma = \frac{\lambda^2}{2\pi}\frac{A}{\Delta\omega} \tag{2}$$

where λ—transition wavelength, $\Delta\omega$—line width, A—transition probability. The amplifying medium ($\alpha > 0$) requires maintaining population inversion: Population of the upper level must exceed population of the lower level (adjusted to degeneracy multiplicity). Formation of population inversion requires selectivity of population of the upper or lower level. The inversion can be provided not only by the predominant population of upper laser level, but also through selective cleaning of the lower level.

The active media of gas NPLs are often the double mixtures A-B (A—a buffer gas with a high ionization and excitation potential, B—a gas with a lower ionization potential, and lasing occurs in its transitions) or triple A-B-C. In triple mixtures, the third C gas usually plays the role of deactivator of lower level and is not involved in upper level population, but can quench it to some extent. Therefore, we consider the kinetics of processes in plasma in the example a two-component mixture.

The first stage includes ionization and excitation of the buffer gas atoms A (formation of A^+ ions and excited atoms A*), in some cases, direct excitation of active gas B [31, 33]. The main channels of energy transfer from A^+ and A* to particles B are as follows:

1. Charge exchange processes

$$A^+ + B \rightarrow (B^+)^* + A \tag{3}$$

$$A_2^+ + B \rightarrow (B^+)^* + 2A \tag{4}$$

2. Penning process (if A* energy is higher than B ionization potential)

$$A^* + B \rightarrow (B^+)^* + A + e \tag{5}$$

3. Excitation transfer

$$A^* + B \rightarrow B^* + A \tag{6}$$

The main type of ions in high-pressure plasma is molecular ions A_2^+, B_2^+, $(AB)^+$ which are formed in triple processes:

$$A^+ + A + M \rightarrow A_2^+ + M \tag{7}$$

$$B^+ + B + M \rightarrow B_2^+ + M \tag{8}$$

$$A^+ + B + M \rightarrow (AB)^+ + M \tag{9}$$

where M—third particle (A or B). Plasma neutralization occurs as a result of recombination processes, which, depending on specific conditions, may prevail or have dissociative recombination.

$$A_2^+ + e \rightarrow A^* + A \tag{10}$$

$$B_2^+ + e \rightarrow B^* + B \tag{11}$$

$$(AB)^+ + e \rightarrow B^* + A \tag{12}$$

triple or shock-radiative recombination

$$A^+(B^+) + 2e \rightarrow A^*(B^*) + e \tag{13}$$

$$A^+(B^+) + e + M \rightarrow A^*(B^*) + M \tag{14}$$

Population of laser levels occurs during processes (3–5) for B^+ atomic ions, (6, 11–14) for B neutral particles, as well as in cascade transitions from B** high levels. It was previously considered [34, 35] that the processes of dissociative recombination of molecular ions are predominantly populated by p-states of atoms, but in recent years this conclusion was questioned [3].

In [36] based on radioluminescence intensity dependence from mercury vapor pressure (10^{-3}–10^{-7} Torr) in ^{3}He-Hg mixture was made a conclusion that in the process of Hg^+ three-body recombination mostly populated d-states of mercury atoms. Thus, D-levels may also be populated in the processes of dissociative recombination of molecular ions (at a higher density of mercury atoms).

In low-pressure gas discharge laser, the lower laser level is usually deactivated in optical transitions to lower levels, and in lasers with nuclear pumping of atmospheric pressure, the deactivation occurs in collisions with media atoms or plasma electrons, and in Penning reaction with the particles of additional gas. In excimer lasers, where at photon emission the excimer molecule passes in the lower dissociated or weakly coupled state, the lower level deactivation is feasible.

Characteristics of laser radiation at pumping by hard ionizer depend on the power and duration of energy input into active medium, but do not depend on the type of ionizer [18]. This means that kinetics of processes in active media of lasers excited by an electron or ion beam and for nuclear-pumped lasers will be identical [37, 38]. Calculation of plasma param-

eters and laser characteristics implies for kinetic models, representing the balance of rates of formation and decay of individual components in plasma. Kinetic equations are supplemented by the equations of electron energy balance. In some kinetic models, the number of plasma chemical reactions reaches several hundred (see, for example, [29, 39]). Typically, the relevant description of plasma and laser parameters' calculation suffices it to include 10–15 basic reactions. In this regard, it is sometimes advisable to use the so-called small models for calculation, which includes only the basic plasma processes, examples of such models [40, 41]. It should be noted that in many cases the basic level population process is either not defined (e.g., lasers with Xe, Kr, Ar IR transitions), or under discussion (e.g., laser on the 3p–3s transitions of neon [30, 31]). In other cases, relevant calculation is hindered by a large uncertainty in the values of (or even the order of magnitude) processes rate constants [42], the uncertainty in coefficient of light absorption by active medium particles [43].

2.3. Design and development of experimental methods for nuclear-induced plasma research

Pulsed nuclear reactors were used as a source of neutron radiation for NPLs research [3, 27, 44–47]: in Russia—VIR-1, VIR-2, TIBR-1M, BR-1, BIGR (VNIIEF), EBR-L (VNIITF, All-Russian Scientific Research Institute of Technical Physics), BARS-6 (FEI, Institute of Physics and Power Engineering), IIN-3 (Kurchatov Institute of Atomic Energy); in USA—TRIGA Mark-II (University of Illinois), SPR-III (Sandia Labs), APRF (NASA), Godiva-IV (Los Alamos National Laboratory). Relatively recent reports were issued about experimental NPL investigations in China on the CFBR-II [48]. First, NPL works in China were carried out on a stationary INPC nuclear reactor [49].

Thermal neutron flux density at stationary nuclear reactor reaches 10^{13} to 10^{14} n/cm^{2}s, and gas mixtures' pumping power does not exceed a few W/cm^3. Therefore, research on stationary reactors (IRT-2000 in Moscow Engineering Physics Institute (MEPhI), our works on WWR-K reactor) was mainly associated with the study of the spectral characteristics of plasma [50, 51], as well as the development of lasers with non-self-maintained discharge (WWR-K reactor) [52].

WWR-K reactor (**Figure 2**) is a heterogeneous unit of water-cooled type, operating on thermal neutrons. Desalinated water serves as moderator, reflector, and coolant. Uranium is used as reactor fuel enriched by uranium-235 isotope to 36%. WWR-K reactor is a powerful source of neutrons and gamma rays. The maximum thermal neutron flux in the central channel of the reactor reaches $2°10^{14}$ n/cm^{2}s. The reactor core is placed in an aluminum tank filled with water and is designed as hexagonal lattice containing fuel elements, control and protection system channels and experimental channels. The water temperature is kept constant and does not exceed 40°C. The core has a shape similar to cylindrical, with diameter of 645 mm and height of 600 mm. Central vertical experimental channels with diameter of 96 mm, which was used for nuclear-pumped laser works, pass through the core center. Biological protection of staff from the reactor radiation in horizontal plane is provided by layers of water of 850 mm wide, cast iron—210 mm and limonite concrete—2250 mm. Biological protection in vertical direction is formed of 3700 mm of water layer and removable cast iron lids of 800 mm wide.

Figure 2. General view of WWR-K reactor.

The upper part of reactor tank includes rotating cast-iron lid, through which experimental channels are loaded. The left side includes the base made of plates on which vacuum pumps for pumping mixtures from laser devices under the reactor lid were placed.

Three designs of reactor core laser systems [53] were developed and tested on WWR-K reactor. One design was intended for testing mixtures of xenon laser pumped by uranium fission fragments, the second for lasers on inert gas mixtures excited by the products of $^{3}He(n,p)^{3}H$ reactions and the third to run the laser on transitions of mercury triplets [54]. **Figure 3** shows the design intended for lasers on mixtures of inert gases excited by the products of $^{3}He(n,p)T$ reactions. The laser cell is designed as electropolished pipe of 36 mm in diameter with flanges for mirrors on the edges. The distance between the mirrors is 2.1 m, and the mirrors are on a quartz substrate with a dielectric multilayer coating. Mirrors are distanced for 0.5 m (non-transmitting) and 1.0 m (half-transmitting) from the reactor core. Laser channels cutting after a 6-month settling showed that KU-1 quartz substrate has sufficiently high radiation resistance. De-gassing and gas puffing were also conducted through waveguide pipe Ø36 mm. The laser light from this tube was extracted through the window of LiF or CaF_2 and analyzed by registration system. IR radiation was simultaneously recorded by calorimeter located above the exit window and reflected on the LiF plate portion through the matrix of five PD-7G photodiodes. Radiation within the visible range was recorded by photodiodes matrix and the system for measuring the luminescence spectra based on the SPM-2 monochromator and FEU-106 photomultiplier operating in photon counting mode.

http://dx.doi.org/10.5772/63823

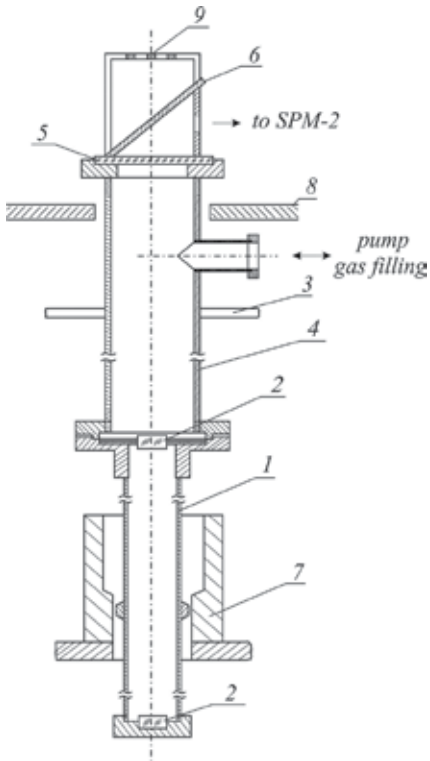

Figure 3. Scheme of laser cell of inert gases excited by ^{3}He(n,p)T reaction products. 1—laser pipe, 2—mirrors, 3—aluminum lid of reactor, 4—waveguide pipe, 5—window, 6—LiF plate, 7—propellant, 8—cast iron lid of reactor, 9—photodiodes matrix.

Although we were not able to create a continuous laser with a direct nuclear pumping, the use of continuous ionizing radiation sources: stationary nuclear reactors and radioactive sources provide for detailed study of plasma properties of gas mixtures, and stationary state of pumping simplifies the analysis of processes kinetics in plasma [53].

Currently, the research is being conducted on DC-60 heavy ion accelerator [55]. The main parameters of the accelerated ion beam: ion type—from lithium to xenon, and ion energy—from 0.5 to 1.75 MeV/nucleon. The intensity of ion beam is from 10^{12} to 10^{14} particles/s depending on type and energy of ions. Ion impulse duration is several nanoseconds and repetition rate of ions is 1.84–4.22 MHz. Mainly, the ions of argon were used as a source of ionization and excitation. The accelerated ion beam passes from evacuated transportation channel through 3-mm hole in the flange to irradiation chamber (**Figure 4**). The hole in the flange is closed by membrane of 2-μm titanium foil or 2.5-μm-thick havar foil. The gas pressure in the cell is measured by capacitance diaphragm gauge mounted at the top of the chamber. The ions passed through the foil ionize and excite the gas mixture in irradiation chamber (**Figure 5**). Argon ion energy after separation foil is about 50 MeV. The emerging light radiation passes through quartz window and condenser and focused on optical fiber. The beam falls on

a compact spectrometer through the fiber, and the recorded spectrum is displayed on a computer.

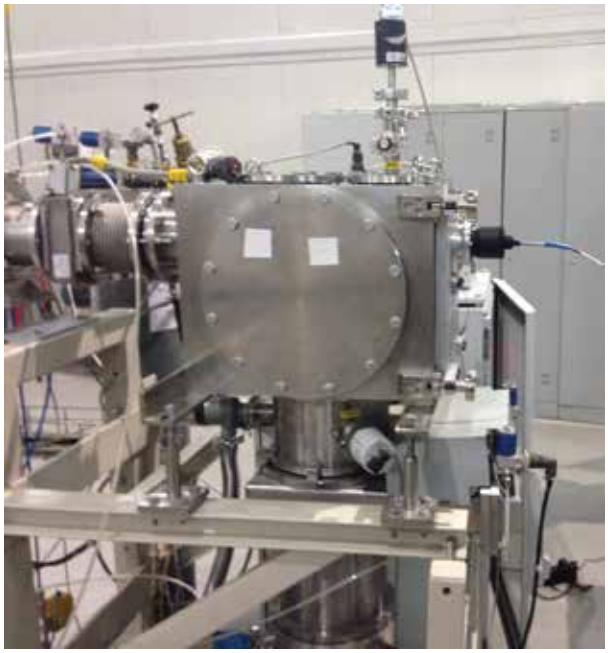

Figure 4. View of the experimental setup on the DC-60 accelerator.

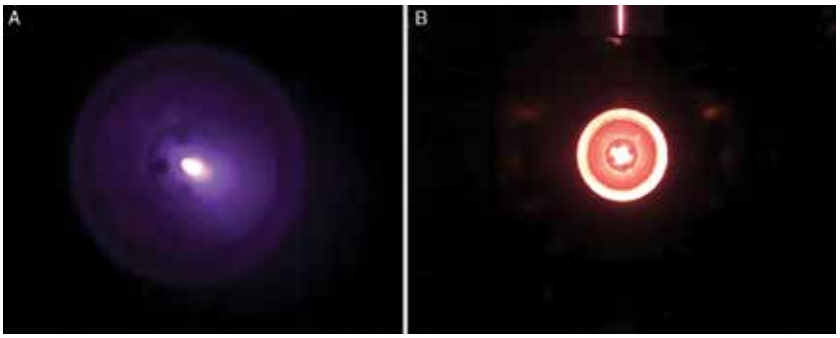

Figure 5. 400 Torr helium (a) and 600 Torr neon (b) luminescence induced by argon ions.

Beam from the narrow ion-excited region is reflected on the separating flange (a, b) and on the top of the chamber (b).

Studies on luminescence spectra of gaseous media were also conducted with the use of radioactive isotopes [36, 56–58] and pulsed nuclear reactors [59–61].

http://dx.doi.org/10.5772/63823

3. NPL active media on transitions of atoms and atomic ions

3.1. IR lasers operating on transitions of Xe, Kr, and Ar

Nuclear-pumped lasers operating on IR transitions of Xe, Kr, and Ar were investigated in detail and have maximum output parameters for NPL. The research by VNIIEF in 1972 during the first experiments was performed with the VIR-2 reactor; the output power of xenon laser with an optimal pressure and composition of the He-Xe was 25 W with efficiency ~0.5%, but the results were not published that time [62]. In 1974, obtained laser action on He-Xe composition (λ = 3.51 μm) with excitation by uranium fission fragments [63]. It was one of the first publications on the achievement of lasing under direct nuclear pumping [63, 64].

Most of the lines with laser action refer to nd-(n + 1)p transitions of Xe, Kr, and Ar atoms (n = 5, 4, 3 for Xe, Kr, Ar, respectively). Xenon laser (λ = 1.7–3.5 μm) has received the most studies, as it has the highest output parameters. He, Ar, Kr, and compounds thereof served as buffer gases. The first NPL xenon laser has the maximum achieved energy parameters:

- output power 1.3 MW and energy 526 J per pulse with duration 400 ms in He-Ar-Xe compounds, with a wavelength 2.03 μm [65],
- 5.6% efficiency in Ar–Xe mixture [66], 2.5% in He-Ar-Xe [67] with λ = 1.73 μm and ~3% with 2.03 μm [65]. The differences in efficiency values may be related to differences in the evaluation of energy deposited in gas [3].

Xenon laser also has the lowest lasing threshold: $1.5°10^{12}$ n/cm^{2}s in Ar-Xe mixture (λ = 2.03 μm) [7, 68]. These advantages, as well as the absence of degradation of the laser mixture as a result of radiation and chemical reactions, join the lasers operating on IR transitions of Xe, Kr, Ar the ranks of most promising in terms of reactor-laser creation [18].

Upper location of laser levels suggests a weak temperature dependence of its output parameters. However, in the case of lasers operating on IR transitions of inert gases, the output power is halved at the temperature of the mixture 350–550 K [3, 69]. The reasons for this are still not fully understood and are the matter of discussions. The most probable reasons were considered:

- reduction in the rate of formation of heteronuclear $ArXe^+$ ions and mixing laser levels by electrons [69],
- destruction of $ArXe^+$ ions by buffer gas atoms [70],
- collisional quenching and mixing laser levels by buffer gas atoms [71],
- active medium contamination by impurities as a result of their desorption from laser cell walls as long as it is warming [72].

Although lasers operating on IR transitions of inert gases are studied for over 40 years and considered to be the most promising, there is still no clarity with mechanism of upper nd-levels population [3, 73]. The processes of deactivation of lower (n + 1)p-levels can be considered well established; it is a collisional quenching in collisions with atoms of active medium, and with

electrons at high-power pumping. The main problem in determining nd-levels population mechanism is associated with complexities of IR radiation registration within the reactor experiment.

The main presently discussed mechanisms of levels population (B—Xe, Ar, Kr; A—buffer gas atom) [73] are as follows:

1. Shock-radiative recombination: $B^+ + e + e\ (M) \rightarrow B(nd) + e(M)$, M— third particle.
2. Electron-ion recombination: $B_2^+ + e \rightarrow B(nd) + e$.
3. Recombination of heteronuclear ionic molecules: $AB^+ + e \rightarrow B(nd) + A$.
4. Transfer of excitation in inelastic collisions: $Ar^* + Xe \rightarrow Xe(5d) + Ar$.
5. Step excitation: $Xe(6s, 6s') + e \rightarrow Xe(5d) + e$.

Widely held hypothesis implies for levels population in processes (3) of dissociative recombination of heteronuclear ionic molecules with electrons [29, 74]. In works [3, 73, 75], the main channel of population is considered to be the process (2) of electron-ion recombination of B_2^+ ions. In recombination mechanism of Xe levels' population, the lasing failure with addition of 5 Torr of uranium hexafluoride to Ar-Xe mixture [16] can be explained not only by quenching xenon levels by UF_6 molecules, and also by electron attachment to UF_6, by recombination of xenon ions with negative ions in the mixture.

According to [33, 76], dissociative electron-ion recombination of molecular ions of inert gases cannot be the main process of nd-levels population of inert gas atoms. It is expected to populate levels by direct excitation of secondary electrons from the ground state of atom, as well as transfer of excitation from buffer gas atom [33].

3.2. Visible-range lasers operating on Ne atom transitions

Atomic neon laser created in 1961 by Javan A. and others is the first laser with active gas medium. Therefore, the first proposals [1] and first experiments [2] on NPL creation were associated with well-known transitions of He-Ne laser with a wavelength of 632.8 nm and 1.15, 3.39 μm. In 1980, it was reported [77] on laser action of $5s'[1/2]_1^0$–$3p'[3/2]_2$ neon atom transition (λ = 632.8 nm, **Figure 6**) after excitation of ^{3}He–Ne mixture by products of nuclear reaction ^{3}He(n,p)T in stationary nuclear reactor. At the same time, laser efficiency was approximately 0.03% and the lasing threshold was reached at a very low thermal neutron flux $F = 2 \cdot 10^{11}$ n/cm^{2}s. High gain in a mixture of ^{3}He-Ne ($1.7 \cdot 10^{-2}$ cm^{-1} at $F = 2 \cdot 10^{12}$ n/cm^{2}s) was also measured in work of Chinese authors [49]. The results of these studies are questionable and subject to discussion [78, 79]. Simple estimates [78] show that in these conditions [77] population cannot be obtained even in the extreme case, when all power deposited in gas is fully transferred to the upper laser level, and the level is not quenched in collisions with atoms. In our experiments, the neutron flux density was gradually changed from 10^{11} to 10^{14} n/cm^{2}s; however, the lasing threshold in ^{3}He:Ne = 5:1 mixture was not reached [53, 79]. In addition, the luminescence spectrum of He-Ne mixtures at ionized radiation pumping has no 632.8 nm line (**Figure 7**).

http://dx.doi.org/10.5772/63823

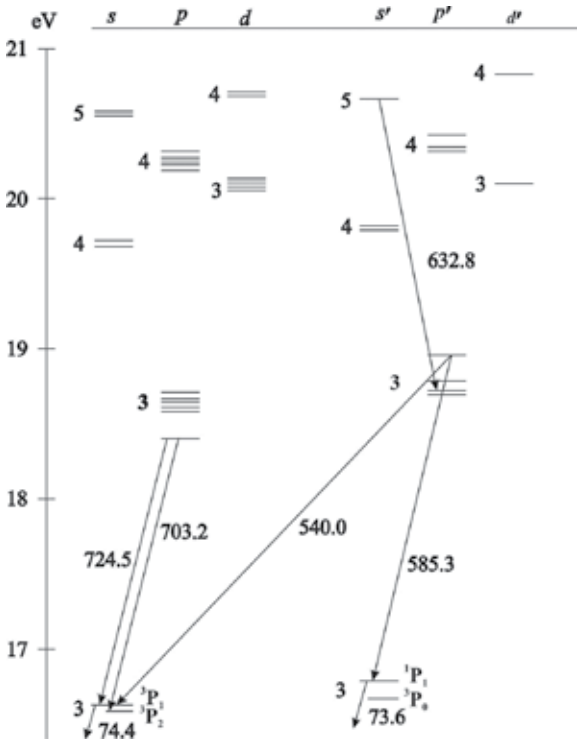

Figure 6. Scheme of laser transitions in neon. The wavelengths of laser and resonant transitions are indicated in nm.

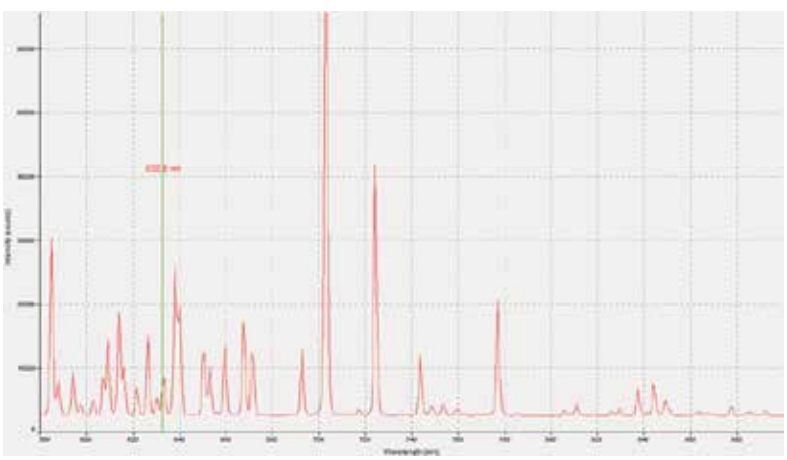

Figure 7. Emission spectrum of neon at a pressure of 605 Torr under ion beam excitation in the 570–900 nm region. The vertical green line indicates the wavelength of 632.8 nm.

3p levels of neon atoms are efficiently populating during excitation by the products of nuclear reactions of neon and its mixtures [57, 80] (see **Figure 7**). To create laser operating on 3p–3s

transitions of neon, it is necessary to solve the problem of lower s-levels deactivation. These levels are metastable or resonantly coupled to the main level and have trapped radiation at neon pressures important for nuclear pumping radiation. Rapid depletion of lower laser levels at a relatively low concentration of quenching particles can be achieved in the processes occurring with Coulomb cross-sections. In Ref. [20], authors show the possibility of deactivation of excited states in the Penning process. The required selectivity of deactivation of the upper and lower levels can be achieved using the lower levels states as resonantly coupled to the main, for which the ionization cross-section of quenching by additives is particularly high [81].

Quasi-continuous lasing in allowed neon atom transition $3p'[1/2]_0$–$3s'[1/2]_1^0$ ($\lambda = 585.3$ nm) was first observed in the afterglow of discharge [82], and then at pumping by powerful electron beam of Ne-H_2, Ne-Ar, Ne-Ar-He mixtures [83]. In [84] by reducing the concentration of neon and quenching the lower level of additives by an order compared to [83], and pumping power by electron beam ~100 kW/cm^3 with He:Ne:Ar = 96:3:1 mixtures at a pressure of 3 atm at the same transition obtained laser efficiency of 1–2%. The laser efficiency with ionizing pumping at λ = 585 nm in the opinion of other authors cannot exceed 0.5% [85]. The electron beam pumping provided for laser action in a row of 3p–3s neon transitions in the spectrum red region [86] (see **Figure 6**).

Progress in creating efficient lasers of visible range operating on neon at the electron beam pumping power 10–100 W/cm^3 stimulated work on nuclear-pumped lasers operating on 3p–3s transitions of neon atom. Laser action operating on 3p–3s neon transitions at pumping by uranium fission fragments was obtained in 1985 at VNIIEF on VIR-2 reactor. These results were published in 1990 [3, 87]. In 1985, we have also conducted experiments on WWR-K stationary nuclear reactor for excitation of triple mixtures of argon or krypton, neon, and ^{3}He, which has led to a negative result [53, 79].

Obtained within the experiment efficiency values for NPL operating on neon (to 0.1%) are much lower than at pumping by electron beam [84, 85]. Threshold values of thermal neutron flux density are significantly higher than 10^{14} n/cm^{2}s [87–93]. Report [90] on NPL lasing in ^{3}He-Ne-H_2 mixture with a lasing threshold of 10^{14} n/cm^{2}s is doubtful, as hydrogen at a pressure of 0.57 bars must be considerably quenching the upper laser level. Unlike lasers operating on IR transitions of Xe, Kr, Ar, the lasing mechanism in lasers on 3p–3s transitions of neon was considered reliably established [39, 87, 94]. Already the first works on neon lasers pumped by an electron beam or nuclear radiation contain roughly the same ideas about the lasing mechanism. The lower 3s-states are deactivated in the processes of:

- Penning for metastable states $3s[3/2]_2^0$, $3s'[1/2]_0^0$ [20],
- release of an electron for resonance states $3s[3/2]_1^0$, $3s'[1/2]_1^0$ [81].

The main process of 3p levels population is considered to be dissociative recombination of Ne_2^+ ions with electrons; most studies assumed that all of these levels are populated in recombination of molecular ions in the main vibrational state. In [80, 84] to explain changes in the efficiency of various levels pumping with the neon pressure, was made a conclusion on population of $3p'[1/2]_0$-level in processes of recombination of vibrationally excited levels of

Ne_2^+. Population efficiency of level $3p'[1/2]_0$ increases in triple mixtures with high helium content, which is explained in [80] by the formation of vibrationally excited levels of Ne_2^+ in the following processes:

$$Ne^+ + 2He \rightarrow HeNe^+ + He \tag{15}$$

$$HeNe^+ + Ne \rightarrow Ne_2^+(v>0) + He \tag{16}$$

Another mechanism for neon levels' population when excited by a hard ionizer is proposed in [79]. Based on the study of spectral-temporal characteristics of pure neon and He-Ne mixtures pumped by heavy charged particles, the conclusion was made that the population of neon levels occurs in direct excitation by nuclear particles and secondary delta electrons, and in He-Ne mixtures also in the process of excitation transfer from metastable helium atoms (He^m):

$$He^m + Ne + He \rightarrow Ne(3p) + 2He \tag{17}$$

However, this work did not receive recognition: In the review article [18], it was not mentioned, and in monograph [3], it was questioned with reference to [95]. During the study of luminescence of He-Ne mixtures with quenching additives [30], we have obtained results confirming the main conclusion in [79]—the principal and clearly dominant channels of neon 3p levels population in pumping by a hard ionizer are the processes unrelated to dissociative recombination of molecular ions of neon.

3.3. Metal vapor lasers

3.3.1. Mercury vapor lasers

HgII laser. The first report on the lasing of ion NPL operating on mercury vapor appeared in 1970 [96]. This work presents results obtained at ^{3}He(350 Torr)+Hg(3 Torr) mixture pumping on IIN pulsed reactor with neutrons flux up to $5°10^{16}$ n/cm^{2}s. According to authors, the registered lights power ~10 mW was associated with laser action of mercury ion transition $7^2P_{3/2}$–$7^2S_{1/2}$ (λ = 615.0 nm). Further on, these results were questioned, and in ^{4}He(600 Torr) +Hg (2.5–10 mTorr) mixture pumping by $^{10}B(n,\alpha)^7Li$ reaction products has proved lasing with a wavelength of 615 nm [97]. The conditions [97] had no lasing at partial pressure of mercury vapor ~3 Torr.

Pumping mechanism at the transition of $7^2P_{3/2}$–$7^2S_{1/2}$ mercury ion at ionizing pumping was considered in [53, 98, 99]. Discrepancy between the results of [96, 97] is possibly due to the difference in mechanisms of upper laser level population at low density and high density of mercury vapor [53, 98]. Calculations [99] indicate a low energy laser characteristics at λ = 615 nm (0.04% maximum efficiency) even with optimal parameters.

HgI laser. The emission spectra of mixtures of ^{3}He + Hg and ^{3}He + Hg + Kr in excitation by products of nuclear reaction ^{3}He(n,p)T studied in [100]. It was concluded that the excitation of low-lying HgI levels by electron impact is predominant in high-pressure plasma:

$$\mathrm{Hg}(6^1\mathrm{S}_0)+\mathrm{e}\rightarrow\mathrm{Hg}(6^3\mathrm{P}_1)+\mathrm{e} \tag{18}$$

$$\mathrm{Hg}(6^3\mathrm{P}_{0,1,2})+\mathrm{e}\rightarrow\mathrm{Hg}(\mathrm{nx})+\mathrm{e} \tag{19}$$

Continuous laser λ = 546.1 nm with optical pumping [101] uses similar scheme of excitation (electron replaced with photon): a beam with a wavelength of 253.7 nm, corresponding the mercury resonance line, excites 6^3P_1 mercury level and beam λ = 435.8 nm transmits excitation to 7^3S_1-level. However, an attempt to ensure deactivation of 6^3P_2 state by N_2 molecules according to the scheme used in optically pumped laser at ionizing radiation pumping was not successful [102].

We have proposed another scheme of creating inverse population in laser on mercury triplet lines [54]. Our works [36, 98] have shown that population of 7^3S_1-level of mercury atom occurs in the process of dissociative recombination of molecular ions and not in direct or stepwise excitation by electrons. It is proposed to use H_2 to destruct the lower level at the transition of 7^3S_1–6^3P_2; H_2, D_2—on the transition of 7^3S_1–6^3P_1. As the pumping is carried out through ion channel, xenon should be used as buffer gas and charge exchange from xenon to hydrogen is slow. The use of krypton is less justified due to low value of rate constant of Kr_2^+ ion recharge on mercury atoms. High selectivity of dissociative recombination of Hg_2^+ is largely driven by relatively low temperatures involved in recombination of electrons. Therefore, by increasing the pumping power to the level required for laser operation, it is useful to use helium to cool the secondary electrons. Thus, the optimal gas mixture of laser operating on mercury triplet must be four-component He-Xe-Hg-H_2 [54].

Quasi-continuous lasing at 7^3S_1–6^3P_2 transition of mercury atoms using this scheme was obtained on pulsed nuclear reactor EBR-L in VNIITF [103]. Kinetic model of He-Xe-Hg-H_2 nuclear-pumped laser based on VNIITF experiments was developed in [104]. Externally similar scheme is implemented in excitation of mercury mixtures with inert gases by electron beam [105]. This work uses a mixture of He+Ne+Ar as a buffer gas at a total pressure of 2300 Torr. With reference to the paper later than [36, 98], recombination of Hg_2^+ as the main population channel of 7^3S_1 has been specified. An attempt to use H_2 for 6^3P_2 level population was unsuccessful, and at hydrogen pressure of 20 Torr laser action failed. What was also interesting in this study was the absence of molecular additives quenching the lower level. Apparently, the de-excitation of lower laser level took place in formation of excimer molecules (HgR)*:

$$\mathrm{Hg}(6^3\mathrm{P}_2)+\mathrm{R}+\mathrm{M}\rightarrow(\mathrm{HgR})^*+\mathrm{M} \tag{20}$$

http://dx.doi.org/10.5772/63823

where R—Ne or Ar.

3.3.2. Cadmium and zinc vapor lasers

The first nuclear pumping of visible range laser operating on cadmium vapor was carried out by MEPhI researches on BARS pulse reactor [106]. In ^{3}He-^{116}Cd mixture was obtained laser action on $4f^2F^0_{5/2,7/2}$–$5d^2D_{3/2,5/2}$ transitions of ion Cd^+ (λ = 533.7 and 537.8 nm), and later on transition from λ = 441.6 nm [107]. The first successful experiments on laser pumping on metal vapor (mixture of He-^{116}Cd, λ = 441.6; 533.7 and 537.8 nm) by uranium fission fragments were carried out in 1982 by researches of VNIIEF and VNIITF on EBR-L reactor [3]. Maximum parameters of Cd^+-laser with nuclear pumping is also obtained in this reactor: 1000 W at an efficiency of 0.4% on the blue line and 470 W on the green lines [44].

At present, the basic processes of population of upper laser levels of Cd^+ are considered to be established:

$4f^2F^0_{5/2,7/2}$ upper levels of laser transitions from λ = 533.7 to 537.8 nm are populated due to charge exchange processes

$$He^+ + Cd \rightarrow (Cd^+)^* + He \tag{21}$$

forming higher-lying levels of 6f, 6g, 8d, 9s [108] and subsequent cascade transitions in 4f state.

$5s^2{}^2D_{3/2,5/2}$ upper levels for transitions with λ = 441.6 and 325 nm are populated in Penning and charge exchange processes

$$He_2^+ + Cd \rightarrow (Cd^+)^* + He \tag{22}$$

$$He^*(2S) + Cd \rightarrow (Cd^+)^* + He \tag{23}$$

Laser action at 325 nm was achieved only when pumped by an electron beam, although the threshold pumping power was only 10 W/cm^3 [109].

Deactivation of lower levels can occur as a result of radiative transitions, quenching by electrons, conversion processes of atomic ions into molecular ions

$$(Cd^+)^* + Cd + He \rightarrow Cd_2^+ + He \tag{24}$$

and for the levels lying above $6^2S_{1/2}$, in Penning process on its own atom

$$(Cd^+)^* + Cd \rightarrow Cd^+ + Cd^+ + e \tag{25}$$

Lasing mechanisms of NPLs on ion transitions of cadmium and zinc are very similar. Laser action by pumping ^{3}He-Zn mixture observed on transition of $4s^2{}^2D_{5/2}$–$4p^2P_{3/2}$ (λ = 747.9 nm) [110], 60 W output power obtained during pumping by uranium fission fragments at this transition [44].

Information about cadmium-vapor atomic lasers with ionizing pumping is scarce. During experiments was registered laser action (1–2 W) with a threshold density of 10^{16} n/cm^{2}s neutron flux on the lines of 1.648 and 1.433 μm at pumping He-Cd mixture by uranium fission fragments [44]. When pumping He-Cd mixture by an electron beam was obtained laser action on the line 361 nm of cadmium atom [111]. Kinetic model [112] included processes involving excited cadmium atoms and attempted to calculate some laser characteristics for 1.648 μm line.

Luminescence of ^{3}He-Cd and ^{3}He-Xe-Cd mixtures in the radiation region of stationary nuclear reactor investigated in [113]. Measured value of rate constant of Xe_2^+ charge exchange on cadmium atoms is small (~10^{-13} cm^{3}s^{-1}), in contrast to the constant of charge exchange on mercury atoms. A sufficiently high density of cadmium vapor (~3×10^{18} cm^{-3}) was established at a temperature of about 700°C, and such density of cadmium requires consideration of quenching 6^3S_1 state by its own atoms. Perhaps krypton ions charge exchange on Cd will be faster. In addition, cadmium atoms in krypton can be ionized in the Penning processes.

4. NPL active media on molecular transitions

4.1. Lasers operating on first negative system of nitrogen and carbon monoxide

N_2^+. When pumping active medium of a high pressure by electron beam with moderate (~3 A/cm^2) current density was obtained quasi-continuous lasing mode on the first negative system of nitrogen (λ = 391.4 and 427.8 nm) with an efficiency ~1% [114, 115]. In this collision lasers on $B^2\Sigma^+_{u,v=0} \rightarrow X^2\Sigma^+_{g,v''=0,1}$ transitions of nitrogen ion, deactivation of lower level was carried out at low hydrogen concentrations (~0.1%) in He-N_2-H_2 mixture in the process with proton transfer:

$$N_2^+(X) + H_2 \rightarrow N_2H^+ + H \tag{26}$$

In 1996 was obtained laser action at λ = 391.4 nm with excitation of He-N_2-H_2 mixture by uranium fission fragments on EBR-L [116]. This was the first NPL emitting in the UV spectral region: Laser power was ~10 W, efficiency ~0.01%. To date, it remains to be the most short-wavelength nuclear-pumped laser. On BARS-6 reactor were conducted studies of facility with active core length of 250 cm and volume of 4 liters with the average over the length of the laser element-specific energy deposition to 300 W/cm^3 [117]. The lasing threshold on B-X nitrogen ion transitions with λ = 391.4 and 427.8 nm was achieved with low for molecular laser power density of energy deposition 50–60 W/cm^3. It was determined that active medium had non-resonant losses ~5×10^{-5} cm^{-1}. These authors explain the laser efficiency (~0.1–0.2%) was significantly lower than expected. In [118] developed a multi-

component spatially homogeneous model of kinetic processes of NPL active medium on He-N_2-H_2 mixture. According to the model, the maximum laser efficiency (0.5–0.8%) was achieved at pumping power of 0.5–3 kW/cm^3, for specific pumping power 90–130 W/cm^3 the maximum instantaneous efficiency is 0.1%.

The [119] searched mixture compounds that improve NPL efficiency on 1^-—nitrogen system, including study of deuterium and neon impact on the laser parameters. Replacement of hydrogen additive deactivating lower level by deuterium provided no improvements to laser efficiency. The use of neon as the buffer gas at partial pressure of 30 Torr resulted in efficiency decrease for 30–40% for both wavelengths. It has previously been shown [120] that helium replacement with neon impairs laser parameters for B-X transitions of N_2^+. At pumping by an electron beam, lasing energy of mixture with addition of 60 Torr of neon was 1.5 times less than for three-component mixture of He-N_2-H_2 with a total pressure of 6 atm.

In [121], the constants of quenching processes rates of N_2^+ (B) with nitrogen and helium, as well as two- and three-particle charge exchange processes of He_2^+ to H_2, D_2, Kr, CO, were determined on the luminescence in 0–0 transition of the first negative system of nitrogen in excitation by ∝–particles of polonium-210.

CO^+. Gain on the first negative system of carbon monoxide by powerful electron beam pumping was obtained in 1975, the same way as in N_2^+-laser, by Waller et al. [122]. Quasi-continuous lasing mode can be implemented with addition of H_2, D_2 or Kr to He-CO [123]. In [123, 124] by spectra of radioluminescence of the gas mixtures with carbon monoxide was determined constants of quenching rate of CO^+(B) with helium, neon, CO molecules, evaluated the upper limit of constant of quenching rate with hydrogen, deuterium and krypton.

Kinetic model of nuclear-pumped laser on $B^2\Sigma^+_{u,v'} \rightarrow X^2\Sigma^+_{g,v''}$ transition of carbon monoxide ion was developed in [125]. Unfortunately, the only information given on the results of calculations of medium gain, efficiency, but there is no information on considered processes, values of constants for processes rate. This provides for the opportunity to discuss the work. In addition, specified calculated wavelength transition for which the calculations were made, 210 nm; the closest wavelength—211.2 nm—corresponds to 1–0 transition [126]. That is, laser action, according to [125], should not take place from the ground vibrational level of CO^+(B), as the wavelength of 0–0 transition—219.0 nm. It should be noted that the gain in [122] was observed at 0-2 transition (242 nm) and Baldet-Johnson's system (391 and 425 nm, B→A transitions) from the ground vibrational level of CO^+(B).

4.2. Excimer lasers operating on halides of inert gases

Excimer lasers operating on halides of inert gases have been studied for a long time [127]. At present, they are the most powerful lasers that emit in UV region of spectrum. Optimal operation of excimer lasers corresponds to pumping powers of several megawatts per cm^3 and a pressure of several atmospheres. Such pumping powers are achieved by electron beams or space discharge. Radiation of nuclear explosions [128] and ion beams [129] also has been used to pump these lasers.

Excimer lasers can operate in a quasi-continuous mode, as in the photon emission, an excimer molecules pass into the lower dissociating or weakly bound state. Much of the research on creation of NPL operating on the inert-gas halides is associated with XeF-laser (λ = 351 and 353 nm). Experiments on SPR-III reactor have shown that in ^{3}He-Xe-NF_3 mixture the gain on the 351 nm band is about $7°10^{-3}$ cm^{-1} at pumping power q≈5 kW/cm^3 [130], and at pumping by uranium fission fragments of Ne(Ar)-Xe-NF_3 mixture, registered gain of ~$2°10^{-3}$ см$^{-1}$ at q≈2 kW/cm^3 [131]. Experiments in pulsed nuclear reactors with neutron flux up to 10^{17} n/cm^{2}s aimed at obtaining lasing at XeF [131] and XeF, KrF [59] did not yield positive result. The work [132] contains theoretically investigated characteristics of laser operating on Ne-Xe-NF_3 mixture at 1 atm with nuclear pumping duration 0.1–1 ms at half-height in the near-threshold lasing region. The lasing threshold is 400–500 W/cm^3, and the maximum calculated efficiency of ~1% is achieved at pumping power of 1.5–5 kW/cm^3. Predicting the possibility to create XeF-nuclear pumped laser is mainly limited by the uncertainty of absorption coefficient in active medium, which greatly affects calculation results.

The luminescence efficiency in chlorine-containing gas mixtures with xenon (to 15% [133], ~11% [134]) is about three times higher than the efficiency of emission at the transition of XeF. The maximum luminescence efficiency can be achieved at low chloride content (<0.7 Torr [134], 0.05 Torr [135]). In [133] reported about the lasing on XeCl molecule (λ = 308 nm) by pumping Ar-Xe-HCl(CCl_4) mixture by uranium fission fragments in experiments on EBR-L reactor. According to the authors, the narrowing in emission spectrum in 308 nm band, the height of film blackening, 1.3–1.5 times less than at other wavelengths, indicates the presence of laser radiation. However, these data are not sufficient for this conclusion [3].

High radiation resistance of ^{3}He-Xe-CCl_4 mixture was noted in [134, 136]. The densities of electrons and negative ions in the plasma of gas mixture of ^{3}He-Xe-CCl_4 and ^{3}He-Xe-NF_3 irradiated with thermal neutron flux 10^{11}–10^{14} n/cm^{2}s into the active core of stationary nuclear reactor, measured in [137].

4.3. Lasers operating on vibrational transitions of carbon monoxide and carbon dioxide

CO. Molecular nuclear-pumped laser operating on carbon monoxide was one of the first NPLs, the creation of which was reported in the press [64]; the laser action was observed in vibrational-rotational transitions of the CO molecule with λ = 5.1–5.6 μm. Potential of medium on carbon monoxide was determined by the fact that, unlike lasers on electronic transitions, active medium of CO-laser does not require high pumping selectivity. It is important to get energy into the broad band of vibrational levels of the ground electronic state of CO molecule. Furthermore due to the autonomy of vibrational subsystem and anharmonicity of molecular vibrations, this energy at relatively low translational temperature redistributing in the process of exchange of vibrational molecules to provide full or partial inversion on vibrational levels of CO [138]. This property associated with the anharmonicity of the vibrational levels, as well as the cascade mechanism of lasing in CO, allows directing significant energy share of nuclear reaction products to the laser level.

Experiments have not yet confirmed this finding. In [64], carbon monoxide pumping at a pressure of 0.13 atm and temperature of 77 K was carried out by uranium fission fragments,

and the radiation power was 2–6 W with an efficiency of 0.1–0.3%. In further work, the authors [64] achieved lasing power of about 100 W by using a multiple-pass resonator with an active length of 120 cm. Lasing on vibrational transitions of CO was also obtained in [139] at excitation of ^{3}He-CO by nuclear reaction products of ^{3}He(n,p)T. Laser radiation power at the mixture pressure of 3 atm exceeded 200 W from an active volume of 300 cm^3, and the lasing threshold was reached at F = 3×10^{16} n/cm^{2}s.

Excitation of vibrational levels of CO can occur due to molecular collisions with plasma electrons. In [140] based on calculation of electrons spectrum formed in a molecular gas under the action of ionizing radiation, it was shown that the efficiency of CO nuclear-pumped laser cannot exceed 0.5%. Further work [141] showed the main mechanism of molecular formation in the form of dissociative recombination of cluster ions with formation of electronically excited molecules and subsequent collision of these molecules with molecules in ground state. According to the authors [141] plasma chemical processes in active medium can make a significant contribution to the energy pumping into vibrational modes of molecules and allow achieving the efficiency pumping up to 18%. The use of argon as a buffer gas instead of helium should increase 1.5-fold the efficiency of pumping in vibrational levels and reduce by an order the threshold energy for active medium pumping. It should be noted that a record efficiency of electron beam-controlled laser operating on carbon monoxide—63% [142]—was achieved due to Ar:CO = 10:1 mixture.

Presently achieved low parameters of NPL operating on CO, the need to cool down an active medium reaching cryogenic temperatures, apparently, makes carbon monoxide medium insufficient for creation of nuclear-pumped lasers.

CO_2. The possibility of CO_2-laser pumping (λ = 10.6 μm) by nuclear radiation was considered in the earliest stages of NPL study [2], and gas-discharge laser operating on carbon dioxide had the highest output parameters for that time. Numerous attempts to create NPL on CO_2 have yield negative results. Experiments on pumping ^{3}He-CO_2 and ^{3}He-CO_2-N_2 mixtures with products of ^{3}He(n,p)T reaction showed no gain in band of 10.6 μm at a wide variation of pressure (0.28–0.8 atm) and composition of mixture [143]. Moreover, these experiments showed probe laser radiation absorption, which indicates preferential population of the lower laser level of CO_2 when excited by ionizing radiation. Calculations of kinetic processes in CO_2-N_2-He mixture also support the conclusion on ineffectiveness of direct pumping of CO_2-laser with nuclear radiation [144].

Apparently, the most promising method of nuclear energy conversion into radiation on vibrational transitions of CO or CO_2 is the creation of nuclear power plant with electroionization laser based on thermionic converter reactor [145, 146].

4.4. Radiation of heteronuclear ionic molecules of inert gases

Molecular bands in radiation spectra of pair inert gas mixtures were first discovered more than half a century ago. The [147] recorded the band of 507–550 and 496–508 nm in Ar-Xe mixture, and the authors attributed the presence of these bands with emission of heteronuclear molecules or ions. When pumping Ar-Xe mixture by electron beam, the molecular band at 510

nm was detected and the band of 495–460 nm in Kr-Xe was registered for the first time [148]. Two emission systems were observed, in 600–670 and 670–685 nm regions, when Xe was added to Kr flowing afterglow at a pressure of 30 Pa [149]. Kugler [150] obtained similar results for Ar-Xe mixture and discovered new band in Ar-Kr in the region of 605–642 nm. He explained these bands as transitions of neutral heteronuclear molecule formed in the processes of metastable atoms of argon.

In 1975, Tanaka et al. [151] have published data on radiation spectra of 10 pair mixtures of inert gases in the region of 100–700 nm. Molecular bands observed in radiation spectra in the discharge were identified as transitions between states of heteronuclear ionic molecules:

$$M^+N \rightarrow MN^+ + h\nu \tag{27}$$

where molecular states of M^+N asymptotically correspond to states of M^++N, and MN^+ to the state of M+N^+; here M, N—atoms of inert gases, and N—a heavier atom. If the plasma of low pressure in an electric discharge in paired mixtures of inert gases has up to 5 similar bands [151], there are no transitions from levels corresponding to the states of atomic ions $^2P_{3/2}$ [152, 153] when excited by ionizing radiation of medium- and high-pressure mixtures.

Kinetics of Ar-Kr, Ar-Xe, and Kr-Xe mixtures' excitation by low activity ^{241}Am alpha particles was studied in [152, 154]. Constants of processes rates in these mixtures were identified; however, constants' values of a number of processes are underestimated: ~10^{-15} cm^3/s for two-particle and ~10^{-34} cm^6/s for three-particle processes. Emission of Ar-Xe and Kr-Xe mixtures when excited by ^{210}Po alpha particles with activity of ~0.5 Cu investigated in [153, 155–157] determined the rate constants of processes of formation and destruction of levels of heteronuclear ionic molecules. In [153] includes first noted high luminescence efficiency of $(ArXe)^+$, $(KrXe)^+$ at pumping by ionizing radiation. Luminescence of Ar-Xe mixture pumped by powerful electron beam was studied in [158], attempts to obtain lasing on transitions of $(ArXe)^+$ at pumping by an electron beam had yield negative results [155, 158].

In [42] was built kinetic model of Ne-Ar mixture relaxation pumped by a hard ionizer with regard to the possibility of lasing on transition $Ne^+Ar \rightarrow NeAr^+$. When using typical rates of plasma chemical reactions, calculations show that lasing is only possible at high pressure (above 16 atm) and powerful pumping (1 MW/cm^3), and lasing efficiency should not exceed 0.05–0.25%. In this work were considered the triple (with Kr) instead of the binary mixtures of inert gases, as the authors suggested that the constant of deactivation rate of the lower level in exchange processes:

$$NeAr^+ + Ar \rightarrow Ar_2^+ + Ne \tag{28}$$

may occur negligible. It was assumed that the lower laser level will be deactivating in the processes with Kr atoms:

$$NeAr^{+} + Kr \rightarrow Kr^{+} + Ne + Ar \quad (29)$$

$$NeAr^{+} + Kr + M \rightarrow Kr^{+} + Ne + Ar + M \quad (30)$$

5. Conclusions

Nuclear-pumped lasers are of great interest as the way to extract high-quality energy from a nuclear reactor core. Presently achieved pulse power of NPL in quasi-continuous mode exceeds 1 MW. However, the most promising active media on transitions of inert gas atoms have a number of disadvantages: relatively low efficiency, radiation in IR region, low operating temperature. There is no clarity as to the basic mechanism of upper laser level population: direct excitation by secondary electrons, excitation transfer from buffer gas atoms, electron-ion recombination of molecular ions (dimers or heteronuclear ions). This area requires further research.

Acknowledgements

This work has been supported by the Ministry of Education and Science of the Republic of Kazakhstan (Grant No. 0681/GF4). Author is grateful to staff of the WWR-K reactor and DC-60 accelerator for their assistance in conducting experiments.

Author details

Mendykhan U. Khasenov*

Address all correspondence to: mendykhan.khassenov@nu.edu.kz

National Laboratory Astana, Nazarbayev University, Astana, Kazakhstan

References

[1] Herwig L.O. Concepts for direct conversion of stored nuclear energy to laser beam power. Trans Am Nucl Soc. 1964;7:131–132.

[2] Thom K., Schneider R.T. Nuclear pumped gas lasers. AIAA J. 1972;10:400–406.

[3] Mel'nikov S.P., Sizov A.N., Sinyanskii A.A., Miley G.H. Lasers with nuclear pumping. New York: Springer; 2015. 455 p. DOI: 10.1007/978-3-319-08882-2.

[4] Ebert P.J., Ferderber L.J., Koehler H.A., et al. Amplified spontaneous emission in xenon pumped by gamma rays. IEEE J Quantum Electron. 1974;QE-10:736.

[5] Dondes S., Hartek P., Kunz C. A spectroscopic study of alpha-ray-induced luminescence in gases. Radiat Res. 1966;27:174–210.

[6] Thiess P.E., Miley G.H. New near-infrared and ultra-violet gas proportional scintillation counters. IEEE Trans Nucl Sci. 1974;21:125–145.

[7] Voinov A.M., Konak A.I., Melnikov S.P., Sinyanskiy A.A. Feasibility of developing a cw laser with a radionuclide pump source. Quantum Electron (Sov J). 1991;21:1179–1181.

[8] Bigio I.J. Preionization of pulsed gas laser by radioactive source. IEEE J Quantum Electron. 1978; QE-14:75–76.

[9] Batyrbekov G.A., Batyrbekov E.G., Tleuzhanov A.B., Khasenov M.U. Electrodischarge laser with radioisotope pre-ionization. Tech Phys (Sov J). 1987;57:783–785.

[10] Nemez O.F., Hofman J.V. Handbook on nuclear physics. Kiev: Naukova dumka; 1975. 415 p. (in Russian).

[11] Wilson J.W., DeYoung R.G. Power density in direct nuclear-pumped ^{3}He lasers. J Appl Phys. 1978;49:980–988.

[12] Pikulev A.A. Energy deposition in helium-3 based nuclear-pumped lasers. Tech Phys. 2006;51:1344–1350.

[13] Wilson J.W., DeYoung R.G. Power deposition in volumetric $^{235}UF_6$–He fission-pumped nuclear lasers. J Appl Phys. 1978;49:989–993.

[14] Pikulev A.A., Vlokh G.V., Limar' Y.M., et al. Determination of energy deposition into the cells of nuclear-pumped lasers. Tech Phys. 2012;57:1127–1134.

[15] Gudzenko L.I., Slesarev I.S., Yakovlenko S.I. Proposed nuclear laser reactor. Tech Phys (Sov J). 1975;20:1218–1220.

[16] De Yong R.G., Shiu Y.J., Williams M.D. Fission-fragment nuclear lasing of Ar(He)–Xe. Appl Phys Lett. 1980;37:679–681.

[17] Voinov A.M., Vorontsov S.V., Krivonosov V.N., et al. Studies performed at VNIIEF, on investigating the possibility for creating a reactor laser. In: Proceedings of the 4th International Conference "The physics of nuclear-pumped lasers and pulsed reactors". Obninsk: FEI; 2009. vol. 1. pp. 17–33 (in Russian).

[18] Karelin A.V., Sinyanskii A.A., Yakovlenko S.I. Nuclear-pumped lasers and physical problems in constructing a reactor-laser. Quantum Electron. 1997;24:375–402.

[19] Budnik A.P., Kosarev V.A. Kinetic model of the helium nuclear inducted plasma containing nanoclusters. Phys Chem Kinet Gas Dyn. 2010;9:art. 130.

[20] Gudzenko L.I., Yakovlenko S.I. Plasma lasers. Moscow: Atomizdat; 1978. 256 p. (in Russian).

[21] Starodubzev S.V., Romanov A.M. Passage of the active particles through matter. Tashkent: Uzbek SSR Academy of Sciences Printing House; 1962. 228 p. (in Russian)

[22] Moratz T.J., Kushner M.J. Fission fragment pumping of a neon plasma. J Appl Phys. 1988;63:1796–1798.

[23] Moratz T.J., Saunders T.D., Kushner M.J. Heavy-ion versus electron-beam excitation of an excimer laser. J Appl Phys. 1988;64:3799–3810.

[24] Tyukavkin A.V. Electron energy distribution in helium excited by ions. Plasma Phys Rep. 1999;25:90–93.

[25] Dymshits Y.I., Neverov V.G., Khoroshev V.G. Calculation of outputs of primary products of irradiation of rare gases by fast electrons. High Energy Chem (Sov. J). 1982;16:201–208.

[26] Pikaev A.K. Modern radiation chemistry, vol. 2. Moscow: Nauka; 1987. 439 p. (in Russian).

[27] Dyachenko P.P. Experimental and theoretical works performed by the Institute of Physics and Power Engineering on the physics of nuclear-induced plasmas. Laser Part Beams. 1993;11:619–634.

[28] Budnik A.P., Dobrovol'skaya I.V. Characteristics of the kinetics of the active media of gas lasers excited by fission fragments. Quantum Electron. 1997;27:492–496.

[29] Karelin A.V., Simakova O.V. Kinetics of the active medium of a multiwave IR xenon laser in hard-ioniser-pumped mixtures with He and Ar. II. Nuclear pumping. Quantum Electron. 1999;29:687–693.

[30] Khasenov M.U. On the mechanism of populating 3p levels of neon under pumping by a hard ionizer. Quantum Electron. 2011;41:198–201.

[31] Poletaev E.D., Dorofeev Y.B., Dyachenko P.P., et al. Emission characteristics of pure neon and He–Ne mixture excited by a high-pressure nuclear particles. Tech Phys. 1992;37:114–121.

[32] Svelto O. Principles of lasers. 5th edition. Heidelberg: Springer; 2010. 620 p. DOI: 10.1007/978-1-4419-1302-9.

[33] Khasenov M.U. Mechanisms of population of the levels in gas lasers pumped by ionizing radiation. Laser Part Beams. 2014;32:501–508.

[34] Kolokolov N.B., Kudryavtsev A.A., Romanenko V.A. A spectroscopic investigation of recombination populating of the $5p^5 6p$ and $5p^5 5d$ states of the Xe Atom. Opt Spectrosc (Sov J). 1989;67:292–296.

[35] Ivanov V.A. Dissociative recombination of molecular ions in noble-gas plasmas. Sov Phys Uspekhi. 1992;35:17–36.

[36] Batyrbekov G.A., Dolgikh V.A., Khasenov M.U., et al. Luminescence of mixtures of mercury and inert gases containing molecular additives with excitation by ionizing radiation. J Appl Spectrosc (Sov J). 1988;49:1139–1143.

[37] Fedenev F.V., Tarasenko V.F. Simulation of NPL in experiments with e-beam pumping. Laser Part Beams. 1998;16:327–380.

[38] Ulrich A. Light emission from the particle beam induced plasma: an overview. Laser Part Beams. 2012;30:199–205.

[39] Karelin A.V., Yakovlenko S.I. Kinetic model of an He–Ne–Ar–H_2 laser pumped by hard ionising radiation. Quantum Electron. 1995;25:739–745.

[40] Voinov A.M., Melnikov S.P., Sinyanskiy A.A. A kinetic model of recombination lasers at xenon atom transitions. Tech Phys (Sov J). 1990;35:1172–1182.

[41] Miskevich A.I. A kinetic model of a nuclear-pumped laser operating on cadmium vapors. Tech Phys (Sov J). 1987;32:1056–1063.

[42] Boichenko A.M., Yakovlenko S.I. The possibility of lasing in Ne^+Ar ionic molecules pumped by a hard ionizer. Quantum Electron. 2000;30:681–686.

[43] Dem'yanov A.V., Dyatko N.A., Kochetkov I.V., Napartovich A.P. Simulation of excimer lasers with nuclear pumping. In: Proceedings of the Specialist Conference "Physics of Nuclear-Excited Plasma and Problems of Nuclear-Pumped Lasers", Obninsk: FEI; 1992. vol. 1. pp. 252–261.

[44] Magda E.P. Analyses of experimental and theoretical research of nuclear pumped lasers at the Institute of Technical Physics. Laser Part Beams. 1993;11:469–476.

[45] Miley G.H. Overview of nuclear pumped lasers. Laser Part Beams. 1993;11:575–581.

[46] Hebner G.A., Hays G.N. Reactor-pumped laser experimental results. Proc SPIE. 1994;2121:10–20.

[47] Prelas M. Nuclear-pumped lasers. New York: Springer; 2016. 417 p. DOI: 10.1007/978-3-319-19845-3.

[48] Yang C., Chen H., Zheng C., Zhao X., Han H. The progress of nuclear pumped laser in CFBR-II reactor. Chin Opt Lett. 2003;1:292–293.

[49] Xingxing J., Kaisu W., Iluaming Z., Hande C. Gain test of nuclear-pumped ^{3}He–Ne laser. Chin J Lasers. 1992;19:N 7. (Chinese, Engl. resume).

[50] Mis'kevich A.I. Visible and near-infrared direct nuclear pumped lasers. Laser Phys. 1991;1:445–481.

[51] Khasenov M.U. Optical emission of the nuclear-induced plasmas of gas mixtures. Int J Opt. 2014;ID748763. 16 p.

[52] Batyrbekov E. Converting nuclear energy into the energy of coherent optical radiation. Laser Part Beams. 2013;31:673–687.

[53] Khasenov M.U. Nuclear-induced plasma of gas mixtures and nuclear pumped lasers. Almaty, Kazakhstan; 2011. 187 p. (in Russian).

[54] Batyrbekov G.A., Khasenov M.U., Soroka A.M., et al. Feasibility of construction of a quasi-cw laser utilizing 7s–6p transitions in mercury pumped by ionizing radiation. Quantum Electron (Sov J). 1987;17:774–775.

[55] Zdorovets M., Ivanov I., Koloberdin M., et al. Accelerator complex based on DC-60 cyclotron. In: Proceedings of the 24th Russian Particle Accelerator Conference. Obninsk: FEI; 2014. pp. 287–289.

[56] Bennett W.R. Optical spectra excited in high pressure noble gases by alpha impact. Ann Phys. 1962;18:367–420.

[57] Dmitriev A.B., Il'yashenko V.S., Mis'kevich A.I., Salamakha B.S. Luminescence of neon and some of its mixtures at high pressures. Opt Spectrsc (Sov J). 1977;43:687–688.

[58] Khasenov M.U. Kinetics of CO first negative system excitation by ionized radiation. Proc SPIE. 2004;5483:14–23.

[59] De Young R.J., Weaver W.R. Spectra from nuclear-excited plasmas. J Opt Soc Am. 1980;70:500–506.

[60] Gorbunov V.V., Grigor'ev V.D., Dovbysh L.E., et al. The luminescence spectra in the 350–875 nm range of the dense gas excited by uranium fission fragments. Proc RFNC-VNIIEF, 2004;iss.6:148–185 (in Russian).

[61] Abramov A.A., Gorbunov V.V., Melnikov S.P., et al. Luminescence of nuclear-induced rare-gas plasmas in near infrared spectral range. Proc SPIE. 2006;6263:279–296.

[62] Sinyanskii A.A., Melnikov S.P. Research on development of continuous nuclear-laser setups in VNIIEF. Proc SPIE. 1998;3686:43–55.

[63] Helmick H.H., Fuller J.I., Schneider R.T. Direct nuclear pumping of helium–xenon laser. Appl Phys Lett. 1975;26:327–328.

[64] McArthyr D.A., Tollefsrud P.B. Observation of laser action in CO gas excited only by fission fragments. Appl Phys Lett. 1975;26:187–190.

[65] Zagidulin A.V., Bochkov A.V., Mironenko V.V., Sofienko G.S. A 500-J nuclear-pumped gas laser. Tech Phys Lett. 2012;38:1059–1062.

[66] Alford W.J., Hays J.N. Measured laser parameters for reactor-pumped He/Ar/Xe and Ar/Xe lasers. J Appl Phys. 1989;65:3760–3766.

[67] Melnikov S.P., Sinyanskii A.A. Ultimate efficiency of nuclear-pumped gas lasers. Laser Part Beams. 1993;11:645–654.

[68] Voinov A.M., Zobnin V.G., Konak A.I., et al. Quasi-cw low-threshold lasing and line competition in the nuclear-pumped lasers based on atomic xenon transitions. Tech Phys Lett (Sov J). 1990;16:297–300.

[69] Hebner G.A., Shon J.W., Kushner M.J. Temperature dependent gain of the atomic xenon laser. Appl Phys Lett. 1993;63:2872–2874.

[70] Barysheva N.M., Bochkov A.V., Bochkova N.V., et al. On the possible mechanism of overheating of the active medium of an NPL operating on ir transitions of the xenon atom. In: Proceedings of the Specialist Conference "The Physics of Nuclear-Excited Plasma and the Problems of Nuclear-Pumped Lasers". Obninsk: FEI: 1992. vol. 1. pp. 374–380.

[71] Konak A.I., Melnikov S.P., Porkhaev V.V., Sinyanskii A.A. Nuclear-pumped gas lasers at temperatures up to 800°C. Laser Part Beams. 1993;11:663–668.

[72] Kryzhanovskii V.A., Mavlyutov A.A., Miskevich A.I. Lasing characteristics of a nuclear-pumped Ar–Xe laser at high temperatures. Tech Phys Lett. 1995;21:535–536.

[73] Mel'nikov S.P. Mechanisms of generation of nuclear-pumped lasers on IR transitions of inert gas atoms. In: Proceedings of the 4th International Conference "The physics of nuclear-pumped lasers and pulsed reactors". Obninsk: FEI; 2009. vol. 1. pp. 167–176 (in Russian).

[74] Shon J.W., Kushner M.J. Excitation mechanism and gain modeling of the high pressure atomic Ar laser in He/Ar mixture. J Appl Phys. 1994;75:1883–1890.

[75] Apruzese J.P., Giuliani J.L., Wolford M.F., et al. Experimental evidence for the role of the Xe_2^+ in pumping of the Ar–Xe infrared laser. Appl Phys Lett. 2006;88:121120.

[76] Denezhkin I.A., D'yachenko P.P. Population and relaxation kinetics of $5d[3/2]_1$ level upon pulsed electron-beam excitation of pure xenon. Quantum Electron. 2009;39:135–138.

[77] Carter D.D., Rowe M.J., Schneider R.T. Nuclear pumped CW lasing of the ^{3}He–Ne system. Appl Phys Lett. 1980;36:115–117.

[78] Prelas M.A., Schlapper G.A. Comments on nuclear pumped CW lasing of the ^{3}He–Ne system. J Appl Phys 1981;52:496–497.

[79] Batyrbekov G.A., Khasenov M.U., Tleuzhanov A.B., et al. Investigation of the active media of lasers operating in the nuclear reactor. Final Scientific Report, no. GR 81032078. Institute of Nuclear Physics. Almaty. 1986 (in Russian).

[80] Batyrbekov G.A., Batyrbekov E.G., Danilychev V.A., Khasenov M.U. Efficiency of populating neon 3p-levels under ionized pumping. Opt Spectrsc (Sov J). 1990;68:1241–1245.

[81] Smirnov B.M. Excited Atoms. Moscow: Energoizdat; 1982. 232 p. (in Russian).

[82] Schmieder D., Brink D.J., Salamon I.J., Jones E.G. A high pressure 585.3 nm neon–hydrogen laser. Opt Commun. 1981;36:223–226.

[83] Bunkin F.V., Derzhiev V.I., Mesyaz G.A., et al. Plasma laser emitting at the wavelength of 585.3 nm with Penning clearing of the lower level in dense mixtures with neon excited by an electron beam. Quantum Electron (Sov J). 1985;15:159–160.

[84] Aleksandrov A.Yu., Anan'ev V.Yu, Basov N.G., et al. Efficient visible laser based on neon 3p–3s transitions. Sov Phys Dokl. 1985;30:875–879.

[85] Karelin A.V., Tarasenko V.F., Fedenev A.V., Yakovlenko S.I. Ultimate efficiency of a Penning neon plasma laser. Quantum Electron. 1996;26:291–294.

[86] Basov N.G., Baranov V.V., Danilychev V.A., et al. High-pressure power laser utilizing 3p–3s transitions in NeI generating radiation of wavelengths 703 and 725 nm. Quantum Electron (Sov J). 1985;15:1004–1006.

[87] Voinov A.M., Krivonosov V.N., Mel'nikov S.P., et al. Quasicontinuous lasing on the 3p–3s transitions of a neon atom in mixtures of inert gases excited by uranium fission fragments. Sov Phys Dokl. 1990;35:568–572.

[88] Kopai-Gora A.P., Mis'kevich A.I., Salamakha B.S. Emission of laser radiation at a wavelength of 585.2 nm in a dense ^{3}He–Ne–Ar plasma. Tech Phys Lett (Sov J). 1990;16:411–414.

[89] Hebner G.A., Hays G.N. Fission-fragment-excited lasing at 585.3 nm in He/Ne/Ar gas mixtures. Appl Phys Lett. 1990;57:2175–2177.

[90] Shaban Y., Miley G.H. A practical visible wavelength nuclear-pumped laser. In: Proceedings of Specialist Conference on Physics of Nuclear Induced Plasma and Problems of Nuclear Pumped Lasers. Obninsk: FEI; 1993. vol. 2. pp. 241–247.

[91] Konak A.I., Mel'nikov S.P., Porkhaev V.V., Sinyanskii A.A. Characteristics of nuclear-pumped lasers based on the 3p–3s transitions in the neon atom. Quantum Electron. 1995;25:209–214.

[92] Bochkov A.V., Kryzhanovskii V.A., Magda E.P., Mukhin S.L. Quasi-cw lasing at λ = 585.2 nm in an Ne–H_2 mixture. Tech Phys Lett. 1993;12:750–751.

[93] Hebner G.A. Fission-fragment excitation of the high-pressure atomic neon laser at 703.2 and 724.5 nm. J Appl Phys. 1993;74:2203–2207.

[94] Aleksandrov A.Y., Dolgikh V.A., Kerimov O.M., et al. Basic mechanisms of inversion of the 3p–3s transitions of neon. Quantum Electron (Sov J). 1987;17:1521–1526.

[95] Shon J.W., Rhodes R.L., Verdeyen J.T., Kushner M.J. Short pulse electron beam excitation on the high-pressure atomic Ne laser. J Appl Phys. 1993;73:8059–8065.

[96] Andriyakhin V.M., Vasil'tsov V.V., Krasilnikov S.S., et al. On emission of the gas mixture Hg–He^3 irradiated by neutron flux. JETP Lett (Sov J). 1970;12:58–60.

[97] Akerman M.A., Miley G.H., McArthur D.A. A helium–mercury direct nuclear pumped laser. Appl Phys Lett. 1977;30:409–412.

[98] Batyrbekov G.A., Khasenov M.U., Soroka A.M., et al. Kinetics of excited states of Hg pumping by ionizing radiation. Preprint Inst Nucl Phys. 1987;3/87, Alma-Ata, Kazakhstan, (in Russian).

[99] Yakovlenko S.I., Karelin A.V. Kinetics of the active media of high-pressure metal-vapor lasers. Quantum Electron. 1993;23:545–563.

[100] Dmitriev A.B., Il'yashenko V.S., Mis'kevich A.I., Salamakha B.S. Spectroscopy of ^{3}He–Hg and ^{3}He–Kr–Hg high-pressure plasmas excited by ^{3}He(n,p)T reaction products. Opt Spectrosc (Sov J). 1979;47:34–36.

[101] Djeu N., Burnham R. Optically pumped CW Hg laser at 546.1 nm. Appl Phys Lett. 1974;25:1350–1351.

[102] Dmitriev A.B., Il'yashenko V.S., Mis'kevich A.I., et al. Excitation of laser transitions in parametallic gas mixtures using reaction products from nuclear reactions. Tech Phys (Sov J). 1982;27:1373–1374.

[103] Bochkov A.V., Kryzhanowskii V.A., Magda E.P., et al. Quasi-cw lasing on the 7^3S_1–6^3P_2 atomic mercury transition. Tech Phys Lett. 1992;18:241–243.

[104] Barysheva N.M., Bochkova N.V., Kosorukova A.A., Magda E.P. Kinetic model of He–Xe–Hg–H_2 laser with nuclear pumping. In: Proceedings of the 3rd International Conference on "Problems of Lasers with Nuclear Pumping and Pulsed Reactors". Snezhinsk: VNIITF; 2002. pp. 218–224 (in Russian).

[105] Rhoades R.A., Verdeyen J.T. Electron beam pumping of the 546.1 nm mercury laser. Appl Phys Lett. 1992;60:2951–2953.

[106] Mis'kevich A.I., Dmitriev A.B., Il'yashenko V.S., et al. Lasing of Cd vapor excited by the products of the nuclear reaction ^{3}He(n,p)T. Tech Phys Lett (Sov J). 1980;6;352–355.

[107] Mis'kevich A.I., Il'yashenko V.S., Salamakha B.S., et al. Lasing at wavelength 441.6 nm in a high-pressure ^{3}He–^{116}Cd mixture. Tech Phys (Sov J). 1982;27;260–262.

[108] Baltayan P., Peboy-Peyroula J.C., Sadeghi N. Determination of the rate constants for population of the individual Cd^{+*} levels in the thermal Penning and charge-transfer reactions of $He^*(2^3S)$ and He^+ with cadmium. J Phys B. 1985;18:3615–3628.

[109] Novoselov Yu.N., Tarasenko V.F., Uvarin V.V., Fedenev A.V. Influence of impurities and of pump power on the operational characteristics of a high-pressure He–Cd laser. Quantum Electron. 1996;26:205–210.

[110] Kopai-Gora A.P., Mis'kevich A.I., Salamakha B.S. Quasi-cw generation on the ZnII Beitler transition in dense ^{3}He–Zn plasma. Tech Phys Lett (Sov J). 1990;16:348–351.

[111] Bugaev S.P., Goryunov F.G., Nagornyii D.Y., et al. UV generation by electron beam pumping of He–Cd mixture. Opt Spectrosc (Sov J). 1988;65:442–445.

[112] Karelin A.V., Shirokov R.V. Kinetics of the active medium of a nuclear-pumped laser based on transitions in the cadmium atom. Quantum Electron. 1998;28:893–897.

[113] Khasenov M.U. Emission of the ^{3}He–Xe–Cd mixture in the active zone of a nuclear reactor. Quantum Electron. 2004;34:1124–1126.

[114] Basov N.G., Aleksandrov A.Y., Danilychev V.A., et al. Efficient high-pressure quasi-cw laser using the first negative system of nitrogen. JETP Lett (Sov J). 1985;42:47–50.

[115] Aleksandrov A.Y., Dolgikh V.A., Rudoi I.G., et al. Energy characteristics of visible-range and UV lasers based on the first negative system of nitrogen. Pis'ma v Zhurnal Tekhnicheskoi Fiziki. 1987;13:1370–1373 (in Russian).

[116] Barysheva N.M., Bochkov A.V., Bochkova N.V., et al. First nuclear-pumped ultraviolet laser. Tech Phys Lett. 1996;22:636–637.

[117] Dyuzhov Y.A., Poletaev E.D., Smol'skii V.N. Investigation of lasing on transitions of the first negative system of nitrogen (λ = 391.4, 428.1 nm) in the He–N_2–H_2-mixtures pumped by fission fragments from the pulse reactor BARS-6. In: Proceedings of the 4th International Conference "The physics of nuclear-pumped lasers and pulsed reactors". Obninsk: FEI; 2009. vol. 1. pp. 151–155 (in Russian).

[118] Budnik A.P., Kuznetsova E.A. Mathematical modeling of the lasing characteristics of a helium–nitrogen–hydrogen laser medium from the pressure of the mixture and the specific power of energy input. In: Proceedings of the 4th International Conference "The physics of nuclear-pumped lasers and pulsed reactors". Obninsk: FEI; 2009. vol. 1. pp. 160–166 (in Russian).

[119] Bochkov A.V., Zagidulin A.V., Magda E.P., et al. Effect of deuterium and neon on the laser parameters to the first negative system of nitrogen. In: Proceedings of the 4th International Conference "The physics of nuclear-pumped lasers and pulsed reactors". Obninsk: FEI; 2009. vol. 1. pp. 319–321 (in Russian).

[120] Aleksandrov Yu., Dolgich V.A., Kerimov O.M., et al. Effective collision lasers in the visible and UV regions of spectrum. Izvestija Akademii Nauk SSSR, Ser Phys. 1989;53:1474–1483 (in Russian).

[121] Khasenov M.U. Kinetics of the nitrogen first negative system excitation by ionising radiation. Quantum Electron. 2005;35:1104–1106.

[122] Waller R.A., Collins C.B., Cunningham A.J. Stimulated emission from CO^+ pumped by charge transfer from He_2^+ in the afterglow of an e-beam discharge. Appl Phys Lett. 1975;27:323–325.

[123] Khasenov M.U., Dolgich V.A., Soroka A.M. Kinetics of CO first negative system excitation by ionized radiation. Abstracts of Specialist Conference on "Physics of nuclear induced plasmas and problems of nuclear pumped lasers. Obninsk: FEI; 1992. p. 224.

[124] Khasenov M.U. Kinetics of CO first negative system excitation by ionized radiation. Proc SPIE. 2004;5483:14–23.

[125] Barysheva N.M., Bochkova N.V., Kosorukova A.A., Magda E.P. Kinetics of nuclear-pumped lasers on ultraviolet electronic transitions in molecular ions. In: Proceedings of the 3rd International Conference "Problems of Lasers with Nuclear Pumping and Pulsed Reactors". Snezhinsk: VNIIEF; 2002. pp. 51–55 (in Russian).

[126] Pearse R.W.B., Gaydon A.G. The identification of molecular spectra. 2nd ed., New York: Wiley; 1950. 276 p.

[127] Rhodes C.K., editor. Excimer lasers. 2nd ed. Berlin: Springer-Verlag; 1984. 271 p. DOI: 10.1007/3-540-13013-6.

[128] Yakovlenko S.I., Karelin A.V., Morovov A.P., et al. Investigation of an XeF laser pumped by gamma radiation from a nuclear explosion. Quantum Electron. 1996;26:410–412.

[129] Ulrich A., Adonin A., Jacoby J., et al. Excimer laser pumped by an intense, high-energy heavy-ion beam. Phys Rev Lett. 2006;97:153901.

[130] Hays G.N., McArthur D.A., Neal D.R., Rice J.K. Gain measurements near 351 nm in $^3He/Xe/NF_3$ mixtures excited by fragments from the $^3He(n,p)^3H$ reaction. Appl Phys Lett. 1986;49:363–366.

[131] Bochkov A.V., Kryzhanowskii V.A., Magda E.P., et al. Investigation of the characteristics of excimer laser media. In: Proceedings of the Specialist Conference "The Physics of Nuclear-Excited Plasma and the Problems of Nuclear-Pumped Lasers". Arsamas-16:VNIIEF; 1995. vol. 1. pp. 154–161.

[132] Yakovlenko S.I., Karelin A.V., Boichenko A.M. Calculation of the threshold characteristics of a nuclear-pumped Ne–Xe–NF_3 laser. Quantum Electron. 1995;25:521–524.

[133] Mavlyutov A.A., Miskevich A.I. Nuclear-pumped excimer laser with a wavelength of 308 nm. Tech Phys Lett. 1996;22:326–327.

[134] Khasenov M.U., Nakiskozhaev M.T., Syrlybaev A.S., Smirnova I.I. Emission of inert gas halides at excitation by alpha-particles. Atmos Ocean Opt. 2009;22:1057–1059 (in Russian).

[135] Mis'kevich A.I., Guo Jinbo, Dyuzhov Yu.A. Spontaneous and induced emission of XeCl* excimer molecules under pumping of Xe–CCl_4 and Ar–Xe–CCl_4 gas mixtures

with a low CCl_4 content by fast electrons and uranium fission fragments. Quantum Electron. 2013;43: 1003–1008.

[136] Batyrbekov G.A., Khasenov M.U., Kuzmin Yu.E., et al. Radiation resistance of elements of the laser system in the core of nuclear reactor. Izvestija Akademii Nauk KazSSR, Phys Math Ser. 1986;6:23–26 (in Russian).

[137] Batyrbekov G.A., Khasenov M.U., Kostriza S.A., et al. Feasibility of excimer lasers with ionization by radiation from a nuclear reactor. Tech Phys Lett (Sov J). 1982;8:789–791.

[138] Treanor C.E., Rich J.W., Rehm R.J. Vibrational relaxation of anharmonic oscillators with exchange-dominated collisions. J Chem Phys. 1968;48:1798–1803.

[139] Jalufka N.W., Hohl F. A direct nuclear-pumped ^{3}He–CO–laser. Appl Phys Lett. 1981;39:139–142.

[140] Gudzenko L.I., Malyshevskii V.S., Yakovlenko S.I. CO laser pumping with high-energy particles. Tech Phys. 1978;23:1228–1231.

[141] Zherebtsov V.A. Nuclear pumping of a carbon monoxide laser. Tech Phys. 1998;43:818–823.

[142] Mann M.M., Rice D.K., Eguchi R.G. An Experimental Investigation of High Energy CO lasers. IEEE J Quantum Electron. 1974;QE-10:682–685.

[143] Jalufka N.W. Direct nuclear excitation of a ^{3}He–CO_2 mixture. Appl Phys Lett. 1981;39:190–192.

[144] Hassan H.J. Kinetics of a CO_2 nuclear pumped laser. AIAA J. 1980;18:1221–1222.

[145] Batyrbekov G.A., Danilychev V.A., Kovsh I.B., Mardenov M.P., Khasenov M. Preionization CO_2 laser operating in the active zone of a stationary nuclear reactor. Quantum Electron (Sov J). 1977;7:667–668.

[146] Batyrbekov G.A., Danilychev V.A., Kovsh I.B., Khasenov M.U. Operation of a cooled electroionization CO laser in the active zone of a nuclear reactor. Tech Phys Lett (Sov J). 1979;5:345–346.

[147] Jongerius H.M., Van Koeveringe J.L., Oskam H.L. Argon–xenon bands. Physica. 1959;25:406–408.

[148] Friedl W. Krypton–Xenon Banden. Z Naturforsch. 1959;14A:848–848a.

[149] Tsuji M., Tanaka M., Nishimura Y. New emission spectra of $KrXe^+$ produced from Kr afterglow reactions of Xe. Chem Phys Lett. 1996;262:349–354.

[150] Kugler E. Über die Lumineszenze der Edelgasgemische Ar/Xe, Kr/Xe, Ar/Kr und der Gemische Xe/N_2 und Kr/N_2 bei Angerung mit schnellen Elektronen. Ann Phys Leipz. 1964;B14:137–146.

[151] Tanaka Y., Yoshino K., Freeman D.E. Emission spectra of heteronuclear diatomic rare gas positive ions. J Chem Phys. 1975;62:4484–4496.

[152] Millet P., Barrie A.M., Birot A., et al. Kinetic study of $(ArKr)^+$ and $(ArXe)^+$ heteronuclear ion emissions. J Phys Ser B. 1981;14:459–472.

[153] Batyrbekov G.A., Batyrbekov E.G., Tleuzhanov A.B., Khasenov M.U. Molecular band in an emission spectrum of Ar–Xe. Opt Spectrosc (Sov J). 1987;62:212–214.

[154] Millet P., Birot A., Brunet H., et al. Kinetic study of the $KrXe^+$ heteronuclear ion emissions. J Phys Ser B. 1983;16:1383–1392.

[155] Khasenov M.U. On the possibility of the creation of nuclear-pumped lasers on transitions of the heteronuclear ionic molecules of inert gases. In: Abstracts of Specialist Conference on "Physics of nuclear induced plasmas and problems of nuclear pumped lasers". Obninsk: FEI; 1992. pp. 351–352.

[156] Khasenov M.U. Emission of the heteronuclear ionic molecules $(ArXe)^+$ at excitation by a hard ionizer. Proc SPIE. 2006;6263:141–148.

[157] Khasenov M.U. Emission of ionic molecules $(KrXe)^+$ at excitation by a hard ionizer. J Appl Spectrosc. 2005;72:316–320.

[158] Laigle C., Collier F. Kinetic study of $(ArXe)^+$ heteronuclear ion in electron beam excited Ar–Xe mixture. J Phys Ser B. 1983;16:687–697.

Free-electron Laser

Chapter 8

Undulators for Short Pulse X-Ray Self-Amplified Spontaneous Emission-Free Electron Lasers

K. Zhukovsky

Additional information is available at the end of the chapter

http://dx.doi.org/10.5772/64439

Abstract

We review the synchrotron type radiation sources with focus on undulator and free-electron laser (FEL) schemes, aimed on working in X-ray range and ultra-short time interval. Main FEL schemes, useful for generation of high frequency radiation, extending to X-rays, are presented. High harmonic generation is explored. The advantages and disadvantages of single pass and of multipass designs are discussed. The viable ways to reduce the duration of the pulse, with the goal to generate femtosecond pulses, are indicated. Future developments of X-ray FELs (X-FELs) and the ways to improve the quality of the FEL radiation in this context are discussed.

Keywords: undulator radiation, harmonics generation and broadening, homogeneous and inhomogeneous losses, free-electron laser

1. Introduction

Synchrotron radiation (SR) and undulator radiation (UR) have been attracting researcher's attention for more than half a century. The reasons for that varied with time passing as the challenges for the scientists evolved and the technical progress stepped forward. UR was predicted [1] and then discovered [2] in the middle of the twentieth century. During the following 70 years, the study of the radiation, emitted by ultra-relativistic electrons, was performed, and the SR theory was refined; extensive theoretical studies of the electron motion in periodic magnetic fields of various configurations have been performed [3–7]. Now UR is

again in focus due to the request for coherent X-ray sources [8], while free-electron lasers (FELs) extend to X-range [9]. Both, SR and UR are due to the radiation of relativistic electrons, executing curved trajectories [10]. The difference between them is in the length on which the radiation is formed: short part of the circle for UR and the full length of the undulator for the UR. This determines the fundamental difference in the quality of the radiation obtained from these two sources: short pulses with very broad spectrum for the SR and relatively long-lasting radiation bursts with narrow spectrum for the UR. Nowadays, the research frontier is represented by studies of ultra short attosecond time intervals and Röntgen range [11, 12]. To achieve these characteristics, the devices require extremely high quality and intense magnetic fields, long undulators with many periods. To obtain high frequency radiation, sometimes undulator periodic structures with double or even triple period are used [13–18], facilitating control over high harmonics and regulating their emission [6, 19]. Maintaining best quality UR line is important. Nowadays, electron accelerators provide ultra fast and high coherent electron beams and intense emission even in Röntgen range. Modern undulators allow for the harmonic emission regulation [19], which can be achieved by superimposing different periodic magnetic fields in many period undulators. It should be noted that in long undulators the distortions of the magnetic field and of unavoidable inhomogeneities of periodic magnetic field have very strong effect on the operation of the devices. High gain in undulators is essential in FEL with self-amplified spontaneous emission (SASE), with high-gain harmonic generation (HGHG), and in other modern schemes. The quality of the electron beams, fed into the undulators, is extremely important for such new FELs [20], in particular at high frequencies. The requirements for the periodicity of the field are particularly rigid in long undulators [21]. Deviation from the ideal oscillatory trajectories of electrons results in degradation of the beam quality and of the FEL output in terms of power, brightness FEL gain. Therefore, the emitted UR can be exploited for diagnosing the quality of the undulator itself.

The radiation spectrum lines from undulators inevitably broaden due to a number of reasons, first of all due to the electron beam energy spread and the beam divergency, as well as due to inhomogeneity of the periodic magnetic field in undulators. They may have internal or external origin [22–26], but their presence is eminent also due to the fact that the ideal $\vec{H} = H_0 sin(2\pi z / \lambda)$ periodic magnetic field simply does not satisfy Maxwell equations. The electron energy spread is the most common detrimental factor; some researchers even concluded that the spectral properties of higher UR harmonics should be limited only by the electron beam properties and not by the undulators [24]. The role of the divergence was underlined, for example, in Refs. [22, 27]. At the same time the constant magnetic field shifts the resonance frequencies and causes loss of intensity [28–31].

The demand for radiation with specific properties and high requirement to the UR and undulator quality stimulated analytical study of their spectral properties [32–39]. There appear generalized Bessel and Airy functions naturally, as well as in other mathematical problems of radiation, emitted by charges, executing complicated oscillating trajectories. The mathematical apparatus of inverse differential operators and orthogonal polynomials was developed for treating broad spectrum of physical problems, which include radiation and propagation of

electron beams [40–45]. The contributions of all sources of broadening in various undulator schemes were analyzed by means of precise analytical treatment of the UR, employing extended forms of special functions of Airy and Bessel types [34–37, 39, 42]. In these works, the role of the various broadening terms, accounting for the real size and the emittance of the electron beam, for the energy spread and for the constant field component, was explored. It was shown that the undulator length has strong detrimental effect on the spontaneous harmonic emission; partial compensation of the beam divergences by constant magnets was also demonstrated.

2. Synchrotron radiation, undulator radiation, and free-electron lasers

Charged particle radiates energy in the form of electromagnetic radiation when it accelerates. Following relativistic Lorentz transforms $\tan\theta = \frac{\sin\theta'}{\gamma(\beta + \cos\theta')}$, it is easy to conclude that the radiation emission of the relativistic electron is focused in the narrow angle $\theta \approx \frac{1}{\gamma}$ (see, for example, [46]). While the charge is moving on a circular orbit of radius R, it emits SR in a narrow cone of emission, which illuminates the receiver for a very short period of time, while passing from the point A to the point B. Lorentz transforms is applied to the period of time in the reference frames, related to the electron and to the observer and yield the time of the SR pulse $\Delta t = \frac{m}{2eB\gamma^2} = \frac{R}{2c\gamma^3}$, where $R \cong \frac{\gamma mc}{eB}$. For the UR, it is not so, since it is gathered all along the undulator and the characteristic length then equals that of the undulator, by far exceeding the arc, from which the SR, reaching the user, is gathered. Denoting the unit vector $\vec{n} = \vec{R}/R$ and $\vec{n} \cong (\psi\cos\phi,\ \psi\sin\phi,\ 1-\psi^2/2)$, it is easy to obtain the wavelength of the radiation, emitted off the axis in the angle θ

$$\lambda_n = \frac{\lambda_u}{2n\gamma^2}\left(1 + \gamma^2\left\langle\theta^2\right\rangle + \gamma^2\psi^2\right) \tag{1}$$

from the simple condition of positive interference of the wavelengths, emitted on each magnetic poles of the undulator. Since the SR from a relativistic charge is emitted in a narrow cone, which includes the undulator axis all the time, the electron drifts in the undulator at relativistic speed, if the electrons transversal oscillations are small. At the exit of the undulator the intense radiation appears (see **Figure 1**).

The spectral range of SR and UR extends up to Röntgen band. However, due to the fact that the SR is perceived as a very short pulse, its spectral range is very broad, starting from the synchrotron frequency $\omega_0 = v/R$, while the UR has few harmonics and in some cases, such as that of a spiral undulator, it can contain a single harmonic.

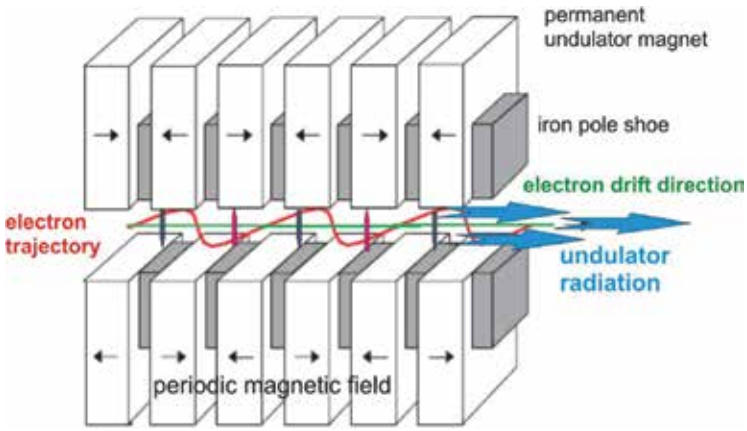

Figure 1. Schematic drawing of a planar undulator.

For spontaneous radiation, emitted by an electron, the undulator selects resonant UR wavelengths. The idea about it can be given by the simple consideration, demonstrated in **Figure 2**, where electric fields for two resonant wavelengths λ_n at the fundamental ($n = 1$; red) and at the third harmonics ($n = 3$; blue) are shown. A non-resonant electric field for the second harmonic is shown in green. The fundamental and the third harmonics are phase-matched with the electron after one undulator period as highlighted in **Figure 2**. The electron trajectory is drawn in gray. Such a phase matching of the radiation proceeds on each next undulator period. Thus, the radiation from one electron constructively interferes over many periods, and in this sense we obtain coherent radiation from one electron along the whole length of the undulator.

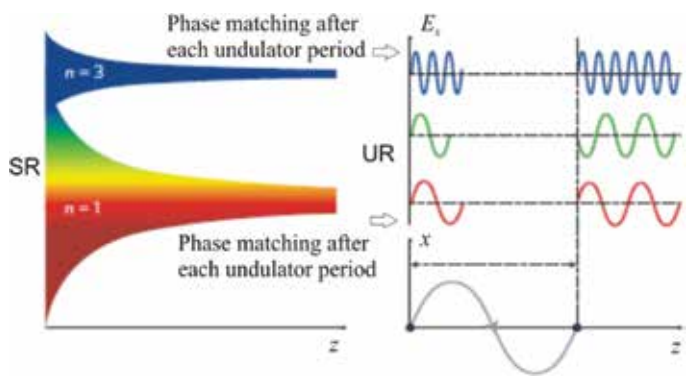

Figure 2. Undulator selects resonant frequencies for the emitted SR.

The following conditions are common in modern undulators: the electrons are ultrarelativistic, which is natural in contemporary accelerators, they have small transverse momentum, and the electric field is absent:

http://dx.doi.org/10.5772/64439

$$\gamma >> 1, \beta_{\perp} << 1, H_{||} << H_{\perp}, \vec{E} = 0 \tag{2}$$

The UR from a planar undulator with N periods of λ_0 with the undulator parameter $k = \frac{e}{mc^2}\frac{H_0}{k_\lambda}$, where $k_\lambda = 2\pi/\lambda_u$, λ_u is the undulator period, $H_y = H_0 sin(k_\lambda z)$ is the sinusoidal magnetic field, has the following peak frequencies:

$$\omega_n = n\omega_R = \frac{2n\omega_0\gamma^2}{1+\frac{k^2}{2}+(\gamma\psi)^2}, \omega_{R0} = \frac{2\omega_0\gamma^2}{1+k^2/2}, \omega_{n0} = n\omega_{R0}, \tag{3}$$

where $\omega_0 = k_\lambda \beta_z^0 c$, $\beta_z^0 = 1 - \frac{1}{2\gamma^2}\left(1+\frac{k^2}{2}\right)$ is the average drift speed of the electrons along the undulator axis, $k \approx H_0\lambda_0$ $[Tcm]$ and ψ is off the undulator axis angle. The shape of the UR emission line is described by the $\frac{sin(\nu_n/2)}{\nu_n/2} = sinc\frac{\nu_n}{2}$ function, dependent on the detuning parameter

$$\nu_n = 2\pi Nn\left(\frac{\omega}{\omega_n}-1\right). \tag{4}$$

The homogeneous bandwidth, sometimes called half-width of UR spectrum line at its half-height or simply half-width, is $\frac{1}{2nN}$ and the half-width equals

$$\frac{\Delta\omega}{\omega_{n0}} = \frac{\omega-\omega_{n0}}{\omega_{n0}} = \frac{1}{nN}. \tag{5}$$

In real devices $\frac{1}{nN} << 1$. The emitted wavelength $\lambda_n = 2\pi/k_n$ can be expressed through the speed of the electrons in the undulator as follows:

$$\lambda_n = \frac{\lambda_1}{n} = \frac{\lambda_u}{n}\left(\frac{1-u/c}{u/c}\right) \cong \frac{\lambda_u}{2n\gamma^2}\left(1+\tilde{k}^2\right), \tag{6}$$

where λ_u is the undulator period, u is the electron speed

$$u = c\left(1-\left(1+\tilde{k}^2\right)/2\gamma^2\right), \tag{7}$$

The undulator parameter is k or $\tilde{k}$:

$$\tilde{k}^2 \equiv \frac{k^2}{2} = \gamma^2 \beta_\perp^2 = \gamma^2 \left\langle \theta^2 \right\rangle, k = eH_0 \lambda_u / 2\pi mc^2, \tag{8}$$

θ is the off-axis angle, which in essence indicates how much the electron deviates from the axis in its motion along the undulator due to transversal oscillations, caused by the periodic magnetic field. In real conditions for a weak undulator $k \sim 1$, while for wiggler or strong undulator $k \sim 10$. Thus, for a weak undulator the radiation is essentially directed all along the undulator axis, while for the wiggler, it is in much wider angle. Considering $n = 1$, i.e., the fundamental harmonic, we write $u = ck_1/(k_1 + k_u)$, $k_1 = 2\pi/\lambda_1$. Both SR and spontaneous UR are incoherent. In the full spectrum of the radiation, the components, whose wave length is longer than the bunch length, are coherent, while the radiation of the length, significantly exceeding the size of the bunch, is approximately coherent. The region of coherent radiation will enlarge as the bunch gets shorter. The difference between the radiations, emitted by various SR sources, is demonstrated in **Figure 3**. It shows how the radiation intensity and the degree of coherency of the emitted radiation varies from one device scheme to the other; $\boldsymbol{N}_f$ is the number of emitted photons, $\boldsymbol{N}_e$ is the number of the electrons in the beam, $\boldsymbol{N}$ is the number of undulator periods. For SR from a bending magnet, the intensity is roughly proportional to the number of electrons emitting photons in a bending magnet. Wiggler, or strong undulator, is essentially a number of bending magnets, where electrons deviate significantly from the axis; the character of the radiation remains that from the bending magnets, but the intensity is $\boldsymbol{N}$ times higher. The radiation is incoherent. In a weak undulator, where the electrons slightly oscillate in transversal to the axis plane, so that the cone of the emission of the radiation always includes the undulator axis, the radiation of one single electron is coherent along the undulator axis, but the radiation of the bunch of electrons is incoherent in between them. The intensity of the radiation is proportional to $\boldsymbol{N}^2$. In free-electron laser, the electrons within a bunch emit largely coherent radiation, which transforms into a significant increase of the intensity $\boldsymbol{N}_f \sim (\boldsymbol{N}_e \boldsymbol{N})^2$.

New type of radiation source—X-ray free-electron laser (X-FEL)—provides a combination of sub-picosecond pulse duration of a conventional laser with the X-ray wavelength of a synchrotron radiation source. Practical research potential of short wave radiation in nature and in technology can hardly be overestimated. Indeed, wavelength about 200 nm allows study of viruses, the scale of an atomic corral is ~14 nm, and the wavelength of 1–2 nm gives the potential to resolve DNA helix width and carbon nanotubes, while shorter wavelengths could visualize the small molecules, such as water molecule, and atoms. On the other hand, studies of processes at mircoscale often require very short time resolution. Indeed, the processes of a water molecule dissociation takes as short time as 10 fs, Bohr period of valence electron is ~1 fs, shock wave propagates by 1 atom in 100 fs, and electron spin processes in the magnetic field of 1 T within 10 ps. Thus, it is of great practical importance to have a device, which produces radiation with a combination of very short wavelength and short duration. One of the most prominent devices of such a kind is a free-electron laser.

http://dx.doi.org/10.5772/64439

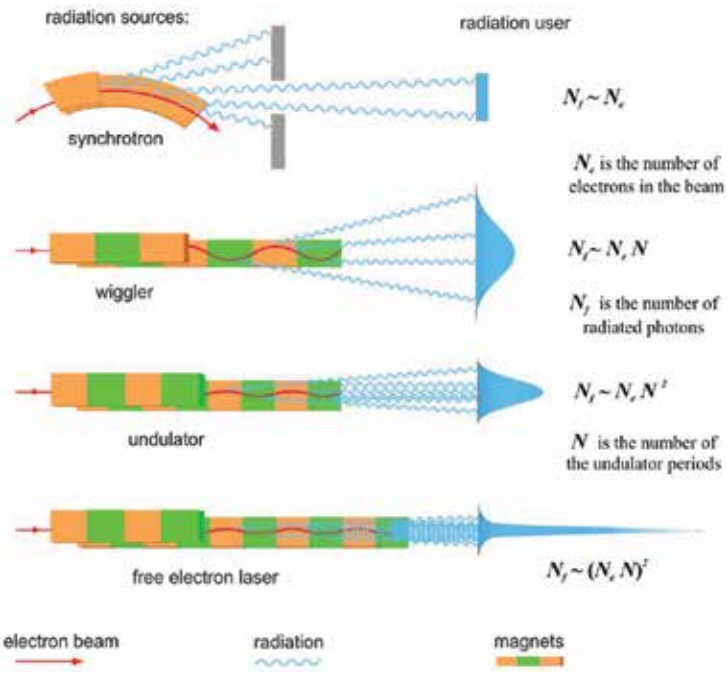

Figure 3. Different sources of SR: synchrotron, wiggler, undulator, and free-electron laser.

3. Keynotes on free-electron lasers

In 1971, Madey published a theory of the FEL [47], where he described a small gain process in a system: relativistic electron beam/undulator. In his study he hypothesized that it could generate coherent X-ray radiation. Few years later the first demonstration of FEL amplification and lasing was performed in a low-gain infrared oscillator FEL at Stanford. At approximately the same time, Colson and Hopf described classically the FEL interaction, which had god quantum description by Madey before. Since 1970s, extensive classical description of the high-gain regime of FEL operation has been developed. Since the first X-rays were discovered by Wilhelm Röntgen in Würzburg in 1895, the peak "brilliance" of X-ray sources has increased by ~16 orders of magnitude. The so-called first-generation synchrotron sources were in fact particle accelerators, designed for experiments in high-energy physics. The second-generation labs were custom-built facilities, while the third-generation sources at labs such as the European Synchrotron Radiation Facility (ESRF) feature undulators, emitting light in a very narrow cone. The fourth generation of synchrotron-radiation sources includes free-electron lasers.

To account for the processes, which occur in a free-electron laser, we need to understand the fundamental difference between the coherent and non-coherent radiation, emitted by many electrons, which pass through undulator at the same time. The power, emitted by electrons

$$P \propto \left| \sum_{j=1}^{N_e} E_j e^{i\varphi_j} \right|^2 = \sum_{j=1}^{N_e} E_j^2 + \left| \sum_{j=1, j\neq k}^{N_e} \sum_{k=1}^{N_e} E_j E_k e^{i(\varphi_j + \varphi_k)} \right|^2, \tag{9}$$

where φ_j are the relative phases of the emitted radiation electric fields E_j in a system of big number of electrons $N \gg 1$, includes two terms. For a system with uncorrelated phases, the terms in the second double sum, which is of the order of ~N^2, tend to destructively interfere. This happens in incoherent spontaneous UR sources. Total power emitted then approximately equals to the sum of the powers from the N independent scattering electrons, which originates from the first term in Eq. (9). For correlated phases of the electric fields, we have $\varphi_j \approx \varphi_k$ for all the electrons and then the coherent second term ~N^2 contributes. For it to happen, the electron sources must be periodically bunched at the resonant radiation wavelength. **Figure 4** demonstrates how incoherent radiation from a bunch of electrons in an undulator becomes coherent toward the undulator's end. Indeed, at the beginning, the electrons in the bunch enter the undulator with initially random phases, which ensures that mostly incoherent radiation is emitted at the resonant radiation wavelength. Because of the electrons interact collectively with the radiation they emit, small coherent fluctuations in the radiation field grow along the undulator length and simultaneously begin to bunch the electrons at the resonant wavelength. This collective process continues until the electrons are strongly bunched toward the end of the undulator, where the process saturates and the electrons begin to de-bunch.

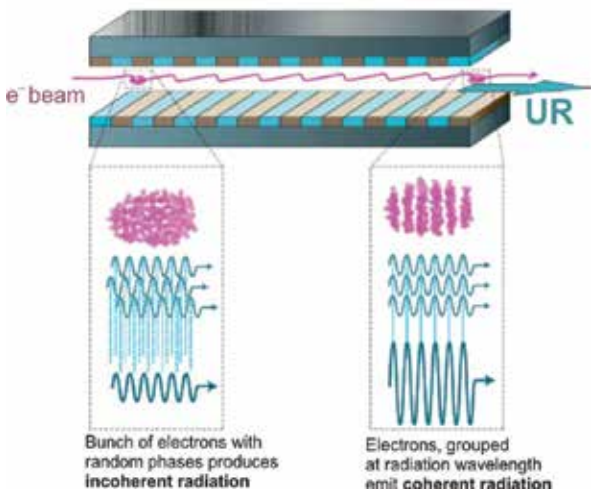

Figure 4. From incoherent to coherent emission along the undulator length.

Behind this phenomenon stands a simple physical mechanism, which is based on the fact that the speed of electrons, while being close to that of the radiation, is still smaller, and, therefore, the electrons appear behind its radiation, propagating in the undulator. It can be best illustrated in **Figure 5**.

http://dx.doi.org/10.5772/64439

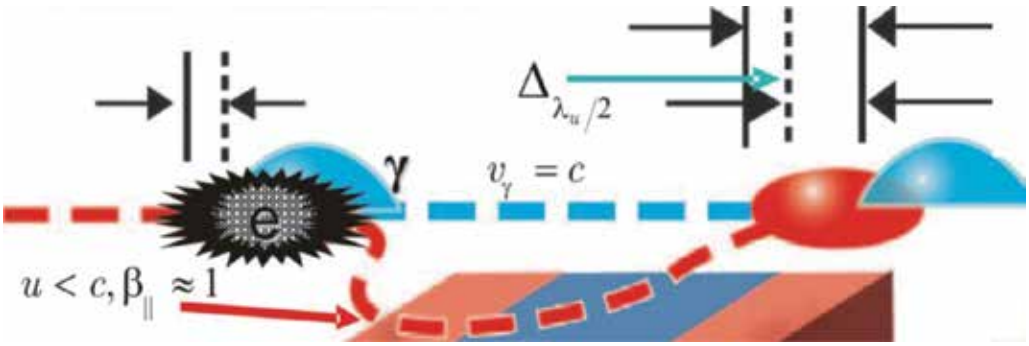

Figure 5. Slippage of the radiation and the electron bunch in FEL.

Indeed, the photons move at the speed of light $v_\gamma = c$, while the electrons move at the speed $u < c$, $\beta_{||} \approx 1$, i.e., slower than photons. Therefore a full slip between the electron bunch and the photon pulse accumulates along the length of the undulator and reads as follows:

$$\Delta = (1 - \beta_{\|}) N \lambda_u \cong N\lambda, \tag{10}$$

where λ is the emitted wavelength $\lambda = \frac{\lambda_u}{2\gamma^2}\left(1 + \frac{k^2}{2}\right)$ and the parallel component of the β is $\beta_{||} \cong 1 - \frac{1}{2\gamma^2}\left(1 + \frac{k^2}{2}\right)$. Thus the slip on the whole undulator length is N times the emitted wavelength. Respectively, the slip on a distance, equal half an undulator period equals half of the emitted wavelength:

$$\Delta_{\lambda_u/2} = N\lambda/(2N) = \lambda/2. \tag{11}$$

In other words, as the radiation wave travels over a distance $\lambda/2$ in a time $\lambda/(2c)$, the electron travels over a smaller distance $u\lambda/(2c)$, and on one undulator period the electrons slip, respectively, to the photons by one emitted wavelength. The whole photon packet, having a higher velocity that the electrons, slips over the electron packet and the wave emitted by the electrons on a certain undulator period comes in phase with the wave, emitted on the next undulator period. To illustrate the formation of microbunches, which lead to coherent radiation of the electrons within a bunch, we present the following explanation in **Figure 6** (see [48]).

Suppose we have the magnetic field B_w of the already existing electromagnetic wave. Then its interaction with the electron transverse velocity v_t creates Lorentz force F_{bunch}, which we denote as f for brevity (see **Figure 6**). This force pushes the electron toward a wave node as seen in **Figure 6**. After the electron travels over one-half undulator period, its transverse velocity becomes reversed. In the meantime the electromagnetic wave travels ahead of the electron by one-half wavelength as follows from (10) and (11). Its field B_w is now also reversed, so that the

Lorentz force keeps its direction and the microbunching continues. For the charge, which is ahead with respect to the microbunch, which is in the wave node (see **Figure 6**), the Lorentz force F_{bunch} or f pushes the charge back to the node, thus grouping electrons in a bunch at the wave node. So it proceeds on other periods, because while the electrons move through a full oscillation period λ_u, the electromagnetic wave propagates by λ_u plus one wavelength λ. Consequently, the transverse movement of each electron has a constant phase with respect to the electromagnetic field.

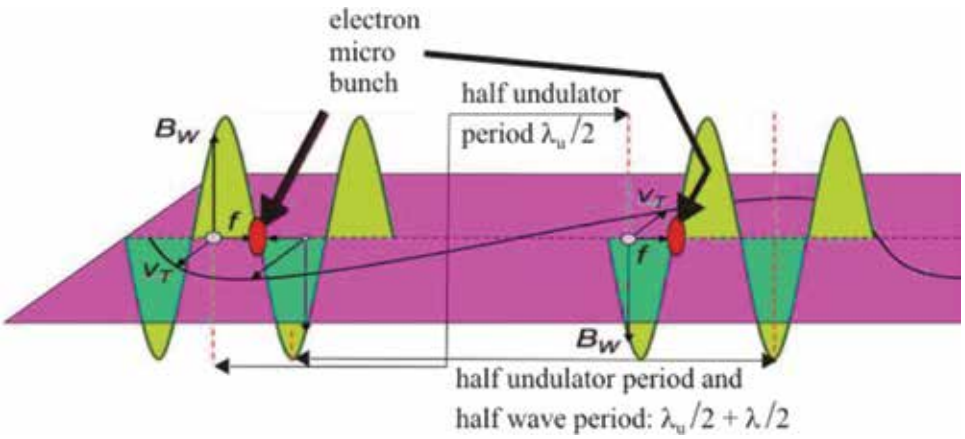

Figure 6. Interaction of the radiation with the electrons and formation of microbunches.

4. Correlated amplification in FEL

Amplification in FEL occurs because of the energy is transferred from the electrons to the previously emitted waves. This effect is due to the negative work of the force, produced by the transverse electric field of the wave, since the magnetic field of the wave does not work. The time rate of the energy transfer for a single electron is proportional to the product $E_W v_t$, where E_W is the electric field of the radiation wave and v_t is the electron transverse velocity. Then $E_W \propto I^{1/2}$, where I is the wave intensity and $dI/dt \propto I^{1/2} v_t$. Note that uncorrelated combination of the effects of individual electrons would not lead to an exponential increase of the intensity with the distance (or time), but to a quadratic law: $I(z) \propto z^2$. Transverse velocity and the field B produce longitudinal Lorentz force $F_{\text{bunch}} = v_t B_W$, which pushes the electrons and forms microbunches. This force is proportional to the transverse electron velocity, and it is also orthogonal to the wave field B of the strength B_W. Since $B_W \propto I^{1/2}$, the microbunching force is also proportional to $I^{1/2}$: $B_{\text{bunch}} \propto I^{1/2}$. We now assume that this force enhances the correlated emission by a factor, proportional to the microbunching force. Multiplied by the energy

http://dx.doi.org/10.5772/64439

transfer rate for each electron, this factor gives $dI/dt = AI$, A = constant. Proceeding on the supposition that $A = u/L_G$, where L_G is the gain length, we obtain the exponential growth:

$$I = I_0 \exp\left(\frac{ut}{L_G}\right) = I_0 \exp\left(\frac{z}{L_G}\right). \tag{12}$$

The exponential gain only occurs after bunching is established. This process continues until the saturation is reached. Provided at the beginning, the initial position of the electron, respectively, the existing wave, is favorable for the energy transfer from the electron to the wave and the direction of the electron transverse velocity, respectively, to the wave electric field E result in negative work, the electron energy is successfully transferred to the wave. This results in the decrease in the electron energy and of the longitudinal speed of the electron u, which becomes $u - \Delta u$. This decrease in longitudinal speed in its turn changes the above conditions, making them less favorable for the energy transfer from the electron to wave. At a certain point, as this process continues and the electron speed reduction Δu becomes more and more significant, the electrons can give no more energy to the wave and the wave starts giving its energy to the electrons of the beam. It increases the electron speed u and restores the favorable for the energy transfer from the electrons to the wave conditions. Thus, in this regime the exponential wave energy growth is over and instead the energy oscillates between the wave and the electrons.

To find the amplification value, we must evaluate v_t and the degree of bunching. The transverse speed of the electron reads as follows:

$$v_t = \left(\frac{euH_0}{\gamma m_0}\right)\left(\frac{\lambda_u}{2\pi u}\right)\cos\frac{2\pi ut}{\lambda_u}. \tag{13}$$

The energy transfer rate by a single electron to preexisting wave is proportional to $I^{1/2}H_0\lambda_u/\gamma$; the field B_W of the electromagnetic wave is proportional to the square root of the wave intensity $B_W \propto I_0^{1/2}\exp(ut/2L_G)$. Then the bunching force, which is the longitudinal force, can be written as follows:

$$F_{\text{bunch}} = \text{const} \times \left(\frac{H_0\lambda_u}{\gamma}\right) I_0^{1/2} \exp\left(\frac{ut}{2L_G}\right), \tag{14}$$

which, in turn, yields the following equation of motion for longitudinal mass $\gamma^3 m$:

$$\gamma^3 m\frac{d^2\Delta x}{dt^2} = F_{\text{bunch}} = \text{const}\times\left(\frac{H_0\lambda_u}{\gamma}\right)I_0^{1/2}\exp\left(\frac{ut}{2L_G}\right). \tag{15}$$

The bunching force F_{bunch} induces a small longitudinal electron displacement Δx:

$$\Delta x = \text{const}\times\frac{1}{\gamma^3}\frac{H_0\lambda_u}{\gamma}L_G^2 I_0^{1/2}\exp\left(\frac{ut}{2L_G}\right) = \frac{H_0\lambda_u L_G^2}{\gamma^4}I^{1/2}. \tag{16}$$

As discussed above, the electrons are concentrated in narrow slabs, separated from each other by a distance of the wavelength λ. The degree of microbunching, corresponding to the fraction of electrons that emit in a correlated way, can be assumed to be proportional to $(\Delta x/\lambda)$. The corresponding number of electrons is proportional to $\mathbf{N}_e(\Delta x/\lambda)$. Their contribution to the wave intensity reads as follows:

$$j\frac{\Delta x}{\lambda}\propto j\frac{I^{1/2}H_0\lambda_u L_G^2/\gamma^4}{\lambda_u/\gamma^2} = jI^{1/2}H_0L_G^2/\gamma^2, \quad j\equiv\frac{i}{\Sigma} = \frac{\text{current}}{\text{cross-section}}. \tag{17}$$

Microbunching effects correspond to a factor, proportional to the longitudinal microbunching force F_{bunch} and, therefore, proportional to ~ $I^{1/2}$, where I is the electromagnetic wave intensity. Multiplying this factor by the energy transfer rate for electrons, we obtain the total transfer rate as follows:

$$\frac{dI}{dt} = \text{const}\times j\frac{H_0L_G^2}{\gamma^2}I^{1/2}\left(I^{1/2}\frac{H_0\lambda_u}{\gamma}\right) = \text{const}\times j\frac{H_0^2\lambda_u L_G^2}{\gamma^3}I. \tag{18}$$

The solution of this equation reads $I = I_0\exp(z/L_G)$ and for ultrarelativistic electrons $u/L_G \cong c/L_G \propto jH_o^2\lambda_u L_G^2/\gamma^3$. Thus we obtain the FEL gain length

$$L_G = \text{const}\times j^{-1/3}H_0^{-2/3}\lambda_u^{-1/3}\gamma. \tag{19}$$

Gain length is related to the Pierce parameter as follows:

$$\rho = \frac{\lambda_u}{4\pi\sqrt{3}L_G}\propto j^{1/3}H_0^{2/3}\lambda_u^{4/3}\gamma^{-1} \tag{20}$$

http://dx.doi.org/10.5772/64439

which can be also written as $\rho = \frac{1}{2\gamma}\left(\frac{I_e}{I_A}\left(\frac{\lambda_u \tilde{k} f_B}{2\pi\sigma_r}\right)^2\right)^{1/3}$, where $I_A \cong 17$ kA is the Alfven current, I_e is the electron beam current, σ_r is the beam radius, $f_B(J_n)$ is the bunching coefficient, and J_n are the Bessel functions. The arguments and the varieties of the Bessel functions, in charge of the description of the harmonics of the UR, will be explored in what follows.

5. Cavity-based FELs

There are essentially two main types of design for FEL: cavity-based FELs and single-pass FELs. Cavity-based FELs exploit many passes of the UR in the undulator and use mirrors. Relativistic electron beam passes through periodic magnetic field of an undulator and the mirrors feed spontaneous emission back onto the beam. Consequently, the spontaneous emission is enhanced by the stimulated emission.

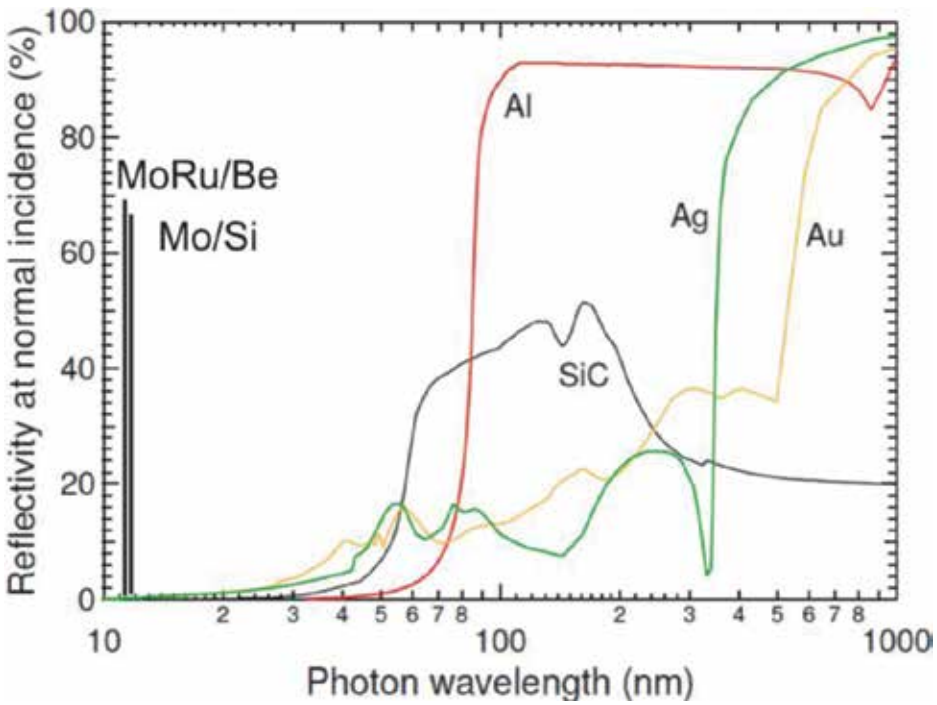

Figure 7. FEL mirror limitations.

Mirror design imposes limitations on the wavelength due to the mirror material. Common mirror materials limit the wavelength to IR-UV (see **Figure 7**). Recent improvements in materials and technology result in new multilayer X-ray reflective mirrors, which have the efficiency up to 70%, such as MoRu/Be mirrors have 69.3% reflectivity maximums at 11.43 nm, Mo/Si mirrors have 67.2% reflectivity peak at 13.51 nm.

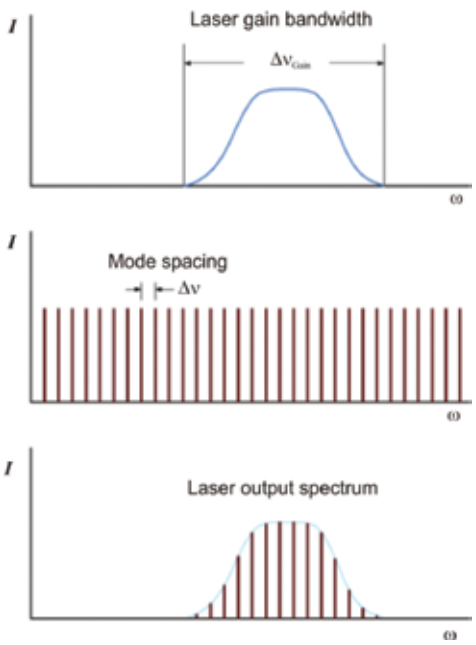

Figure 8. Longitudinal mode structure in mirror-based FEL design.

The mirror design has significant advantage: mirrors naturally select longitudinal modes, which are determined by the integer number of half-periods of the wavelength in between them. The longitudinal modes in optical cavity are equally spaced in frequency and time (see the middle plot in **Figure 8**):

$$\Delta\nu = \frac{c}{2L}, \Delta\tau = \frac{1}{\Delta\nu}. \tag{21}$$

The interval between them depends on the cavity length L (see the middle plot in **Figure 8**).

Taking into account the laser gain bandwidth

$$\Delta\nu_{\text{Gain}} \approx \frac{1}{\tau_{\text{Pulse}}} = \frac{c}{2\Delta} \tag{22}$$

where $\Delta = N\lambda$ (see (10), see the top plot in **Figure 8**) and, imposing it on the longitudinal picture of the middle plot in **Figure 8**, we obtain the laser spectrum as shown in the bottom plot of **Figure 8**. Inside the gain bandwidth, the longitudinal modes of the laser will periodically and constructively interfere with each other when in phase, producing an intense burst of light. These light bursts are separated by the period of time $\tau = 2L/c$, necessary for the light to make

http://dx.doi.org/10.5772/64439

exactly one round trip of the laser cavity; the comb of equally spaced modes in the output spectrum with spacing

$$\Delta\nu_{\text{RoundTrip}} = \Delta\nu = \frac{1}{\tau_{\text{RoundTrip}}}, \text{ where } \tau_{\text{RoundTrip}} = \frac{2L}{c} \tag{23}$$

and L is the cavity size. In other words, only phase-matched wavelengths will constructively interfere and form the modes of the radiation field to create a comb of equally spaced modes in the output frequency spectrum. Such a laser is said to be mode-locked or phase-locked. Mode locking modifies the temporal envelope of the output field from a continuous wave to a series of short, periodically spaced pulses. The homogeneous gain bandwidth of a FEL is determined by the slippage length $\Delta = N\lambda$ (10). This last plays central role in FEL physics. Indeed, it is easy to see that only finite number of longitudinal modes with positive gain N_{Gain} exist: $\Delta\nu_{\text{Gain}} \approx \frac{1}{\tau_{\text{Pulse}}} = \frac{c}{2\Delta}$ (see (21)–(23)), where $\Delta = N\lambda$, λ is the radiated wavelength, and N is the number of the undulator periods. Therefore the number of gained modes reads as follows:

$$N_{\text{Gain}} = \frac{\Delta\nu_{\text{Gain}}}{\Delta\nu_{\text{RoundTrip}}} \approx \frac{L}{\Delta}, \tag{24}$$

and the duration of the pulse is evidently

$$\tau_{\text{Pulse}} \approx \frac{1}{\Delta\nu_{\text{Gain}}} = \frac{\tau_{\text{RoundTrip}}}{N_{\text{Gain}}}. \tag{25}$$

For a Gaussian-shaped pulse, we have $\tau_{\text{Gaussian Pulse}} \cong \frac{0.44}{\Delta\nu_{\text{Gain}}}$. Thus, a laser macro pulse of, to say, microsecond duration consist of a train of short micro pulses, which are picoseconds or less in length. Such a short duration of the pulses is useful for studies of ultrashort physical and chemical processes. It is used for ultrafast spectroscopy and in femto-chemistry. The macro pulses repeat at a repetition ratio, limited by the accelerator usually at 10–100 Hz. The micro pulse repetition rate can vary from several MHz to even THz.

We omit in this work the field gain equations, which are well known and can be found elsewhere, and without derivation we just state the formulation of the Madey's theorem [47], which claims that the gain in the so-called Compton or low-gain regime is proportional to the slope of the spontaneous UR spectrum $f(\nu)$: $G(\nu) \propto \frac{\partial f(\nu)}{\partial \nu}$, $f(\nu) = sinc^2(\nu)$, and, therefore,

$$G(\nu) = -\frac{j}{2}\partial_\nu \left[\sin\frac{\nu}{2}\Big/\frac{\nu}{2}\right]^2, \tag{26}$$

where j is the current density, ν is the detuning parameter (4). **Figure 9** demonstrates the FEL gain; the homogeneous bandwidth is given by $\frac{\Delta\omega}{\omega_0} = \frac{1}{2N}$. In the presence of constant magnetic field, the line shape is described by the Airy-type function $S(\nu_n, \beta) \equiv \int_0^1 d\tau e^{i(\nu_n \tau + \beta \tau^3)}$ and the derivative modifies into $-\partial S^2/\partial \nu_n$. The commonly known shape $-\partial(sinc^2 \nu_n)/\partial \nu_n$ is seen in **Figure 9** in the rear vertical plane, where $\beta = 0$. The constant magnetic field $H_d = \kappa H_0$, where H_0 is the amplitude of the undulator periodic field, produces the bending angle $\theta_H = \frac{2}{\sqrt{3}} \frac{k}{\gamma} \pi N \kappa_1$, resulting in nonzero values of $\beta = \frac{(2\pi n N + \nu_n)(\gamma \theta_H)^2}{1 + (k^2/2) + (\gamma \theta_H)^2}$ [35, 37, 39] and shifts the maximum of the curve to lower frequencies (see **Figure 9**).

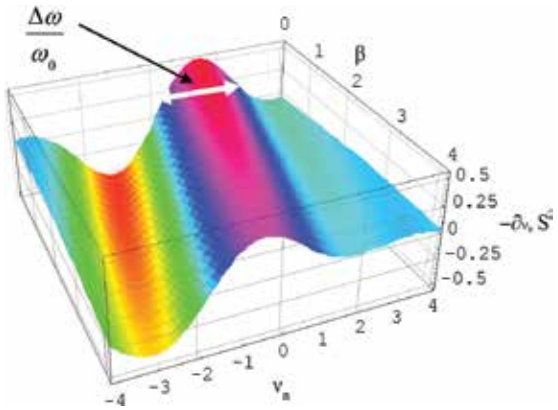

Figure 9. Function $-\frac{\partial(S^2(\nu_n))}{\partial \nu_n}$, which describes FEL gain in an undulator in external field.

6. High-gain single-pass FELs

There are several reasons why it is more difficult to build free-electron lasers for X-ray region that is for larger wavelengths. First of all, for small wavelengths we need high-energy electrons, but high electron energy also increases the gain length $L_G \propto \gamma$, and we must keep the gain length short, as required for an X-FEL. Then, the undulator parameters H_0 and λ_u must be maximized, keeping in mind, however, that λ_u also determines the radiation wavelength: $\lambda \propto \lambda_u/\gamma^2$. Then, the electron beam current i must be high and its transverse cross section σ small. However, the γ-factor cannot be freely decreased if we want to obtain X-ray wavelengths. These challenges can be better faced in single-pass FELs with typical high-gain regime.

In the high-gain regime the radiation power increases exponentially as the electron beam and radiation co-propagate along the FEL undulator, and this happens on a single pass of the radiation along the FEL. These kinds of FELs are sometime called amplifiers, since everything starts from an initially small source, which may originate as noise, and it can be amplified

http://dx.doi.org/10.5772/64439

by many orders of magnitude before the process saturates. In such FEL, there are no mirrors to form an oscillator cavity and this is particularly good for X-ray region, where mirrors are the most compromised element of the cavity-based FEL. Such FEL essentially works as an amplifier, in which the radiation forms on the single pass through a very long undulator, reaching peak pulse power ~ 10^{10} *W* for few dozens of femto-seconds. Overwhelming majority of current X-ray FELs are based on this type of design, which has been made possible due to the twenty-first century advances in magnet technology, accelerator constructions, and electron beam production.

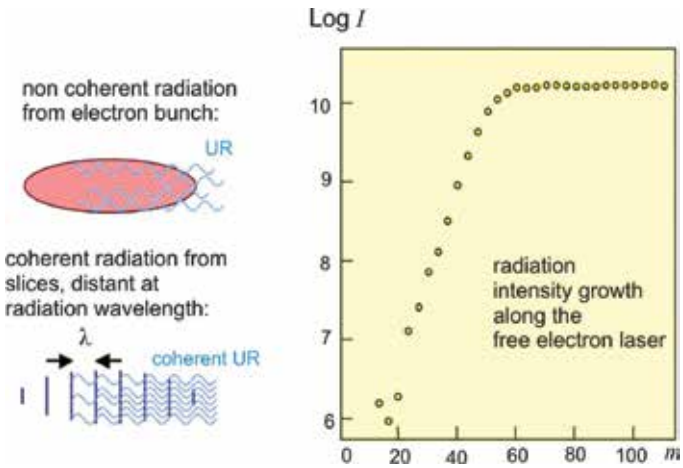

Figure 10. Radiation mechanism in a SASE FEL (amplifier).

The principle of the high-gain FEL interaction is based on the positive feedback process. The electrons emit undulator radiation, which corrects their position in space and their phase with respect to the electromagnetic wave; this groups the electrons on the radiation wavelength scale and thus the more and more coherent radiation is emitted along the undulator. First, the electrons in the bunch have random phases and produce incoherent emission. Already the first waves, emitted by these electrons, trigger formation of microbunches as discussed above (see **Figures 4**, **6** and **10**). Contrary to non-micro-bunched electrons, which emit incoherent waves, the emission of electrons, collected in micro-bunches, which are separated from each other by one wavelength, is correlated (see **Figures 4** and **10**). This causes an exponential intensity increase with the distance that continues until saturation is reached (see **Figure 10**). The schematic drawing in **Figure 10** represents modeling of the performance of the Linac Coherent Light Source—LCLS, with the parameters of the undulator: L = 100 m, λ_u = 3 cm, L_G = 3.3 m, λ = 1.5Å = 0.15 nm. The whole installation has the length of L = 1 km, current I = 3 kA, E = 13.6 GeV, Linac and bunch compression: $\gamma\varepsilon_{x,y}$ = 0.4 μm (slice), σ_E/E = 0.01% (slice).

Simulation of the electron density in a bunch of the electron beam as it develops from the entrance toward the exit of the undulator is demonstrated in **Figure 11**. Left picture simulates the electron density in the bunch at the beginning of the undulator, middle picture

represents the simulation in the middle of the undulator length, and the right picture demonstrates the electron density in the bunch at the end of the undulator.

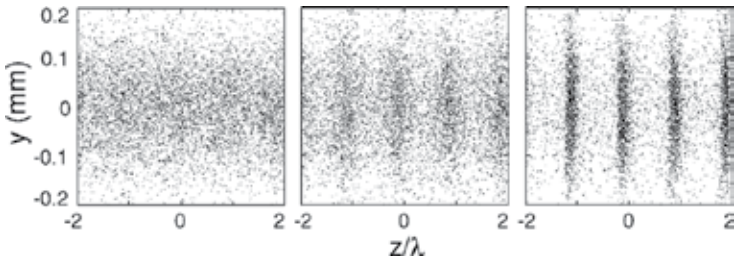

Figure 11. Simulation of the density modulation of the electron beam along the undulator: undulator beginning—left picture, undulator middle—middle picture, undulator end—right picture.

The transverse structure of the electron bunch is much larger than its longitudinal substructure. Note the length between the slices can be of the order of nm, and there can be up to hundreds of thousands of slices in a bunch.

7. Some advanced single-pass FEL schemes

Perhaps, the most common development of the basic SASE FEL scheme, where the amplification starts from noise with random phase, is represented by SASE FEL with seeding. In this case, already at the beginning of the undulator, unbunched electrons with random phase interact with coherent laser seed radiation, which bunches them accordingly. This scheme has the advantage of the stability of the phase, because the process is controlled by the seeding laser.

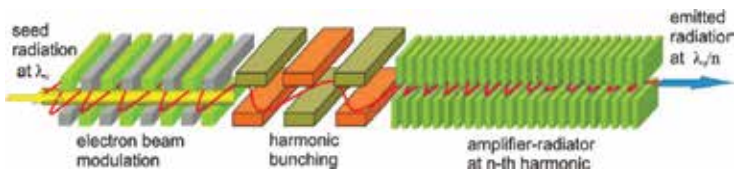

Figure 12. HGHG FEL with laser seed, harmonic generator, buncher, and amplifier.

To achieve extremely high frequencies, for example, those of the X-ray band, the following modification of SASE FEL with high-gain harmonic generation (HGHG) is sometimes employed (see schematic drawing in **Figure 12**).

It consists of the seed laser, harmonic generator, and the amplifier. The coherent seed laser radiation first passes the short undulator, called modulator, which is tuned to the seed frequency. The interaction with the electron beam gives the latter small longitudinal energy modulation. The following section of the installation converts this energy modulation into a

http://dx.doi.org/10.5772/64439

beam density modulation in a magnetic dispersion unit. Then the modulated electron beam and the UR pass the second undulator, which is tuned to the *n*th harmonic of the modulator. When they pass the second undulator, the *n*th harmonic of the UR is fully amplified to saturation levels in this second undulator, frequently called radiator. At the exit the pulses with <20 fs duration can be obtained.

One of the most important advantages of the mirror FEL is the possibility to select optical modes with the help of the mirrors. SASE FEL in its classical scheme is lacking this ability: there are no mirrors, which, in turn, gives other advantages. Together the advantage of the cavity-based mirror design with those of SASE FEL, the magnetic chicanes (small blocks in **Figure 13**) can be introduced between a sequence of undulators (big blocks in **Figure 13**) to impose a sort of mode locking in mirrorless single-pass FEL. The proper scheme is given in **Figure 13**.

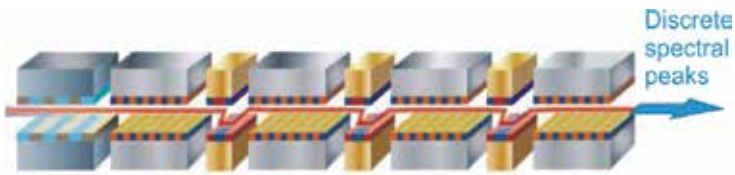

Figure 13. SASE FEL design with chicane mode-locking (big blocks are undulators, small blocks are chicanes).

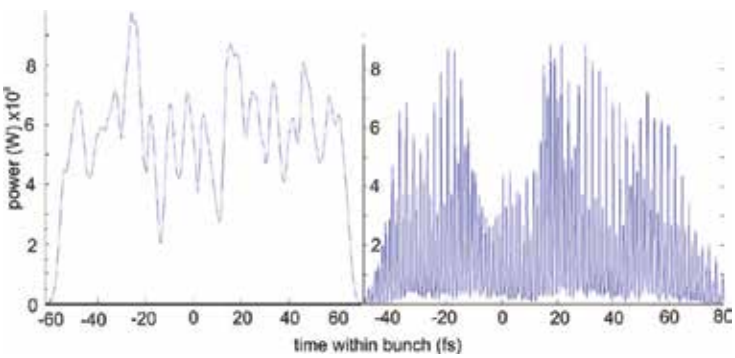

Figure 14. SASE output power after the undulator without (left) and with (right) chicanes.

The magnetic chicanes introduce an extra slippage of the radiation with respect to the electron bunch. Only those radiation wavelengths that have an integer number fit into the relative slippage of the radiation with respect to the electron bunch in one module will remain phase-matched. Only they will constructively interfere over many such modules. In this way form the modes of the radiation field, which create a comb of equally spaced modes in the output frequency spectrum. Such a mode locking can be achieved by the beam energy modulation or by a beam current modulation of the same period. The result is similar to that created by the optical mode locking. We present the example of the power output and the spectrum of a

common SASE FEL (see **Figures 14** and **15** left, respectively) to compare it with the example of the power output and of the spectrum of a FEL with chicane mode locking (see **Figures 14** and **15** right, respectively). Note that instead of the relatively broad SASE FEL spectrum, we now see the series of sharp equidistant peaks. The same regards the output power. At the end of the undulator-chicane line we achieve higher spectral power from the FEL.

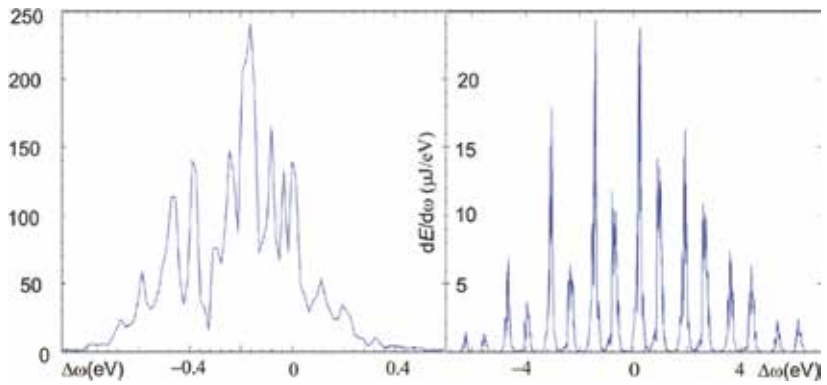

Figure 15. SASE spectrum after the undulator without (left) and with (right) chicanes.

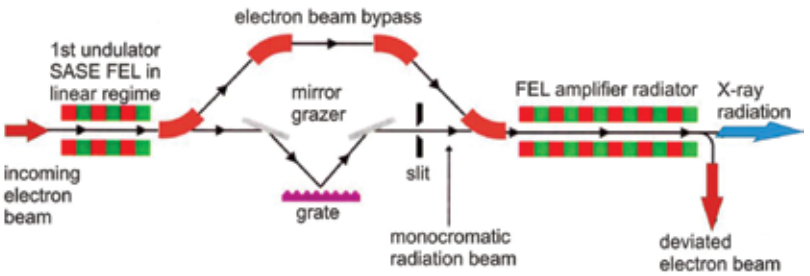

Figure 16. Schematic design of a self seed FEL.

Eventually, we touch on the functioning of the so-called self-seed FEL scheme, demonstrated in **Figure 16**. The advantage of this type of FELs consists in that they are independent of any external radiation source, which must be otherwise very stable and precisely matched to the electron beam in space and time. Both undulators in the self-seed design are tuned to the same frequency. First undulator is in essence a short SASE FEL, which operates in the linear gain regime far from the saturation level. It produces the radiation in the form of typical SASE FEL pulses at the power level approximately 1000 times below the saturation level. Then the electron beam is fed through a magnetic chicane, which eliminates the density modulation, introduced in the first undulator, and delays the electron bunch to match the UR pulse at the next undulator. The radiation from the first undulator, which works in linear regime, is spectrally filtered by a narrow-band grating monochromator. The latter stretches the radiation pulse, where the coherence length now exceeds that of the electron bunch. After all, the

reshaped radiation pulse and the delayed electron bunch meet. The filtered UR becomes the seed for the second undulator—radiator—which amplifies the UR to saturation level.

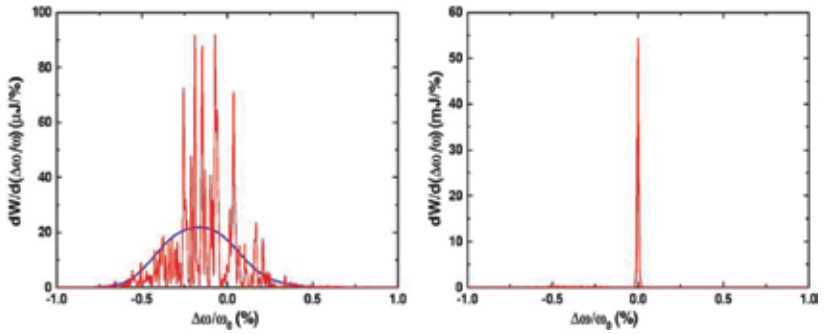

Figure 17. Spectrum after the first SASE FEL and after the second undulator-amplifier.

Not only this FEL is independent on any external radiation source, but due to its design it also produces remarkably good radiation pulses with given characteristics.

In **Figure 17** we demonstrate the example of the output characteristics of such a self-seed FEL. Note that the spectral power distribution after the first (left) and the second undulator (right) differ from each other. The common SASE FEL spectrum (left) is rather broad and consists of many spectral lines even far below the saturation level. The output radiation on the contrary represents a narrow spectral line with only a small background of spontaneous radiation (right). Spectral brightness has increased by almost two orders of magnitude.

8. Challenges and future developments of X-ray FELs

To conclude the review of some of the most prominent for X-FEL schemes, let us formulate main challenges for the X-ray FEL:

1. The radiation wavelength $\lambda = \frac{\lambda_u}{2\gamma^2}\left(1 + \frac{k^2}{2}\right)$ should be reduced to 1 Å. For small wavelengths we need high-energy electrons, but high electron energy also increases the gain length L_G. Longer undulator period λ_u also determines longer radiation wavelength λ and longer gain length L_G.

2. The electron beam energy has to be 10–20 GeV. There is a compromise to contain the gain length and obtain short wave radiation.

3. The gain length $L_G = \frac{1}{\sqrt{3}}\left(\frac{4mc}{\mu e}\frac{\gamma^3\lambda_u}{k^2}\frac{\sigma_r^2}{I}\right)^{1/3}$ has to be contained preferably about of 10 m or so. Note that $\frac{\sigma_r^2}{I} = \frac{\sigma_r^2 L_{\text{bunch}}}{qc}$, where L_{bunch} is the longitudinal size of the bunch and q is the electric charge.

4. The electron beam current I must be high and its transverse cross section σ small. However, the γ-factor cannot be freely decreased if we want to obtain X-ray wavelengths.

5. As follows from the expression for L_G high peak current is requested for it, such as $I \sim$ kA or more.

6. Transverse electron beam size has to be small, possibly $\sigma_R \sim 10$ μm or so.

7. The energy spread of the electron beam σ_e has to be as small as possible, preferably $\sigma_e \approx 10^{-4}$ or less.

8. The electron and the photon beams have to be overlapped properly.

Note also that in the light of the above said the following requirements arise for the electron beam in transverse: low emittance of the beam and preservation of this low emittance; for the longitudinal dimension good compression and acceleration are required. The main negative factors, which affect the amplification, are the electron energy spread, the angular divergence, the transverse electron beam size, the diffraction of the wave and others. The electron energy spread has negative effect on both the amplification and FEL saturation level. Amplification mainly starts with the optimal electron energy, whose γ-factor determines the wavelength. As the energy is transferred from the electrons to the radiated electromagnetic wave, the energy of the electrons naturally decreases. The wave emissions from all the electrons differ from each other, because different electrons have different energies. After the wave-electron interaction, the electron beam energy spread increases and at a certain point it grows to a level, where no gain occurs. Moreover, well before the electrons loose a substantial portion of their energy, they slow down by emitting electro-magnetic energy and change their phase with respect to the wave. Thus they begin to take the energy from the wave rather than giving it.

In conclusion, let us state some areas, where the performance of the X-ray sources of coherent radiation can be further improved. First of all, the temporal coherence of SASE FELs can be improved. The improved temporal coherence would in turn improve the spectral brightness of the sources, which means the users will have more useful photons. The way to accomplish it could consist, for example, in seeding X-FEL from a radiation source with good temporal coherence.

An alternative approach to single-pass high-gain amplifier schemes is to use cavity feedback in a relatively low-gain system. The development of relatively high-reflectivity diamond crystal mirrors in the X-ray regime makes them feasible.

Reducing X-ray pulse durations to the attosecond regime will provide spatiotemporal resolution of atomic processes. Two techniques have so far been reported that can take pulse durations significantly below 100 as toward the atomic unit of time 24 as. The first technique employs a variation of an echo-enabled harmonic generation method and produces pulses of ~20 as duration at a wavelength of 1 nm with the power, which in peaks reaches ~200 MW. The second technique is based on mode-locking in conventional cavity lasers—oscillators. It could generate radiation at 1.5 Å wavelength in sequences of pulses with ~150 as intervals

between them. The peak power in each pulse could reach ~5 GW and the duration of the pulse could be as short as ~20 as.

Eventually, γ-ray FEL would be extremely interesting for studying nuclear processes. This may be the future of X-FEL.

Author details

K. Zhukovsky

Address all correspondence to: zhukovsk@physics.msu.ru

Department of Theoretical Physics, Physical Faculty, M.V. Lomonosov Moscow State University, Leninskie Gory, Moscow

References

[1] Ginzburg VL. "On the radiation of microradiowaves and their absorbtion in the air". *Isvestia Akademii Nauk SSSR (Fizika)*, vol. 11, N 2, 947, 1651.

[2] Motz H, Thon W, Whitehurst RNJ. "Experiments on radiation by fast electron beams". *Appl. Phys.*, vol. 24, 826, 1953.

[3] Artcimovich AL, Pomeranchuk IJ. "Radiation from fast electrons in a magnetic field". *J. Phys. USSR*, vol. 9, 267, 1945.

[4] Ternov IM, Mikhailin VV, Khalilov VR. *Synchrotron Radiation and its Applications*, Harwood Academic Publishers, Chur, London, Paris, New York, 1985.

[5] Alferov DF, Bashmakov YuA, Bessonov EG. "Radiation of relativistic particles in an undulator". *Sov. Phys. Tech. Phys.*, vol. 17, N 9, 1540, 1973.

[6] Alferov DF, Bashmakov UA, Cherenkov PA. "Radiation from relativistic electrons in a magnetic undulator". *Uspehi Fisicheskih Nauk*, vol. 32, 200, 1989.

[7] Bordovitsyn VA (Ed.), *Synchrotron Radiation Theory and its Development: in the Memory of I.M.Ternov*. Series on Synchrotron Radiation Technique and Applications, vol. 5, World Scientific Publishing, Singapore, 1999.

[8] Bessonov EG, Gorbunkov MV, Ishkhanov BS, Kostryukov PV, Maslova Yu YA, Shvedunov VI, Tunkin VG, Vinogradov AV. Laser-electron generator for X-ray applications in science and technology, *Laser Part. Beams*, vol. 26, N 3, 489–495, 2008.

[9] Mcneil BWJ, Thompson NR. X-ray free-electron lasers, *Nat. Photon.*, vol. 4, N 12, 814–821, 2010. doi: 10.1038/nphoton.2010.239.

[10] Sokolov AA, Ternov IM. *Radiation from Relativistic Electrons* (edited by C.W. Kilmister), American Inst. of Physics, New York, 1986.

[11] Feldhaus J, Sonntag B. Strong field laser physics. *Springer Ser. Opt. Sci.*, vol. 134, 91, 2009.

[12] Zholents AA. "Attosecond X-ray pulses from free-electron lasers". *Laser Phys.*, vol. 15, N 6, 855, 2005.

[13] Bessonov EG. Light sources based on relativistic electron and ion beams. *Proc. SPIE*, vol. 6634, 66340X, 2007.

[14] Zhukovsky KV. "Harmonic radiation in a double frequency undulator with account for broadening". *Moscow Univ. Phys. Bull.*, vol. 70, N 4, 232, 2015.

[15] Zhukovsky K. "Undulator radiation in multiple magnetic fields". *Synchrotron: Design, Properties and Applications*, vol. 39, Nova Science Publishers Inc., USA, 2012.

[16] Zhukovsky K. "Harmonic Generation by ultrarelativistic electrons in a planar undulator and the emission-line broadening". *J. Electromagn. Wave*, vol. 29, N 1, 132–142, 2015.

[17] Tripathi S, Mishra G. "Three frequency undulator radiation and free electron laser gain". *Rom. J. Phys.*, vol. 56, N 3–4, 411, 2011.

[18] Mishra G, Gehlot M, Hussain J-K. "Spectral properties of bi-harmonic undulator radiation". *Nucl. Instrum. A*, vol. 603, 495, 2009.

[19] Dattoli G, Mikhailin VV, Ottaviani PL and Zhukovsky K. "Two-frequency undulator and harmonic generation by an ultrarelativistic electron". *J. Appl. Phys.*, vol. 100, 084507, 2006.

[20] D. Iracane and P. Bamas, "Two-frequency wiggler for better control of free-electron-laser dynamics", Phys. Rev. Lett. 67 (1991) 3086.

[21] V. N. Korchuganov, N. U. Sveshikov, N. V. Smolyakov, C. I. Tomin, "Special-purpose radiation sources based on the Siberia-2 storage ring", *J. Surf. Invest.: X-ray, Synchrotron and Neutron Tech.*, Vol.11, p. 22, 2010.

[22] Walker RP. "Interference effects in undulator and wiggler radiation sources". *Nucl. Instrum. Methods*, vol. A335, 328, 1993.

[23] Onuki H, Elleaume P. *Undulators, Wigglers and Their Applications*, Taylor & Francis, New York, 2003.

[24] Vagin PV, Englisch U, Müller T, et al.. "Commissioning experience with insertion devices at PETRA III". *J. Surf. Invest.: X-ray, Synchrotron Neutron Tech.*, vol. 6, N 5, 1055, 2011.

[25] Hussain J, Gupta V, Mishra G. "Effect of two-peak beam energy spread on harmonic undulator radiation and free-electron laser gain". *Nucl. Instrum. A*, vol. 608, 344, 2009.

[26] Reiss HR. "Effect of an intense electromagnetic field on a weekly bound system". *Phys. Rev*., vol. A22, 1786, 1980.

[27] Smolyakov NV. "Focusing properties of a plane wiggler magnetic field". *Nucl. Instrum. A*, vol. 308, 83–85, 1991.

[28] Hussain J, Mishra G. "Harmonic undulator radiations with constant magnetic field". *Opt. Commun*., vol. 335, 126, 2015.

[29] Dattoli G, Mikhailin VV, Zhukovsky KV. "Influence of a constant magnetic field on the radiation of a planar undulator". *Moscow Univ. Phys. Bull.,* vol 64, 507, 2009, c/c of Vestnik Moskovskogo Universiteta Ser. 3 Fizika Astronomiya, vol. 5, 33, 2009.

[30] Mikhailin VV, Zhukovsky KV, Kudiukova AI. "On the radiation of a planar undulator with constant magnetic field on its axis taken into account". *J. Surf. Invest.: X-ray Synchrotron Neutron Tech*., vol. 8, N 3, 422, 2014.

[31] Dattoli G, Mikhailin VV, Zhukovsky K. "Undulator radiation in a periodic magnetic field with a constant component. *"J, Appl. Phys*., vol. 104, 124507, 2008.

[32] K. Zhukovsky, "Emission and tuning of harmonics in a planar two-frequency undulator with account for broadening", *Laser Part. Beams*, 2016, doi: 10.1017/S0263034616000264

[33] Mirian NS, Dattoli G, DiPalma E, Petrillo V. "Production and properties of two-color radiation generated by using a Free-Electron Laser with two orthogonal undulators". *Nucl. Instrum. A*, vol. 767, 227, 2014.

[34] Zhukovsky K. "Inhomogeneous and homogeneous losses and magnetic field effect in planar undulator radiation". *Prog. Electromagn. Res. B*, vol. 59, 245, 2014.

[35] Zhukovsky K. "Analytical account for a planar undulator performance in a constant magnetic field". *J. Electromagn. Wave*, vol. 28, N 15, 1869, 2014.

[36] Zhukovsky KV. "A model for analytical description of magnetic field effects and losses in a planar undulator radiation". *J. Surf. Invest.: X-ray Synchrotron Neutron Tech*., vol. 8, N 5, 1068, 2014.

[37] Zhukovsky K., High harmonic generation in undulators for FEL, *Nuclear Instrum. Methods Phys. Res. B*, vol. 369, 9–14, 2016, DOI: 10.1016/j.nimb.2015.10.041.

[38] Quattromini M, Artioli M, Di Palma E, Petralia A, Giannessi L. Focusing properties of linear undulators, *Phys. Rev. ST Accel. Beams*, vol. 15, 080704, 2012, DOI: 10.1103/PhysRevSTAB.15.080704.

[39] Zhukovsky K. "High harmonic generation in the undulators for free electron lasers". *Opt. Commum*., 353, 35–41, 2015.

[40] Dattoli G, Srivastava HM, Zhukovsky K. "Orthogonality properties of the Hermite and related polynomials". *J. Comput. Appl. Math*., vol. 182, 165–172, 2005.

[41] Dattoli G, Srivastava HM, Zhukovsky K. "A new family of integral transforms and their applications". *Integral Transform. Spec. Funct.*, vol. 17, N 1, 31–37, 2006.

[42] Dattoli G, Zhukovsky K. "Evolution of time dependant linear potentials and non-spreading airy wave packets". *Appl. Math. Comput.*, V 217, 7966–7974, 2011.

[43] Zhukovsky KV. "A method of inverse differential operators using ortogonal polynomials and special functions for solving some types of differential equations and physical problems". *Moscow Univ. Phys. Bull.*, vol. 70, N 2, 93–100, 2015, DOI: 10.3103/S0027134915020137 .

[44] Zhukovsky K. "Solution of some types of differential equations: operational calculus and inverse differential operators". *Sci. World J.*, vol. 2014, 8 pages, 2014, article ID 454865.

[45] Zhukovsky KV. "Operational method of solution of linear non-integer ordinary and partial differential equations". *SpringerPlus*, vol. 5, 119, 2016, DOI: 10.1186/s40064-016-1734-3.

[46] Jackson JD, *Classical Electrodynamics*. 2nd ed., Wiley, New York, 1975.

[47] Madey JMJ. Stimulated emission of bremsstrahlung in a periodic magnetic field. *J. Appl. Phys.*, vol. 42, 1906–1913, 1971.

[48] Margaritondo G, Rebernik Ribic P. A simplified description of X-ray free-electron lasers. *J. Synchrotron Rad.*, vol. 18, 101–108, 2011.